



THÈSE

En vue de l'obtention du

DOCTORAT DE L'UNIVERSITÉ DE TOULOUSE

Délivré par l'Université Toulouse III - Paul Sabatier
Discipline ou spécialité : *Ingénierie des plasmas*

Présentée et soutenue par *Namjun KANG*
Le 12 juillet 2011

Titre : *Modeling and experimental study of low pressure
inductively coupled discharges*

JURY

Président	<i>Olivier Eichwald</i>	<i>Professeur UPS</i>
Rapporteurs	<i>Young dong Park</i> <i>Jean-Paul Booth</i>	<i>Professeur Ajou</i> <i>Directeur de Recherche CNRS</i>
Examineurs	<i>Soo-ghee Oh</i> <i>Freddy Gaboriau</i> <i>André Ricard</i>	<i>Professeur Ajou</i> <i>Maître de Conférences UPS</i> <i>Directeur de Recherche CNRS</i>

Ecole doctorale : *GEET*
Unité de recherche : *UMR 5213*
Directeur(s) de Thèse : *Freddy Gaboriau & Soo-ghee Oh*
Rapporteurs : *Jean-Paul Booth & Young-dong Park*

Abstract

Low pressure inductively coupled plasmas (ICPs) are investigated using theoretical modeling and experimental diagnostic methods. For various ICP discharges, time dependent global (volume averaged) models are developed and a number of diagnostic tools are used.

In a low pressure argon discharge, a new method is proposed to improve the precision of the pressure-dependent electron temperature calculated by the line ratio method. Using the electron energy distribution functions (EEDFs) and the electron density from Langmuir probe, the coefficient of the cascade cross-section are provided as a function of the pressure for argon $4p_1$ and $4p_5$. The effective electron temperature calculated by the corrected cascade cross-section is shown and compared with Langmuir probe results.

The production of argon excited states in the afterglow of pulse discharge is investigated. Experimentally time resolved optical emission spectroscopy (OES), optical absorption spectroscopy (OAS) and Langmuir probe are used to measure the emission of highly excited states, metastable atom density, electron density and electron temperature. From the time dependent global model, it is found that during the pulse-on time the electron impact excitation and the ionization from the ground state and Ar ($3p^54s$) are the dominant population processes for all excited states. On the other hand, during the afterglow the main source of all excited states is the three body electron-ion recombination. As a consequence argon highly excited state can be populated more than during the pulse-on time.

The E - H mode transition and hysteresis in low pressure argon inductively coupled discharges are investigated using the previous global model and a transformer model. The total absorbed power by plasma electrons and coil current are calculated as a function of the electron density at fixed injected power. We found that the transition is due to the difference of the absorbed power between the two modes. Moreover the calculation results show that the existence of an inaccessible region between E and H mode, as well as a threshold coil current and a minimum absorbed power for the H mode.

The dissociation of the nitrogen molecule in an Ar- N_2 ICP discharge is studied both experimentally and theoretically. Using the two-photon absorption laser-induced fluorescence (TALIF) an increase of the dissociation rate in highly Ar-diluted region is observed. A complete kinetic model is developed to understand the behavior of the Ar- N_2 discharge. The calculated results are compared with the measured results, obtaining reasonably good agreement. In pure nitrogen discharge the N atoms are mainly created by electron impact dissociation at low pressure (20 mTorr) while it is due to metastable-metastable pooling dissociation at high pressure (200 mTorr). In Ar- N_2 discharge, the N atom density increases despite less amount of N_2 molecule in highly Ar-diluted region at 200 mTorr. From the model the charge transfer from Ar^+ to N_2 is an important source of nitrogen dissociation in Ar- N_2 discharge.

The global kinetic models are developed in low pressure He, Ne, Ar and Xe discharges to calculate the electron temperature and the electron density. The calculated results are compared with experiments and the dominant creation sources and the routes of loss for electron and metastable atoms are discussed as function of pressure. Finally the transformer model is used to calculate the electrical properties of He, Ne, Ar and Xe discharges.

Contents

Abstract	i
List of figures	vii
List of tables	xiii
1. General introduction	1
1.1 The fourth state of matter: plasma	2
1.2 The science of plasma processing	2
1.3 DC glow discharge	6
1.4 High frequency discharge	7
1.5 Aim of this work and outline	9
1.6 References	11
2. Characteristic of ICP discharge	13
2.1 Introduction	14
2.2 Heating mechanism in RF inductive discharge	14
2.2.1 Effective electrical conductivity and effective collision frequency	14
2.2.2 Classical skin effect	17
2.2.3 Anomalous skin effect	18
2.2.4 Ohmic (collisional) and stochastic (collisionless) heating	20
2.3 The power transferred to the plasma electrons in TCP reactor	21
2.4 Transformer model and plasma impedance	24
2.5 References	28
3. Global (volume averaged) model	29
3.1 Introduction.	30
3.2 Power balance	31
3.2.1 Energy loss by collision	31
3.2.2 Energy loss by diffusion to the wall	32
3.3 Particle balance	35
3.3.1 Electron impact excitation coefficient	35
3.3.2 Radiative decay.	35
3.3.3 Diffusion loss.	37
3.3.4 Pumping loss	37
3.4 References	38

4. Survey of plasma diagnostic methods	41
4.1 Introduction.	42
4.2 Optical emission spectroscopy (OES)	42
4.2.1 Principle	42
4.2.2 Emission intensity in the corona model and line ratios method . .	43
4.2.3 Molecular spectroscopy.	44
4.2.3.1 Rotational spectra.	44
4.2.3.2 Vibrational spectra	46
4.2.3.3 Spectra of diatomic molecules	47
4.2.3.4 Ro-vibrational spectra of N_2 and N_2^+	48
4.3 Optical absorption spectroscopy (OAS)	54
4.4 Two-photon absorption laser-induced fluorescence (TALIF)	56
4.4.1 Principle	57
4.4.2 Measurement of absolute density.	57
4.5 Langmuir probe.	59
4.6 References	63
 5. Low pressure argon ICP discharge	 65
5.1 Introduction	66
5.2 Experimental setup	67
5.3 Determination of the electron temperature in a planar inductive argon plasma with emission spectroscopy and electrostatic probe	68
5.3.1 Measurement of EEPF and optical emission	68
5.3.2 Radiation trapping and line ratio method.	70
5.3.3 Pressure dependence of the cascade cross-section	71
5.4 Modeling and experimental study of pulse modulated ICP afterglow: production of Ar highly excited states	74
5.4.1 Experiments.	74
5.4.2 Discharge model	78
5.4.3 Results and discussion	80
5.4.3.1 Electron density and electron temperature in continuous mode	80
5.4.3.2 Electron temperature and electron density in pulse mode	81
5.4.3.3 Ar excited states in pulse mode.	83
5.5 Modeling of E-H mode transition and hysteresis in low pressure argon ICP discharges	91
5.5.1 E-H mode transition and hysteresis.	91
5.5.2 Discharge model	91

5.5.3	Results and discussion	92
5.6	Conclusion	95
5.7	References	97
6.	Modeling and experimental study of molecular nitrogen dissociation in an Ar-N₂ ICP discharge	101
6.1	Introduction	102
6.2	Experiment	102
6.2.1	Measurement of electron temperature and electron density	102
6.2.2	Measurement of Ar (3p ⁵ 4s) density and emission intensity	103
6.2.3	Measurement of atomic nitrogen density by TALIF	104
6.3	Discharge model	106
6.4	Results and discussion	110
6.4.1	Pure nitrogen discharge	110
6.4.2	Ar-N ₂ discharge.	114
6.4.2.1	Electron temperature and charged particles density	114
6.4.2.2	Ar(3p ⁵ 4s) density	117
6.4.2.3	Production of N ₂ (C ³ Π _u) excited molecules	117
6.4.2.4	Production of N(⁴ S).	120
6.5	Conclusion	123
6.6	References	129
7.	Experimental and electrical characteristics of inductively coupled He, Ne, Ar and Xe discharges	131
7.1	Introduction	132
7.2	Experiment	132
7.3	Global model of pure rare gases	134
7.4	Transformer model	137
7.4.1	Effective collision frequency.	138
7.4.2	Skin depth.	138
7.4.3	Plasma impedance	139
7.5	Results and discussion	141
7.5.1	Electron temperature and electron density	142
7.5.2	Metastable atoms	144
7.5.3	Plasma impedance	147
7.6	Conclusion	148
7.7	References	152

8. General conclusion	155
Appendix – Electromagnetic field in TCP reactor	159
A.1 Capacitive coupled discharge	160
A.2 Inductive coupled discharge	162
Curriculum vitae	165

List of Figures

1.1	Space and laboratory plasmas on a $\log n$ versus $\log T_e$ diagram	3
1.2	Transistor counts for integrated circuits plotted against their dates of introduction. The curve shows Moore's law; the doubling of transistor counts every two years	4
1.3	V-I characteristic curve in DC glow discharge	6
1.4	Schematic of (a) parallel-plate capacitive discharge, called a Reactive Ion Etcher (RIE) and (b) transformer coupled plasma (TCP)	8
2.1	Variations of v_{eff}/v_{dc} and ω_{eff}/ω as a function of pressure for different electron temperatures T_e (Maxwellian distribution) of (a) argon and (b) nitrogen gas. . .	16
2.2	The parameter Λ as a function of ω/ν . The anomalous skin effect takes place in the frequency range $\omega_1 < \omega < \omega_2$	19
2.3	Calculated transferred power by capacitive coupling, inductive coupling, stochastic heating and total transferred power at 100 mTorr argon pressure, $T_e = 2.0$ eV and 1 A coil current	22
2.4	(a) Calculated total transferred power at 5 A coil current and $T_e = 2.0$ eV for various argon pressure and (b) total transferred power and the effective frequencies v_{eff} and ω_{eff} as a function of gas pressure at fixed electron density 10^{17} m^{-3} and 5 A coil current	23
2.5	The circuit representation of the discharge which allows for both inductive and capacitive coupling of RF power to the plasma	25
2.6	The equivalent circuit	26
3.1	Calculated escape factors for $\lambda = 104.8 \text{ nm}$ and $\lambda = 106.7 \text{ nm}$ resonance lines of argon as a function of gas pressure	36
4.1	Classification of the cross section	42
4.2	Measured and calculated typical emission spectra of SPS $N_2(C^3\Pi_u, v - B^3\Pi_g, v')$ and FNS $N_2(B^2\Sigma_u^+, v - X^2\Sigma_g^+, v')$	49
4.3	(a) Measured rotational spectra of N_2^+ FNS in an ICP discharge at 100 mTorr and calculated rotational spectra with 0.3 \AA of FWHM at 550 K. (b) Linear fitting of $-\ln[I_j/(2J+1)]$ as function of E_r/k with measured data.	50

4.4	Calculated rotational spectrum of P , Q and R branches and corresponding Fortrat diagram of $N_2(C^3\Pi_u, v' = 0 - B^3\Pi_g, v'' = 0)$	51
4.5	Measured vibrational spectra of (a) the second positive system (SPS), (b) the first positive system (FPS) and (c) the first negative system (FNS) in the nitrogen ICP discharge at 100 mTorr. (d) Correspond vibrational distributions by normalizing $[N_2(C,0)] = 1$, $[N_2(B,3)] = 1$ and $[N_2^+(B,0)] = 1$ for $N_2(C^3\Pi_u)$, $N_2(B^3\Pi_g)$ and $N_2^+(B^2\Sigma_u^+)$	52
4.6	Calculated optical depth $k_{\sigma\theta}L$ variations versus the absorption coefficient for α values between 0 and 5	56
4.7	Energy diagram for typical LIF excitation of (a) atom, (b) a diatomic molecule, radical or ion, and (c) a multiphoton transition	57
4.8	Schematic diagram of a typical arrangement used in LIF diagnostics	58
4.9	An idealized I - V curve. The left curve is expanded 10 \times to show the ion current.	59
4.10	(a) Typical probe I - V characteristic and its second derivative measured in an argon ICP discharge at 20 mTorr, and (b) the semi-log plot of the EEPF from the I - V curve	61
4.11	Measured I_p curves at each fixed probe voltage in a pulse modulated argon RF discharge (pressure = 20 mTorr, frequency = 500 Hz)	62
5.1	Schematic diagram of the TCP chamber and diagnostics system	68
5.2	Evolution of the EEPF with the argon pressure ranging from 3 to 100 mTorr for an argon inductively coupled discharge at a RF frequency of 13 MHz and a power of 200 Watt	69
5.3	(a) Effective electron temperature T_{eff} of the EEPF in figure 5.2 against the pressure, and (b) measured electron density.	70
5.4	Pressure dependence of $\alpha(P)$, the coefficient of the cascade cross-section; $\sigma^{app}(E,P) = \sigma^{dir}(E) + \alpha(P)\sigma^{cas}(E)$. $\alpha(P) = 1$ at 3 mTorr. The open squares are for 4p ₁ (750.4 nm) and the solid circles for 4p ₅ (751.5 nm).	72
5.5	Solid circles, which are T_e according to the line ratio with non-corrected cross-sections, are substantially below the open squares T_e according to the line ratio with corrected cross-sections. The trend of the pressure dependence of the electron temperature from the line ratio with the corrected cross-sections is identical to that of the effective electron temperature from the single Langmuir probe (solid line)	73
5.6	Calculated rotational spectra of $N_2(B,2-A,0)$ first positive band for different set of T_{rot} and full width half maximum (FWHM) values	75

5.7	(a) The intensity ratio of the two P_1 , P_2 peaks with the resolution from 0.05 nm to 0.15 nm, and (b) the measured rotational spectra of the hollow cathode lamp and plasma	77
5.8	Energy level scheme of the argon atom excited levels used in the model	78
5.9	Measured and calculated electron density and electron temperature in continuous mode plasma varying pressure from 10 mTorr to 200 mTorr.	80
5.10	Calculated and measured temporal (a) electron temperature, (b) electron density at 10 mTorr and 200 mTorr and (c) temporal net loss rate for electron at 200 mTorr; lighter curve indicates negative loss	82
5.11	Calculated and measured temporal atom density of (a) Ar ($1s_5$), (b) Ar ($1s_4$) at 10 mTorr and 200 mTorr and (c) net production rate of each reaction for Ar ($1s_5$) at 200 mTorr	84
5.12	Calculated and measured temporal atom density and emission intensity of (a) Ar 4p, (b) Ar(5p) and (c) Ar ^{**}	85
5.13	Calculated reaction rates for R15 and R16 vs. time in the afterglow at 200 mTorr	86
5.14	Variation of (a) the absorbed power P_{abs} and the loss power P_{loss} by electrons and (b) the coil current i_{coil} as a function of the electron density n_e at different fixed source applied powers from 5 to 50 Watts	93
5.15	Variation of the absorbed power P_{abs} as a function of the electron density. The steady state was first calculated for 20 Watts applied power and then from this steady point ($n_e = 1 \times 10^{17} \text{ m}^{-3}$) the applied power was decreased to 13, 10, 8 and 5 Watt	94
5.16	The calculated electron density versus the coil current as shown experimentally by Kortshagen <i>et al</i>	94
6.1	The measured substrate temperature by thermocouple in Ar-N ₂ mixed discharge	103
6.2	Simplified energy level diagrams of atomic nitrogen and krypton indicating the excitation scheme and the observed fluorescence wavelength	104
6.3	Time variation of absolute nitrogen atomic density during pulse-off period at 20 mTorr and 200 mTorr in the pure nitrogen discharge	105
6.4	Measured EEPFs in Ar-N ₂ discharges at (a) 20 mTorr and (b) 200 mTorr	107
6.5	Measured and calculated diffusion loss rates of N atoms for various γ_n at 400 K gas temperature. The measured sticking coefficient is around 0.02.	108
6.6	Flow chart of calculation algorithm	109

6.7	(a) Calculated and measured electron temperature and electron density, (b) calculated collisional energy loss per electron – ion pair created versus electron temperature assuming a Maxwellian electron energy distribution, and (c) calculated charged particle densities versus pressure at fixed RF power in pure nitrogen discharge	111
6.8	(a) Calculated and measured absolute N atom density and dissociation fraction, (b) calculated relative production rates for creation of N atoms, and (c) calculated rate coefficients of electron impact excitation to $N_2(A^3\Sigma_u^+)$, electron impact ionization, electron impact dissociation and electron-ion dissociative recombination as function of mean electron energy.	112
6.9	Calculated and measured (a) electron temperature and (b) electron density as a function of the N_2 fraction at 20 mTorr, 50 mTorr and 200 mTorr	115
6.10	Calculated density of charged particles versus N_2 fraction at (a) 20 mTorr, (b) 200 mTorr and (c) relative loss rates of Ar^+ by the ambipolar diffusion (R114) and the charge transfer between Ar^+ and N_2 (R108) at 20 mTorr, 50 mTorr and 200 mTorr	116
6.11	Calculated and measured (a) metastable state $Ar(1s_5)$, (b) resonance state $Ar(1s_4)$ atom densities, (c) Measured emission intensity of $N_2(C^3\Pi_u)-N_2(B^3\Pi_g)$ and calculated density of $N_2(C^3\Pi_u)$ versus N_2 fraction at 20 mTorr, 50 mTorr and 200 mTorr. (d) Change of relative production rates from 20 mTorr (black line) to 200 mTorr (lighter line) of $N_2(C^3\Pi_u)$ by electron impact excitation (R7), metastable-metastable excitation (R57) and excitation transfer (R109 ~ R112)	118
6.12	Calculated and measured (a) absolute N atom density and (b) dissociation fraction function of N_2 mixing ratio at 20mTorr, 50 mTorr and 200 mTorr. Calculated relative production rate of N atoms at (c) 20 mTorr and (d) 200 mTorr	121
7.1	Measured rotational spectrum of N_2 1 st positive (B,0-A,2) band from the Ar- N_2 and Xe- N_2 mixture discharge	133
7.2	Calculated ε_c as a function of T_e for Ar, He, Ne and Xe, when assuming a Maxwellian electron energy distribution	135
7.3	Measured EEPFs at pressure of 50 mTorr.	136
7.4	Calculated escape factors of $He(2^1P-1^1S, \lambda = 58.4 \text{ nm})$, $Ne(^3P_1-^1S_0, \lambda = 74.4 \text{ nm})$, $Ar(^3P_1-^1S_0, \lambda = 106.7 \text{ nm})$ and $Xe(^3P_1-^1S_0, \lambda = 147.0 \text{ nm})$ as a function of the pressure	137
7.5	The equivalent circuit used in the transformer model.	137
7.6	The flow chart of calculation algorithm	141

7.7	Measured and calculated (a) electron temperature and (b) electron density versus pressure at a fixed RF power in pure He, Ne, Ar and Xe discharge . . .	143
7.8	Calculated relative production rate of the atomic ion by the direct electron impact ionization from ground state (R7), the electron impact ionization from excited states (R8-R10) and ionization by excited particle collision (R21-R22).	144
7.9	Calculated and measured metastable atom density from the absorption spectroscopy of He(2^3S), Ne($1s_5$), Ar($1s_5$) and Xe($1s_5$) as a function of the gas pressure	145
7.10	Calculated loss frequencies of He, Ne, Ar and Xe metastable atoms by diffusion as well as those by electron collision	146
7.11	Calculated ratio of (a) electron-neutral collision frequency to the effective collision frequency (b) effective collision frequency to the effective driving frequency versus pressure for He, Ne, Ar and Xe discharges.	147
7.12	Calculated the resistance R_p , and the inductance L_p , in He, Ne, Ar and Xe discharges	148
A.1	A schematic diagram of the planar ICP reactor used in this study	159

List of Tables

3.1	The developed global models for various gas mixture and discharge sources . . .	30
3.2	Useful experimental and theoretical literatures in the global model	31
4.1	The spectroscopic constant terms (cm^{-1}) of N_2 excited states	51
4.2	The wavelength and the transition probability of second positive system (SPS), $N_2(C^3\Pi_u, v - B^3\Pi_g, v')$, $\Delta v = -2$	53
4.3	The wavelength and the transition probability of the first positive system (FPS), $N_2(B^3\Pi_g, v - A^3\Sigma_u^+, v')$, $\Delta v = +3$	53
4.4	The wavelength and the transition probability of the first negative system (FNS), $N_2^+(B^2\Sigma_u^+, v - X^2\Sigma_g^+, v')$, $\Delta v = -2$	54
5.1	Reaction set used in the model.	88
5.2	Relative contributions of the most important population and loss processes during pulse on time and afterglow	89
6.1	The species used in the discharge model	106
6.2	Reaction set used in the discharge model	124
7.1	Selected spectral lines and spectroscopic data of rare gases used for the resonant absorption measurement	133
7.2	Species used in the discharge model	134
7.3	Reaction set used in the model	150
7.4	Reaction set used in the model	151

Chapter 1

General introduction

Contents

1.1	The fourth state of matter: plasma	2
1.2	The science of plasma processing	2
1.3	DC glow discharge	6
1.4	High frequency discharge	7
1.5	Aim of this work and outline	9
1.6	References	11

1.1 The fourth state of matter: plasma

PLASMA is the most common form of matter in the universe and it is often considered the fourth state of matter. As we know, a solid substance in thermal equilibrium generally passes into a liquid state as the temperature is increased at a fixed pressure. The liquid passes into a gas as the temperature is further increased. At a sufficiently high temperature, the molecules in the gas decompose to form a gas of atoms that move freely in random directions, except for infrequent collisions between atoms. If the temperature is further increased, then the atoms decompose into freely moving charged particles (electrons and positive ions), and the substance enters the plasma state. So plasma is a partially or fully ionized gas, but plasma must be a quasi-neutral gas of charged and neutral particles which exhibit collective behavior. The quasi-neutrality means that the same amount of positive and negative charged particles $n_i \approx n_e$, is probably the most important characteristic of a plasma. In a plasma, the different species (ions, electrons, and neutrals) have different temperatures: T_i , T_e and T_g . Parameters such as the degree of ionization (ratio of ions to neutral particles density, $n_i / (n_i + n_g)$), density of electrons n_e , and the electron temperature T_e can be used to characterize a plasma in a broad sense. Figure 1.1 identifies different kinds of plasmas on a $\log n$ versus $\log T_e$ diagram. In this work we study a very specific type of plasmas, generally called “cold plasma” or “low pressure discharges”. The typical pressure range of such a discharge is 1 mTorr \sim 1 Torr, and the ionization degree is 0.1 \sim 1 %. As a consequence of the very low charged-to-neutral particle ratio, collisions of electrons with neutrals are very important and often dominant over charged-charged particle collisions for the determination of the electron transport parameters. These discharges are characterized by $T_e \approx 1 \sim 10$ eV, and $n_e \approx 10^8 \sim 10^{13}$ cm $^{-3}$. Such discharges are sustained in a non-equilibrium steady state by the electric field that allows the ion temperature to be much lower than the electron temperature $T_i \ll T_e$. In most cases the electrons are close enough to thermal equilibrium that their temperature is relatively well-defined, even when there is a significant deviation from a Maxwellian distribution. Due to the large difference in mass, the electrons come to thermodynamic equilibrium among themselves much faster than they come into equilibrium with the ions or neutral atoms. For this reason, the ion temperature is different from (usually lower than) the electron temperature.

1.2 The science of plasma processing

Plasma processing is the most widely used chemical process in microelectronic industry for thin film deposition and etching. Its application extends to surface cleaning and modification, flat panel display fabrication, plasma micro discharge and many other rapidly growing areas. Plasma processing is a combination of several different branches of science such as plasma physics, gas-phase chemistry, atomic and molecular physics, and surface science [3-5].

The number of industrial applications of plasma-based systems for processing of materials and for surface modification is extensive, and many industries are impacted. Some of these processes and corresponding applications are following:

- Plasma-controlled anisotropic etching in the fabrication of microelectronic chips.

- Plasma deposition of silicon nitride for surface passivation and insulation.
- Surface oxidation used in the fabrication of silicon-based microelectronic circuits.
- Plasma-enhanced chemical vapor deposition of amorphous silicon films used in solar cells.
- Plasma-surface treatment for improved film adhesion to polymer surfaces.
- Plasma nitriding, which is used to harden the surface of steel.
- Plasma-enhanced chemical vapor deposition and thermal plasma chemical vapor deposition of diamond thin films.
- Plasma spray deposition of ceramic or metal alloy coatings used for protection against wear of corrosion in aircraft and automotive engines.
- Plasma spray deposition of clearance control coatings.
- Plasma melting and refining of alloys.
- Plasma-assisted manufacture of optical fibers used in communications.

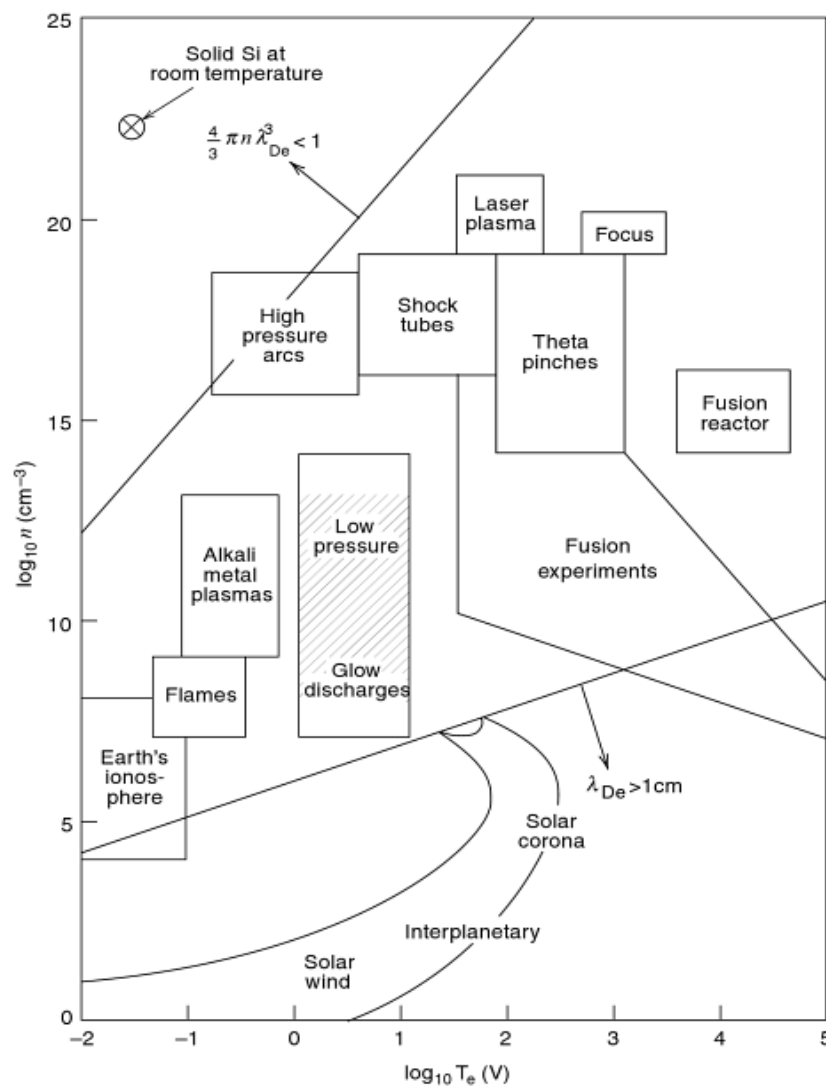


Figure 1.1 Space and laboratory plasmas on a $\log n$ versus $\log T_e$ diagram adapted from references [1,2]. The shaded area indicates the regions studied in this study

- Plasma synthesis of ultrapure powders used as ceramic precursors.
- Plasma spray deposition and thermal plasma chemical vapor deposition of high-temperature superconductors and refractory materials.
- Plasma welding and cutting.
- Plasma sputter deposition of magnetic films for memory devices.

In each case, the plasma is used as a source of ions and/or reactive neutrals, and is sustained in a reactor so as to control the flux of neutrals and ions to a surface.

The science of plasma processing is largely motivated by the semiconductor industry that for the past three decades has been accelerating towards faster computing and larger memory volumes. Moore's law has characterized the microelectronics industry since 1980, when Gordon Moore observed that the number of transistors in microprocessors doubles every 18 months, and it was extended to 24 months to compensate for expected increases in the complexity of semiconductors (see figure 1.2). The industry has obeyed Moore's law for over 20 generations. This has lead to smaller devices and features and improved capabilities over the years. The process of fabricating these devices involves hundreds of steps while critical dimensions have shrunk to 10's of Å (a few atomic mono-layers).

In plasma etching, the plasma produces both highly reactive neutrals and ions that

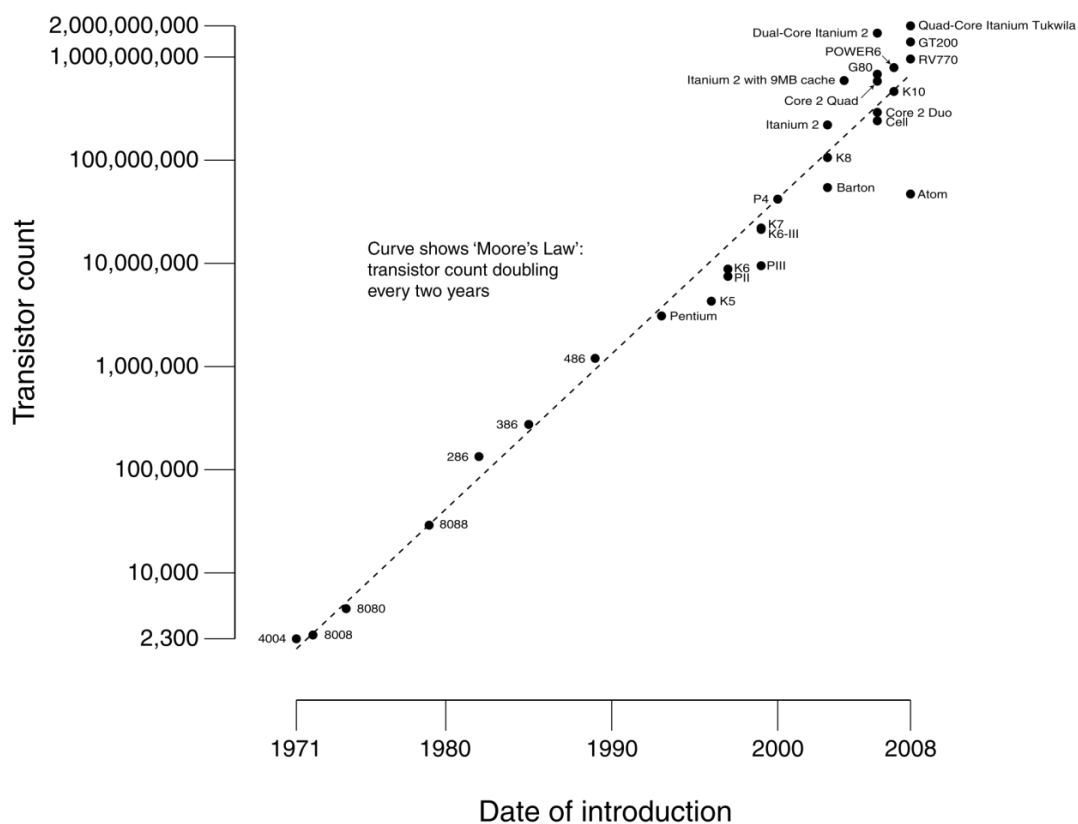


Figure 1.2 Transistor counts for integrated circuits plotted against their dates of introduction. The dotted line shows Moore's law: the doubling of transistor counts every two years.

bombard the surface being etched. The process can be chemically selective, removing one type of material while leaving other materials unaffected, and can be anisotropic, removing material at the bottom of a trench while leaving the same material on the sidewalls unaffected. The neutrals react with the surface to produce volatile species that absorb and are pumped away. Ion bombardment often increases the etching rate by removing surface contaminants that block the etching or by directly enhancing the kinetics of the etching. Directional plasma etching processes must be used to pattern such features to obtain the necessary fidelity of pattern transfer. Wet etching processes and chemical based plasma etching processes are typically isotropic, and produce undercutting of the pattern at least equal to the film thickness.

Reactive ion etching (RIE) consists of bombarding the material to be etched with highly energetic chemically reactive ions. Such bombardments with energetic ions dislodge atoms from the material, in effect achieving material removal by sputtering. In addition to sputter-removal, the bombarding ions used in RIE were chosen so that they will chemically react with the material being bombarded to produce highly volatile reaction byproducts that can simply be pumped out of the system. This is the reason why RIE is widely used in wafer fabrication; it achieves the required anisotropy (by means of sputter-removal) and the required selectivity (through chemical reactions).

Plasma-assisted deposition, implantation, and surface modification are important material processes for producing films on surfaces and modifying their properties. The deposition processes can be divided into two large groups, namely the Physical Vapor Deposition (PVD) and Chemical Vapor Deposition (CVD), in which plasma is utilized extensively in order to improve the process characteristics. The PVD techniques can be subdivide further into:

- Cathodic Arc Deposition, in which a high power arc discharge the target material blasts away some into highly ionized vapor
- Electron Beam Physical Vapor Deposition, in which the material to be deposited is heated to a high vapor pressure by electron bombardment in high vacuum
- Evaporative Deposition, in which the material to be deposited is heated to a high vapor pressure by electrically resistive heating in low vacuum
- Pulsed Laser Deposition, in which a high power laser ablates material from the target into a vapor
- Sputter Deposition, in which a glow plasma discharge (usually localized around the “target” by a magnet) bombards the material sputtering some away as a vapor

Also PVD coating is used to improve hardness, wear resistance and to reduce friction. The use of such coatings is aimed at improving efficiency through improved performance and longer component life.

CVD processes normally involve the chemical processing for producing of high-purity solid materials including thin film, but in some cases CVD is enhanced by plasma. These cases normally refer to as Plasma-Enhanced CVD (PECVD), which are the CVD processes that utilize a plasma to enhance chemical reaction rates of the precursors. PECVD uses a discharge to reduce the temperature at which films can be deposited from gaseous reactants through the creation of free radicals and other excited species that react at lower temperatures

within the gas-phase and on the surface. The quality of the deposited film often can be improved by the use of the plasma ion flux to clean the surface before the deposition begins and by heating during processing. In addition, the ion flux can alter the film during deposition by cleaning, enhancing the mobility of adsorbed species.

Plasma implantation can introduce elements into the surface of the materials without thermodynamic constraints. In particular, plasma immersion ion implantation (PIII), sometimes also referred to as plasma implantation, the specimens are surrounded by a high-density plasma and pulse biased to a high negative potential relative to the chamber wall. Ions generated in the overlying plasma are accelerated across the sheath formed around the samples and implanted into the surface of the targets. Plasma implantation has many potential applications in biomaterials engineering. For example, sample possessing a sophisticated shape can be treated with good conformality and uniformity without beam scanning and special target manipulation. In addition, multiple processes such as simultaneous and consecutive implantation, deposition, and etching are possible by varying the instrumental parameters without breaking vacuum.

1.3 DC glow discharge

The direct current (DC) glow discharge has been studied for a long time. It works in a glass tube filled with a given gas at low pressure, between two electrodes, called cathode and anode [6]. The potential (V) between the two electrodes is related to the discharge current (I) by $V = V_0 - RI$ where R is the charge resistance and V_0 is the voltage applied to the cathode.

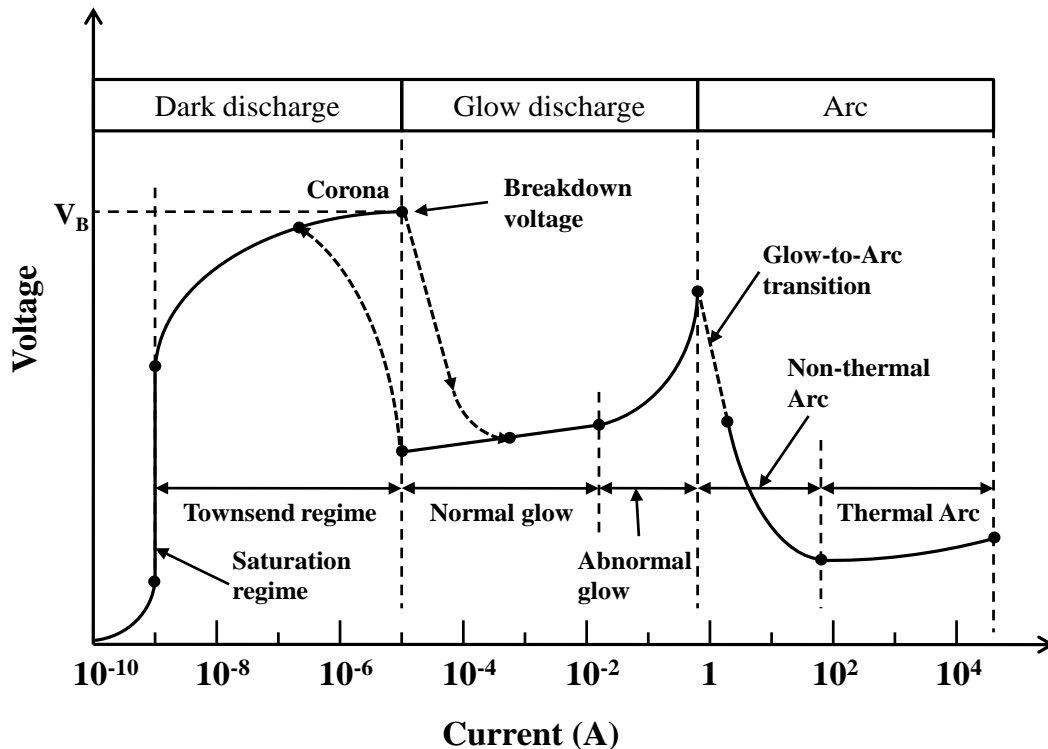


Figure 1.3 V-I characteristic curve in DC glow discharge.

The V-I curve as schematized in figure 1.3, is the discharge characteristic for a given gas. The resistance (R) value must be sufficiently high to obtain a stable working point. This stable working point will be easy to find in the growing part of the V-I characteristic, called the glow discharge. A increasing the current the breakdown occurs at the end of the Townsend regime, and then the voltage decreases and becomes stable. This regime corresponds to a normal glow discharge in which the voltage slightly increases with the current. In the abnormal glow regime the voltage increases steeply with current, this regime is established until the arc transition at high discharge currents. In the arc regime, the voltage is weak and the discharge current is strong.

1.4 High frequency discharge

High frequency discharge or radio-frequency is one of the most widely used discharge types for film treatment. This is because it is able to produce a large volume of stable plasma [7,8]. Using an alternative current (AC) the displacement current will flow through the electrode whether it is dielectric or not and so the discharge can be sustained. In AC discharge the positive charge accumulated during one half-cycle can be neutralized by electron bombardment during the next half cycle. For the power source, whole range of frequencies can be available. If the frequency exceeds about 300 kHz, the high frequency power can be supplied from an external electrode to the load. This can be done through a discharge tube which is made of glass (usually quartz) because of its heat resisting property and low dielectric loss. The high frequency discharge is also called the *electrodeless discharge*, because the external electrode is not directly in contact with the plasma. It makes possible to reduce the effect of the electrode materials, such as metal impurities on the plasma processing. The frequency most often chosen is 13.56 MHz. At this frequency the plasma impedance is relatively low. This frequency is allowed for industrial, scientific and medical uses by international communications authorities. However, the discharge system including the high frequency generator radiates many harmonics of the parent frequency. Such high frequencies as 13.56 MHz can cause problems in electronics, especially instruments used for precise measurements. The operating frequency affects the composition, the densities and the potentials of the plasma and therefore has a strong influence on the properties of the deposited films.

The high frequency discharges have been classified onto two types according to the method of coupling the high frequency power with the load: the capacitive coupled plasma (CCP) and the inductively coupled plasma (ICP). In the capacitive coupled plasma, one of the most widely used low pressure discharge is sustained by RF currents and voltages applied directly to an electrode immersed in the plasma. This creates a high voltage capacitive sheath between the electrode and the bulk plasma. The RF currents flowing across the sheath and the bulk plasma led to stochastic or collisionless heating in the sheath and ohmic heating in the bulk. Inductive coupled discharges are nearly as old as the invention of electric power, with the first report of an “electrodeless ring discharge” by Hittorf in 1884 [9]. He wrapped a coil around an evacuated tube and observed a discharge when the coil was excited with a Leyden jar. Inductive coupled discharges have two main advantages: no internal electrodes are

needed as in capacitively coupled systems and no dc magnetic field is required. These benefits make ICPs probably the most common of the plasma tools. These devices come in many different configurations. In the simplest form, the antenna consists of one or several turns of water-cooled tubing wrapped around a ceramic cylinder, which forms the sidewall of the plasma chamber. Another configuration called the transformer coupled plasma (TCP) uses a top-mounted antenna in the shape of a flat coil, like the heating element on an electric stove. In addition to inductive coupling, there can also be capacitive coupling, since a voltage must be applied at least to one end of the antenna to drive the RF current through it. Since this voltage is not uniform distributed, as it is in a plane-parallel capacitive discharge, it can cause an asymmetry in the plasma density. On the other hand, this voltage can help to breakdown the plasma, creating enough density for inductive coupling to take hold. Figure 1.4 shows typical (a) parallel-plate capacitive discharge, called a Reactive Ion Etcher (RIE) and (b) transformer coupled plasma (TCP) [10].

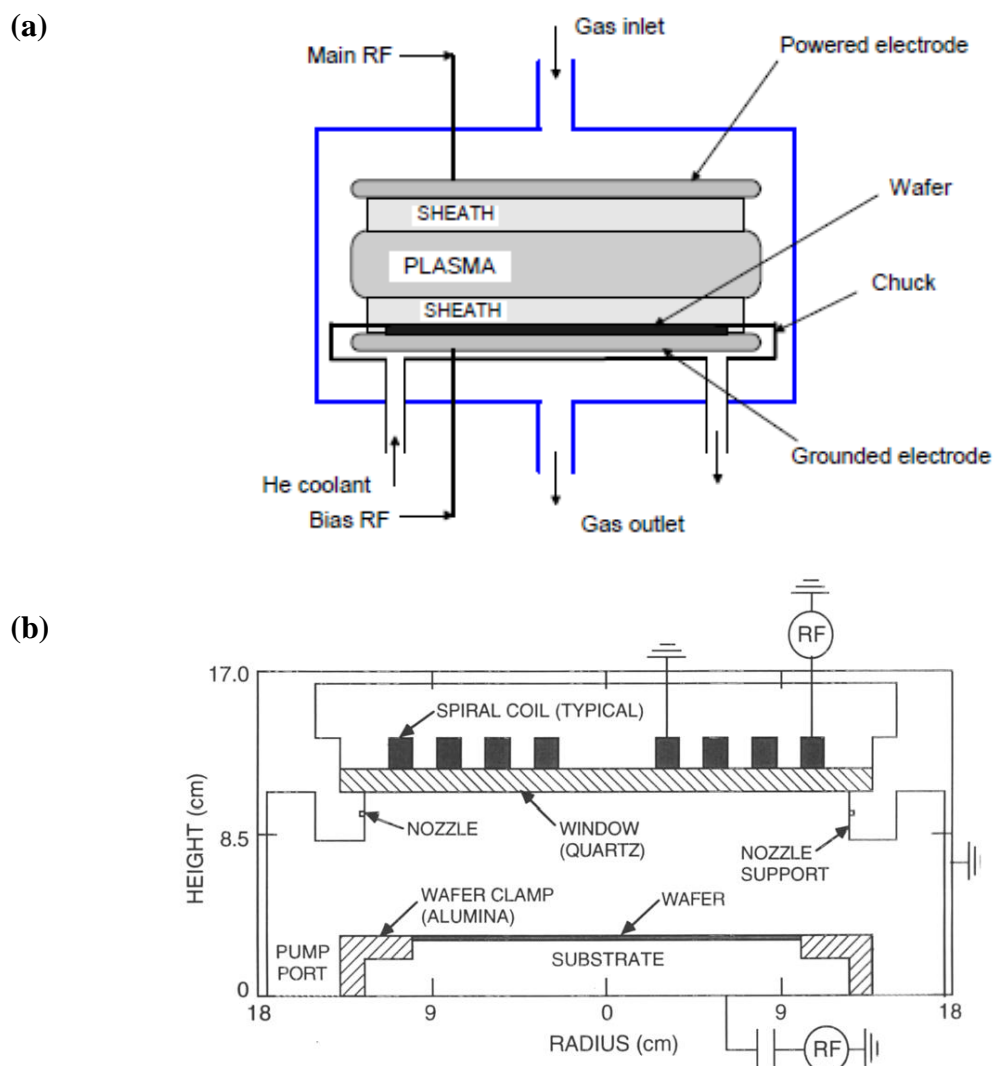


Figure 1.4 Schematic of (a) parallel-plate capacitive discharge, called a Reactive Ion Etcher (RIE) and (b) transformer coupled plasma (TCP).

1.5 Aim of this work and outline

In spite of the extensive use of low pressure glow discharges in a wide range of application fields as mentioned before, the underlying physics of the discharge is not yet fully understood. For a better understanding, it is necessary to know not only the physics of plasma such as electron heating, collision, diffusion and transport, but also the plasma chemistry such as gas-phase kinetics and physical/chemical reaction with surface. To do this, integrated diagnostic tools are needed to quantify the concentrations of various reactive species as well as the important plasma parameters such as the electron temperature and electron density in the discharge. Indeed, the plasma modeling is essential by virtue of theoretical interpretation and prediction of experimental results.

The aim of this work is therefore to understand the physical/chemical properties of low pressure glow discharges. This work is devoted to diagnostics of low pressure inductively coupled plasma (ICP) discharge, both of the physical and chemical interaction within plasma using theoretical modeling and experimental diagnostic methods for plasma processing. To understand the chemical kinetics in the discharge, a time dependent global model (volume averaged) is developed for various gases. Also a transformer model is developed to understand the electrical properties of the low pressure ICP discharge. A number of traditional plasma diagnostic methods are used to compare with calculated results such as Langmuir probe, optical emission spectroscopy (OES), optical absorption spectroscopy (OAS) and laser-induced fluorescence (LIF).

In Chapter 2 we discuss some important characteristics of typical ICP discharge such as the heating mechanisms, power transferred to the plasma electrons and we present a transformer model of the discharge. We show variation of the effective collision frequency and the effective RF driving frequency with the pressure and the electron temperature to calculate the electrical conductivity in RF discharge. The electrical conductivity is an important parameter in understanding the mechanism by which the power is coupled to a RF discharge, as well as determining the external electrical characteristics of the discharge. Using these values we also give the electromagnetic field components of a planar ICP reactor with analytical expressions to calculate the transferred power to the plasma electrons by the capacitive coupling and the inductive coupling. Finally using the transformer model we show the plasma impedance, current and voltage.

In Chapter 3 we describe the global model which consists of the particle and the electron energy balance equations. We provide the general expression of energy balance for non-Maxwellian electrons. Also we provide the particle balance by electron impact excitation, ionization, radiative decay, diffusion and pumping loss.

In Chapter 4 we briefly introduce basic principles of some methods of plasma diagnostics used in this study such as OES, OAS, TALIF and Langmuir probe. We provide the calculation of ro-vibrational spectra of N_2 discharge, and the estimation of rotational and vibrational temperature from measured spectra. We apply this technique to deduce the gas temperature in discharges containing N_2 gas.

Chapter 5 is devoted to the study of low pressure argon ICP discharges. First, we propose a new method of improving the precision of the pressure-dependent electron temperature calculated by the line ratio method. Using the electron energy distribution functions (EEDFs) and the electron density from Langmuir probe, we provide the coefficient of the cascade cross-section as a function of the pressure for argon $4p_1$ and $4p_5$. We show the effective electron temperature calculated by the corrected cascade cross-section and compare with Langmuir probe. Second, we study the production of argon excited states in the afterglow of pulse discharge. Experimentally time resolved OES, OAS and Langmuir probe are used to measure the emission of highly excited states, metastable atom density, electron density and electron temperature. To understand the behavior of the afterglow a time dependent global model is developed. We discuss the dominant creation sources and the routes of loss for each level during the discharge and in the afterglow. Finally, the $E-H$ mode transition and hysteresis in low pressure argon inductively coupled discharges are investigated using the global model and the transformer model.

In Chapter 6 the dissociation of the nitrogen molecule in an Ar- N_2 ICP discharge is studied both experimentally and theoretically. Using TALIF we found an increase of the dissociation rate in highly Ar-diluted region. A global model is developed to understand the behavior of the Ar- N_2 discharge. The calculated results are compared with the measured results, obtaining reasonably good agreement. We discuss in detail the dominant creation sources and the routes of loss for each level in pure N_2 discharge as well as in Ar- N_2 mixture.

In Chapter 7 we develop the global model for He, Ne, Ar and Xe discharges to calculate the electron temperature and the electron density. We compare the calculated results with experiments and discuss the dominant creation sources and the routes of loss for electron and metastable atoms as function of pressure. The transformer model is used to calculate the electrical properties of He, Ne, Ar and Xe discharges. We discuss the differences of the kinetics and the electrical properties in He, Ne, Ar and Xe discharges.

Finally a short conclusion is provided.

1.6 References

- [1] Lieberman M A and Lichtenberg A J 2005 *Principles of Plasma Discharges and Materials Processing 2nd ed.* (New York: Wiley)
- [2] 2009 *NRL Plasma Formulary*, Naval Research Laboratory, Washington, DC
- [3] Rossnagel S M, Westood W D and Haber J J 1991 *Handbook of Plasma Processing Technology: Fundamental, Etching, Seposition and Surface Interations (Material Science and Process Technology)* (New Tork: Noyes)
- [4] Ohring M 1992 *The Material Science of Thin Films* (California: Academic Press)
- [5] Konuma M 1992 *Film Deposition by Plasma Techniques* (Springer)
- [6] Ricard A 1966 *Reactive Plasmas* (SFV Editions)
- [7] Keller J H, Forster J C and Barnes S M 1993 *J. Vac. Sci. Technol. A* **11** 2487
- [8] Hopwood J, Guarnieri C R, Whitehair S J and Cuomo J J 1993 *J. Vac. Sci. Technol. A* **11** 147
- [9] Hittort W 1884 *Wiedemanns. Ann. Phys.* **21** 90
- [10] Chen F F and Chang J P 2003 *Lecture Notes on Principles of Plasma Processing* (New York: Kluwer Academic)

Chapter 2

Characteristic of ICP discharge

Contents

2.1	Introduction	14
2.2	Heating mechanism in RF inductive discharge	14
2.2.1	Effective electrical conductivity and effective collision frequency . . .	14
2.2.2	Classical skin effect	17
2.2.3	Anomalous skin effect	18
2.2.4	Ohmic (collisional) and stochastic (collisionless) heating	20
2.3	The power transferred to the plasma electrons in TCP reactor	21
2.4	Transformer model and plasma impedance	24
2.5	References	28

2.1 Introduction

INDUCTIVELY coupled plasma (ICP) provide compact high density reactors operating at low pressures and they are full of promise as innovative sources applicable to various plasma processings [1,2]. Although inductively coupled plasmas have over 100 years of history, the use of these sources for plasma-assisted materials processing was first described in patents by Ogle of Lam Research Corporation [3] and by Coultas and Keller of IBM Corporation [4] as devices to generate high density plasma at low pressures. Later many researchers indicate that these discharges are capable of producing plasma densities on the order of 10^{11} - 10^{12} cm⁻³ at low pressures, and that under optimized conditions, uniform plasma densities can be achieved [5-8].

In high-frequency discharges there are two distinct mechanisms by which power is coupled into the plasma [9]. The first of these is the plasma joule heating, which is principally due to collisions between electrons and atoms of the background gas. The second mechanism is the stochastic heating, due to the voltage across the sheaths which occurs, for example, at the electrodes of capacitively coupled discharges on is due to the inhomogeneous radio-frequency fields in the neighborhood of the coil in inductively coupled discharges. In order to correctly interpret the power balance in a high-frequency discharge, it is necessary to know the complex electrical conductivity due to the electron-atom collisions, which determines the joule heating component.

In section 2.2 we first discuss the effective electrical conductivity and the effective collision frequency developed by Lister *et al* [10]. And then we introduce the classical skin effect which is the penetration depth of an electromagnetic field, and the collisional heating and collisionless heating mechanism.

In section 2.3 we give the transferred power to the plasma electrons by the capacitive coupling, the inductive coupling and the stochastic heating in a planar ICP reactor. Also we discuss the influence of the effective collision frequency and the effective driving frequency to the transferred power.

In section 2.4 we show a transformer model which considers the plasma to be a ring acting as the secondary coil of a transformer in the low pressure inductive discharges. Using this model we calculate the plasma impedance, current and voltage.

2.2 Heating mechanism in RF Inductive discharge

2.2.1 Effective electrical conductivity and effective collision frequency

The collisional electrical conductivity σ_p expresses the relation between the local current J in the discharge and the local electric field E through Ohm's law,

$$J = \sigma_p E \quad (2.1)$$

The classical definition of the collisional electrical conductivity in a high-frequency plasma is

$$\sigma_p = \frac{n_e e^2}{m_e (\nu_m + j\omega)} \quad (2.2)$$

where e and m_e are the electronic charge and mass, respectively, n_e is the electron density, ν_m is the electron collision frequency, and ω is the applied frequency. Equation (2.2) is strictly valid only when the electron collision frequency is independent on the electron velocity. If ν_m is a function of the electron energy, ε , equation (2.2) is replaced by the more general form:

$$\sigma_p = \frac{n_e e^2}{m_e (\nu_{eff} + j\omega_{eff})} \quad (2.3)$$

where the effective electron-neutral collision frequency ν_{eff} and the effective driving frequency ω_{eff} depend on both $\nu(\varepsilon)$ and ω .

The general formula for the electrical conductivity in a weakly ionized plasma in which the electric field $E \propto e^{j\omega t}$ is

$$\sigma_p = -\frac{2n_e e^2}{3m_e} \int_0^\infty \frac{\varepsilon^{3/2}}{\nu_c(\varepsilon) + j\omega} \frac{dF(\varepsilon)}{d\varepsilon} d\varepsilon \quad (2.4)$$

where $\nu_c(\varepsilon) = Nv\sigma_c(\varepsilon)$ is the differential collision frequency for electron momentum transfer at energy ε , N is the background neutral density, $v = (2e\varepsilon/m_e)^{1/2}$ is the electron velocity, and $\sigma_c(\varepsilon)$ is the effective collision cross section for momentum transfer, which includes both elastic and inelastic cross section, and $F(\varepsilon)$ denotes the electron energy distribution function (EEDF) with the normalization,

$$\int_0^\infty \varepsilon^{1/2} F(\varepsilon) d\varepsilon = 1 \quad (2.5)$$

Using equation (2.3) and (2.4), we find general expressions of ν_{eff} and ω_{eff} .

$$\frac{\nu_{eff}}{\nu_{eff}^2 + \omega_{eff}^2} = -\frac{2}{3} \int_0^\infty \frac{\varepsilon^2 \nu_c(\varepsilon)}{\nu_c^2(\varepsilon) + \omega^2} \frac{dF(\varepsilon)}{d\varepsilon} d\varepsilon \quad (2.6)$$

$$\frac{\omega_{eff}}{\nu_{eff}^2 + \omega_{eff}^2} = -\frac{2}{3} \int_0^\infty \frac{\varepsilon^{3/2} \omega}{\nu_c^2(\varepsilon) + \omega^2} \frac{dF(\varepsilon)}{d\varepsilon} d\varepsilon \quad (2.7)$$

Moreover we can define two important limiting cases, the dc limit and the high-frequency limit. When $\nu_{eff}^2 \gg \omega^2$ (dc limit), $\nu_{eff} = \nu_{dc}$ where

$$\nu_{dc}^{-1} = -\frac{2}{3} \int_0^\infty \frac{\varepsilon^{3/2}}{\nu_c(\varepsilon)} \frac{dF(\varepsilon)}{d\varepsilon} d\varepsilon \quad (2.8)$$

$$\frac{\omega_{eff}}{\omega} = -\frac{2\nu_{dc}^2}{3} \int_0^\infty \frac{\varepsilon^{3/2}}{\nu_c^2(\varepsilon)} \frac{dF(\varepsilon)}{d\varepsilon} d\varepsilon \quad (2.9)$$

When $\nu_{eff}^2 \ll \omega^2$ (high-frequency limit), $\nu_{eff} = \nu_{hf}$, $\omega_{eff}/\omega = 1$ in equation (2.3) and

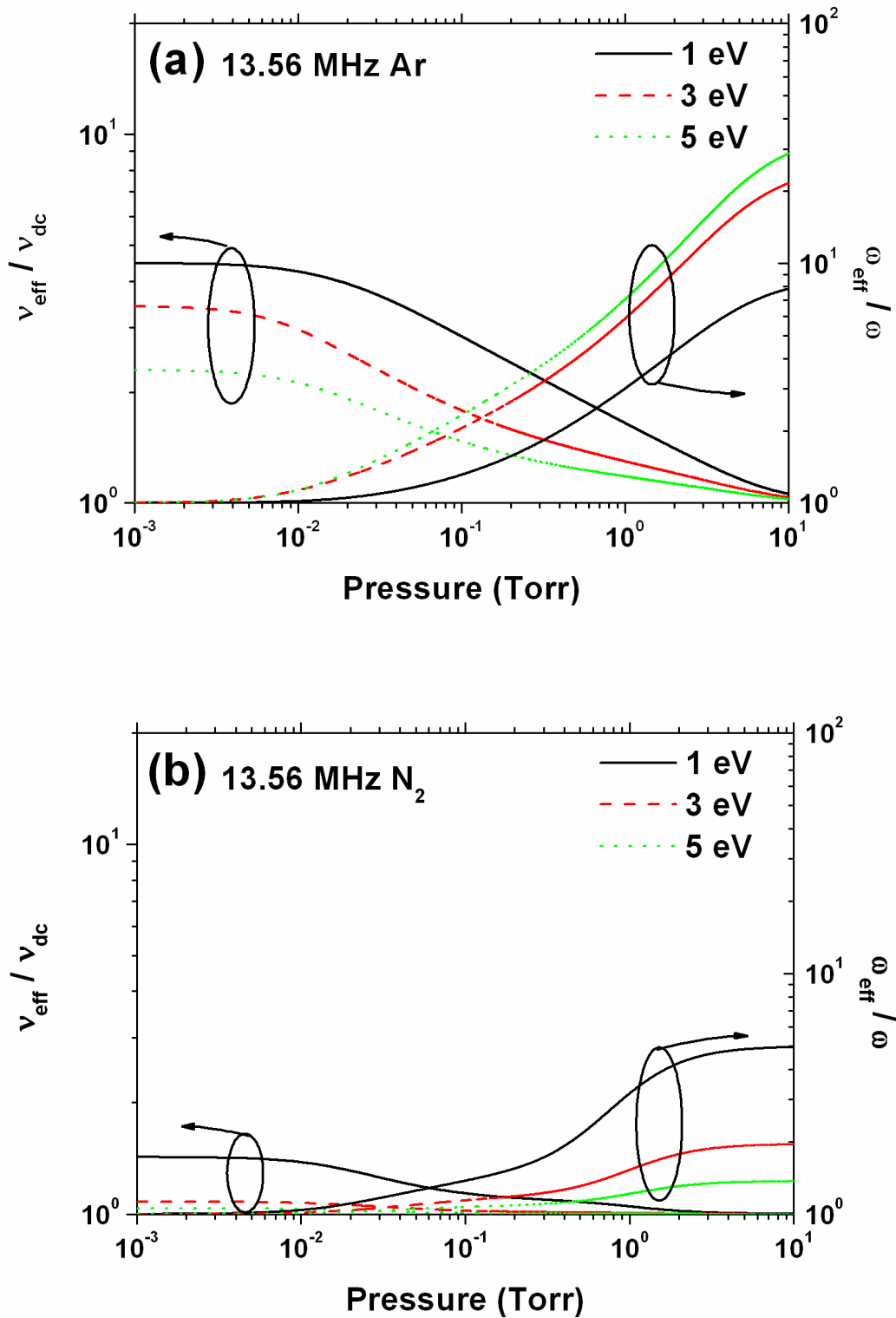


Figure 2.1 Variations of $v_{\text{eff}}/v_{\text{dc}}$ and $\omega_{\text{eff}}/\omega$ as a function of pressure for different electron temperatures T_e (Maxwellian distribution) of (a) argon and (b) nitrogen gas.

$$\nu_{hf} = -\frac{2}{3} \int_0^\infty \nu_c(\varepsilon) \varepsilon^{3/2} \frac{dF(\varepsilon)}{d\varepsilon} d\varepsilon \quad (2.10)$$

Figures 2.1(a) and 2.1(b) show the variations of ν_{eff}/ν_{dc} and ω_{eff}/ω as a function of pressure for different electron temperatures T_e which the EEDF is assumed Maxwellian for argon and nitrogen gas. The high-frequency and dc limits at low and high pressures, respectively, and the deviation from these limits, are clearly illustrated. Indeed, for nitrogen gas, ν_{eff}/ν_{dc} and ω_{eff}/ω decrease as increasing the electron temperature, due to the vibrational and rotational energy levels between 1 ~ 3 eV in nitrogen molecule.

2.2.2 Classical skin effect

In an inductively coupled plasma, the power is transferred from the electric fields to the plasma electrons within a skin depth layer of thickness δ near the plasma surface by collisional (ohmic) dissipation and by a collisionless (stochastic) heating process in which bulk plasma electrons “collide” with the oscillating inductive electric fields within the skin layer.

We consider the classical or normal skin effect accompanied by ohmic (collisional) electron heating in a semi-infinite spatially uniform plasma. The normal skin effect occurs when the electron thermal motion is negligible and there is a local coupling between the RF current density \mathbf{J} and the RF electric field \mathbf{E} within the skin layer given by $\mathbf{J} = \sigma_p \mathbf{E}$. We consider the case when $\omega \ll \omega_{pe}$, which is always true for inductively coupled plasmas, where ω_{pe} is the electron plasma frequency, defined as $\omega_{pe}^2 = (e^2 n_e / \varepsilon_0 m_e)$. We also assume a Maxwellian EEDF and an energy-independent electron-atom collision frequency $\nu_m(\varepsilon) = \text{const}$.

According to Maxwell's equations, the penetration of the transverse electric field into the plasma is described by the complex wave equation

$$\frac{d^2 E_y}{dx^2} = j\omega\mu_0\sigma_p E_y \quad (2.11)$$

having solution

$$E_y = E_{y0} e^{-x/\delta} \cos(\omega t - \beta x) \quad (2.12)$$

where

$$\delta^{-1} = \text{Re}(j\omega\mu_0\sigma_p)^{1/2} \quad (2.13)$$

is the inverse skin depth and

$$\beta = \text{Im}(j\omega\mu_0\sigma_p)^{1/2} \quad (2.14)$$

is the propagation constant. Substituting (2.2) into (2.13), one obtains the general expression for the classical (normal) skin depth

$$\delta = \frac{\delta_0}{\cos(\varepsilon/2)} \quad (2.15)$$

where

$$\delta_0 = \frac{c}{\omega_{pe}} \left(1 + \frac{\nu_m^2}{\omega^2} \right)^{1/4} \quad (2.16)$$

and

$$\varepsilon = \tan^{-1}(\nu_m/\omega) \quad (2.17)$$

In the collisional limit ($\nu_m \gg \omega$), typical for the nonsuperconducting metals and high pressure plasma, $\varepsilon = \pi/2$ and

$$\delta = \delta_c = \frac{c}{\omega_{pe}} \left(\frac{2\nu_m}{\omega} \right)^{1/2} = \delta_p \left(\frac{2\nu_m}{\omega} \right)^{1/2} \quad (2.18)$$

and the RF energy collisionally dissipates within the skin layer.

In the high frequency limit ($\nu_m \ll \omega$), called the nondissipative or high frequency skin effect $\varepsilon = 0$ and

$$\delta = \delta_p = \frac{c}{\omega_{pe}} \quad (2.19)$$

In this case the electrons collisionlessly oscillate within the skin layer with no net energy gain. For an electromagnetic wave incident on the plasma boundary this case corresponds to the total reflection of the wave from the plasma. For discharge maintenance in this case, the wave reflection is not perfect, and a small fraction of the incident wave power is locally and/or nonlocally deposited within the skin layer.

2.2.3 Anomalous skin effect

There is a third situation for which electrons incident on a skin layer of thickness δ_a satisfy the condition

$$\frac{\bar{v}_e}{2\delta_a} \gg \omega, \nu_m \quad (2.20)$$

where δ_a is determined below. In this case, the interaction time of the electrons with the skin layer is short compared to the RF period of the collision time. That means the electrons can gain energy from the wave without losing it during all the period. In analogy to collisionless heating at a capacitive sheath, a stochastic collision frequency can be defined

$$\nu_{stoc} = \frac{C_e \bar{v}_e}{4\delta_a} \quad (2.21)$$

where C_e is a quantity of order unity that depends weakly on \bar{v}_e , δ_a , and ω , provided the ordering (2.20) is satisfied. We then substitute v_{stoc} for v_m in (2.16) and expand for $v_{stoc} \gg \omega$, to obtain

$$\delta_a = \frac{c}{\omega_{pe}} \left(\frac{C_e \bar{v}_e}{2\omega\delta_a} \right)^{1/2} \quad (2.22)$$

Solving for δ_a , we find

$$\delta_a = \left(\frac{C_e c^2 \bar{v}_e}{2\omega\omega_{pe}^2} \right)^{1/3} = \left(\frac{C_e \bar{v}_e}{2\omega\delta_p} \right)^{1/3} \delta_p \quad (2.23)$$

where δ_a is the anomalous skin depth.

A general nonlocality parameter for the nonlocal interaction of electrons with the electromagnetic field has been given by Fried and Conte [11] and used in the analysis of the anomalous skin effect by Weibel [12] and Saysov [13]

$$\Lambda = \frac{\pi}{4} \left(\frac{\bar{v}_e \omega_{pe}}{c} \right)^2 \frac{\omega}{(\omega^2 + \nu_{en}^2)^{3/2}} \quad (2.24)$$

Formulae for the classical skin effect are applicable when $\Lambda \ll 1$; for $\Lambda > 1$, the anomalous skin effect takes place. Figure 2.2 shows the nonlocality parameter Λ as a function of ω/ν .

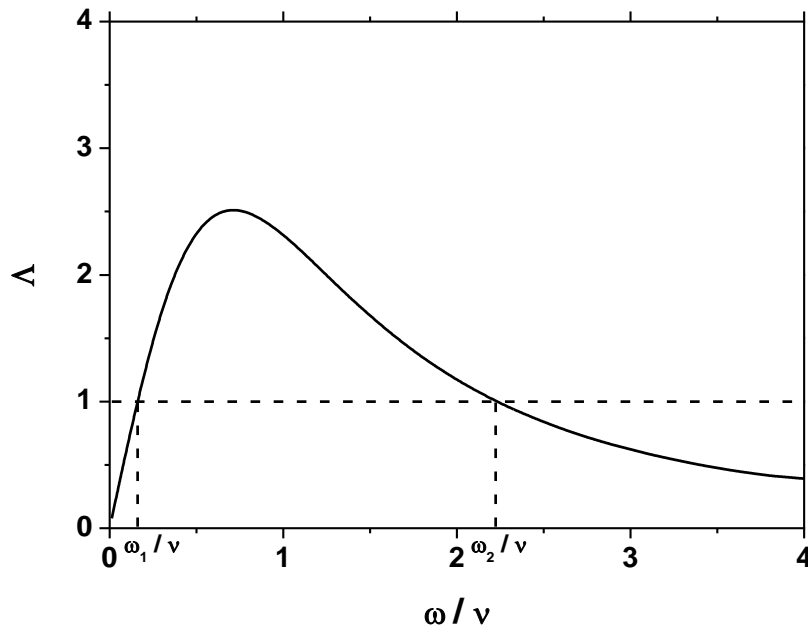


Figure 2.2 The parameter Λ as a function of ω/ν . The anomalous skin effect takes place in the frequency range $\omega_1 < \omega < \omega_2$.

The anomalous skin effect takes place in the frequency range $\omega_1 < \omega < \omega_2$.

In the extreme anomalous case (a) neither the skin depth δ nor the energy dissipation in the skin layer depend on the collision frequency ν , (b) the dissipation of energy is present even if $\nu = 0$, (c) the damping of the field is characterized by at least two characteristic lengths (the skin depth δ and the mean free path λ), and (d) the field profile can be non-monotonic, and in some places the current can even flow against the field [14].

2.2.4 Ohmic (collisional) and stochastic (collisionless) heating

The heating of electrons of time-varying fields is fundamental to the operation of radio frequency discharges. In a uniform oscillating electric field, $E(t) = \text{Re}E_0 e^{j\omega t}$, a single electron has a coherent velocity of motion that lags the phase of electric field force $-eE$ by 90° . Hence, the time-average power transferred from the field to the electron is zero. Electron collisions with other particles destroy the phase coherence of the motion, leading to a net transfer of power. For an ensemble of n electrons per unit volume, it is usual to introduce the macroscopic current density $\mathbf{J} = en\mathbf{u}$, with \mathbf{u} the macroscopic electron velocity, and to relate the amplitudes of \mathbf{J} and \mathbf{E} through a local conductivity equation (2.1). The average electron velocity oscillates coherently but lags the electric field by less than 90° , leading to an ohmic power transfer per unit volume

$$P_{ohm} = \frac{1}{2} \text{Re} \tilde{\mathbf{J}}_0 \cdot \tilde{\mathbf{E}}_0^* = \frac{1}{2} |\tilde{\mathbf{E}}_0|^2 \text{Re}(\sigma_p) = \frac{1}{2} |\tilde{\mathbf{J}}_0|^2 \text{Re}(\sigma_p^{-1}) \quad (2.25)$$

So in the planar inductively coupled discharge, the ohmic heating power flux is

$$\begin{aligned} S_{ohm} &= \frac{1}{2} \int_0^\infty dz \left(E_0 e^{-z/\delta} \right)^2 \frac{e^2 n_s}{m_e} \frac{\nu_{en}}{\nu_{en}^2 + \omega_{eff}^2} \\ &= \frac{1}{4} \frac{e^2 n_s \delta}{m_e} \frac{\nu_{en}}{\nu_{en}^2 + \omega_{eff}^2} E_0^2 \end{aligned} \quad (2.26)$$

where n_s is the sheath edge density and z is the distance from the quartz window.

To determine the stochastic heating at low pressure, we consider an electron from the bulk plasma incident on the RF electric field within a skin depth layer in slab geometry. We assume a simple model in which the transverse electric field within the slab decays exponentially with distance z from the edge into the slab [15]

$$E_y(z, t) = E_0 e^{-|z|/\delta} \cos(\omega t + \phi) \quad (2.27)$$

We also assume that the collisionality is weak, $\nu_m \ll \nu_e/\delta$; hence there are no electron collisions within the skin layer. Because there are no z -directed forces, we can write the position of the electron as:

$$z(t) = \begin{cases} -v_z t, & t < 0 \\ v_z t, & t > 0 \end{cases} \quad (2.28)$$

where the electron reflects from the surface at $t = 0$. Substituting (2.28) into (2.27) yields the transverse electric field seen by the electron

$$\begin{aligned} E_y(t) &= \text{Re } E_0 e^{(j\omega + v_z/\delta)t + j\phi}, & t < 0 \\ &= \text{Re } E_0 e^{(j\omega - v_z/\delta)t + j\phi}, & t > 0 \end{aligned} \quad (2.29)$$

The transverse velocity impulse

$$\Delta v_y = - \int_{-\infty}^{\infty} dt \frac{e E_y(t)}{m_e} \quad (2.30)$$

is calculated by substituting (2.29) into (2.30) and integrating to obtain

$$\Delta v_y = \frac{2eE_0\delta}{m_e} \frac{v_z}{v_z^2 + \omega^2\delta^2} \cos \phi \quad (2.31)$$

The energy change $\Delta\epsilon$, averaged over a uniform distribution of initial electron phase ϕ , is then

$$\Delta\epsilon = \frac{1}{2} m_e \left\langle (\Delta v_y)^2 \right\rangle_{\phi} = \frac{1}{4} m_e \left(\frac{2eE_0\delta}{m_e} \right)^2 \frac{v_z^2}{(v_z^2 + \omega^2\delta^2)^2} \quad (2.32)$$

which can be integrated over the particle flux to obtain the stochastic heating power

$$S_{stoc} = \int_{-\infty}^{\infty} dv_x \int_{-\infty}^{\infty} dv_y \int_{-\infty}^{\infty} dv_z F_e v_z \Delta\epsilon(v_z) \quad (2.33)$$

For a Maxwellian electron distribution F_e , the integral over v_x and v_y are easily done, and the v_z integral can be evaluated in terms of the exponential integral E_1 . For the regime of large nonlocality ($\Lambda \gg 1$)

$$\zeta = \frac{4\omega^2\delta^2}{\pi \bar{v}_e^2} \ll 1 \quad (2.34)$$

we obtain

$$S_{stoc} = \frac{m_e n_s}{\bar{v}_e} \left(\frac{eE_0\delta}{m_e} \right)^2 \frac{1}{\pi} \left[\ln \left(\frac{1}{\zeta} \right) - 1.58 \right] \quad (2.35)$$

2.3 The power transferred to the plasma electrons in TCP reactor

The power transferred to the plasma electrons in planar inductively coupled discharge can be calculated from the electric field components induced by the induction coil current [16-20]. The planar induction coil excites RF magnetic fields B_r , B_θ and B_z , which are respectively the radial, azimuthal and axial components and the corresponding components of RF electric fields E_r , E_θ and E_z . The electromagnetic field components of B_θ , E_r and E_z are capacitively

coupled with plasma electrons while the remaining field components E_θ , B_r and B_z are inductively coupled. We derive the each component of electromagnetic field in Appendix.

The averaged power transferred by capacitive coupling, P_e , can be calculated by integrating the Poynting vector using calculated E_r , E_z and B_θ as follows:

$$P_e = -\frac{2\pi}{\mu_0} \left[\int_0^R r E_r(r, L+D) B_\theta^*(r, L+D) dr + \int_0^R r E_z(r, L+D) B_\theta^*(r, L+D) dr \right] \quad (2.36)$$

In a similar manner, the average power, P_{ind} , delivered from the RF coil to the plasma through inductive coupling is given by integrating the Poynting vector over the surface area of the coil:

$$P_{ind} = \frac{1}{2\mu_0} \int_0^R 2\pi r E_\theta(r, L+D) B_r^*(r, L+D) dr \quad (2.37)$$

The total transferred power to the electrons is given by

$$P_{trans} = \text{Re}(P_e + P_{ind}) + P_{stoc} \quad (2.38)$$

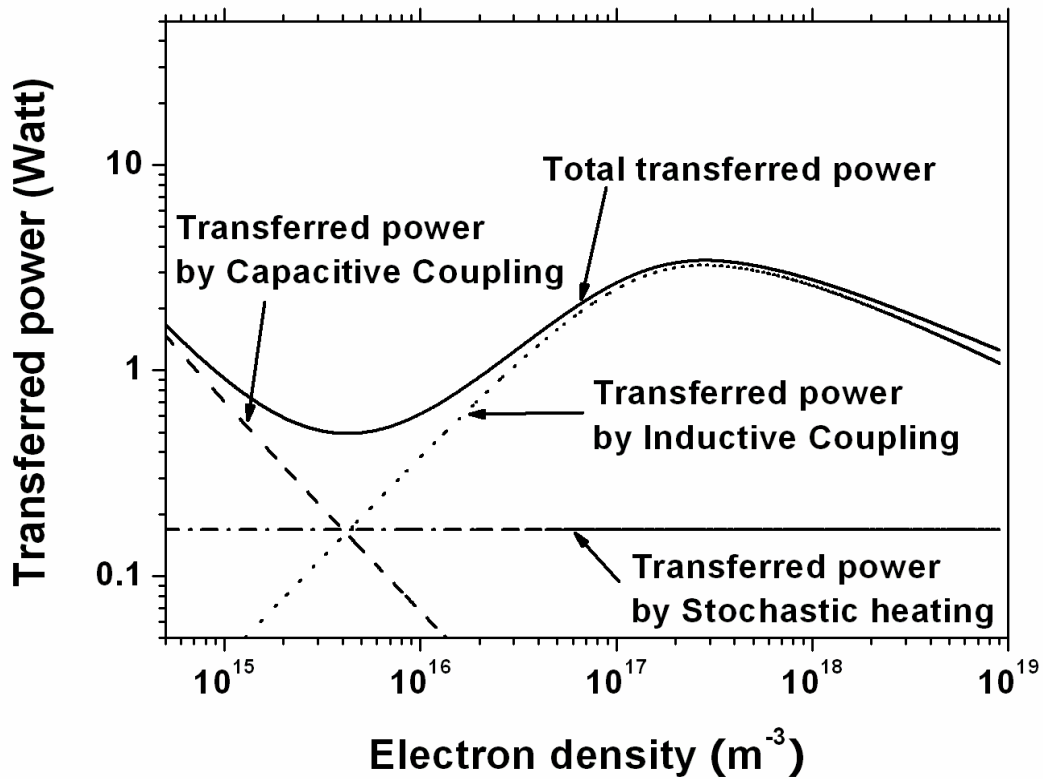


Figure 2.3 Calculated transferred power by capacitive coupling, inductive coupling, stochastic heating and total transferred power at 100 mTorr argon pressure, $T_e = 2.0$ eV and 1 A coil current.

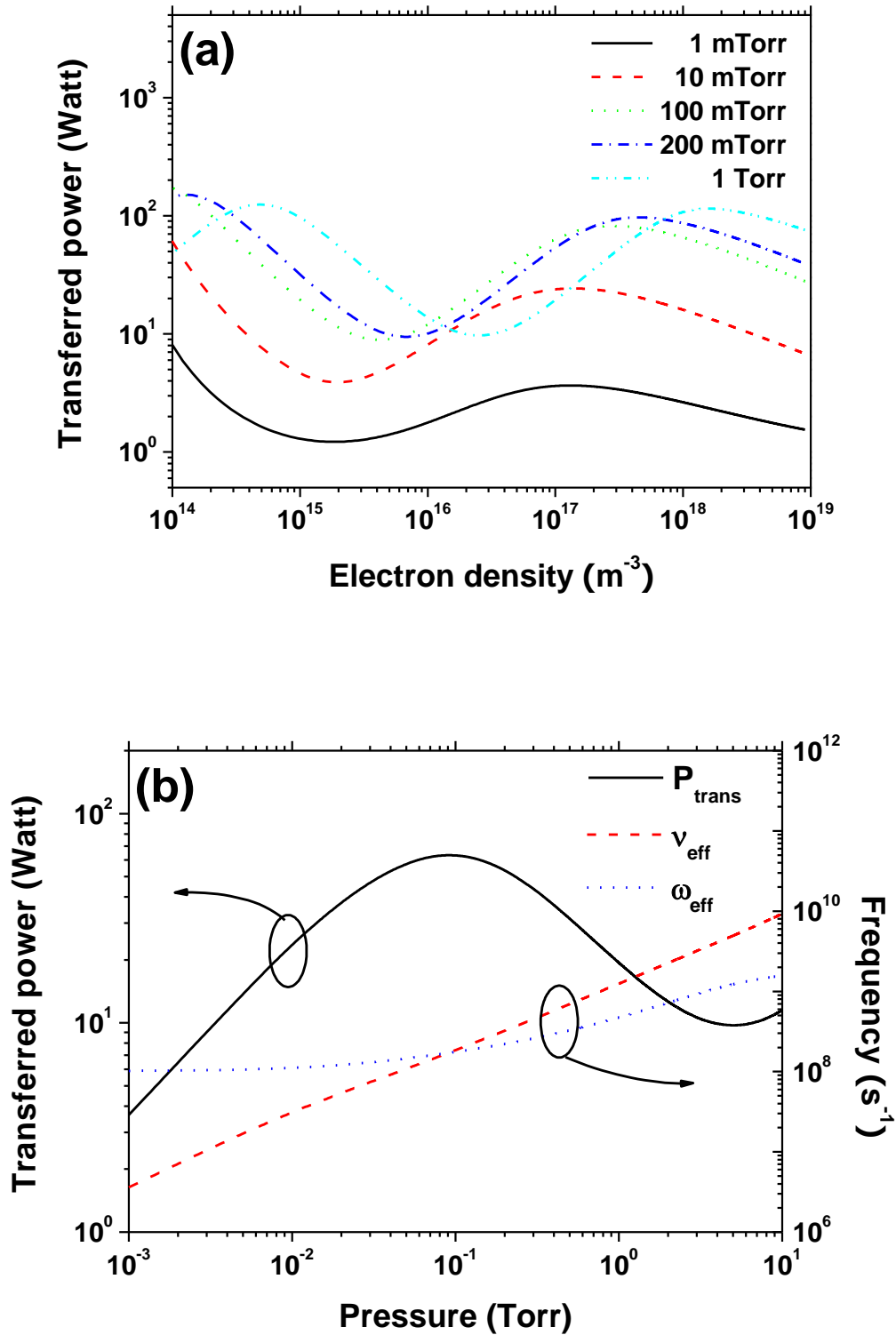


Figure 2.4 (a) Calculated total transferred power at 5 A coil current and $T_e = 2.0$ eV for various argon pressure and (b) total transferred power and the effective frequencies ν_{eff} and ω_{eff} as a function of gas pressure at fixed electron density 10^{17} m^{-3} and 5 A coil current.

where P_{stoc} is the power absorbed by the stochastic heating, which is given by

$$P_{stoc} \approx 0.45 \sqrt{\frac{m_e}{e}} \varepsilon_0 \omega^2 T_e^{1/2} \int_0^R \frac{V_c}{R} 2\pi r^2 dr \quad (2.39)$$

where V_c is the voltage difference between the centre and end of the coil. Figure 2.3 shows the calculated transferred power by capacitive coupling, inductive coupling, stochastic heating and total transferred power at 100 mTorr argon pressure, $T_e = 2.0$ eV and 1 A coil current. In the calculation we assume that the voltage across RF coil V is [17]

$$V \approx i_{coil} \omega L_1 \quad (2.40)$$

where L_1 is the inductance of the coil. The chamber parameters in our calculation are $R = 10$ cm, $L = 5$ cm, $D = 1$ cm and $N = 3$ turns. The frequency of RF power is 13.56 MHz, and the inductance coil is 1 μ H. When the electron density is lower than $4.0 \times 10^{15} \text{ m}^{-3}$, the capacitively transferred power is dominant and the system is in E mode. As increasing the electron density the inductively transferred power increases, and the system is in H mode. The transferred power by the stochastic heating is independent of electron density, and constant at fixed coil current and electron temperature.

Figure 2.4(a) shows the calculated total transferred power at 5 A coil current and $T_e = 2.0$ eV for various argon pressure. When the gas pressure is lower than 100 mTorr, the total transferred power increases with the pressure. At the opposite when the gas pressure is higher than 100 mTorr, the curves slightly shift to the right side and no increase in the total transferred power is observed. It means that more electrons are needed to transfer the same power in the given system at high pressure. Figure 2.4(b) shows the total transferred power and the effective frequencies ν_{eff} and ω_{eff} as a function of gas pressure at a fixed electron density 10^{17} m^{-3} and 5 A coil current. The total transferred power increases as increasing the pressure and it reaches a maximum around 100 mTorr. The power transferred to electrons per unit volume by collisional (ohmic) heating is given in equation (2.26). This equation shows that, for a given electric field strength, the transferred power by the collisional heating becomes its maximum when the effective collision frequency ν_{eff} coincides with the effective RF frequency ω_{eff} as shown in figure 2.4(b).

2.4 Transformer model and plasma impedance

Low-pressure inductive discharges have been modelled by considering the plasma a ring acting as the secondary coil of a transformer [21-23]. The equivalent circuit is shown in figure 2.5. The voltage required to power the coil of an inductive discharge is supplied by a 50 Ω RF power source through a capacitive matching network. Here C_L (loading capacitor) and C_T (tuning capacitor) are variable series and parallel capacitors, and $R_T (= 50 \Omega)$ is the Thevenin-equivalent RF source resistance. The inductive branch is represented as an air-cored transformer having the planar coil inductance L_1 and resistance R_1 as a primary. R_1 can be measured without plasma as $R_1 = (P_{in} - P_{ref}) / i_{coil}^2$, where P_{in} and P_{ref} are the injected power and the reflected power, respectively, and i_{coil} is the coil current. The secondary circuit can be

described by two components of inductance and one resistance; a geometric inductance L_2 , an electron inertia inductance L_{pi} , and a resistance R_{pi} of the plasma loop. The capacitive branch is represented by the combination of circuit elements C_d , L_{pc} , R_{pc} , C_s , R_{st} and R_{ion} . C_d is the quartz window capacitance, L_{pc} is the inductance due to the electrons' inertia in the capacitive coupling, and R_{pc} is the capacitive power dissipation due to ohmic (collisional) heating. C_s is the sheath capacitance, R_{st} is the stochastic (collisionless) heating resistance due to oscillating sheath and R_{ion} is the heating of ions that fall through the dc sheath potential. It is customary to transform the secondary load into the primary circuit of the transformer, as shown in figure 2.6. ΔR and ΔL are the change in resistance and inductance due to the plasma given by

$$\Delta R = \frac{\omega^2 M^2 R_{pi}}{R_{pi}^2 + \omega^2 (L_2 + L_{pi})^2} \quad (2.41)$$

$$\Delta L = \frac{\omega^2 M^2 (L_2 + L_{pi})}{R_{pi}^2 + \omega^2 (L_2 + L_{pi})^2} \quad (2.42)$$

where M is the mutual inductance.

In appendix, we have derived analytic expressions for the electromagnetic fields inside the reactor, and the effective collision frequency ν_{eff} . Using these expressions we can calculate the circuit parameters in figure 2.5. The collisional resistances R_{pi} , R_{pc} and the stochastic resistance can be calculated

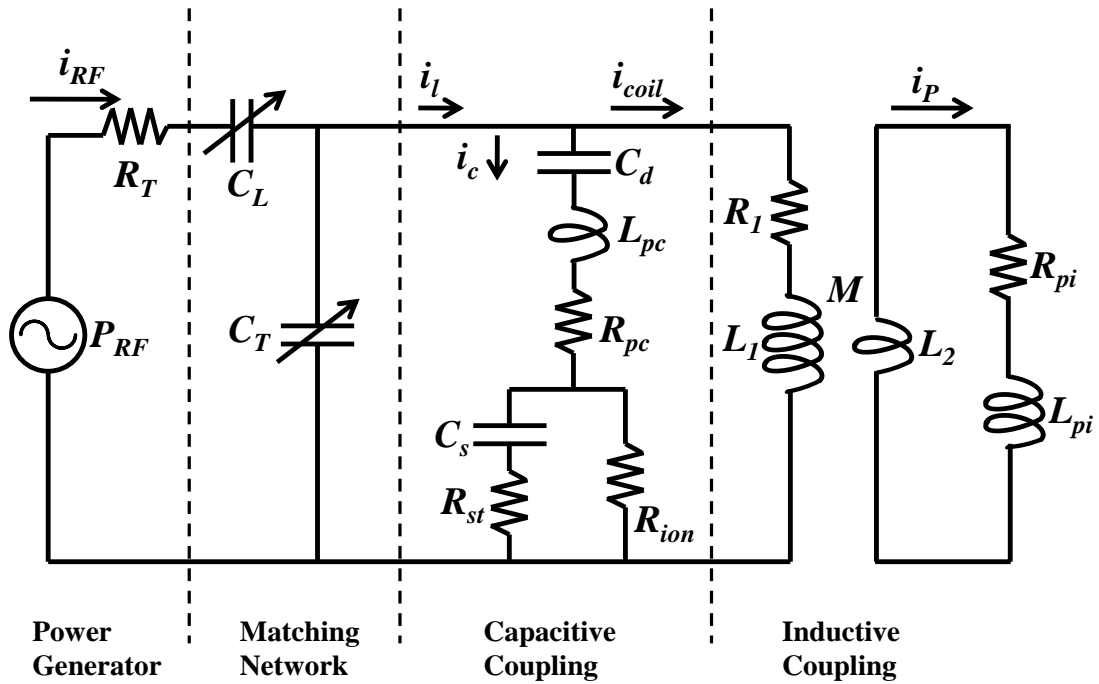


Figure 2.5 The circuit representation of the discharge which allows for both inductive and capacitive coupling of RF power to the plasma

$$\frac{1}{2} i_c^2 R_{pc} = P_e \quad (2.43)$$

$$\frac{1}{2} i_{coil}^2 \Delta R = \frac{1}{2} i_p^2 R_{pi} = P_{ind} \quad (2.44)$$

$$\frac{1}{2} i_{st}^2 R_{st} = P_{st} \quad (2.45)$$

where i_c and i_{coil} are currents flowing in the capacitive and inductive branches, respectively, i_p is the total induced plasma current, and i_{st} is the in the stochastic branch. An analytical expression for the total induced plasma current can be found by applying the integral form of Ampere's law

$$i_p(t) = \frac{1}{\mu_0} \oint_C \mathbf{B}(t) \cdot d\mathbf{l} \quad (2.46)$$

where the path of integration C is from $(r = 0, z = 0)$ to $(r = 0, z = L)$ to $(r = R, z = L)$ to $(r = R, z = 0)$ (see figure A.1 in appendix). Using the theoretical expressions for B_r and B_z , we can obtain the ratio of amplitudes of the coil and plasma current, i_{coil} / i_p , and the phase difference, ϕ . The inductance L_{pi} due to the electron inertia can be written as

$$L_{pi} = \frac{R_{pi}}{v_{eff}} \frac{\omega_{eff}}{\omega} \quad (2.47)$$

and L_2 can be found

$$\tan \phi = \frac{R_{pi}}{\omega(L_2 + L_{pi})} \quad (2.48)$$

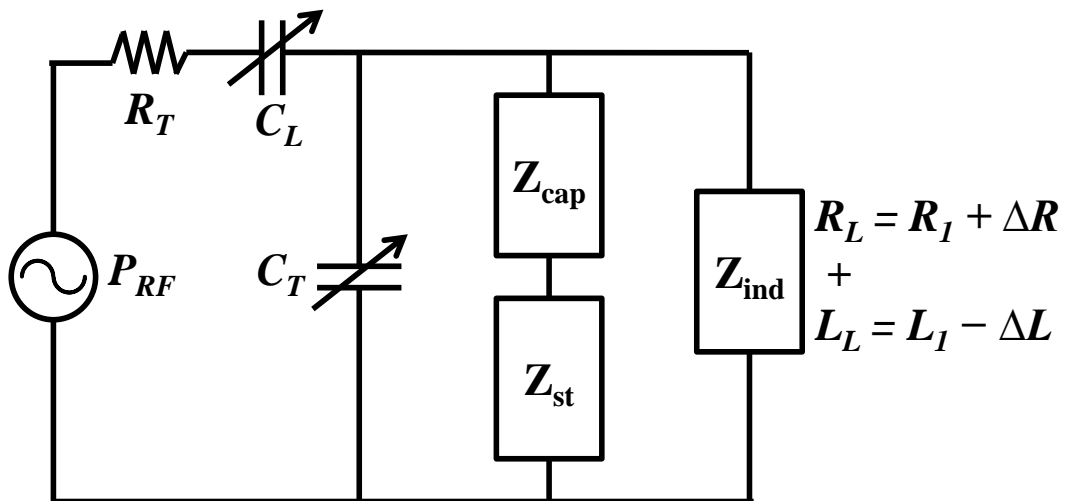


Figure 2.6 The equivalent circuit.

The impedance of the inductive branch, Z_{ind} , in figure 2.6 can be written as

$$Z_{ind} = (R_l + \Delta R) + \frac{1}{j\omega(L_l - \Delta L)} \quad (2.49)$$

In a similar manner the impedance of the capacitive branch, Z_{cap} , and the stochastic branch, Z_{st} , can be written as

$$Z_{cap} = R_{pc} + j\omega L_{pc} + \frac{1}{j\omega C_d} \quad (2.50)$$

$$Z_{st} = \frac{(R_{st} + 1/j\omega C_s)R_{ion}}{(R_{st} + 1/j\omega C_s) + R_{ion}} \quad (2.51)$$

The values of capacitive components are given in the literature [23,24]. The sheath capacitance can be calculated from the expression given by Godyak and Sternberg [24], $C_s' = \epsilon_0 A_d / s$, where A_d is the area of the quartz window and s is the sheath thickness. By averaging the voltage along the coil, C_s can be expressed as $C_s = \frac{1}{2} C_s'$. In this study the quartz window capacitance C_d is 36 pF.

Finally the effective impedance seen in the primary circuit can be written as

$$Z_{tot} = \frac{(Z_{cap} + Z_{st})Z_{ind}}{Z_{cap} + Z_{st} + Z_{ind}} \quad (2.52)$$

The RF power is transferred through the matching network, and the capacitances C_L and C_T can be calculated with the following relations:

$$R_T = 50 = \text{Re} \left[jX_L + \frac{jX_T Z_{tot}}{jX_T + Z_{tot}} \right] \quad (2.53)$$

$$0 = \text{Im} \left[jX_L + \frac{jX_T Z_{tot}}{jX_T + Z_{tot}} \right] \quad (2.54)$$

where $X_L = (-\omega C_L)^{-1}$ and $X_T = (-\omega C_T)^{-1}$.

For a given RF power we can obtain the values of all components including currents and voltages using these relations

$$P = \frac{1}{2} \text{Re}[Z] i^2 \quad (2.55)$$

$$V = i \left(\text{Re}[Z]^2 + \text{Im}[Z]^2 \right)^{1/2} \quad (2.56)$$

2.5 References

- [1] Hopwood J 1992 *Plasma Sources Sci. Technol.* **1** 109
- [2] Keller J H 1995 *Plasma Sources Sci. Technol.* **5** 166
- [3] Ogle J S 1990 U.S.Patent No. 4,948,458
- [4] Coultas D K and Keller J H 1990 European Patent, Publication No. 0 379 828 A2
- [5] Keller J H, Forster J C and Barnes S M 1993 *J. Vac. Sci. Technol. A* **11** 2487
- [6] Hopwood J, Guarnieri C R, Whitehair S J and Cuomo J J 1993 *J. Vac. Sci. Technol. A* **11** 147
- [7] Hopwood J, Guarnieri C R, Whitehair S J and Cuomo J J 1993 *J. Vac. Sci. Technol. A* **11** 152
- [8] Mahoney L J, Wendt A E, Barriros E, Richards C J and Shohet J L 1994 *J. Appl. Phys.* **76** 2041
- [9] Lieberman M A and Lichtenberg A J 2005 *Principles of Plasma Discharges and Materials Processing 2nd ed.* (New York: Wiley)
- [10] Lister G G, Li Y M and Godyak V A 1996 *J. Appl. Phys.* **79** 8993
- [11] Fried B D and Conte S D 1961 *The Plasma Dispersion Function* (New York: Academic)
- [12] Weibel E S 1967 *Phys. Fluids* **10** 741
- [13] Sayasov Yu S 1979 *Helvetica Physica Acta* **52** 288
- [14] Kolobov V I and Economou 1997 *Plasma Sources Sci. Technol.* **6** R1
- [15] Lieberman M A and Godyak V A 1998 *IEEE Trans. Plasma Sci.* **26** 955
- [16] El-Fayoumi I M and Jones I R 1998 *Plasma Sources Sci. Technol.* **7** 162
- [17] El-Fayoumi I M, Jones I R and Turner M M 1998 *J. Phys. D: Appl. Phys.* **31** 3082
- [18] Yoon N S, Hwang S M and Choi D I 1997 *Phys. Rev. E* **55** 7536
- [19] Lee M H and Chung C W 2006 *Phys. Plasmas* **13** 063510
- [20] Zhao S X, Xu X, Li X C and Wang Y N 2009 *J. Appl. Phys.* **105** 083306
- [21] Piejak R B, Godyak V A and Alexandrovich B M 1992 *Plasma Sources Sci. Technol.* **1** 179
- [22] El-Fayoumi I M and Jones I R 1998 *Plasma sources Sci. Technol.* **7** 179
- [23] Gudmundsson J T and Lieberman M A, 1998 *Plasma Sources Sci. Technol.* **7** 83
- [24] Godyak V A and Sternberg N 1990 *Phys. Rev. A* **42** 2299

Chapter 3

Global (volume averaged) model

Contents

3.1	Introduction	30
3.2	Power balance	31
3.2.1	Energy loss by collision	31
3.2.2	Energy loss by diffusion to the wall	32
3.3	Particle balance	35
3.3.1	Electron impact excitation coefficient	35
3.3.2	Radiative decay	35
3.3.3	Diffusion loss	37
3.3.4	Pumping loss	37
3.4	References	38

3.1 Introduction

LOW-temperature plasma discharges are widely used in many different industries, for instance to modify surfaces, deposit thin films, produce light or provide thrust for satellites. The simplest level of modeling of such plasma discharges is the so-called ‘global model’, which consists of particle number and electron energy balance equations. The main idea of a global model is to neglect the complexity which arises when spatial variations are considered and to generate a model that encompasses a large number of reactions in order to model processing plasma with a limited computing power. Thus the model does not describe

Table 3.1 The developed global models for various gas mixture and discharge sources.

Gases	Source	Pressure (mTorr)	EN	References
Ar	TCP	1–70		[27,35,36]
	RF magnetron sputtering	0.3- 2.3 Pa		[29]
	Pulse TCP	5		[16]
N ₂ /Ar	ICP	15-30		[4]
	TCP	30-110		[30]
H ₂ /Ar	TCP	1-100	○	[24]
	TCP	20-60		[23]
O ₂ /Ar	TCP	1-100	○	[6,7]
Cl ₂ /Ar	TCP	1-100	○	[5]
	Pulse TCP	1-100	○	[15]
CF ₄ /Ar	TCP	3-30		[11]
SF ₆ /Ar	ICP	3-20	○	[13]
Ar, O ₂ , Cl ₂ , O ₂ /Ar	TCP	0.5-200	○	[3]
Ar, Cl ₂	Pulse TCP	5		[14]
O ₂	TCP	3-60	○	[20,26,31]
	Pulse TCP	1-100	○	[19]
N ₂	TCP	1-100		[37]
	Pulse TCP	1-100		[17]
Cl ₂	Pulse TCP	2-20	○	[8]
	TCP	1-100	○	[9]
C ₄ F ₈	ICP	1.29 Pa	○	[34]
CF ₄	TCP	2-30	○	[28]
CF ₄ /O ₂	TCP	8-25	○	[10]
Ne/Xe	DBD	100-600 Torr		[25]
O ₂ /F ₂	TCP	1-100	○	[32]
O ₂ /SiCl(CH ₃) ₃	ECR	0.1-100 Pa	○	[33]
SF ₆	ICP	0.1-4.5 Pa	○	[12]
Cl ₂ /He	CCP	0.1-1 Torr	○	[18]
He/H ₂ O	CCP	atm		[22]
H ₂	ICP	10-100		[38,39]

Table 3.2 Useful experimental and theoretical literatures in the global model.

Subject	References
Experimental study of total energy losses per electron-ion lost	[40]
Experimental study of edge-to-center density ratio	[41]
Effect of the electron energy distribution function	[36]
Effect of the electronegative ion and practical recommendations	[21]
Edge-to-center plasma density ratio	[42]
Global model approximation	[43]

spatial distribution but captures scaling of plasma parameters with control parameters. This model allows us to investigate various phenomena, such as the effects of plasma parameters on excited species, negative ions and particular reactions on the overall discharge.

The volume averaged global model for high density discharges was developed by Lieberman and Gottscho [1] for noble gases and extended to molecular gases by Lee *et al* [2] and Lee and Lieberman [3]. Many works have been done for various gas mixtures such as Ar diluted O₂, N₂ and Cl discharge [4-9], CF₄ [10,11], SF₆ [12,13] and discharge sources such as pulse discharge [14-17] and electronegative (EN) plasma [18-21]. Recently Lin *et al* [22] developed the global model of low temperature atmospheric pressure H₂/H₂O discharge, and Ar diluted H₂ discharge was developed [23,24]. The developed global models for various gas mixture and discharge sources are presented in table 3.1. Also some useful experimental and theoretical literatures in the global model are presented in table 3.2.

3.2 Power balance

In the global model the absorbed power can be written as [44]:

$$P_{abs} = P_c + P_i + P_e \quad (3.1)$$

where P_c , P_i and P_e are the power losses by inelastic and elastic collision, ion and electron flow to the wall, respectively. We assume a cylindrical stainless steel chamber of radius R and length L . The content of the chamber is assumed to be nearly spatially uniform and the power deposited uniformly into the plasma bulk.

3.2.1 Energy loss by collision

The power loss due to inelastic and elastic collision in the discharge can be expressed as:

$$P_c = en_e V \left(\sum n_j^X K_{iz}^X \varepsilon_{iz}^X + \sum n_j^X K_{ex}^X \varepsilon_{ex}^X + n_j^X K_{el}^X \varepsilon_{el}^X \right) \quad (3.2)$$

where V is the discharge volume, e is the charge of electron and n_j^X is the density of initial state of each collision for species X. K_{iz}^X , K_{ex}^X and K_{el}^X are the rate coefficients and ε_{iz}^X , ε_{ex}^X and ε_{el}^X are the energy lost per ionization, excitation and elastic collision for species X,

respectively. In equation (3.2), the collision energy loss per electron-ion pair created, ε_c , can be defined as [44]:

$$K_{iz}^X \varepsilon_c = K_{iz}^X \varepsilon_{iz} + \sum K_{ex}^X \varepsilon_{ex} + K_{el}^X \frac{3m_e}{M_X} T_e \quad (3.3)$$

The quantity $(3m_e/M_X)T_e$ is the mean energy lost per electron for a polarization (elastic) scattering. ε_c is a function of T_e only, depending on the electron neutral species collisional energy loss processes in the gas. For molecular gases, additional collisional energy losses include excitation of vibrational and rotational energy levels, molecular dissociation, and, for electronegative gases, negative ion formation.

3.2.2 Energy loss by diffusion to the wall

The electron and ion fluxes to the wall are:

$$\Gamma_e = \Gamma_{i,X} = n_s u_{B,X} \quad (3.4)$$

where n_s is the electron density at the sheath edge, $u_{B,X} = (eT_e/M_X)^{1/2}$ is the Bohm velocity, and M_X is the ion mass for species X. The edge to center electron density ratios for each axial and radial sheath edge from low pressure to high pressure are given by [3]:

$$h_L = \frac{n_{s,L}}{n_e} \approx 0.86 \times \left[3 + \frac{L}{2\lambda_i} + \left(\frac{0.86Lu_{B,X}}{\pi D_a} \right)^2 \right]^{-1/2} \quad (3.5)$$

$$h_R = \frac{n_{s,R}}{n_e} \approx 0.8 \times \left[4 + \frac{R}{\lambda_i} + \left(\frac{0.8Ru_{B,X}}{\chi_{01} J_1(\chi_{01}) D_a} \right)^2 \right]^{-1/2} \quad (3.6)$$

where $D_a = D_i(1+T_e/T_i)$ is the ambipolar diffusion coefficient, D_i is the diffusion coefficient (eq. 3.31) for positive ion, T_i is the ion atom temperature which is assumed to be the same as the gas temperature T_g , J_1 is the first order Bessel function, and $\chi_{01} = 2.405$ is the first zero of the J_0 Bessel function. The third term (between parentheses) in the formulas is the scaling factor for constant diffusion at high pressure regime. λ_i is the ion-neutral species mean free path given by :

$$\frac{1}{\lambda_i} = \sum_j n_j \sigma_j \quad (3.7)$$

where n_j is the density of the gas species j and σ_j is the total ion-neutral cross sections for the collision with the gas species j . Using these expressions, the power loss due to charged particle flow to the wall can be described by:

$$P_i + P_e = en_e u_{B,X} (h_L A_L + h_R A_R) (\varepsilon_i + \varepsilon_e) \quad (3.8)$$

where $A_L = 2\pi R^2$ and $A_R = 2\pi RL$ are the areas of the axial and radial sheaths, respectively.

The ion velocity necessary for stable sheath formation is given by the ion acoustic speed. The ion velocity of the sheath formation criterion can be written in terms of the electron energy distribution $F(E)$ as [36]

$$\frac{1}{m_i} \langle v_i^{-2} \rangle = \int_0^\infty \frac{F(E)}{2E} dE \quad (3.9)$$

where m_i is the ion mass and v_i is the ion velocity. Due to the acceleration by a weak electric field on the presheath, positive ions at the sheath edge have a narrow velocity distribution and thus $\langle v_i^{-2} \rangle^{-1} \approx \langle v_i^2 \rangle$ and the kinetic energy at the sheath edgy can be obtained from

$$\frac{1}{2} m_i \langle v_i^2 \rangle \approx \left[\int_0^\infty \frac{F(E) dE}{E} \right]^{-1} \quad (3.10)$$

and

$$v_i \approx \left(\frac{2}{m_i} \right)^{1/2} \left[\int_0^\infty \frac{F(E) dE}{E} \right]^{-1/2} \quad (3.11)$$

For the Maxwellian electron energy distribution, equation (3.11) leads to the Bohm criterion, $v_i = u_B = (eT_e/m_i)^{1/2}$.

The mean kinetic energy lost per electron ε_e is calculated as the ratio of the average energy flux S_e to the electron flux Γ_e . In spherical coordinates the electron density is obtained from an arbitrary electron speed distribution $f(v)$ [44]:

$$C \int_0^{2\pi} d\phi \int_0^\pi \sin \theta d\theta \int_0^\infty f(v) v^2 dv = n_e \quad (3.12)$$

where C is a constant for normalization and the angle integrals yield the factor 4π . Similarly, the average electron speed \bar{v}_e is given by

$$\bar{v}_e = \int_0^\infty v f(v) 4\pi v^2 dv \quad (3.13)$$

The directed electron flux Γ_z in the z -direction is given by $n_e \langle v_z \rangle$, where the average is taken over $v_z > 0$ only. Using $v_z = v \cos \theta$ in spherical coordinates, we obtain

$$\begin{aligned}
\Gamma_z &= n_e \int_0^{2\pi} d\phi \int_0^{\pi/2} \sin \theta d\theta \int_0^\infty v \cos \theta f(v) v^2 dv \\
&= n_e \bar{v}_e \frac{1}{4\pi} 2\pi \int_0^{\pi/2} \sin \theta \cos \theta d\theta \\
&= \frac{1}{4} n_e \bar{v}_e
\end{aligned} \tag{3.14}$$

Thus for the general electron energy distribution, the electron flux towards the wall is given by

$$\Gamma_e = \frac{1}{4} n_e \bar{v}_e \int_{V_s}^\infty F(E) d(E) \tag{3.15}$$

where V_s is the potential drop within the sheath between a plasma and a floating wall, can be calculated from $\Gamma_i = \Gamma_e$. For a Maxwellian electron energy distribution V_s is given by

$$V_s = \frac{T_e}{2} \ln \left(\frac{M}{2\pi m_e} \right) \tag{3.16}$$

Similarly, the average energy flux $S_z = n_e \left\langle \frac{1}{2} m_e v^2 v_z \right\rangle$ in the z-direction can be obtained

$$\begin{aligned}
S_z &= n_e \int_0^{2\pi} d\phi \int_0^{\pi/2} \sin \theta d\theta \int_0^\infty v \cos \theta \frac{1}{2} m_e v^2 f(v) v^2 dv \\
&= n_e 2\pi \frac{1}{2} \int_0^\infty v \frac{1}{2} m_e v^2 f(v) v^2 dv
\end{aligned} \tag{3.17}$$

Thus for the general electron energy distribution, the average energy flux towards the wall is given by

$$S_e = n_e \frac{\pi}{2} m_e \int_{v_{\min}}^\infty v v^2 f(v) v^2 dv \tag{3.18}$$

where v_{\min} is minimum speed of electron obtained by $v_{\min} = \left(\frac{2eV_s}{m_e} \right)^{1/2}$. For a Maxwellian electron energy distribution the mean electron energy lost per electron lost is $\varepsilon_e = 2T_e$. The mean kinetic energy lost per ion lost, ε_i , is the sum if the ion energy entering the sheath and the energy gained by the ion as it traverses the sheath, can be calculated as

$$\varepsilon_i = \Phi_p + V_s = \frac{1}{2} m_i v_i^2 + V_s \tag{3.19}$$

For a Maxwellian electron energy distribution, $\varepsilon_i = \frac{1}{2} T_e + V_s$.

The entire power balance equation including collisional energy loss and kinetic energy loss of the charged particles to the wall can be therefore written as:

$$P_{abs}(t) = V \left(\frac{d}{dt} \left(\frac{3}{2} e n_e T_e \right) + e n_e \sum n_j^x K_{iz}^x \varepsilon_c \right) + e \left(V_s + \frac{5}{2} T_e \right) (h_L A_L + h_R A_R) n_e u_{B,X} \quad (3.20)$$

3.3 Particle balance

The dynamics of species density n_j (including electrons) is described by the particle balance equation:

$$\frac{dn_j}{dt} = \sum R_{Production}^j - \sum R_{Loss}^j \quad (3.21)$$

where $R_{Production}^j$ and R_{Loss}^j are the production rate and the loss rate of the species j , respectively.

3.3.1 Electron impact excitation coefficient

The rate coefficient k_{jk} for electron impact excitation from level j to level k can be calculated by:

$$k_{jk} = \int \sigma_{jk}(E) F(E) \left(\frac{2E}{m_e} \right)^{1/2} dE \quad (3.22)$$

where $\sigma_{jk}(E)$ is the electron impact excitation cross section and $F(E)$ is the EEDF. The rate coefficients of de-excitation processes k_{kj} are also calculated by the principle of detailed balancing [44].

$$k_{kj} = \frac{g_j}{g_k} \exp \left(\frac{E_{jk}}{kT_e} \right) k_{jk} \quad (3.23)$$

where g_j and g_k are the statistical weight of j and k states, respectively.

3.3.2 Radiative decay

The radiative loss rate from level k to level j is given by:

$$\nu_{kj} = A_k \Lambda_k \quad (3.24)$$

where A_k is the transition probability and Λ_k is the escape factor which is described by radiation trapping. The escape factor Λ_k depends on the density of the lower state in the radiative transition. Usually at low pressure the density of excited level is enough low to neglect the escape factor except for towards the ground state, such as 3P_1 - 1S_0 ($\lambda = 1067\text{\AA}$) and 1P_1 - 1S_0 ($\lambda = 1048\text{\AA}$) resonance lines in an argon discharge. The escape factor of these two resonance lines when Doppler and collision broadenings are present simultaneously is given by [45-47]:

$$\Lambda = T_d \exp\left(-\frac{T_{cd}^2}{T_c^2}\right) + T_c \operatorname{erf}\left(\frac{T_{cd}}{T_c}\right) \quad (3.25)$$

where T_d and T_c are the transmission coefficients for pure Doppler and collisional broadenings, respectively, T_{cd} is the coefficient under conditions of collisional broadening emission with Doppler broadening absorption, and $\operatorname{erf}()$ denotes the error function. T_d , T_c and T_{cd} are given by

$$T_d = \frac{1}{k_0 \rho (\pi \ln k_0 \rho)^{1/2}} \quad (3.26)$$

$$T_c = \frac{1}{\sqrt{\pi}} \left(\frac{\sqrt{\pi} a}{k_0 \rho} \right)^{1/2} \quad (3.27)$$

$$T_{cd} = \frac{2a}{\pi (\ln k_0 \rho)^{1/2}} \quad (3.28)$$

where $k_0 \rho$ is the so-called optical depth at the line centre and a is the damping coefficient given by,

$$a = \left(\frac{1}{\tau} + \frac{1}{\tau_c} \right) \frac{\lambda_0}{4\pi \nu_0} \quad (3.29)$$

where τ_c is an effective collision time for the resonance atom and ν_0 is the average gas

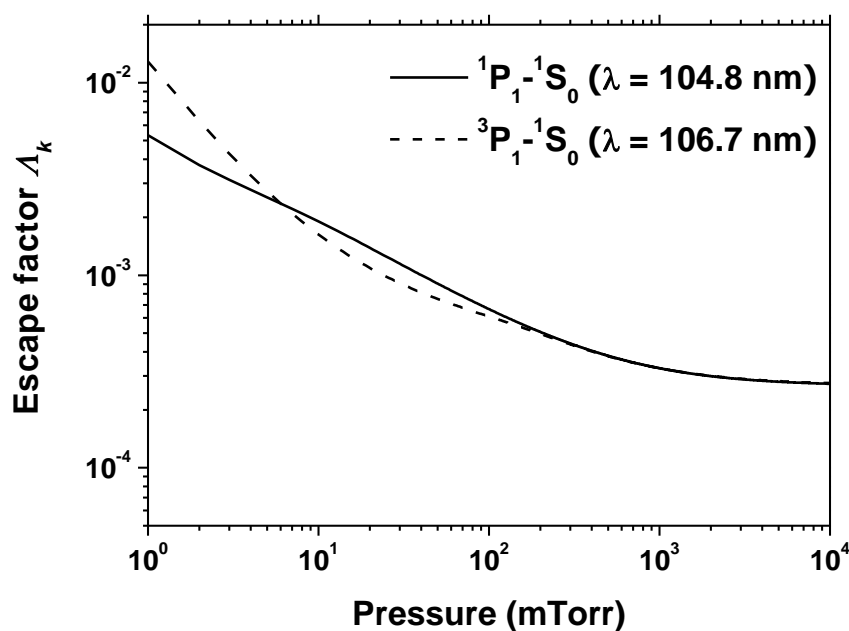


Figure 3.1. Calculated escape factors for $\lambda = 104.8$ nm and $\lambda = 106.7$ nm resonance lines of argon as a function of gas pressure.

velocity at gas temperature T_g , $v_0 = (2kT_g/M)^{1/2}$. Figure 3.1 shows the calculated escape factors for $\lambda = 104.8$ nm and $\lambda = 106.7$ nm resonance lines of argon as a function of gas pressure, for TCP discharge with $R = 10$ cm and $L = 5$ cm at 400 K.

3.3.3 Diffusion loss

The diffusion losses of the neutral species to the wall are estimated by an effective loss rate coefficient given by [48]:

$$k_{n,wall} = \left[\frac{\Lambda^2}{D_n} + \frac{2V(2-\gamma_n)}{A\bar{v}_n\gamma_n} \right]^{-1} \quad (3.30)$$

where D_n is the neutral diffusion coefficient and Λ is the effective diffusion length given by [27]:

$$D_n = \frac{kT_g\lambda_n}{\bar{v}_n M} \quad (3.31)$$

and

$$\frac{1}{\Lambda^2} = \left(\frac{\pi}{L} \right)^2 + \left(\frac{2.405}{R} \right)^2 \quad (3.32)$$

where k is the Boltzmann constant, $\bar{v}_n = (8kT_g/\pi M)^{1/2}$ is the neutral mean velocity, λ_n is the neutral-neutral species mean free path calculated from the neutral-neutral collision cross section data [18], γ_n is the sticking coefficient for the neutral particle on the wall surface, and V and A are the volume and the wall surface area of the reactor chamber.

The diffusion loss rate of the ion flux to the walls can be expressed using equations (3.5) and (3.6) as

$$k_{ion,wall} = 2u_{B,X} \frac{R^2 h_L + RLh_R}{R^2 L} \quad (3.33)$$

3.3.4 Pumping loss

The loss by pumping for species j can be calculated by

$$R = 1.378 \times 10^1 \times \frac{Q_{in} n_j}{pV} \quad (3.34)$$

where Q_{in} is total gas flow into the chamber in sccm, n_j is the density of species j in cm^{-3} , p is pressure in Torr, and V is the discharge volume in cm^3 [37].

3.4 References

- [1] Lieberman M A and Gottscho R A 1994 *Physics of Thin Films* vol. 18 ed Francombe M and Vossen J (New York: Academic)
- [2] Lee C, Graves D B, Lieberman M A and Hess D W 1994 *J. Electrochem. Soc.* **141** 1546
- [3] Lee C and Lieberman M A 1995 *J. Vac. Sci. Technol. A* **13** 368
- [4] Tao K, Mao D and Hopwood J 2002 *J. Appl. Phys.* **91** 4040
- [5] Thorsteinsson E G and Gudmundsson J T 2010 *J. Phys. D: Appl. Phys.* **43** 115201
- [6] Gudmundsson J T, Kimura T and Lieberman M A 1999 *Plasma Sources Sci. Technol.* **8** 22
- [7] Gudmundsson J T and Thorsteinsson E G 2007 *Plasma Sources Sci. Technol.* **16** 399
- [8] Despiau-Pujo E and Chabert P 2009 *Plasma Sources Sci. Technol.* **18** 045028
- [9] Thorsteinsson E G and Gudmundsson J T 2010 *Plasma Sources Sci. Technol.* **19** 015001
- [10] Kimura T and Noto M 2006 *J. Appl. Phys.* **100** 063303
- [11] Kimura T and Ohe K 1999 *Plasma Sources Sci. Technol.* **8** 553
- [12] Kokkoris G, Panagiotopoulos A, Goodyear A, Cooke M and Gogolides E 2009 *J. Phys. D: Appl. Phys.* **42** 055209
- [13] Lallement L, Rhallabi A, Cardinaud C, Peignon-Fernandez M C and Alves L L 2009 *Plasma Sources Sci. Technol.* **18** 025001
- [14] Lieberman M A and Ashida S 1996 *Plasma Sources Sci. Technol.* **5** 145
- [15] Thorsteinsson E G and Gudmundsson J T 2010 *J. Phys. D: Appl. Phys.* **43** 115202
- [16] Ashida S, Lee C and Lieberman M A 1995 *J. Vac. Sci. Technol. A* **13** 2498
- [17] Thorsteinsson E G and Gudmundsson J T 2009 *Plasma Sources Sci. Technol.* **18** 045002
- [18] Lee Y T, Lieberman M A, Lichtenberg A J, Bose F, Baltes H and Patrick R 1997 *J. Vac. Sci. Technol. A* **15** 113
- [19] Kim S, Lieberman M A, Lichtenberg A J and Gudmundsson J T 2006 *J. Vac. Sci. Technol. A* **24** 2025
- [20] Kimura T, Lichtenberg A J and Lieberman M A 2001 *Plasma Sources Sci. Technol.* **10** 430
- [21] Monahan D D and Turner M M 2008 *Plasma Sources Sci. Technol.* **17** 045003
- [22] Liu D X, Bruggeman P, Iza F, Rong M Z and Kong M G 2010 *Plasma Sources Sci. Technol.* **19** 025018
- [23] Kimura T and Kasugai H 2010 *J. Appl. Phys.* **107** 083308
- [24] Hjartarson A T, Thorsteinsson E G and Gudmundsson J T 2010 *Plasma Sources Sci. Technol.* **19** 065008
- [25] Ikeda Y, Veboncoeur J P, Christenson P J and Birdsall C K 1999 *J. Appl. Phys.* **86** 2431

-
- [26] Chung T H, Yoon H J and Seo D C 1999 *J. Appl. Phys.* **86** 3536
- [27] Kimura T and Ohe K 2001 *J. Appl. Phys.* **89** 4240
- [28] Kimura T and Ohe K 2002 *J. Appl. Phys.* **92** 1780
- [29] Palmero A, van Hattum E D, Rudolph H and Habraken F H P M 2007 *J. Appl. Phys.* **101** 053306
- [30] Kimura T and Kasugai H 2010 *J. Appl. Phys.* **108** 033305
- [31] Gudmundsson J T, Marakhtanov A M, Patel K K, Gopinath V P and Lieberman M A 2000 *J. Phys. D: Appl. Phys.* **33** 1323
- [32] Gudmundsson J T 2002 *J. Phys. D: Appl. Phys.* **35** 328
- [33] Yanguas-Gil A, Cotrino J and González-Elipé A R 2007 *J. Phys. D: Appl. Phys.* **40** 3411
- [34] Kokkoris G, Goodyear A, Cooke M and Gogolides E 2008 *J. Phys. D: Appl. Phys.* **41** 195211
- [35] Lee M H and Chung C W 2005 *Phys. Plasmas* **12** 073501
- [36] Gudmundsson J T 2001 *Plasma Sources Sci. Technol.* **10** 76
- [37] Thorsteinsson E G and Gudmundsson J T 2009 *Plasma Sources Sci. Technol.* **18** 045001
- [38] Zorat R, Goss J, Boilson D and Vender D 2000 *Plasma Sources Sci. Technol.* **9** 161
- [39] Zorat R and Vender D 2000 *J. Phys. D: Appl. Phys.* **33** 1728
- [40] Ku J H, Lee Y K and Chung C W 2010 *Phys. Plasmas* **17** 043508
- [41] Kim G H, Lee H C and Chung C W 2010 *Phys. Plasmas* **17** 073504
- [42] Raimbault J L and Chabert P 2009 *Plasma Sources Sci. Technol.* **18** 014017
- [43] Monahan D D and Tuner M M 2009 *Plasma Sources Sci. Technol.* **18** 045024
- [44] Lieberman M A and Lichtenberg A J 2005 *Principles of Plasma Discharges and Materials Processing 2nd ed.* (New York: Wiley)
- [45] Ferreira C M, Loureiro J and Ricard A 1985 *J. Appl. Phys.* **57** 82
- [46] Holstein T 1947 *Phys. Rev.* **72** 1212
- [47] Holstein T 1951 *Phys. Rev.* **83** 1159
- [48] Chantry P J 1987 *J. Appl. Phys.* **62** 1141

Chapter 4

Survey of plasma diagnostic methods

Contents

4.1	Introduction	42
4.2	Optical emission spectroscopy (OES)	42
4.2.1	Principle	42
4.2.2	Emission intensity in the corona model and line ratios method	43
4.2.3	Molecular spectroscopy	44
4.2.3.1	Rotational spectra	44
4.2.3.2	Vibrational spectra	46
4.2.3.3	Spectra of diatomic molecules	47
4.2.3.4	Ro-vibrational spectra of N_2 and N_2^+	48
4.3	Optical absorption spectroscopy (OAS)	54
4.4	Two-photon absorption laser-induced fluorescence (TALIF)	56
4.4.1	Principle	57
4.4.2	Measurement of absolute density	57
4.5	Langmuir probe	59
4.6	References	63

4.1 Introduction

IN order to understand the plasma chemistry, various plasma process diagnostic tools have been developed to quantify the concentrations of various reactive species as well as the important plasma parameters such as the electron temperature and electron density in the discharge. Plasma diagnostic is a broad area of technology that encompasses a diverse, venerable field of experimental techniques designed to provide information about the characteristics of plasmas. In this chapter we briefly introduce basic principles of some diagnostic tools used in this study.

4.2 Optical emission spectroscopy (OES)

4.2.1 Principle

Consider an atom initially in state g that is excited by a collision with an electron to state i as shown in figure 4.1. The atom subsequently decays by photon emission to state j . In order to define the process, four main types of cross section are necessary. The so-called **optical emission cross section** is directly related to the photon flux emerging on the $i \rightarrow j$ transition. The **apparent cross section** for level i is the sum of the optical emission cross sections over all possible decay channels for level i . It is thus related to the apparent rate at which level i is populated by electron-atom collisions. In addition to **direct electron-impact excitation** from level g to level i , the apparent cross section also includes a contribution from electron-impact excitation into higher levels (k) followed by photon decay into level i . Thus the apparent cross section is the sum of the direct excitation cross section and the **cascade cross section**. It is important to note the different types of cross sections since different experimental and theoretical techniques yield the different types of cross sections.

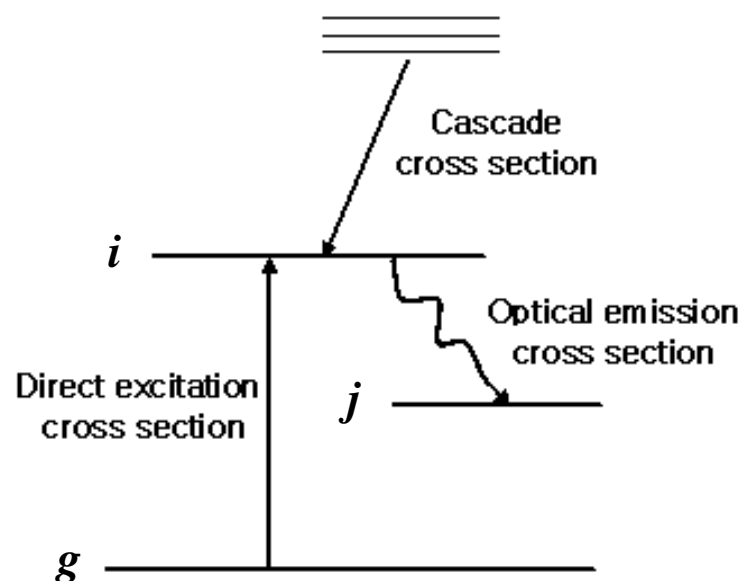


Figure 4.1 Classification of the cross section.

4.2.2 Emission intensity in the corona model and line ratios method

Consider atoms in a small plasma volume excited by electron-atom collisions into an excited level i . These atoms subsequently decay to lower levels l . In corona equilibrium, the electron excitation rate and photon decay rate are equal. The photon flux for a particular $i \rightarrow j$ transition, Φ_{ij} , is equal to [1,2]

$$\Phi_{ij} = \frac{A_{ij}}{\sum_{l<i} A_{il}} n_0 n_e \int_0^\infty \sigma_{ex,i}(E) f(E) \left(\frac{2E}{m_e} \right)^{1/2} dE \quad (4.1)$$

where n_0 is the number density of ground state atoms, n_e is the electron density, $\sigma_{ex,i}(E)$ is the excitation cross section into level i from the ground state as a function of electron energy E , $F(E)$ is the electron energy distribution function, m_e is the electron mass and A is the transition probability for spontaneous emission. By using the apparent cross section one automatically includes the effect of excitation into higher levels followed by radiative decay into level i . Since the $i \rightarrow j$ optical emission cross section, σ_{ij}^{Opt} includes the branching ratio:

$$\sigma_{ij}^{Opt}(E) = \frac{A_{ij}}{\sum_{l<i} A_{il}} \sigma_i^{App}(E) = b_{ij} \sigma_i^{App}(E) \quad (4.2)$$

where b_{ij} is the branching ratio of $i \rightarrow j$ transition, equation (4.1) can be simplified to

$$\Phi_{ij} = n_0 n_e \int_0^\infty \sigma_{ij}^{Opt}(E) f(E) \left(\frac{2E}{m_e} \right)^{1/2} dE \quad (4.3)$$

In addition to the photon flux due to excitation from the atomic ground state, the contribution from other initial states (metastable or ionic levels) can be included by replacing n_0 and σ_{ij}^{Opt} by the appropriate values.

In practice, for the EEDF the simplest form typically assumed is a one-parameter Maxwellian distribution characterized by an electron temperature, T_e ,

$$F(E, T_e) = \frac{2\sqrt{E}}{\sqrt{\pi} (kT_e)^{3/2}} \exp\left(-\frac{E}{kT_e}\right) \quad (4.4)$$

Many alternative functional forms of $F(E)$ can be used, depending on how far one expects the EEDF to deviate from a simple Maxwellian. For example, while the EEDF for inductively coupled plasmas can often be well approximated by a single Maxwellian, many capacitively coupled plasmas are better characterized by a three-parameter bi-Maxwellian distribution with a bulk electron temperature, a tail temperature and a fraction of tail electrons [3]. Druyvesteyn distributions and other more general functional forms can also be used [4]. Combining the simplifications of a Maxwellian distribution with spatially averaged densities, the observed photon flux incident on the detector for a particular $i \rightarrow j$ emission line is equal to:

$$I_{ij}^{Obs} = C_{\lambda} n_0 n_e T_e^{-3/2} \int_0^{\infty} \sigma_{ij}^{Opt}(E) \exp\left(-\frac{E}{kT_e}\right) EdE \quad (4.5)$$

where the constant C_{λ} is the sensitivity of the optical system at wavelength λ . Since the excitation cross section is zero for energies below the threshold energy, one can also make the trivial replacement of the lower limit in the integral with E_{0i} .

A single plasma intensity measurement cannot uniquely determine the electron temperature since the photon flux in equation (4.5) depends upon both the electron density and electron temperature. To overcome these difficulties, it is common to measure the line ratio of two emission lines [5-7]

$$\frac{I_{ij}^{Obs}}{I_{ab}^{Obs}} = \frac{C_{\lambda 1} \int_{E_1}^{\infty} \sigma_{ij}^{Opt}(E) \exp[-E/kT] EdE}{C_{\lambda 2} \int_{E_2}^{\infty} \sigma_{ab}^{Opt}(E) \exp[-E/kT] EdE} \quad (4.6)$$

which is only dependent on the electron temperature. While in principle any two excited states of the same atom can be used to find a unique value of the electron temperature, the line-ratio technique works better if the two states have very different energy thresholds, E_1 and E_2 , or if the energy dependences of the cross sections are radically different.

4.2.3 Molecular spectroscopy

The internal energy of molecule is decided by the rotation of molecule, the vibration of each atom, and the electronic state of electrons. Therefore the molecular spectrum is distinguished by the rotational spectrum, the vibrational spectrum, and the electronic spectrum, defined by the following energies:

- (1) Rotational energy (E_r) due to the rotational motion of the molecule about its centre of mass.
- (2) Vibrational energy (E_v) due to the vibrational motion of the atoms in a molecule about their equilibrium positions.
- (3) Electronic energy (E_n) arising due to the motion of electrons in the molecule.

So the total internal energy of a molecule is expressed by:

$$E_{total} = E_r + E_v + E_n \quad (4.7)$$

In a discharge which contains molecular gas, the rotational, vibrational and excitation temperature can be obtained from rotational, vibrational and electronic spectrum, respectively [8-12].

4.2.3.1 Rotational spectra

To understand the rotational spectra of molecules it is necessary to classify them according to their principle moments of inertia. It is a useful approximation to regard the bonds as rigid rods, and the molecule as a rigid rotor. Considering a molecule with two atoms, the moment of inertia about any axis through the centre of gravity is given by:

$$I = \sum_i m_i r_i^2 = m_1 r_1^2 + m_2 r_2^2 = \mu r^2 \quad (4.8)$$

where $r (= r_1 + r_2)$ is the bond length, and μ is the reduced mass of the two nuclei of masses m_1 and m_2 . The rotational energy of this molecule is

$$E = \frac{1}{2} I \omega^2 = \frac{P^2}{2I} \quad (4.9)$$

Using the Schrödinger equation, one can find that the rotational energy E_r of a diatomic molecule is quantized:

$$E_r = \frac{h^2}{8\pi^2 I} J(J+1) \quad (4.10)$$

where J is the rotational quantum number, $J = 0, 1, 2, \dots$. We convert the energy levels of equation (4.10) to what are known as term values $F(J)$ having dimensions of wavenumber by dividing hc , giving:

$$F(J) = \frac{E_r}{hc} = \frac{h}{8\pi^2 c I} J(J+1) = B J(J+1) \quad (4.11)$$

where B is the rotational constant. For the rotational spectra it is necessary to satisfy the following rotational selection rules:

1. The molecule must have a permanent dipole moment ($\mu \neq 0$).
2. $\Delta J = \pm 1$.
3. $\Delta M_J = 0, \pm 1$. ($M_J = J, J-1, \dots, -J$)

Using equation (4.11) the transition wavenumber can be obtained:

$$\nu = F(J+1) - F(J) = 2B(J+1) \quad (4.12)$$

By equation (4.12) we expect the distance of rotational spectra is constant $2B$, but the transition spacing decreases with increasing J . As increase the J , the speed of rotation increases, and the nuclei tend to be thrown outwards by centrifugal forces. Considering the J -dependent decrease of B , equation (4.11) and (4.12) become:

$$F(J) = B_v J(J+1) - D_v J^2(J+1)^2 \quad (4.13)$$

$$\nu = F(J+1) - F(J) = 2B_v(J+1) - 4D_v(J+1)^3 \quad (4.14)$$

where D is the centrifugal constant and is always positive for diatomic molecules. The rotational constants B and D are both slightly vibrationally dependent so that the term values of equation (4.13) and (4.14) should be rigorously written

$$F_v(J) = B_v J(J+1) - D_v J^2(J+1)^2 \quad (4.15)$$

$$\nu = 2B_v(J+1) - 4D_v(J+1)^3 \quad (4.16)$$

The vibrational dependence of B and D are given by

$$B_v = B_e - \alpha_e \left(v + \frac{1}{2} \right) \quad (4.17)$$

$$D_v = \frac{4B_e^3}{\omega^2} \quad (4.18)$$

where B_e refers to the hypothetical equilibrium state of the molecule at the bottom of the potential energy, α_e is a vibration-rotation interaction constant, v is the vibrational quantum number, and ω is the vibrational wavenumber.

4.2.3.2 Vibrational spectra

The vibration of a diatomic molecule can be expressed by Hooke's law of the harmonic oscillator:

$$F = -\frac{dV(x)}{dx} = -k_c x \quad (4.19)$$

where $V(x)$ is the potential energy and k_c is the force coefficient. Integration of this equation gives

$$V(x) = \frac{1}{2} k_c x^2 \quad (4.20)$$

Using the Schrödinger equation, one can find that the vibration energy level E_v of a diatomic molecule is quantized:

$$E_v = hc\omega \left(v + \frac{1}{2} \right) \quad (4.21)$$

where v is the vibrational quantum number. Equation (4.21) shows the vibrational levels to be equally spaced by $hc\omega$, and that the $v = 0$ level has an energy $\frac{1}{2} hc\omega$, known as the zero-point energy. This is the minimum energy the molecule may have even at the absolute zero of temperature and is a consequence of the uncertainty principle. Just as for rotation it is convenient to use term values $G(v)$ (dimensions of wavenumber) instead of energy levels

$$G(v) = \frac{E_v}{hc} = \omega \left(v + \frac{1}{2} \right) \quad (4.22)$$

However, unlike electrical anharmonicity, mechanical anharmonicity modifies the vibrational term values and wave functions due to distance of two atoms. The harmonic oscillator term values of equation (4.22) are modified to a power series in $(v + \frac{1}{2})$

$$G(v) = \omega_e \left(v + \frac{1}{2} \right) - \omega_e \chi_e \left(v + \frac{1}{2} \right)^2 + \omega_e y_e \left(v + \frac{1}{2} \right)^3 + \dots \quad (4.23)$$

where $\omega_e \chi_e$ and $\omega_e y_e$ are anharmonic constants.

4.2.3.3 Spectra of diatomic molecules

Using spectrum terms, equation (4.7) can be rewritten

$$E_{total} = hc(T_n + G + F) = hcT \quad (4.24)$$

where T_n is the spectral term of electronic transitions. The wavenumber ν , corresponding to a transition from an upper state E' to a lower state E'' is

$$\nu = T' - T'' = (T'_n + G' + F') - (T''_n + G'' + F'') \quad (4.25)$$

The wavelength of each transition can be calculated with selection rules, $\Delta J = J' - J'' = 0, \pm 1$ except for $J' = 0 \rightarrow J'' = 0$. The values of ΔJ yield three branches: P , Q and R -branch, corresponding to $\Delta J = -1, 0$, and $+1$, respectively. Furthermore, the structure is complicated by the triplet splitting of the rotational levels J .

The emission intensity of an individual rotational line between two levels (from $n'v'J'$ to $n''v''J''$) is given by

$$I_{n''v''J''}^{n'v'J'} = N_{n'v'J'} A_{n''v''J''}^{n'v'J'} \frac{hc}{\lambda} \quad (4.26)$$

where $N_{n'v'J'}$ is the population of the emitting level and $A_{n''v''J''}^{n'v'J'}$ is the Einstein transition probability. With the normalization condition of the Hönl-London factors the transition probability may be written as

$$A_{n''v''J''}^{n'v'J'} = \frac{A_{n''v''J''}^{n'v'} S_{JJ''}}{(2 - \delta_{0,\Lambda'}) (2S' + 1) (2J' + 1)} \quad (4.27)$$

where $S_{JJ''}$ is the Hönl-London factor for the considered transition, $\delta_{0,\Lambda'}$ is the Kronecker delta (equal to 1 if $\Lambda = 0$, and 0 for all other values), $2S' + 1$ is the spin multiplicity, and $A_{n''v''}^{n'v'}$ is the band strength or the band transition probability given by

$$A_{n''v''J''}^{n'v'J'} = \frac{64\pi^4}{3h\lambda^3} q_{v'v''} |R_e(\bar{r}_{v'v''})|^2 \quad (4.28)$$

where $q_{v'v''}$ is the Franck-Condon factor of the $v' \rightarrow v''$ band and $|R_e(\bar{r}_{v'v''})|^2$ is the square of the electronic-vibrational transition moment.

Considering the energy levels of upper states in Boltzmann equilibrium, $N_{n'v'J'}$ is given by

$$N_{n'v'J'} = N_0 \frac{g_u}{Q(T)} \exp\left(-\frac{E'}{kT}\right) \quad (4.29)$$

where N_0 is the density of particles, $Q(T)$ is the molecular partition function and g_u is the statistical weight of the upper level. The densities of upper levels for the electronic, vibrational and rotational states can be written:

$$N_{n'} = \frac{N_0}{Q_{el}(T_{el})} (2 - \delta_{0,\Lambda'}) (2S' + 1) \exp\left(-\frac{E_n'}{kT_{el}}\right) \quad (4.30)$$

$$N_{n'v'} = \frac{N_{n'}}{Q_v(T_v)} \exp\left(-\frac{E_v'}{kT_v}\right) \quad (4.31)$$

$$N_{n'v'J'} = \frac{N_{n'v'}}{Q_r(T_r)} g_{J'} \phi_{p'} \exp\left(-\frac{E_J'}{kT_r}\right) \quad (4.32)$$

where $g_{J'} = 2J' + 1$, $\phi_{p'}$ allows for nuclear spin degeneracy (Λ -doubling), and Q_{el} , Q_v and Q_r are electronic, vibrational and rotational partition functions, respectively.

Finally, the emission intensity for a transition of a given system, can be written as

$$I_{n''v''J''}^{n'v'J'} = \frac{64\pi^4 c}{3} N_0 \frac{\bar{R}_e^2 q_{v''v'} S_{JJ'} v^4}{Q_{el} Q_v Q_r} \exp\left[-\frac{hc}{k} \left(\frac{T_n'}{T_{el}} + \frac{G'}{T_v} + \frac{F'}{T_r}\right)\right] \quad (4.33)$$

In actual spectrum measurement, the line spectrum derived here is always broadened due to a finite spectral resolution of an optical system. Introducing the spectral resolution as the full width of the half maximum (FWHM), the spectrum is finally written as follows with the Gaussian profile

$$I(\lambda) = \sum I_{n''v''J''}^{n'v'J'} \exp\left(-\frac{(\lambda - \lambda_{n''v''J''}^{n'v'J'})^2}{\Delta\lambda^2}\right) \quad (4.34)$$

where λ is the wavelength of emission light and $\Delta\lambda$ is given by

$$\Delta\lambda = \frac{FWHM}{2\sqrt{\ln 2}} \quad (4.35)$$

4.2.3.4 Ro-vibrational spectra of N_2 and N_2^+

In a low pressure discharge containing nitrogen, three kind of molecular emission spectra are frequently observed simultaneously; (a) the second positive system (SPS) $N_2(C^3\Pi_u, v - B^3\Pi_g, v')$, (b) the first positive system (FPS), $N_2(B^3\Pi_g, v - A^3\Sigma_u^+, v')$, and (c) the first negative system (FNS) $N_2^+(B^2\Sigma_u^+, v - X^2\Sigma_g^+, v')$. From the measured rotational and vibrational spectrum, the rotational and vibrational temperature can be deduced for each excited state. Furthermore, if the electronic temperature is known the N_2^+/N_2 ratio can be obtained from the electronic spectrum.

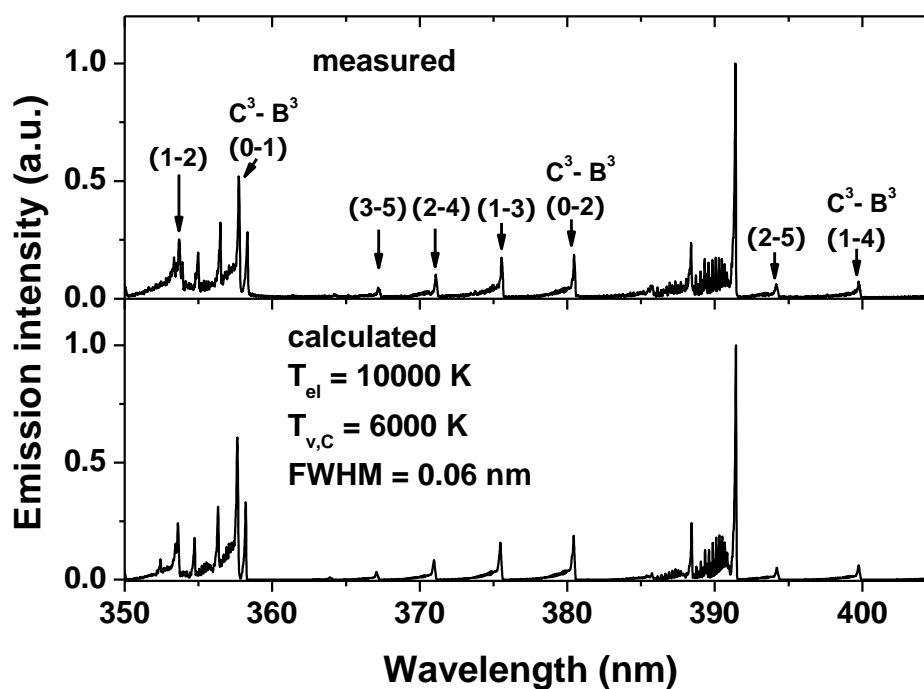
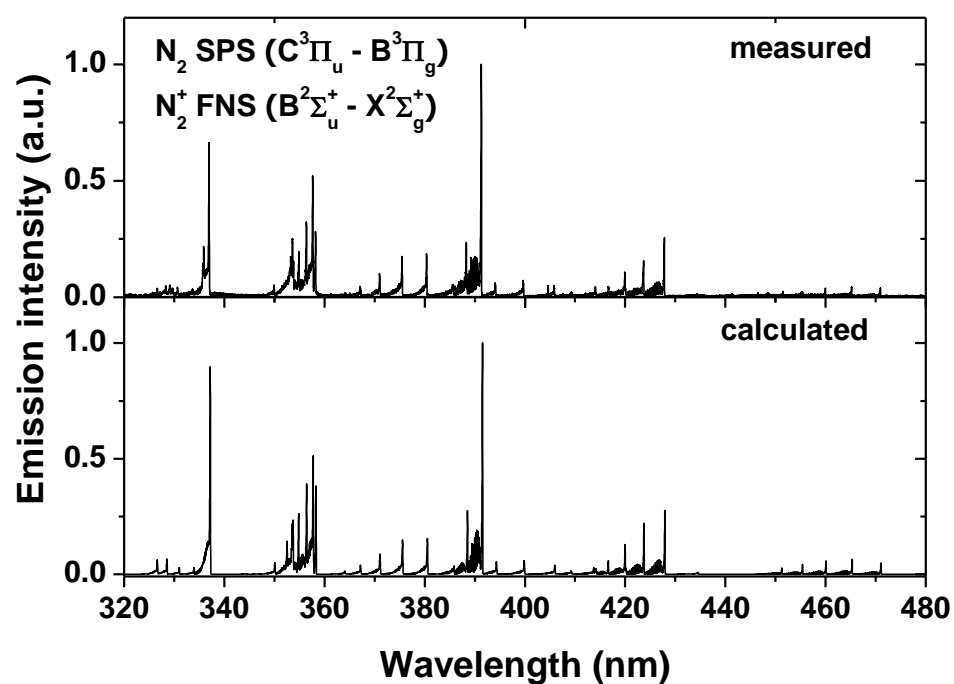


Figure 4.2 Measured and calculated typical emission spectra of SPS $N_2(C^3\Pi_u, v - B^3\Pi_g, v')$ and FNS $N_2^+(B^2\Sigma_u^+, v - X^2\Sigma_g^+, v')$.

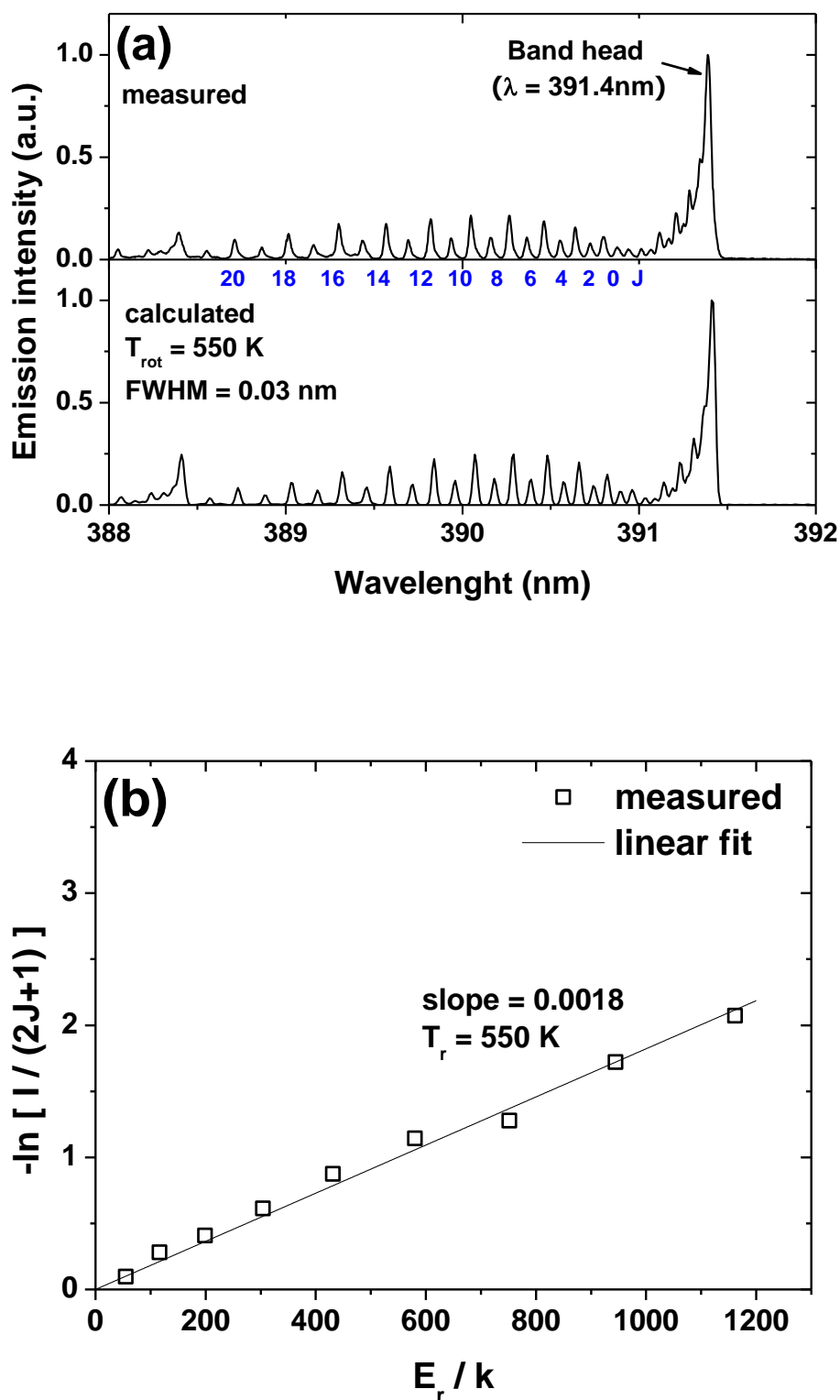


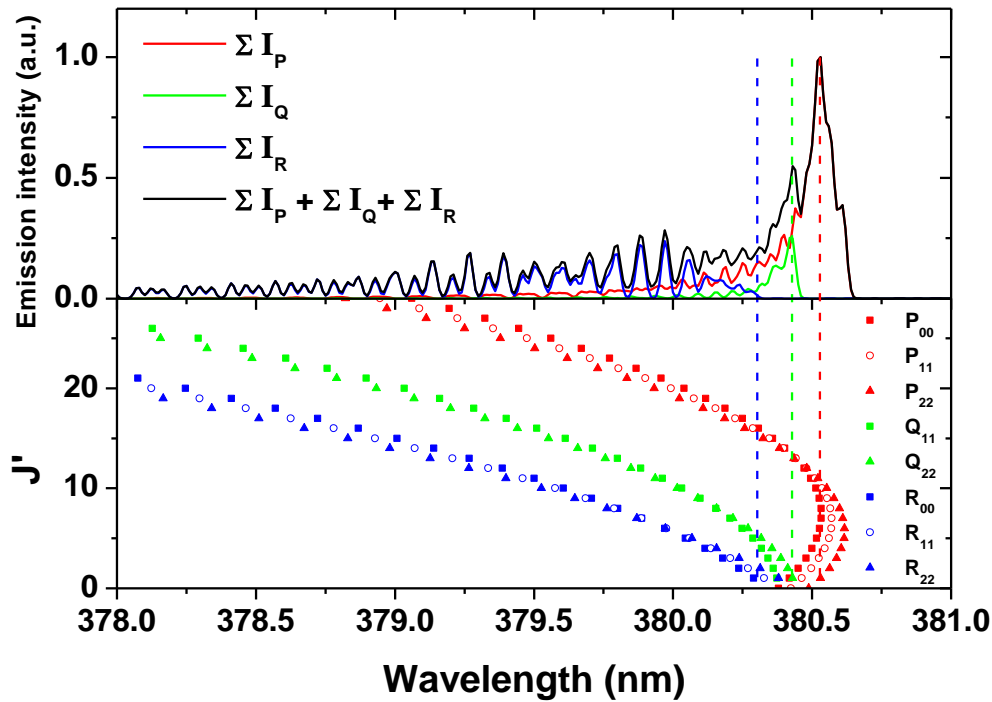
Figure 4.3 (a) Measured rotational spectra of N_2^+ FNS in an ICP discharge at 100 mTorr and calculated rotational spectra with 0.3 \AA of FWHM at 550 K. (b) Linear fitting of $-\ln[I/(2J+1)]$ as function of E_r/k with measured data.

Table 4.1 The spectroscopic constant terms (cm^{-1}) of N_2 excited states.

State	T_e	ω_e	$\omega_e x_e$	$\omega_e y_e$	B_e	α_e
$B^2 \Sigma_u^+$	0	2207.22	16.226	0.004	1.9317	0.0188
$X^2 \Sigma_g^+$	25461.11	2421.14	24.07	-0.30	2.0851	0.0212
$C^3 \Pi_u$	89136.88	2047.78	28.949	2.247	1.8268	0.024
$B^3 \Pi_g$	59619.09	1734.03	14.412	-0.0033	1.6377	0.0179
$A^3 \Sigma_u^+$	50203.66	1460.94	13.980	0.024	1.4539	0.0175

Figure 4.2 shows the measured and calculated typical emission spectra of SPS $\text{N}_2(C^3\Pi_u, v - B^3\Pi_g, v')$ and FNS $\text{N}_2^+(B^2\Sigma_u^+, v - X^2\Sigma_g^+, v')$ for the spectral range 320-480 nm at $T_{el} = 10,000$ K, $T_{v,C} = 6000$ K and FWHM = 0.06nm. The molecular bands of N_2^+ and N_2 can be detected, and the N_2 vibrational bands are characterized by $v' - v''$ transition with $v' > v''$.

Figure 4.3 (a) shows the measured rotational spectrum of N_2^+ FNS in an ICP discharge at 100 mTorr and the calculated rotational spectrum with 0.3 Å of FWHM at 550 K rotational temperature. The term $\phi_{p'}$ characterizing the influence of the Λ -doublings (eq. 4.32) is set at

**Figure 4.4** Calculated rotational spectrum of P , Q and R branches and corresponding Fortrat diagram of $\text{N}_2(C^3\Pi_u, v' = 0 - B^3\Pi_g, v'' = 0)$.

$\phi_{p'}=1/3$ for even J' , and $2/3$ for odd J' . The spectroscopic constant terms (cm^{-1}) of each excited states are given in table (4.1). The rotational temperature can be obtained from the measured emission intensity using equation (4.32),

$$-\ln\left(\frac{I_J}{2J+1}\right) = -\frac{E_r}{kT_r} \quad (4.36)$$

where I_J is the relative emission intensity of rotation quantum number J . Figure 4.3 (b) shows the linear fitting of $-\ln[I_J/(2J+1)]$ as a function of E_r/k with the measured data from figure 4.3 (a). The rotational temperature T_r is obtained from inverse of the slope. The rotational spectrum of each vibrational state in N_2 SPS consists of strong P and R branches and weak Q branches. The P branch of any band is folded, resulting in a well defined intensity maximum and band head towards the red. The structure is further complicated by the triplet splitting of

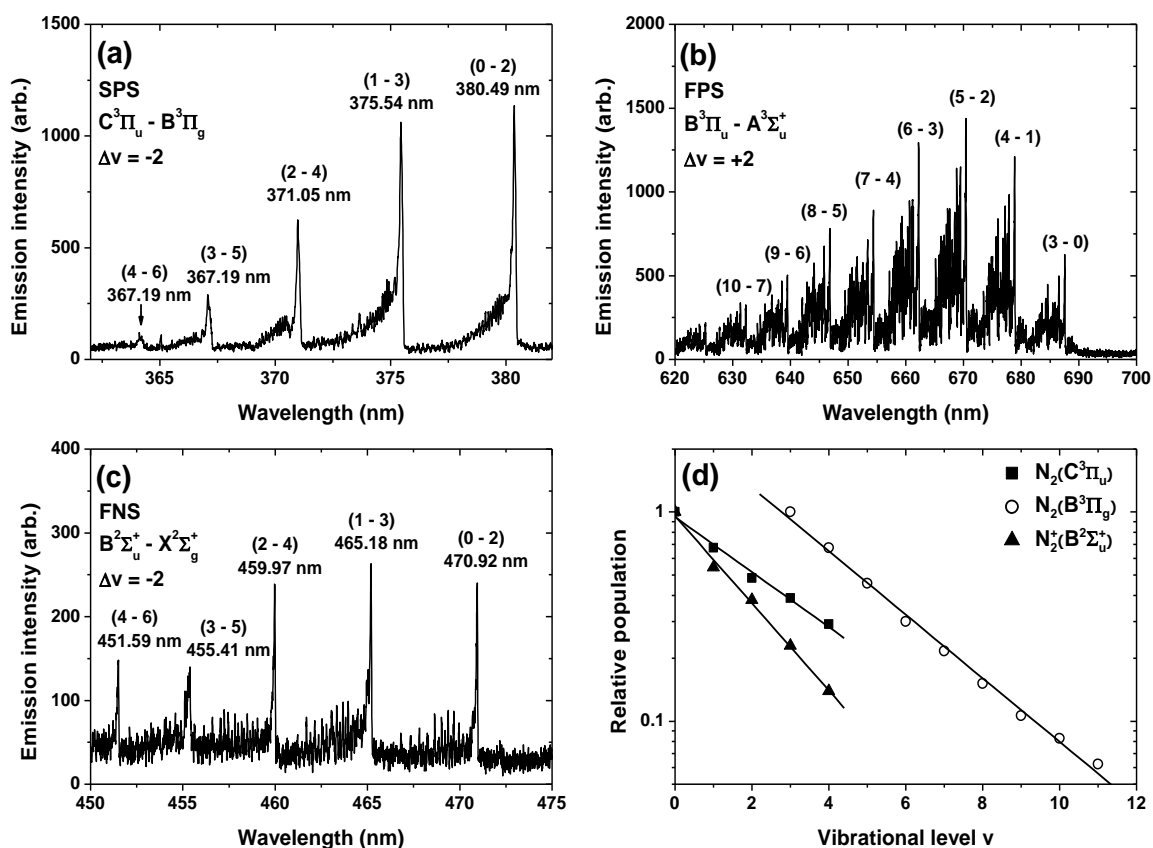


Figure 4.5 Measured vibrational spectra of (a) the second positive system (SPS), (b) the first positive system (FPS) and (c) the first negative system (FNS) in the nitrogen ICP discharge at 100 mTorr and 100 W. (d) Correspond vibrational distributions by normalizing $[\text{N}_2(\text{C},0)] = 1$, $[\text{N}_2(\text{B},3)] = 1$ and $[\text{N}_2^+(\text{B},0)] = 1$ for $\text{N}_2(\text{C}^3\Pi_u)$, $\text{N}_2(\text{B}^3\Pi_g)$ and $\text{N}_2^+(\text{B}^2\Sigma_u^+)$.

the rotational levels J in both states giving three separate P and R sub-branches and two Q sub-branches, corresponding to the J selection rules for multiplet components with the same spin. Figure 4.4 shows the calculated rotational spectrum of P , Q and R branches and the corresponding Fortrat diagram of $N_2(C^3\Pi_u, v' = 0 - B^3\Pi_g, v'' = 0)$. For simplicity, only the principle branches ($i' = i''$) are plotted.

Figure 4.5 show the measured vibrational spectra of:

(a) the second positive system (SPS), $N_2(C^3\Pi_u, v - B^3\Pi_g, v')$, $\Delta v = -2$,

(b) the first positive system (FPS), $N_2(B^3\Pi_g, v - A^3\Sigma_u^+, v')$, $\Delta v = +3$,

(c) the first negative system (FNS), $N_2^+(B^2\Sigma_u^+, v - X^2\Sigma_g^+, v')$, $\Delta v = -2$

in the nitrogen ICP discharge at 100 mTorr. Using equation (4.31) the correspond vibrational distributions are reproduced in figure 4.5 (d) by normalizing $[N_2(C,0)] = 1$, $[N_2(B,3)] = 1$ and $[N_2^+(B,0)] = 1$ for $N_2(C^3\Pi_u)$, $N_2(B^3\Pi_g)$ and $N_2^+(B^2\Sigma_u^+)$, respectively. The vibrational temperature T_v and vibrational distribution can be calculated by Boltzmann's distribution law as done previously for rotational temperature using equation (4.31). The wavelength and the transition probability of SPS, FPS and FNS are given in table (4.2), (4.3) and (4.4), respectively.

Table 4.2 The wavelength and the transition probability of second positive system (SPS), $N_2(C^3\Pi_u, v - B^3\Pi_g, v')$, $\Delta v = -2$.

v	v'	λ (nm)	$A_{vv'} (10^6 s^{-1})$
0	2	380.49	3.34
1	3	375.54	4.62
2	4	371.05	3.80
3	5	367.19	2.19
4	6	364.17	0.90

Table 4.3 The wavelength and the transition probability of the first positive system (FPS), $N_2(B^3\Pi_g, v - A^3\Sigma_u^+, v')$, $\Delta v = +3$

v	v'	λ (nm)	$A_{vv'} (10^6 s^{-1})$
3	0	687.5	0.009975
4	1	678.86	0.0286
5	2	670.48	0.05023
6	3	662.36	0.06889
7	4	654.48	0.08026
8	5	646.85	0.08239
9	6	639.47	0.07563
10	7	632.29	0.06208
11	8	625.28	0.04491

Table 4.4 The wavelength and the transition probability of the first negative system (FNS), $N_2^+(B^2\Sigma_u^+, v - X^2\Sigma_g^+, v')$, $\Delta v = -2$.

v	v'	λ (nm)	$A_{vv'} (10^6 s^{-1})$
0	2	470.92	0.8136
1	3	465.18	1.639
2	4	459.97	2.135
3	5	455.41	2.251
4	6	451.59	2.081

4.3 Optical absorption spectroscopy (OAS)

Optical absorption spectroscopy (OAS) is a powerful tool to evaluate the absolute species density in plasma. It can be used in a wide range of radiation, such as in infrared, visible and ultraviolet ranges. This technique provides the line-of-sight spatial resolution, and gives the quantitative values of absorbance, from which the absolute absorber number densities can be calculated. This method does not disturb the plasma and does not need the procedure of calibration for estimating the absolute density. Usually, the various kinds of light sources are developed for radicals. Ohebsian *et al* [13] used OAS to study the mechanisms of production and loss of the neutral and ionized titanium species in the pulse hollow cathode discharge. For Ar metastable kinetics in argon diluted discharge, Ar metastable density was determined [14,15]. In the magnetron sputtering discharge the OAS is widely used to monitor the sputtering yield and the effects of the gas mixture, the additional excited source, and pulse discharge using hollow cathode lamp (HCL) or continuum light source (Xenon arc lamp) [16-22]. The Si atom densities in parallel-plate RF and ECR SiH_4 plasmas were measured by ultraviolet absorption spectroscopy (UVAS) using an incoherent hollow cathode lamp [23,24]. The incoherent hollow cathode lamp is compact and applied to the measurement of atomic radicals. Also UVAS technique was applied to measure the absolute densities of carbon (C) atoms in an ICP employing CO/H_2 gases and ECR plasma employing fluorocarbon gases [25,26]. By using this technique, the behaviors of C atoms in the etching and deposition plasma processes have been clarified. Vinogradov *et al* [27] measured the concentrations of NO_x and O_3 in the N_2/NO dielectric barrier discharge (DBD). The vacuum ultraviolet absorption spectroscopy (VUVAS) is used for determination of atom density in reactive discharge. Vialle *et al* [28] measured the concentrations of $\text{O}(^1\text{D})$ and $\text{O}(^1\text{S})$ metastable atoms in the positive column of a DC oxygen glow discharge. Nagai *et al* [29] measured O atom density using the micro-discharge hollow cathode lamp (MHCL) in O_2 TCP discharge. This method was used to measure N atom density and F atom density in various discharges [30-33]. Recently, the broad-band UVAS has been widely used to measure the density of molecular radicals such as CF_2 , CF, Cl_2 and BCl using continuum light source or light emitting diodes (LED) [34-39].

The absorption coefficient A_L is given by:

$$A_L = 1 - \frac{I_{transmitted}}{I_{source}} \quad (4.37)$$

where I_{source} is the intensity of the reference source and $I_{transmitted}$ is the intensity of the spectral line transmitted through the plasma. Experimentally we can determine the absorption coefficient as:

$$A_L = 1 - \frac{I_{plasma+source} - I_{plasma}}{I_{source}} \quad (4.38)$$

where $I_{plasma+source}$ is the emission intensity from the reference source through the plasma, and I_{plasma} is the emission intensity from the plasma only.

The absorption coefficient A_L is related to the optical depth $k_{\sigma 0}L$ through [40]:

$$\begin{aligned} A_L &= \frac{\int_{-\infty}^{\infty} e^{-(\omega/\alpha)^2} \left(1 - e^{-k_{\sigma 0}L e^{-\omega^2}}\right) d\omega}{\int_{-\infty}^{\infty} e^{-(\omega/\alpha)^2} d\omega} \\ &= \frac{k_{\sigma 0}L}{(1 + \alpha^2)^{1/2}} - \frac{(k_{\sigma 0}L)^2}{2!(1 + 2\alpha^2)^{1/2}} + \dots + (-1)^n \frac{(k_{\sigma 0}L)^n}{n!(1 + n\alpha^2)^{1/2}} + \dots \\ &= \sum_{n=1}^{\infty} \frac{(-1)^{n+1}}{n!} \frac{(k_{\sigma 0}L)^n}{(1 + n\alpha^2)^{1/2}} \end{aligned} \quad (4.39)$$

where ω is the frequency of the line and α is the dimensionless ratio between the full width at half maximum (FWHM) of the source line and the plasma line:

$$\alpha = \frac{\delta\sigma_{1/2}^S}{\delta\sigma_{1/2}^P} \quad (4.40)$$

Once $k_{\sigma 0}L$ is determined the density of absorbing atoms n_j is given by the following numerical equation:

$$k_{\sigma 0}L = 8.23 \times 10^{-13} \frac{fL}{\delta\sigma_{1/2}^P} n_j \quad (4.41)$$

with $k_{\sigma 0}$, $\delta\sigma_{1/2}^P$ in cm^{-1} and n_j in cm^{-3} . f is the oscillator strength and L is the absorption length expressed in cm. Figure 4.6 shows the optical depth $k_{\sigma 0}L$ variations versus the absorption coefficient for α values between 0 and 5. As increase the absorption coefficient the optical depth is sensitive to the α value. To avoid misestimating the species density, it is necessary to measure precisely the FWHMs of the reference source and the plasma. The FWHMs can be measured with a Fabry-perot interferometer or other high resolution spectrometer. If the gas pressure is low (< 1 Torr), the line width can be calculated by taking a Doppler line profile,

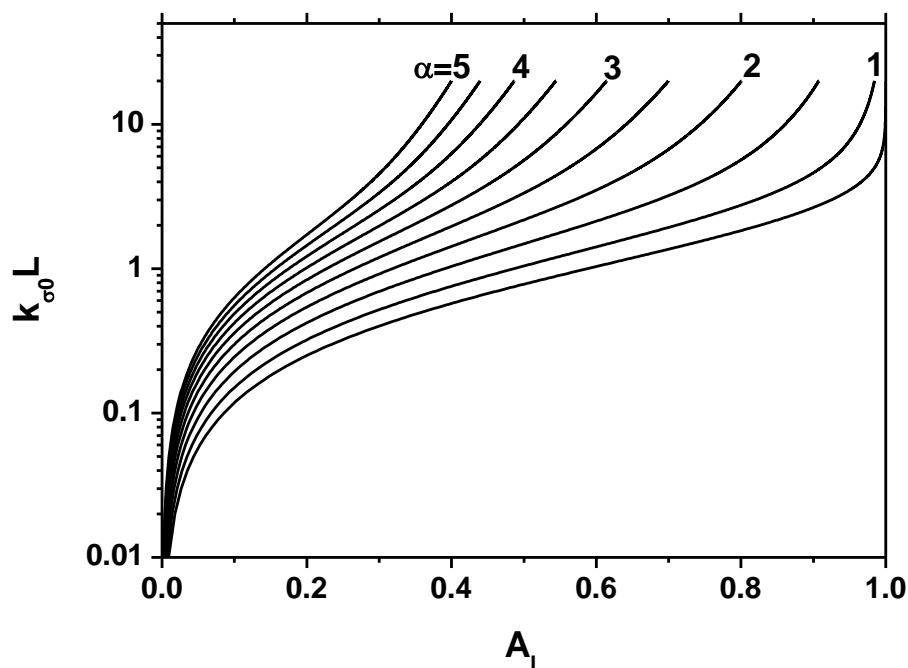


Figure 4.6 Calculated optical depth $k_{\sigma_0}L$ variations versus the absorption coefficient for α values between 0 and 5.

which is the dominant line broadening in glow discharges [41,42]. The Doppler line width is calculated from the equation:

$$\delta\sigma_D = 7.16 \times 10^{-7} \sigma_0 \left(\frac{T}{M} \right)^{1/2} \quad (4.42)$$

where $\sigma_0 = 1/\lambda_0$ (cm^{-1}) is the wavenumber at the center of the spectral peak, T (K) is the plasma temperature in Kelvin, M (g/mol) is the atomic mass.

4.4 Two-photon absorption laser-induced fluorescence (TALIF)

Laser-induced fluorescence (LIF) was firstly used for plasmas to measure the decay rate of helium using the dye laser by Burgess [43] in 1974, and Stern [44] measured the LIF signal of an argon DC discharge using ArII laser in 1975. Laser-based plasma diagnostic techniques have largely contributed to advances in the understanding of active plasma kinetics. This technique gives some advantages such as high spatial resolution by the directionality of laser, high temporal resolution by pulse laser, and the selectivity of specific species in the volume by the narrow FWHM. Therefore the past decades, LIF was used as a powerful technique to measure the ions, neutrals and radicals in the discharge.

4.4.1 Principle

The basic mechanism of LIF has been explained in many articles [45-47]. The LIF mechanism can be briefly described as a two-step process. First, a specific atomic or molecular species in its ground state $|1\rangle$ of energy E_1 is excited by resonant absorption of laser photons of energy $h\nu_{\text{laser}} (= E_3 - E_1)$ to a higher energy electronic level $|3\rangle$ of energy E_3 . Then, the excited state relaxes by spontaneous emission of a fluorescence radiation with $h\nu_{\text{LIF}} (= E_3 - E_2)$ to a lower state $|2\rangle$ of energy E_2 . Basically three types of laser excitation should be distinguished: an atomic excitation, a molecular excitation and an excitation with multi-photon transition. The particular case of an excitation by two photons leads to the so-called Two Photon Absorption LIF (TALIF). TALIF is currently used for the detection of atoms having their first energy level above 6.5 eV. A simplified scheme of these three type excitations is given in figure 4.7.

The basic scheme of LIF experimental setup for plasma diagnostics is presented in figure 4.8. A pump laser is used to pump the dye laser with an ability to tune the wavelength using the internal grating. Typically Nd:YAG (neodymium-doped yttrium aluminum garnet) laser is used for the pump laser with 10 Hz frequency. The wide range of wavelength is possible to investigate by changing the dye. The fluorescence detection is usually made perpendicularly to the laser beam. The fluorescence signal generated in plasma, goes to a monochromator or a filter using simple collimation system. Detection is done by a PMT or a ICCD system and is averaged using a boxcar within a gate time triggered by the pump laser signal. The detection gate time depends on the radiative and collisional lifetime of the fluorescence level. The spatial resolution is obtained by moving together the laser beam and the optical detection system or the set-up itself.

4.4.2 Measurement of absolute density

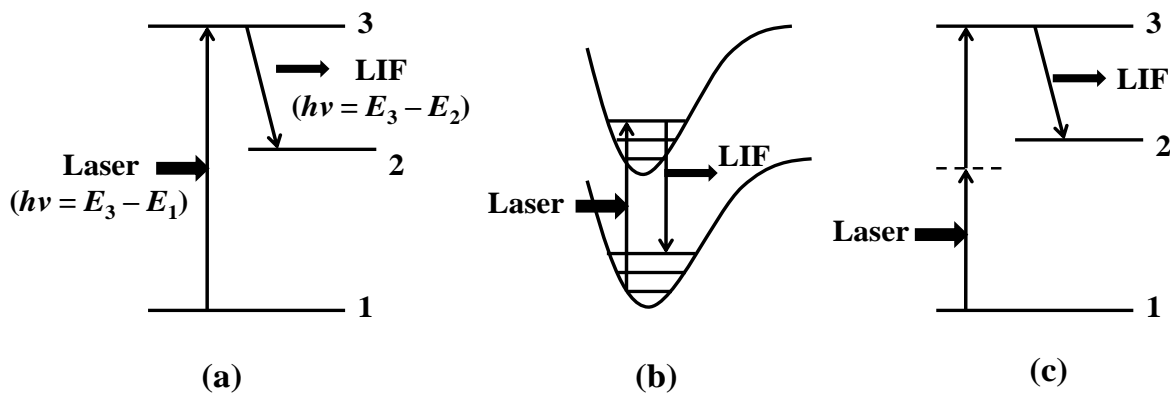


Figure 4.7 Energy diagram for typical LIF excitation of (a) atom, (b) a diatomic molecule, radical or ion, and (c) a multiphoton transition.

Regarding the excitation scheme depicted in figure 4.7 (a), the intensity of the LIF signal I_{LIF} excited by the laser beam is

$$I_{LIF} \propto A_{32}n_3 \quad (4.43)$$

where A_{32} is the Einstein transition probability for the spontaneous emission of $|3\rangle \rightarrow |2\rangle$ and n_3 is the density of level $|3\rangle$. The corresponding rate equation is given by

$$\frac{dn_3}{dt} = \left(n_1 - \frac{g_1}{g_3} n_3 \right) B_{13} I_{laser}^2 - \sum_n A_{3n} n_3 - Q_3 n_3 \quad (4.44)$$

where n_1 is the density of level $|1\rangle$, g_1 and g_3 are the statistical weights of the levels $|1\rangle$ and $|3\rangle$, respectively, B_{13} is the Einstein absorption coefficient, I_{laser} is the laser intensity. $Q_3 = \sum_i q_i P_i$ denotes a term for the collisional depopulation of level $|3\rangle$, where q_i and P_i are the quenching rate constant and partial pressure of species i , respectively. $\sum_n A_{3n}$ is the sum of the spontaneous de-excitation probabilities of level $|3\rangle$ toward all the lower levels and is equal to the inverse of the mean radiative lifetime of the level $|3\rangle$. In a steady state, the LIF signal is proportional to the density of n_1 and to the laser intensity according to

$$I_{LIF} = KB_{13} I_{laser} \frac{A_{32}}{Q_3 + A_3} n_1 \quad (4.45)$$

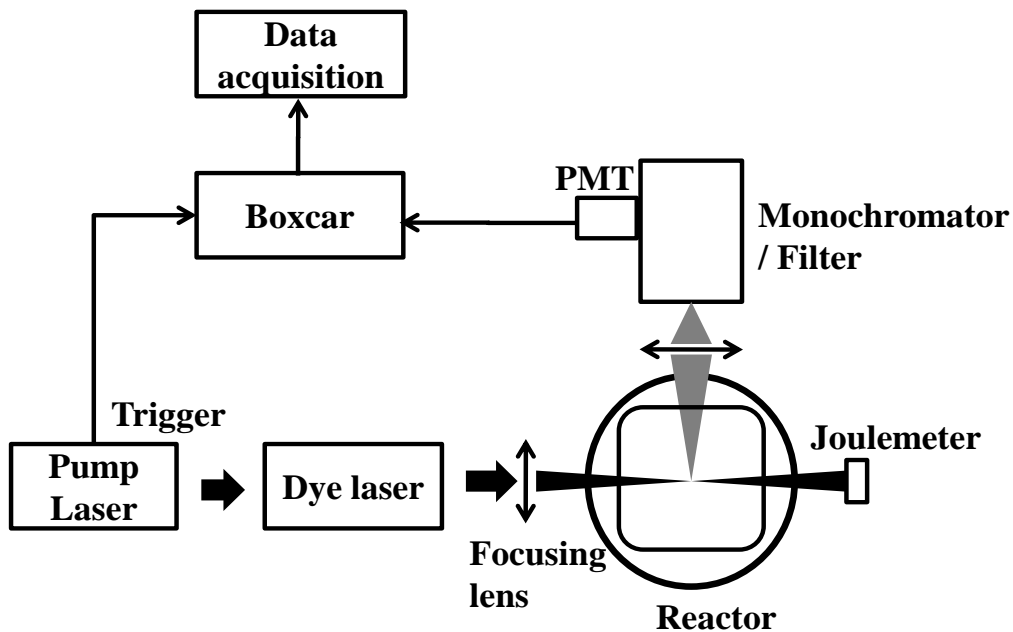


Figure 4.8 Schematic diagram of a typical arrangement used in LIF diagnostics.

where K is a factor, which takes into account the geometry and the spectral response of the optical imaging and detection system, and A_3 is $\sum_n A_{3n}$. In principle, it is possible to calculate the absolute density n_1 , but in practice it is very difficult to evaluate the factor K . Finally, density of the level $|1\rangle$ is given by

$$n_1 = C_1 \frac{I_{LIF}}{I_{laser}} \quad (4.46)$$

with a constant of proportionality C_1 [48]. Based on the last expression we can see, the determination of n_1 is possible when the LIF signal is linearly proportional to the laser intensity.

4.5 Langmuir probe

A metal probe inserted in a discharge and biased positively or negatively to draw electron or ion current, is one of the earliest and still one of the most useful tools for diagnosing a plasma. These probes, introduced by Langmuir and analyzed on considerable detail by Mott-Smith and Langmuir (1926) is usually called *Langmuir probes* [49]. The current vs. voltage, called the *I-V characteristic*, can be analyzed to reveal information about n_e , T_e , V_p , and even the distribution function $F(E)$. Since the probe is immersed in a harsh environment, special techniques are used to protect in from the plasma and vice versa. The probe tip is made of a high-temperature material, usually a tungsten rod or wire 0.1-1 mm in diameter. The rod is threaded into a thin ceramic tube, usually alumina, to insulate it from the plasma except for a short length of exposed tip, about 2-10 mm long. Usually to compensate the RF electric field, a LC-resonance filter is equipped inside the probe [50,51].

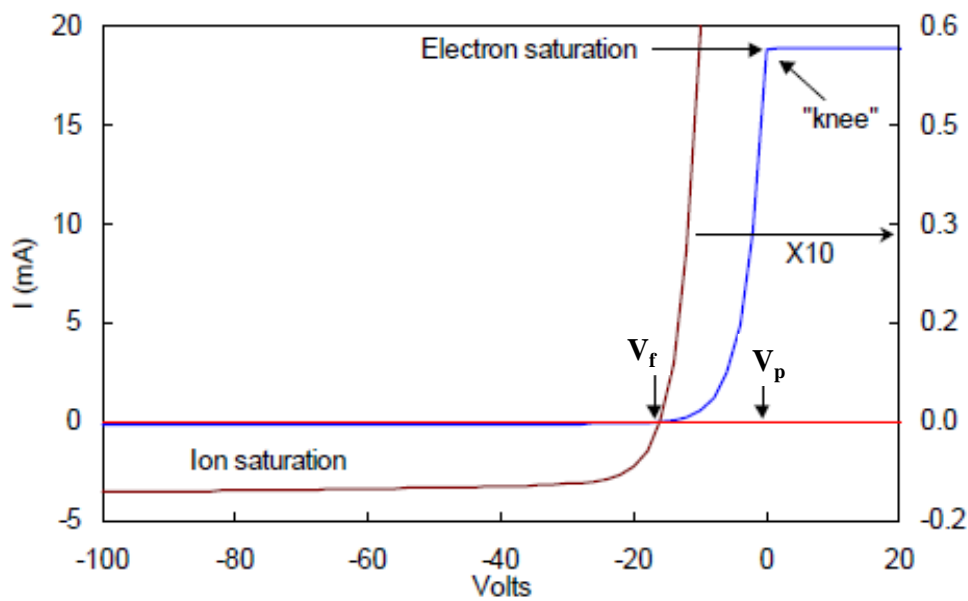


Figure 4.9 An idealized *I-V* curve. The left curve is expanded 10× to show the ion current.

Let the plasma potential is V_p , and the potential applied to the probe is V_b . When $V_b \gg V_p$, an electron current I_e is collected; the probe current is negative. When $V_p \ll V_b$, an ion current I_i is collected. It is customary to plot I - V curves with I_e positive and I_i negative. Such a plot is shown in figure 4.9. There are five main parts. The **plasma potential** V_p is near the “knee” of the curve. At the far left, where all the electrons have been repelled, we have the **ion saturation current**, I_{sat} . The **floating potential** V_f is where the ion and electron currents are equal, and the net current is zero. In the **transition region**, the ion current is negligible, and the electrons are partially repelled by the negative potential $V_b - V_p$. In a Maxwellian plasma, this part of the curve is exponential. When V_b reaches V_p , all of the random thermal flux of electrons is collected. In the **electron saturation region**, I_e grows only slowly because of the expansion of the sheath. From the I - V curve, the plasma density n_e , electron temperature KT_e , and plasma potential V_p can be determined, but not the ion temperature.

The electron energy probability function EEPF $f(E)$ can be obtained from Druyvesteyn formula [52]:

$$f(E) = \frac{2\sqrt{2m_e}}{e^3 A} \frac{d^2 I_p}{dV_b^2} \quad (4.47)$$

where e and m_e are the electron charge and mass, V_b and I_p are the probe voltage and current, and A is the probe surface area. The electron energy distribution function EEDF $F(E)$, the plasma density n_e , the mean electron energy $\langle E \rangle$, and the effective electron temperature T_{eff} are given by:

$$F(E) = \sqrt{E} f(E) \quad (4.48)$$

$$n_e = \int_0^\infty F(E) dE \quad (4.49)$$

$$T_{eff} = \frac{2}{3} \langle E \rangle = \frac{2}{3n_e} \int_0^\infty EF(E) dE \quad (4.50)$$

Figure 4.10 show (a) the typical probe I - V characteristic and its second derivative measured in an argon ICP discharge at 20 mTorr, and (b) the semi-log plot of the EEPF from the I - V curve. The plasma potential V_p is determined from the second derivative curve of the I - V curve, which is minimum point of $|I_p''|$.

In this study, to measure the time evolution of electron temperature and electron density, Maresca *et al* [53] method is used. At each fixed probe voltage, the probe current is obtained from the voltage drop over a resistor using an analog digital convertor card. This measurement is performed several thousand sweeps and then averaged to reduce the noise. After a complete voltage scanning, the probe current is determined as a function of time $I_{p,V=const}(t)$ at a constant probe voltage, and next converted into the I - V probe characteristic curve $I_{p,t=const}(V)$ for a specific time. Figure 4.11 shows the measured I_p curves at each fixed probe voltage in a pulse modulated argon RF discharge (pressure = 20 mTorr, frequency = 500 Hz). The time resolution of the I - V curves is 2 μ sec with a 500 kHz sampling rate of the AD convertor card.

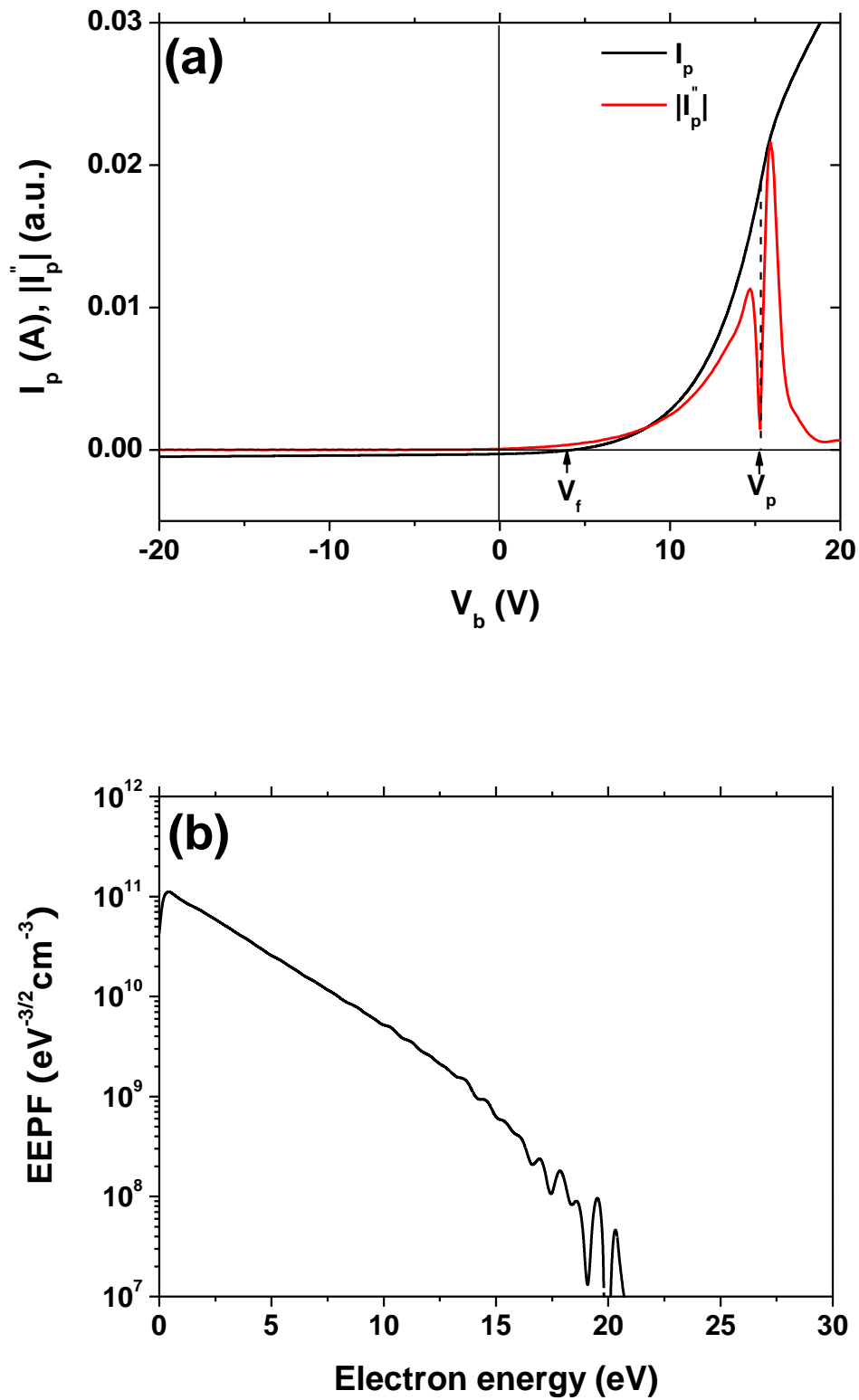


Figure 4.10 (a) Typical probe I - V characteristic and its second derivative measured in an argon ICP discharge at 20 mTorr, and (b) the semi-log plot of the EEPF from the I - V curve.

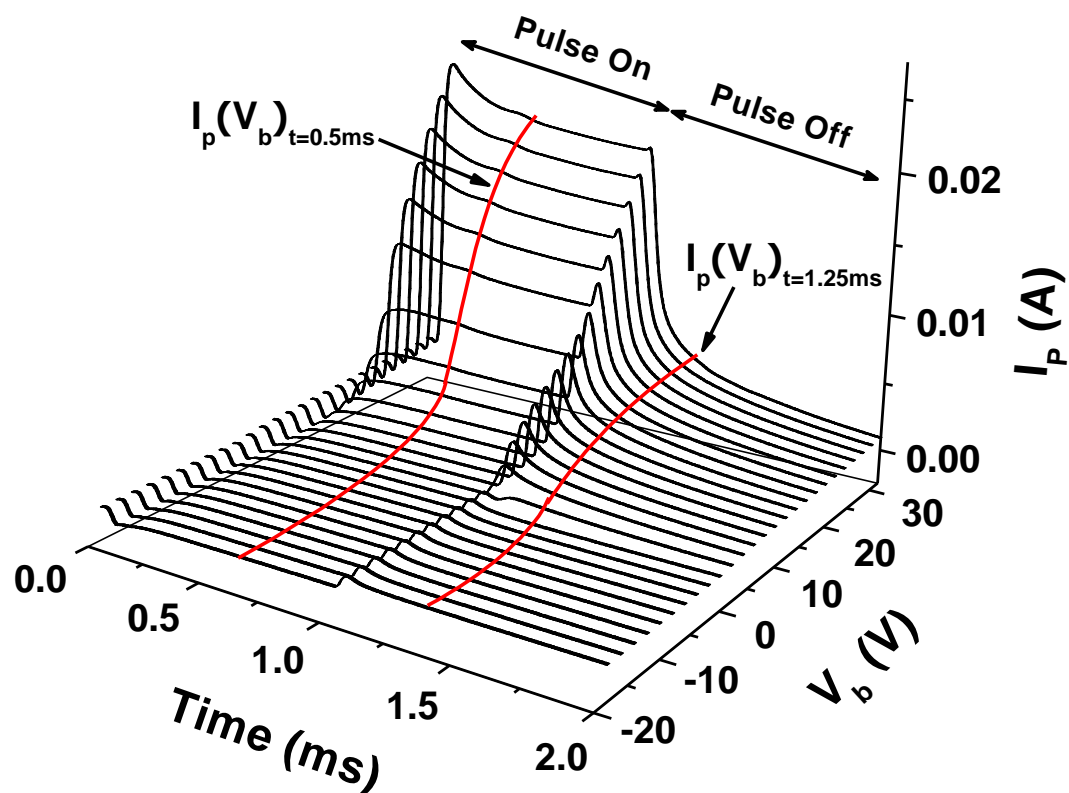


Figure 4.11 Measured I_p curves at each fixed probe voltage in a pulse modulated argon RF discharge (pressure = 20 mTorr, frequency = 500 Hz).

4.6 References

- [1] McWhirter R W P 1965 *Plasma Diagnostics Techniques* ed R H Huddleston and S L Leonard (New York : Academic)
- [2] Boffard J B, Lin C C and DeJoseph Jr C A 2004 *J. Phys. D: Appl. Phys.* **37** R143
- [3] Sugai H, Ghanashev I, Hosokawa M, Mizuno K, Nakamura K, Toyoda H and Yamauchi K 2001 *Plasma Sources Sci. Technol.* **10** 378–85
- [4] Behringer K and Fantz U 1994 *J. Phys. D: Appl. Phys.* **27** 2128–35
- [5] Hood W H and Niemczyk T M 1987 *Appl. Spectro.* **41** 674
- [6] Boivin R F, Kline J L and Scime E E 2001 *Phys. Plasmas* **8** 5303
- [7] Donnelly V M and Schable M J 2002 *J. Appl. Phys.* **91** 6288
- [8] Gerhard Herzberg 1950 *Molecular spectra and molecular structure*
- [9] Hollas J M 2002 *Basic atomic and molecular spectroscopy* (New York: John Wiley&Sons)
- [10] Hollas J M 2004 *Modern spectroscopy* (New York: John Wiley&Sons)
- [11] Pearse R W B and Gaydon A G 1940 *The identification of molecular spectra* (New York: John Wiley&Sons) pp 217-229
- [12] Lofthus A and Krupenie P H 1977 *J. Phys. Chem. Ref. Data* **6** 113
- [13] Ohebsian D, Sadeghi N, Trassy C and Mermet J M 1980 *Optics Communication* **32** 81
- [14] Sansonnels L, Howling A A, Hollenstein C, Dorier J L and Kroll U 1994 *J. Phys. D: Appl. Phys.* **27** 1406
- [15] Hebner H A 1996 *J. Appl. Phys.* **80** 2624
- [16] Dony M F, Ricard A, Wautelet M, Dauchot J P and Hecq M 1997 *J. Vac. Sci. Technol. A* **15** 1890
- [17] Vanderbecq A C, Wautelet M, Dauchot J P, Hecq M, Pointu A M and Ricard A 1998 *J. Appl. Phys.* **84** 100
- [18] Andrew Y, Abraham I, Booske J H, Lu Z C and Wendt A E 2000 *J. Appl. Phys.* **88** 3208
- [19] Nakamura T and Okimura K 2002 *J. Vac. Sci. Technol. A* **20** 1
- [20] Dony M F, Dauchot J P, Wautelet M, Hecq M and Ricard A 2000 *J. Vac. Sci. Technol. A* **18** 809
- [21] Ricard A, Nouvellon C, Konstantinidis S, Dauchot J P, Wautelet M and HecqM 2002 *J. Vac. Sci. Technol. A* **20** 1488
- [22] Konstantinidis S, Ricard A, Dauchot J P, Ranea C and Hecq M 2004 *J. Appl. Phys.* **95** 2900
- [23] Sakakibara M, Hiramatsu M and Goto T 1991 *J. Appl. Phys.* **69** 3467.
- [24] Yamamoto Y, Hori M, Goto T and Hiramatsu M 1996 *J. Vac. Sci. Technol. A* **14** 1999.
- [25] Ito H, Ikeda M, Ito M, Hori M, Takeo T, Hattori H and Goto T 1997 *Jpn. J. Appl. Phys.* **36** L880.

- [26] Den S, Kuno T, Ito M, Hori M, Goto T, O’Keeffe P, Hayashi Y and Sakamoto Y 1997 *J. Vac. Sci. Technol. A* **15** 2880.
- [27] Vinogradov I P and Wiesemann K 1997 *Plasma Sources Sci. Technol.* **6** 307,
- [28] Vialle M, Touzeau M, Gousset G and Ferreira C M 1991 *J. Phys. D: Appl. Phys.* **24** 301
- [29] Nagai H, Hiramatsu M, Hori M and Goto T 2003 *Rev. Sci. Instrum.* **74** 3453
- [30] Tada S, Takashima S, Hori M, Goto T and Sakamoto Y 2000 *J. Appl. Phys.* **88** 1756
- [31] Takashima S, Arai S, Hori M, Goto T, Kono A, Ito M and Yoneda K 2001 *J. Vac. Sci. Technol. A* **19** 599
- [32] Kitajima T, Nakano T, Samukawa S and Makebe T 2008 *Plasma Sources Sci. Technol.* **17** 024018
- [33] Sasaki K, Kawai Y and Kadota K 1997 *Appl. Phys. Lett.* **70** 1375
- [34] Booth J P, Cunge G, Neuilly F and Sadeghi N 1998 *Plasma Sources Sci. Technol.* **7** 423
- [35] Kogelschatz M, Cunge G and Sadeghi N 2004 *J. Phys. D: Appl. Phys.* **37** 1954
- [36] Booth J P, Abada H, Chabert P and Graves D B 2005 *Plasma Sources Sci. Technol.* **14** 273
- [37] Cunge G, Mori M, Kogelschatz M and Sadeghi N 2006 *Appl. Phys. Lett.* **88** 051501
- [38] Cunge G, Vempaire D, Touzeau M and Sadeghi N 2007 *Appl. Phys. Lett.* **91** 231503
- [39] Ramos R, Cunge G, Touzeau M and Sadeghi N 2008 *J. Phys. D: Appl. Phys.* **41** 115205
- [40] Mitchell A C G and Zemanski M W Z 1971 *Resonance Radiation and Excited Atoms* (Cambridge: Cambridge University Press)
- [41] Konstantinidis S, Ricard A, Fanciu M, Dauchot J P, Ranea C and Hecq M 2004 *J. Appl. Phys.* **95** 2900
- [42] Griem H R 1964 *Plasma Spectroscopy* (New York: McGraw-Hill)
- [43] Burgess D D and Skinner C H 1974 *J. Phys. B: At. Mol. Phys.* **7** L297
- [44] Stern R A and Johnson III J A 1975 *Phys. Rev. Lett.* **34** 1548
- [45] Herman I P 1996 *Optical diagnostics for thin film processing* (New York: Academic press)
- [46] Muraoka K and Maeda M 1993 *Plasma Phys. Control. Fusion* **35** 633
- [47] Amorim J, Baravian G and Jolly J 2000 *J. Phys. D: Appl. Phys.* **33** R51
- [48] Petrov G M 2002 *J. Quant. Spectrosc. Radiat. Transfer* **72** 281
- [49] Mott-Smith H M and Langmuir I 1926 *Phys. Rev.* **28** 727
- [50] Godyak V A, Piejak R B and Alexandrovich B M 1992 *Plasma Sources Sci. Technol.* **1** 36
- [51] Seo S H, Chung C W, Hong J I and Chang H Y 2000 *Phys. Rev. E* **62** 7155
- [52] Godyak V A, Piejak R B and Alexandrovich B M 1993 *J. Appl. Phys.* **73** 3657
- [53] Maresca A, Orlov K and Kortshagen U 2000 *Phys. Rev. E* **65** 056405

Chapter 5

Low pressure argon ICP discharge

Contents

5.1	Introduction	66
5.2	Experimental setup	67
5.3	Determination of the electron temperature in a planar inductive argon plasma with emission spectroscopy and electrostatic probe	68
5.3.1	Measurement of EEPF and optical emission	68
5.3.2	Radiation trapping and line ratio method	70
5.3.3	Pressure dependence of the cascade cross-section	71
5.4	Modeling and experimental study of pulse modulated ICP afterglow: production of Ar highly excited states	74
5.4.1	Experiments	74
5.4.2	Discharge model	78
5.4.3	Results and discussion	80
5.4.3.1	Electron density and electron temperature in continuous mode . .	80
5.4.3.2	Electron temperature and electron density in pulse mode	81
5.4.3.3	Ar excited states in pulse mode	83
5.5	Modeling of E-H mode transition and hysteresis in low pressure argon ICP discharges	91
5.5.1	E-H mode transition and hysteresis	91
5.5.2	Discharge model	91
5.5.3	Results and discussion	92
5.6	Conclusion	95
5.7	References	97

5.1 Introduction

THIS chapter describes the experimental and theoretical results of the low pressure argon inductively coupled discharges, which are most widely used not only in plasma science but also in industrial plasma processing, due to the low breakdown voltage and relatively low price of the argon gas.

First, we propose a new method of improving the precision of the pressure-dependent electron temperature calculated by the line ratio method. In the field of industrial plasma processing, the electron temperature is an important parameter related to the use of low-pressure, high-density plasma. Electrostatic probes are indispensable diagnostic tools in low-pressure weakly ionized plasmas. These probes are widely used to estimate the electron temperature of plasma despite the complicated interpretation of the results and the intrusiveness of the procedure. Alternatively, optical methods can be used with confidence in situations where a Langmuir probe analysis is difficult or impossible [1]. Spectral line ratio techniques in optical emission spectroscopy (OES) provide an advantage as they are non-intrusive. However, in plasmas with a gas range that is several tens to hundreds of mTorr, as frequently used in industrial processes, the range of temperature determined by OES using the optical cross-sections from references becomes substantially smaller than the scope measured by a Langmuir probe. This difference has been studied in previous publications [2,3]. First, there is shortage of data related to cross-sections for plasma in all related industries [4-6]. Secondly, the electron temperature is not simply represented by a parameter with a Maxwellian distribution of electron energy [7]. Several studies have attempted to correct the poor estimation of the electron temperature using line ratio methods. Determining the electron temperature via the trace rare gas OES, Schabel *et al* [8] introduced a correction factor, f_{rel} , for high pressures on the electron-impact cross-section for excitation of an Ar ground state to Ar(4p) excited levels, calculated as a function of the electron energy by the empirical function. Crolly *et al* [9] defined the parameters a and b using the numerical approach of : $T_e \cong \left(a \frac{I(ArII)}{I(ArI)} \right)^b$, and the ratios between the ion line Ar II and the selected atomic line Ar I were fitted to describe well the electron temperature curve measured by Langmuir probe. In this section, using the EEPF and the electron density from a single probe, a new method of correcting the electron excitation kinetics is proposed in which the pressure dependency of the electron temperature as calculated by the spectral line ratio, approaches the effective electron temperature measured via a single Langmuir probe.

Second, we study the production of argon excited states in the afterglow of pulse discharge. Recently pulsed glow discharges are widely investigated for its distinct advantages compared with continuous glow discharges. They provide high peak voltages and currents to enhance dissociation, excitation and ionization, gated detection options for temporal discrimination of analytical signal, and fewer problems with thermal effects because of the lower average power [10]. Also pulsed plasma is used for measurements of the rate coefficients of elementary processes and effective lifetimes of various excited states [11]. However the time-behavior of pulsed glow discharge is not yet fully understood. Many studies have been done to understand the behavior of the argon excited species in pulsed

plasma [12-14] since Shiu *et al* [15] discussed the excited states originating from the dissociative recombination process of Ar_2^+ ion with electrons. Bogaerts *et al* [16] discussed the role of Ar_2^+ ions in a direct current argon glow discharge numerically. In their study the dissociative recombination of Ar_2^+ represents 20 % of the total loss of Ar_2^+ . However, Bogaert claims as Shiu *et al* that the highly excited states Ar^{**} are mainly populated through this dissociative recombination process for pressures higher than 500 mTorr. Bultel *et al* [17] calculated the recombination rate coefficient of the Ar_2^+ ions using a nonlinear time-dependent collisional-radiative model, and discussed the influence of the processes involving Ar_2^+ ions on the excitation temperature. Recently, Nafarizal *et al* [13] showed the production of Ar metastable atoms in the late afterglow of a RF magnetron sputtering plasma in a high gas pressure and in a high discharge power, and Kang *et al* [18] reported the appearance of the emission of the highly excited Ar(6d) in the afterglow with intensity much higher compared with that in the discharge. Also the temporal evolution of the absolute density of Ar(1s₅) was reported. In this section, we developed a time-dependent global model of the Ar discharge for calculation of the time evolution of the electron temperature and the electron density. Using these parameters, the time evolution of the densities of Ar excited states are investigated simultaneously. The electron temperature, the electron density and the densities of Ar excited states obtained by the simulation showed the rebound in the duty-off period as the same way in the experimentals. We discuss the dominant creation sources and the routes of loss in each level during the discharge and in the afterglow.

Finally, the *E-H* mode transition and hysteresis in low pressure argon inductively coupled discharges are investigated using global model and transformer model. Inductively coupled plasmas are well known with its two distinct coupled modes between electromagnetic field and plasma, low electron density mainly by capacitive coupling (*E* mode) and high electron density mainly by inductively coupling (*H* mode). *E-H* mode transitions have frequently been described in the literature and shown to exhibit hysteresis [19-22]. In this section, we show the mechanism of *E-H* mode transition and hysteresis by global (volume averaged) model and transformer model in an argon ICP discharge.

5.2 Experimental setup

As shown in figure 5.1, the experimental set-up for this study is composed of a 200 mm diameter quartz window installed on top of a cylindrical vacuum chamber of 200 mm in diameter and 375 mm high. Two 100 mm quartz windows for optical probing are positioned at the cylinder wall with common axis perpendicular to the axis of the chamber cylinder. An anode plate was installed which can be moveable to limit the volume of the discharge. The discharges were excited by the 3 turn-antenna powered by 13.56 MHz of RF frequency which can be modulated by a square pulse with variable frequency and duty ratio. An alternate type matching network is used to match the impedance between the RF generator and the plasma. The chamber was pumped to 10^{-6} Torr base pressure before filling with Ar gas (99.999 % pure). The total flow rate was maintained constant at 50 sccm. Under a constant flow rate, the pressure was controlled by the partial opening of a gate valve.

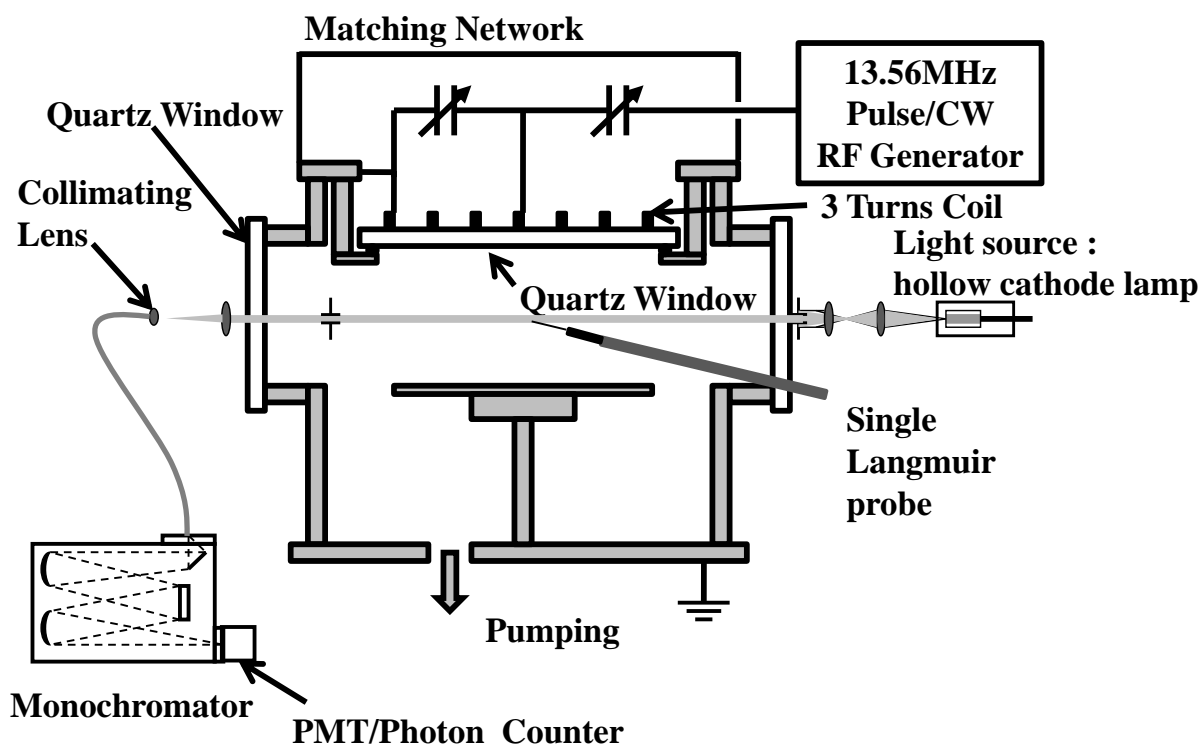


Figure 5.1 Schematic diagram of the TCP chamber and diagnostics system

5.3 Determination of the electron temperature in a planar inductive argon plasma with emission spectroscopy and electrostatic probe

5.3.1 Measurement of EEPF and optical emission

In this study, the anode plate was installed at 100 mm from antenna window to limit the volume of the discharge. To measure the EEPF, T_e and n_e , a lab-made cylindrical electrostatic probe was set in the discharge center ($r = 0$ and $z = 5$ cm) through a feedthrough on the vessel wall allowing radial motion in $z = 5$ cm plane. The probe uses a tungsten wire with a diameter of 100 μm and length of 2 mm, which is small compared to the Debye length for the present glow discharge. The probe tip is supported by a ceramic tube that is glued to the inside of a long stainless steel tube. To reduce RF distortion, a RF resonant filter was installed near the probe tip in the probe holder tube. The probe was biased from -50 to 25 volt by a bipolar amplifier that activates sawtooth waves. The voltage and current were simultaneously measured with two HP 34401 multimeters. The EEPF $f(E)$, the electron density and the electron temperature were obtained from Druyvesteyn formula in equations (4.47)-(4.50).

To analyze plasmas at the same area as the probe measurements, the optical emission from the vicinity of the probe tip was collected. The emissions from the discharge center ($r = 0$ and $z = 5$ cm) were observed via a collimating lens with the iris through a quartz window located 5 cm below the top quartz window and perpendicular to the z -axis. An optical fiber guides the light to a 500 mm focal length monochromator. The intensities of the measured spectra were calibrated using the calibration light source from Ocean Optics (model DH2000-CAL).

The evolution of the EEPF in a planar ICP against argon pressure in the range of 3 ~ 100 mTorr at constant RF power 200 Watt is shown in figure 5.2. At pressures below 3 mTorr, EEPF was not measurable using the probe system utilized here. At pressures greater than several hundreds mTorr, the probe sheath is prone to enter a collision-dominated regime which would cause difficulties with interpretation of the probe measurements [23]. At pressures greater than 3 mTorr and below 50 mTorr, the EEPFs can be described as a two-temperature distribution of electrons with an excessive energy tail. The appearance of this bi-Maxwellian EEPF at a low gas pressure has been reported in the past [23-25]. Between 50 and 100 mTorr, EEPF becomes nearly Maxwellian. From the EEPF, the effective temperature can be calculated by equation (4.50). The pressure dependency of the effective electron temperature T_{eff} is shown in figure 5.3(a), and the trend of the electron density n_e is shown in figure 5.3(b). Although the electron density rapidly increases as the gas pressure increases,

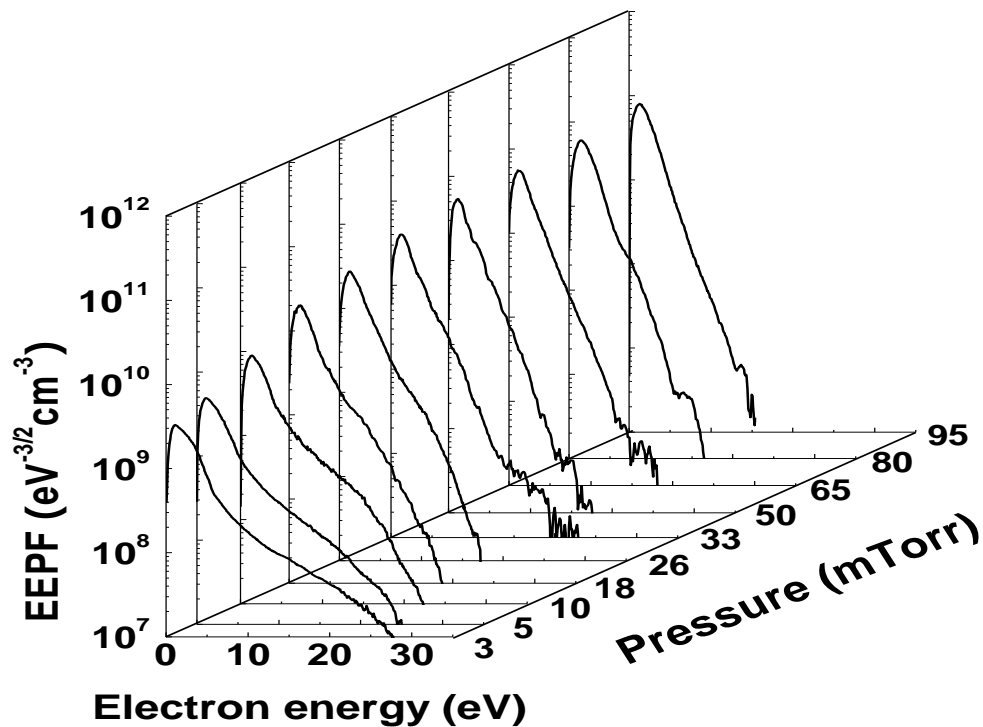


Figure 5.2 Evolution of the EEPF with the argon pressure ranging from 3 to 100 mTorr for an argon inductively coupled discharge at a RF frequency of 13 MHz and a power of 200 Watt.

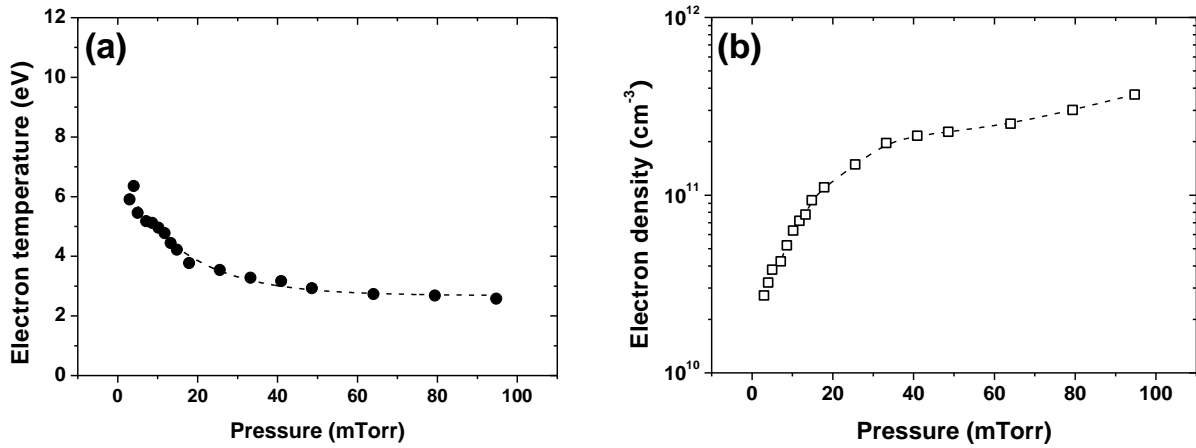


Figure 5.3 (a) Effective electron temperature T_{eff} of the EEPF in figure 5.2 against the pressure, and (b) measured electron density at 200 W.

the effective electron temperature gradually decreases. As the electron density rapidly increases with the gas pressure, the capacitive field is shielded more effectively by the plasma and is localized near the antenna region. Moreover its contribution to the electron heating gradually weakens [26].

5.3.2 Radiation trapping and line ratio method

In corona model, the photon decay dominates the other destruction rates, mainly by electron collisions. But with radiation trapping, this condition can be unsatisfied. We considered here the radiation trapping of the $4p \rightarrow 4s$ emission lines due to the large numbers of atoms in the $3p^5 4s$ metastable and resonance levels. Alternative forms include the direct radiation trapping of resonance levels or secondary trapping through cascades from higher states whose resonance levels are trapped. The large pressure effect due to radiation trapping observed with certain levels can lead to problems related to the use of these levels in plasma diagnostics [7]. A high energy level a with quantum number $J = 1$ decays in an optically allowed transition ($\Delta J = 0, \pm 1$) not only to the ground level g , $J = 0$, but also to a number of other lower levels b , c etc., with $J = 0$ or 2 . Re-absorption of the $a \rightarrow g$ resonant radiation with the subsequent decay into level b results in a pressure-dependent effective branching ratio for the $a \rightarrow b$ transition and therefore a pressure-dependent σ_i^{app} apparent excitation cross-section as previously reported [4]. In addition, levels such as the $3p^5 4p$ levels of Ar which are not optically connected to the ground level, can create pressure dependency as they cascade from higher levels of the $3p^5 4s$ and $3p^5 3d$ configurations and decay to the ground level.

We attempt to quantify the cross-sections experimentally to contain the factors that influence the pressure dependence mainly by radiation trapping. Initially, appropriate lines whose de-excitation can be described by corona model should be chosen. The corona model is an extreme simplification of the dynamics of the plasma. It is well known that the corona model fails for highly excited states that have decreased radiative transition rates and

increased electron-induced collisional mixing. The question is whether the corona model can accurately describe low-lying levels [7]. To use one atomic emission line and one ionic emission line is a common means of obtaining remarkable variation in the line-ratio measurements of the electron temperature, as they maximize the difference in the threshold energies. For excitation from the atomic ground state of Ar, the threshold energies for these two levels differ by approximately 20 eV. However, the possibility of the two-step excitation of ions is occasionally mentioned in the analysis of line-ratio measurements. The effect of two-step excitation on line-ratio measurements using a 488.0 nm Ar^+ emission line has been reported [7]. It is preferred to avoid the use of ion lines when addressing this problem. Emissions from atomic lines have a similar two-step excitation capability by means of excitation from metastable atoms. While excitation of metastable atoms can lead to a significant fraction of the emissions for some levels in a discharge, both cross-section measurements and plasma modeling as well as experiments identify only a minuscule role for metastable excitation of the np_1 , np_5 ($J = 0$) levels [7]. The emissions from these levels can usually be assumed to be completely free of a metastable atom excitation contribution except at very low electron temperatures and very high metastable fractions [5]. For this reason, the 750.4 nm and 751.5 nm lines coming from the $4p_1$ and $4p_5$ levels were chosen for the study.

5.3.3 Pressure dependence of the cascade cross-section

As a starting point, the direct cross-section and cascade cross-section of $4p_1$ (750.4 nm) and $4p_5$ (751.5 nm) at 3 mTorr are borrowed from Chilton *et al* [4]. The effect of pressure was then treated as a multiplication of the cascade cross-section at 3 mTorr by a coefficient that depends on the pressure. The apparent cross-section in equation (4.2) is then given by

$$\sigma^{app}(E, P) = \sigma^{dir}(E) + \alpha(P)\sigma^{cas}(E) \quad (5.1)$$

where $\alpha(P)$ is defined as the coefficient of the cascade cross-section function of the pressure. $\alpha(P) = 1$ at 3 mTorr. Thus, the emission intensity is written from equations (4.2), (4.5) and (5.1) as

$$\begin{aligned} I_{ij} &= C_\lambda n_0 n_e b_{ij} \int_0^\infty [\sigma^{dir}(E) + \alpha(P)\sigma^{cas}(E)] F(E) \sqrt{\frac{2E}{m_e}} dE \\ &= C_\lambda n_0 n_e b_{ij} \left\{ \int_0^\infty \sigma^{dir}(E) F(E) \sqrt{\frac{2E}{m_e}} dE + \alpha(P) \int_0^\infty \sigma^{cas}(E) F(E) \sqrt{\frac{2E}{m_e}} dE \right\} \end{aligned} \quad (5.2)$$

As the gas density n_0 is proportional to the gas pressure P , a constant A may be introduced, written as $C_\lambda n_0 b_{ij} = AP$. Replacing the EEDF $F(E)$ and n_e in the above equation with the values obtained from Langmuir probe, the emission intensity I_{ij} at pressure P can be calculated as

$$I_{cal} = AP[B + \alpha(P)C] \quad (5.3)$$

where $B = \int_0^\infty \sigma^{dir}(E) F(E) \sqrt{\frac{2E}{m_e}} dE$, $C = \int_0^\infty \sigma^{cas}(E) F(E) \sqrt{\frac{2E}{m_e}} dE$ are independent of the pressure. Here, the measured emission intensity $I_{measure}$ can be correlated to the calculated intensity via a constant D as ; $I_{cal} = D I_{measure}$. D is obtained by comparison of calculated emission intensity (5.3) and of measured one. Subsequently,

$$I_{measure} = \frac{I_{cal}}{D} = \frac{AP[B + \alpha(P)C]}{D} \quad (5.4)$$

$$\alpha(P) = \frac{1}{C} \left(\frac{DI_{measure}}{AP} - B \right) \quad (5.5)$$

The coefficient $\alpha(P)$, of the cascade cross-section as a function of the pressure calculated for $4p_1$ and $4p_5$ are shown in figure 5.4. As can be seen from figure 5.4, the coefficient of $4p_5$ (751.5nm) is significantly influenced by the pressure, whereas for $4p_1$ (750.4nm), the amount of influence is less. This is caused by the fact that the np_5 levels both experience moderate to large pressure dependence in their optical emission cross-sections due to radiation trapping of the cascading resonance levels. In contrast, the np_1 levels have minimal pressure dependence [7]. The coefficients of both levels appear to become saturated at high-pressure regions.

Assuming the EEDF as Maxwellian, equation (4.5) becomes

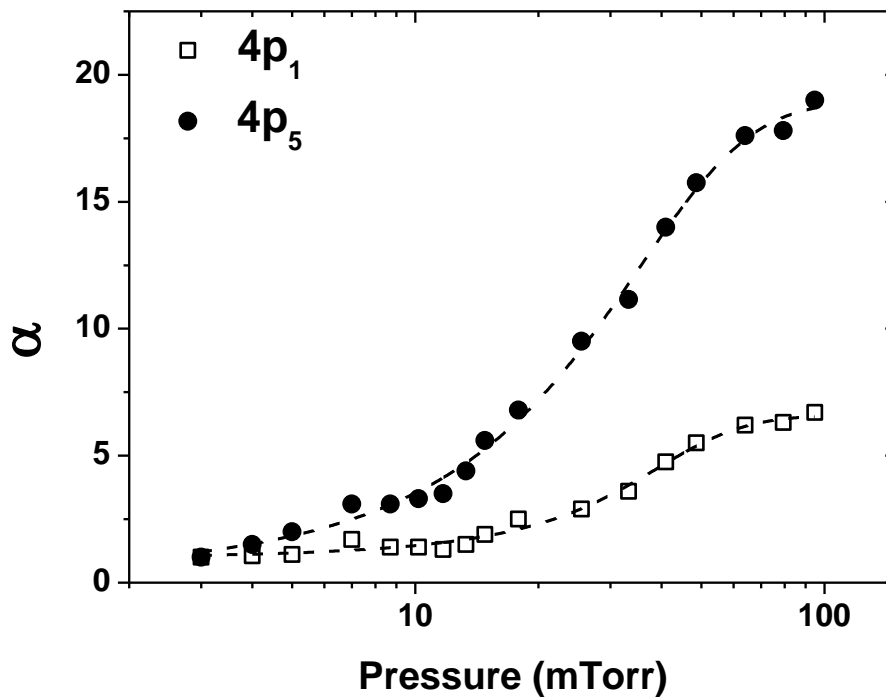


Figure 5.4 Pressure dependence of $\alpha(P)$, the coefficient of the cascade cross-section; $\sigma^{app}(E, P) = \sigma^{dir}(E) + \alpha(P)\sigma^{cas}(E)$. $\alpha(P) = 1$ at 3 mTorr. The open squares are for $4p_1$ (750.4 nm) and the solid circles for $4p_5$ (751.5 nm).

$$I_{ij}^{obs} = C_{\lambda} n_0 n_e b_{ij} T_e^{-3/2} \int_0^{\infty} \sigma_i^{app}(E, P) \exp\left(-\frac{E}{kT_e}\right) EdE \quad (5.6)$$

From equation (5.6), the emissive intensity is function of the electron density and the electron temperature. Accordingly, the electron temperature is calculated by

$$\frac{I_{ij}^{obs}}{I_{ab}^{obs}} = \frac{I_{ij}^{obs} = C_{ij} b_{ij} \int_0^{\infty} \sigma_i^{app}(E, P) \exp\left(-\frac{E}{kT_e}\right) EdE}{I_{ab}^{obs} = C_{ab} b_{ab} \int_0^{\infty} \sigma_a^{app}(E, P) \exp\left(-\frac{E}{kT_e}\right) EdE} \quad (5.7)$$

Equation (5.7) is the well-known line ratios method. In figure 5.5 the open square points show the pressure dependence of the electron temperatures calculated using the line ratio method with corrected cross-sections. In comparison, the solid line is the effective temperature trend obtained from statistical calculation using the EEDF obtained by the Langmuir probe, and the open triangles indicate the temperature from the line ratio with non-

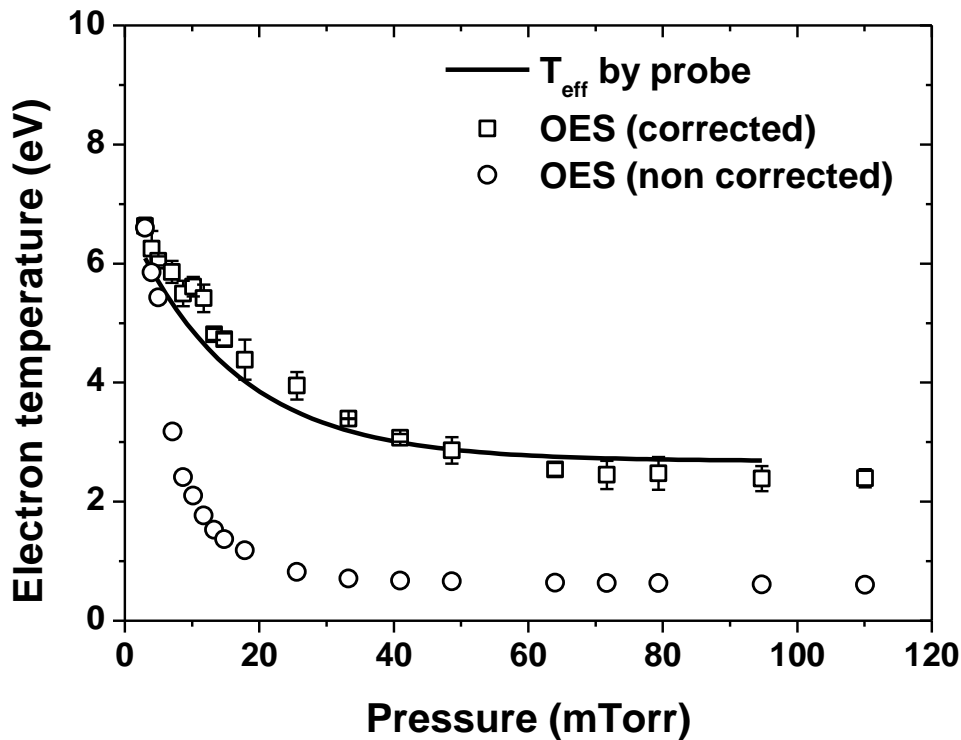


Figure 5.5 Solid circles, which are T_e according to the line ratio with non-corrected cross-sections, are substantially below the open squares T_e according to the line ratio with corrected cross-sections. The trend of the pressure dependence of the electron temperature from the line ratio with the corrected cross-sections is identical to that of the effective electron temperature from the single Langmuir probe (solid line).

corrected cross- sections. Due to the similarity between the two curves, the solid line and the trace of the open squares, and also due to the substantial difference from the temperature according to the line ratio with the uncorrected cross- section, the improvement of the cross- sections by introducing $\alpha(P)$ as the coefficient of the cascade cross- section is evident. From the two weak points in the line ratio method, of the lack of cross-section data and the non-Maxwellian distribution of electrons, it appears impossible to avoid the question regarding the latter point, as with one formula of the line ratio, in principle, only one variable can be determined. If the aim of an application of the line ratio is the determination of the electron temperature, the best choice of an electron distribution with one parameter will be Maxwellian distribution. Although it is clear that the energy distribution of real plasmas deviate from a simple Maxwellian distribution, for the purpose of simplification, the Maxwellian distribution appears to be the inevitable solution. The curves in figure 5.5 indicates that in planar inductive argon plasma from 3 to 100 mTorr, the correction by $\alpha(P)$ has a dominant influence compared to the discrepancy caused by difference in EEDF from distribution Maxwellian condition. Several line ratios may be used to obtain EEDF with a corresponding number of variables, as in TRG-OES. However, without a suitable correction of the cross-sections, the gap in the electron temperature is not tolerable, as in the case of Schabel *et al.* [8].

Many questions arise concerning the inconvenience of using a probe and an optical measurement simultaneously. However, in nearly all applications once the plasma excitation method for a certain chamber is determined, it will be used under the specific condition. Once the EEPF and n_e are measured and the $\alpha(P)$ is determined as a type of calibration at the first time, thus is it possible to benefit from using the simple line ratio method with enhanced precision constantly. Furthermore, the implication of this introduction of the correction coefficient α is not limited to pressure-dependent scenarios. In principle, provided that the corona model is valid, all physical variables that significantly alter the optical cross-section may be converted into the form of the apparent cross-section, as given by

$$\sigma^{app}(E, X) = \sigma^{dir}(E) + \alpha(X) \sigma^{cas}(E) \quad (5.8)$$

where $\alpha(X)$ is defined as the coefficient of the cascade cross-section function of that variable.

5.4 Modeling and experimental study of pulse modulated ICP afterglow: production of Ar highly excited states

5.4.1 Experiments

As shown in figure 5.1, the experimental set-up for this study is the same as section 5.3, except the position of the anode plate. The anode plate was installed at 50 mm from antenna window to limit the volume of the discharge. The discharges were excited by the 3 turn-antenna powered by 13.56 MHz of RF frequency modulated by a square pulse with a

frequency of 100 Hz, a duty ratio of 40 % and 200 Watt constant power. The chamber was pumped to 10^{-6} Torr base pressure before filling with Ar gas (99.999 % pure). The total flow rate was maintained constant at 50 sccm, and the total pressure was fixed at 10 mTorr or 200 mTorr.

To measure the electron temperature and the electron density, a home-built cylindrical electrostatic probe was set in the discharge center ($r = 0$ and $z = 2.5$ cm) through a feedthrough on the vessel wall allowing radial motion in the $z = 2.5$ cm plane. For the time resolved measurement, Maresca *et al* [27] method was used. The bias voltage was applied in a range from -15 V to +15 V by 0.05 V step. At each fixed probe voltage, the probe current was obtained from the voltage drop over a 10 Ω resistor using a 16-bit analog digital convertor card with 1 M samples/sec rate. This measurement was performed 1000 sweeps and then averaged to reduce the noise. After a complete voltage scanning, the probe current was determined as a function of time $I_{p,V=const}(t)$ at a constant probe voltage, and next converted into the I - V probe characteristic curve $I_{p,t=const}(V)$ for a specific time. The EEPF $f(E)$, the electron density and the electron temperature were obtained from Druyvesteyn formula in equations (4.47)-(4.50).

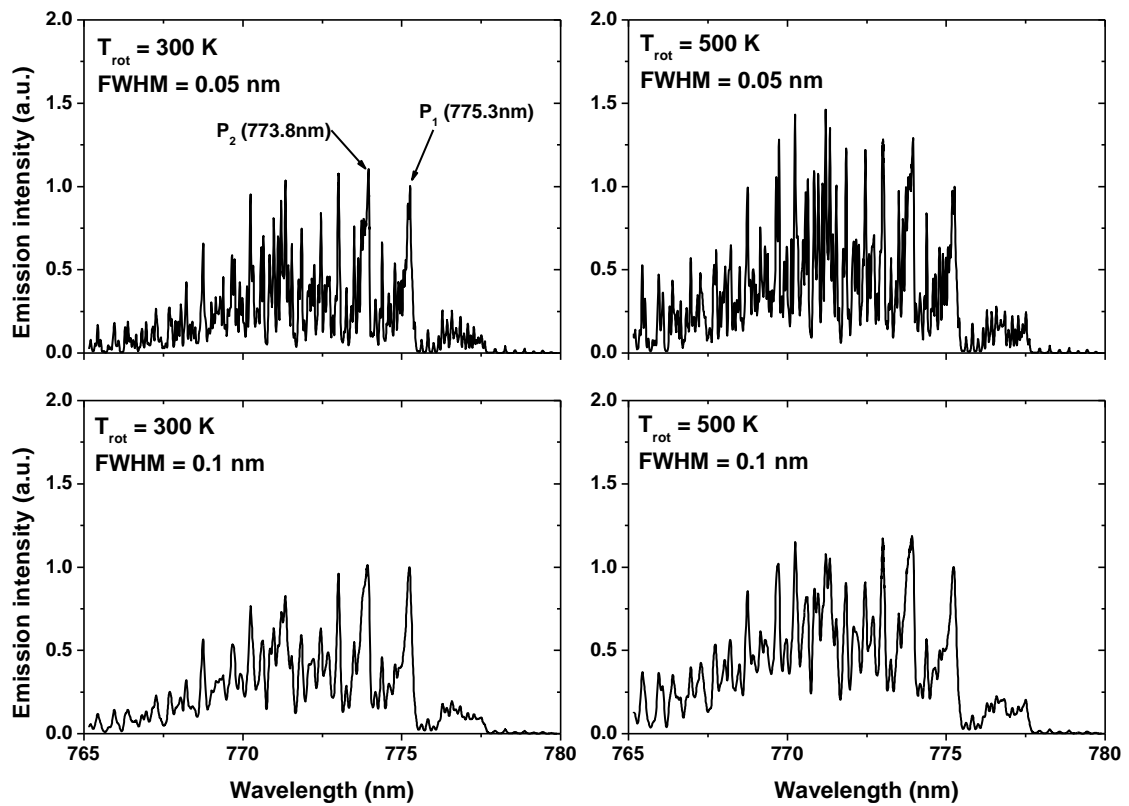


Figure 5.6 Calculated rotational spectra of $N_2(B,2-A,0)$ first positive band for different set of T_{rot} and full width half maximum (FWHM) values.

To measure the density of metastable atoms, the resonance absorption spectroscopy was used, which is widely performed in various plasma processes [28]. The method has been applied successfully for measuring the metastable atoms in DC and RF magnetron discharges [29,30]. A lab-made hollow cathode lamp was used as the reference source. The source light, driven by 35 mA dc current at 1 Torr, has been collimated by a system of lenses and diaphragms to get a probing beam of 5 mm in diameter through plasma. By simply changing the working gas in the discharge, various spectral source lamps can be obtained. To obtain stable emission, the hollow cathode lamp was turned on for 20 minutes or more before each measurement. The probing light beam from the source lamp was sent through the discharge at a distance of 25 mm from the upper quartz window with antenna and collected via collimating optics system at the opposite side of the chamber and then guided into a 500 mm focal length spectrometer. A photo multiplier tube (H7155 Hamamatsu) was used on the spectrometer. A shutter system was used to block the light from source lamp when only the plasma emission was measured.

The principle of the optical absorption spectroscopy is explained in chapter 4. For a time resolved optical absorption spectroscopy equation (4.38) can be written as

$$A_L(t) = 1 - \frac{I_t(t)}{I_{source}(t)} = 1 - \frac{I_{plasma+source}(t) - I_{plasma}(t)}{I_{source}(t)} \quad (5.9)$$

In this study, to measure Ar ($3p_54s$) densities the four spectral lines with wavelength of 750.4 nm, 794.8 nm, 751.5 nm and 763.5 nm were used for Ar ($1s_2$), Ar ($1s_3$), Ar ($1s_4$) and Ar ($1s_5$), respectively.

The plasma line width ($\delta\sigma_{1/2}^P$) is calculated by taking a Doppler line profile, which is the dominant line broadening in glow discharge at low gas pressure [31,32]. The Doppler line width is calculated from the equation (4.42). In the present study, the temperatures of the plasma and that of the reference source have been evaluated from the rotational structure of N_2 band by adding 10 % of N_2 [29]. When N_2 is introduced into the Ar plasma, the N_2 and N_2^+ emission bands are observed. The rotational spectra of N_2^+ first negative band at 391.4 nm is weak to deduce of N_2^+ rotational temperature. The N_2 second positive bands at 357.7 nm are stronger in intensity. The emission is mainly due to the excitation transfer from Ar metastable atoms. This process produces a specific excitation of high rotational levels, canceling any possibility of determining the gas temperature. Then the N_2 first positive bands remain; the band at 775.3 nm is strong enough in intensity to be recorded. Figure 5.6 shows the calculated rotational spectra of $N_2(B,2-A,0)$ first positive band for different set of T_{rot} and full width half maximum (FWHM) values. The rotational temperature is then obtained from the intensity ratio of the two P_1 , P_2 peaks. Figure 5.7 shows (a) intensity ratio of the two P_1 , P_2 peaks for different FWHM as a function of T_{rot} , and (b) the measured rotational spectra of the hollow cathode lamp and the plasma. Using this method, the temperature of the hollow cathode lamp was measured about 800 K. For the plasma temperature, optical emission spectroscopy measurement was integrated during 5 sec, i.e. the average temperature is used. The temperatures of plasma were deduced about 350 K and 500 K at 10 mTorr and 200 mTorr, respectively.

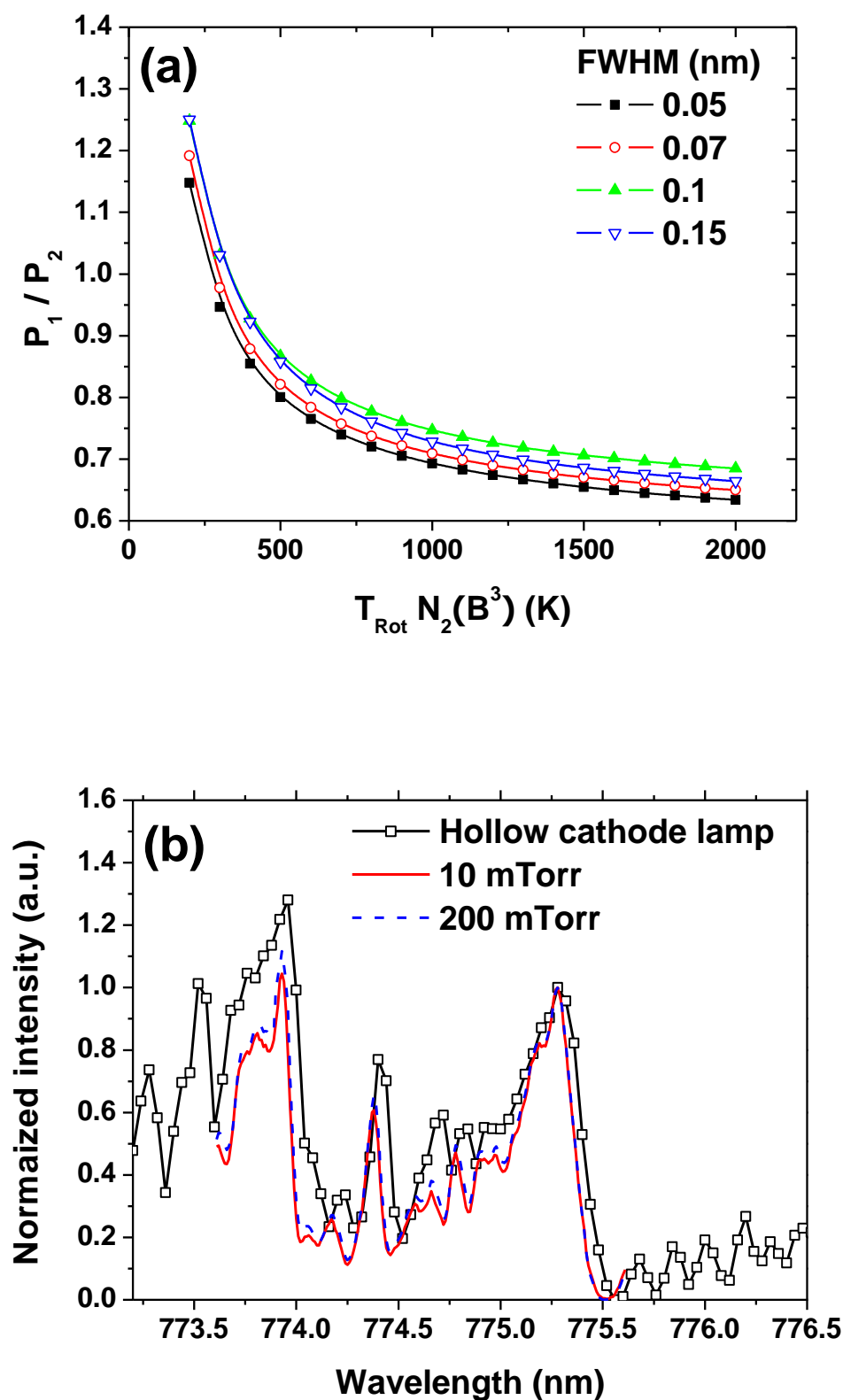


Figure 5.7 (a) The intensity ratio of the two P_1 , P_2 peaks with the resolution from 0.05 nm to 0.15 nm, and (b) the measured rotational spectra of the hollow cathode lamp and plasma.

5.4.2 Discharge model

As shown in figure 5.8, the discharge model takes into account 10 energy levels of Ar (Ar ground state, four levels of Ar ($3p^5 4s$), Ar ($4p$), Ar ($3d$), Ar ($5s$), Ar ($5p$), Ar^{**} (highly excited)), as well as the Ar⁺ and Ar₂⁺ ions. We supposed the excited states between Ar ($3p^5 5p$) and Ar⁺ as a block, i.e. Ar^{**}. A pulse power modulated global (volume averaged) model is used to calculate the time evolution of the electron temperature [33]. We assume a cylindrical discharge chamber of radius $R = 10$ cm and length $L = 5$ cm.

To calculate the electron temperature, equation (3.2)-(3.20) are used. The ion-neutral species mean free path λ_i is calculated from the extrapolated Ar⁺-Ar collision cross section data [34], and the ion atom temperature is assumed to be the same as the gas temperature T_g . The diffusion coefficient of Ar₂⁺ is assumed half the value of Ar⁺ ion, based on the inverse proportionality with the ion mass [32].

The dynamics of species density n_j is described by the particle balance in equation (3.21). The list of species and reactions are converted automatically in a system of kinetic equations and solved numerically using ZDPlasKin tool [35]. The rate coefficients of all reactions are calculated using build-in into the package BOLSIG+ solver. The reactions used in this study are summarized in table 5.1.

The rate coefficient for the electron impact excitation from level j to level k , k_{jk} , is calculated using equation (3.22). Also the rate coefficients of de-excitation processes k_{kj} , are calculated by the principle of detailed balancing [36]. In all the calculations of the rate

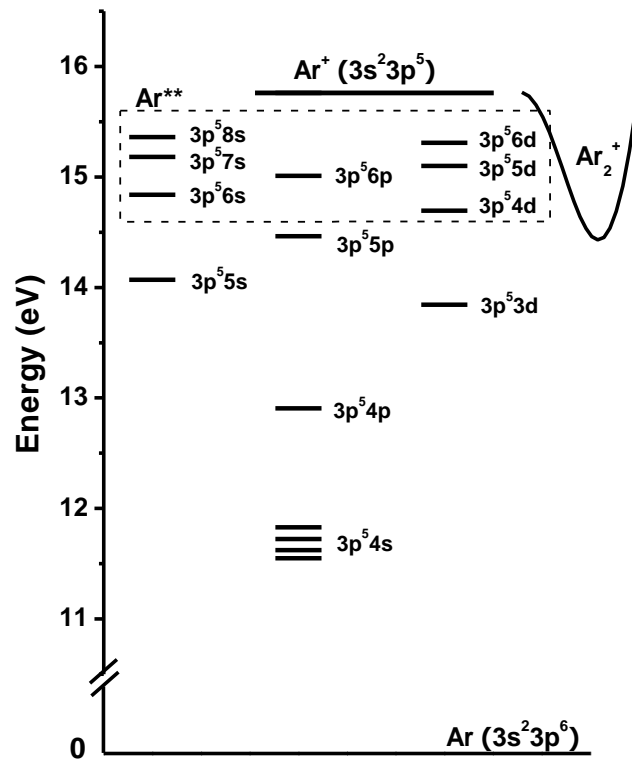


Figure 5.8 Energy level scheme of the argon atom excited levels used in the model.

coefficients, we have assumed that the EEDF is Maxwellian.

The radiative loss rate for decay from level k to level j is calculated using equation (3.24). The escape factor g_k depends on the density of the lower state in the radiative transition. But in the low pressure plasma the density of the excited level is enough low to neglect the escape factor, except for the $^3P_1-^1S_0(\lambda = 1067\text{\AA})$ and the $^1P_1-^1S_0(\lambda = 1048\text{\AA})$ resonance lines because of the radiative decay to the Ar ground level (R18). The calculated escape factor of these two resonance lines are calculated using equations (3.26)-(3.29) as shown in figure 3.1. The radiative decay transitions between the excited states (R19 – R23) were calculated using the sum of the transition probabilities for the transitions between individual sublevels weighted with statistical weights of the upper sublevels.

The diffusion loss rate of the neutral atoms to the wall is calculated using equations (3.31) and (3.32). The neutral-neutral species mean free path, λ_n , is calculated from the Ar-Ar collision cross section data [34].

The power balance equation and the particle balance equation are solved by an ordinary differential equation solver based on Runge-Kutta method, assuming that the power is modulated by an ideal rectangular wave form given by :

$$P_{abs}(t) = \begin{cases} P_0, & 0 \leq t < \alpha\tau \\ 0, & \alpha\tau \leq t < \tau \end{cases} \quad (5.10)$$

where α is the duty ratio and τ is the period of the modulated power. P_0 is fixed at 160 Watt, i.e. the power efficiency is assumed about 80 % of the experimental input power.

One needs to discuss the time evolution of the spatial distribution of charged particles in the plasma afterglow, e.g. the values of the edge to center electron density ratios h_L and h_R (equations 3.5 and 3.6) versus time. We consider that the charged particles are mainly lost by recombination on the walls. Even if volume recombination plays a significant role we can neglect it in the early afterglow as well as ionization because no electric field is applied anymore. We also assume that the electron temperature is spatially uniform. Then the charged particle balance equation is:

$$\frac{\partial n}{\partial t} - D\nabla^2 n = 0 \quad (5.11)$$

where n is the charged particle density and D is the diffusion coefficient of the charged particles. One can therefore show that the plasma density in a diffusion regime decreases exponentially with time:

$$n(\vec{r}, t) = n(\vec{r}, t = 0) \exp(-\nu_d t) \quad (5.12)$$

where ν_d is the diffusion loss frequency. Equation (5.12) clearly shows that when diffusion is the main loss mechanism for the charged particles the density shape in space is not altered with time. In the simulation during the plasma off time we therefore keep h_L and h_R constant and equal to the values just before turning off the plasma.

5.4.3 Results and discussion

In this section we show a comparison between experiment and model results on (i) the electron density n_e and the electron temperature T_e in the continuous mode versus pressure and (ii) n_e , T_e , Ar highly excited state emission, Ar(1s₄) and Ar(1s₅) density in the time afterglow. Our aim is to extract the production and loss rates of the different reactions from the global model to give an explanation on time evolution of species from a kinetic point of view.

5.4.3.1 Electron density and electron temperature in continuous mode

Figure 5.9 shows calculated (solid line) and measured (solid square) electron density and calculated (dotted line) and measured (open circle) electron temperature versus pressure at a fixed RF power and a fixed Ar flow rate. Assuming the error bars for the experimental results estimated to 20%, a very good agreement is found between calculation and measurements. From the simulation, we see that the production of electrons in the continuous mode is mainly related with the production of Ar⁺ and more weakly to the production of Ar₂⁺. Indeed the latter represents less than 2% of the total ions over all the range of investigated pressures. Even if the Ar₂⁺ production increases with pressure through R13 and R15, higher pressure means higher electron density leading to an enhancement of losses through R16 and R17. As a result, the relative population of Ar₂⁺ decreases with increasing pressure from 10 mTorr to 200 mTorr. The main reactions for the electron production are the direct ionization, the step ionization from Ar(4s) state and the ionization from higher states (4p, 3d, 5s, 5p) with around 17 %, 41 % and 37 % at 200 mTorr respectively. The observed pressure-dependent behavior

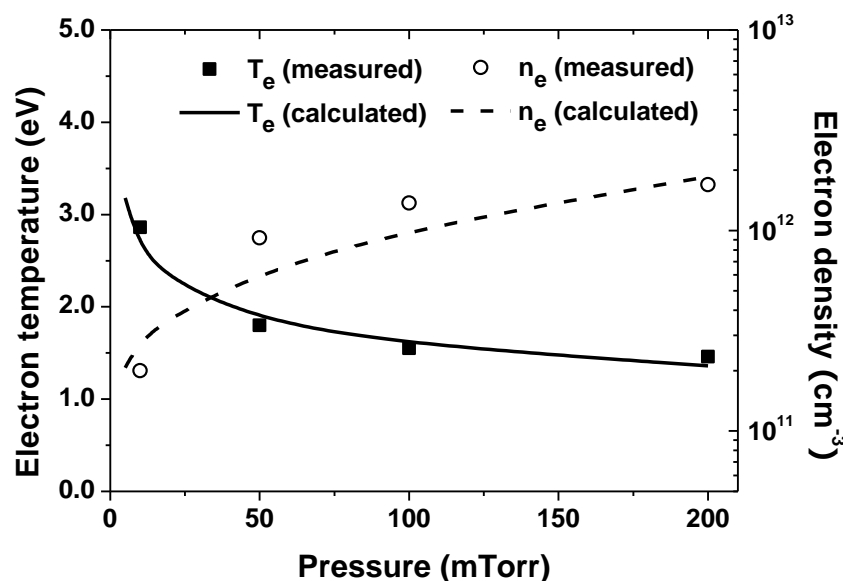


Figure 5.9 Measured and calculated electron density and electron temperature in continuous mode plasma varying pressure from 10 mTorr to 200 mTorr at 200 W.

can be simply explained by writing global particle balance and power balance equations in the source assuming that the charged particle production is due to the direct ionization and the charged particle loss by recombination on the walls. Therefore, we obtain two equations:

$$\frac{k(T_e)}{u_B(T_e)} = \frac{1}{n_g d_{eff}} \quad (5.13)$$

and

$$P_{abs} = an_e u_B(T_e) \varepsilon(T_e) \quad (5.14)$$

where $k(T_e)$ is the ionization rate, $u_B(T_e)$ is the Bohm velocity, n_g is the gas density, d_{eff} is an effective plasma dimension proportional to the source volume over wall surface ratio and $\varepsilon(T_e)$ is the energy loss per electron-ion pair lost on the walls. One can understand that whatever the RF power the electron temperature will decrease with increasing the gas density, e.g. the pressure as it is observed in figure 5.9. As the Bohm velocity $u_B(T_e)$ and the energy loss per electron-ion pair lost on the walls $\varepsilon(T_e)$ increase with the electron temperature, the electron density n_e will increase with pressure as depicted in figure 5.9.

5.4.3.2 Electron temperature and electron density in pulse mode

Figure 5.10 shows the calculated and measured time evolution of (a) the electron temperature and (b) the electron density during 500 μ sec after the end of the pulse for two pressures 10 mTorr and 200 mTorr. In the afterglow the main mechanism leading to a decrease of the electron temperature is the loss of the highest energetic electrons by recombination on the walls. In fact, the wall loss of electrons produces a distinct steep drop of the EEDF at electron energies higher than the wall potential energy. Free energetic electrons are constantly lost from the ambipolar potential while the cold trapped electrons remain confined leading to diffusive cooling of the EEDF. At low pressure the electron temperature decreases faster than at high pressure because the ambipolar diffusion coefficient is inversely proportional with the ion-neutral collision frequency, e.g. the gas density. In figure 5.10(b) we see that the electron density decreases with time resulting mainly from no more electron production by R4-8 because of the low electron temperature. In addition the calculated electron densities are always higher than the measured electron density whatever the pressure. The cause of the overestimation of the electron density from the simulation will be treated later. At low pressure the diffusion loss is absolutely dominant. The particle loss by diffusion at 10 mTorr is 99.9 % in continuous mode and it only decreases to 90% (minimum value at 140 μ sec) even in the afterglow. However, the electron density loss in the afterglow at 200 mTorr needs more analysis. In figure 5.10(c) are plotted the net loss rates (taking into account the inverse reaction of the electron production for R9 and R10) extracted from the global model at 200 mTorr. The lighter curves indicate a negative loss rate meaning that the production of electrons by the inverse reaction is higher than the consumption by the direct one. First, we see that the electron losses by ambipolar diffusion is always the dominant loss process for the

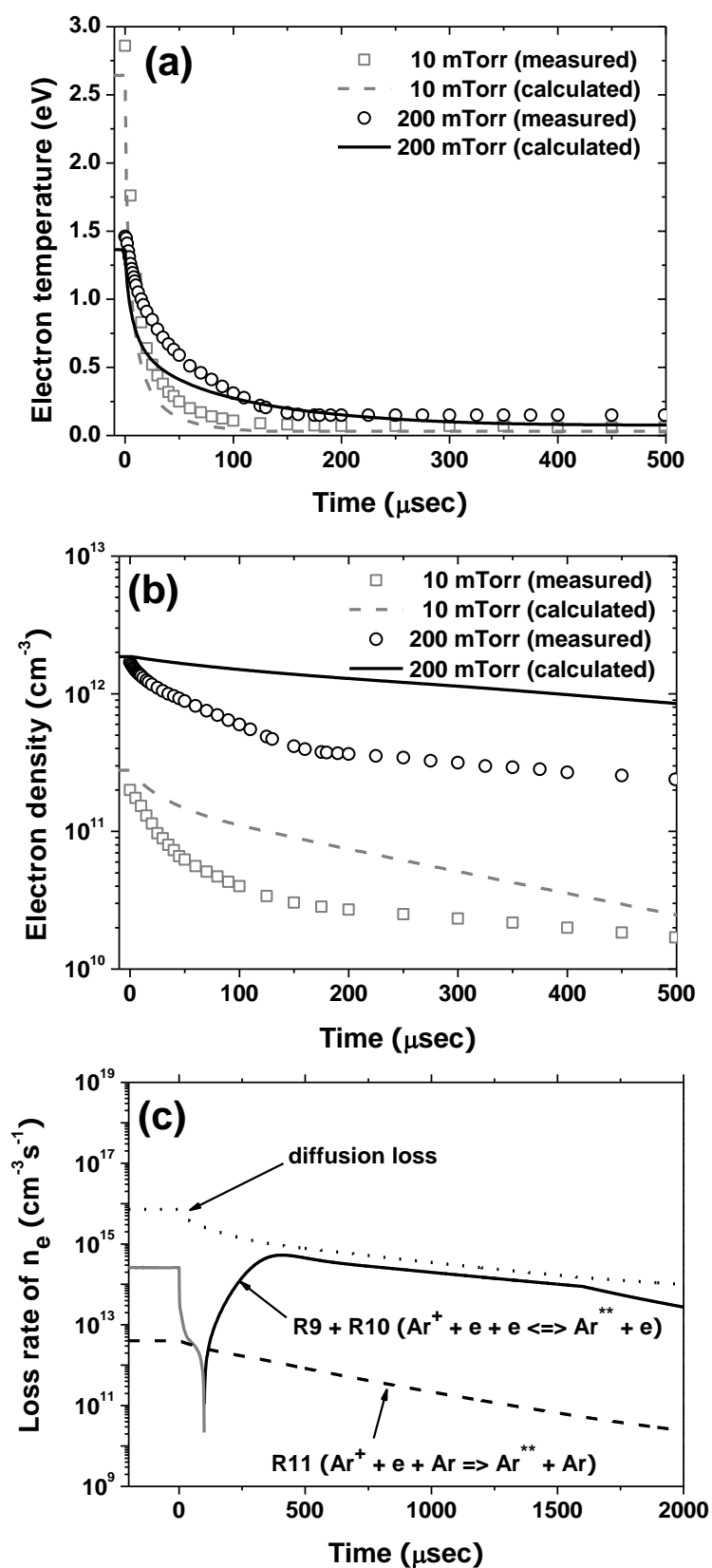


Figure 5.10 Calculated and measured temporal (a) electron temperature, (b) electron density at 10 mTorr and 200 mTorr and (c) temporal net loss rate for electron at 200 mTorr; lighter curve indicates negative loss.

electrons (at least 65 % of the total loss) suggesting that the assumption on constant h_L and h_R in the afterglow done previously is consistent. The electron diffusion loss decreases during the afterglow because of the quasi linear dependence of the ambipolar diffusion coefficient with the electron temperature. During the first 100 μsec , the electron impact ionization frequency of R9 is higher than the three body ion recombination frequency (R10) because the R9 frequency is enhanced by more energetic electrons. The fast increase of the electron loss rate by the three body recombination (4 decades in the range 100-400 μsec) is explained by the strong dependence of the R10 reaction frequency with (i) the inverse of the electron temperature and (ii) the electron density. The low electron temperature and the high electron density lead to a high electron loss rate by three body recombination of Ar ions with two electrons. The discrepancy between measured and calculated electron densities can be explained by the lack of knowledge on R10 reaction coefficient value. Here we used the values in the literature [12,37,38]. The value is not obvious. By increasing the coefficient by a factor of 4 we found that the calculated electron densities approach the measured curve. Changing the coefficient does not modify the results obtained in continuous mode since the electron temperature is high enough to neglect this reaction in all cases. Indeed, our calculation is a zero dimensional simulation following the same value as already used in the literature.

5.4.3.3 Ar excited states in pulse mode

Figure 5.11 (a) and (b) show the calculated and measured atom density of the metastable Ar($1s_5$) and the resonant Ar($1s_4$) respectively. At low pressure (10 mTorr), Ar($1s_5$) and Ar($1s_4$) density exhibit different evolution. Because of its long life time, the former decreases more slowly than the latter. At higher pressure (200 mTorr), both densities decrease sharply during the first 100 μsec and then regain to reach a maximum at 500 μsec before decreasing very slowly with time. Calculated and experimental results are qualitatively in good agreement in particular at the extreme positions. Figure 5.11(c) shows that during the pulse-on time the main production reaction of Ar($1s_5$) is the radiative decay from the higher states (R19, R21, R23) and to a less extent electron impact excitation from the ground state (R1). Upon deactivation of the pulse, no additional argon atoms in ground state are excited to higher levels because of too low electron temperature. The radiative decay from the higher excited levels is always the dominant production mechanism. We also note that the maximum of Ar $_2^+$ ion recombination rate is higher in the afterglow than during pulse-on time partially because the reaction coefficient is inversely proportional with the electron temperature.

Figures 5.12 (a), (b) and (c) show the measured temporal optical emission intensity of Ar 750.4 nm (4p-4s), Ar 425.9 nm (5p-4s) and Ar 549.6 nm (6d-4p) and the calculated atom density of Ar(4p), Ar(5p) and Ar ** respectively. As shown the after-peak intensity of each spectral line is significantly dependent on the gap energy. In fact, the ratio of after-peak to the pulse-on-time emission intensity is 0.04, 0.37 and 2.5 for Ar 750.4 nm ($\epsilon_{th} = 13.48$ eV), Ar 425.9 nm ($\epsilon_{th} = 14.74$ eV) and Ar 549.6 nm ($\epsilon_{th} = 15.33$ eV) respectively. It means that in the discharge the dominant production process is the excitation from the lower states while in the afterglow it is the cascade decay from the higher states. The production rates of Ar ** in the

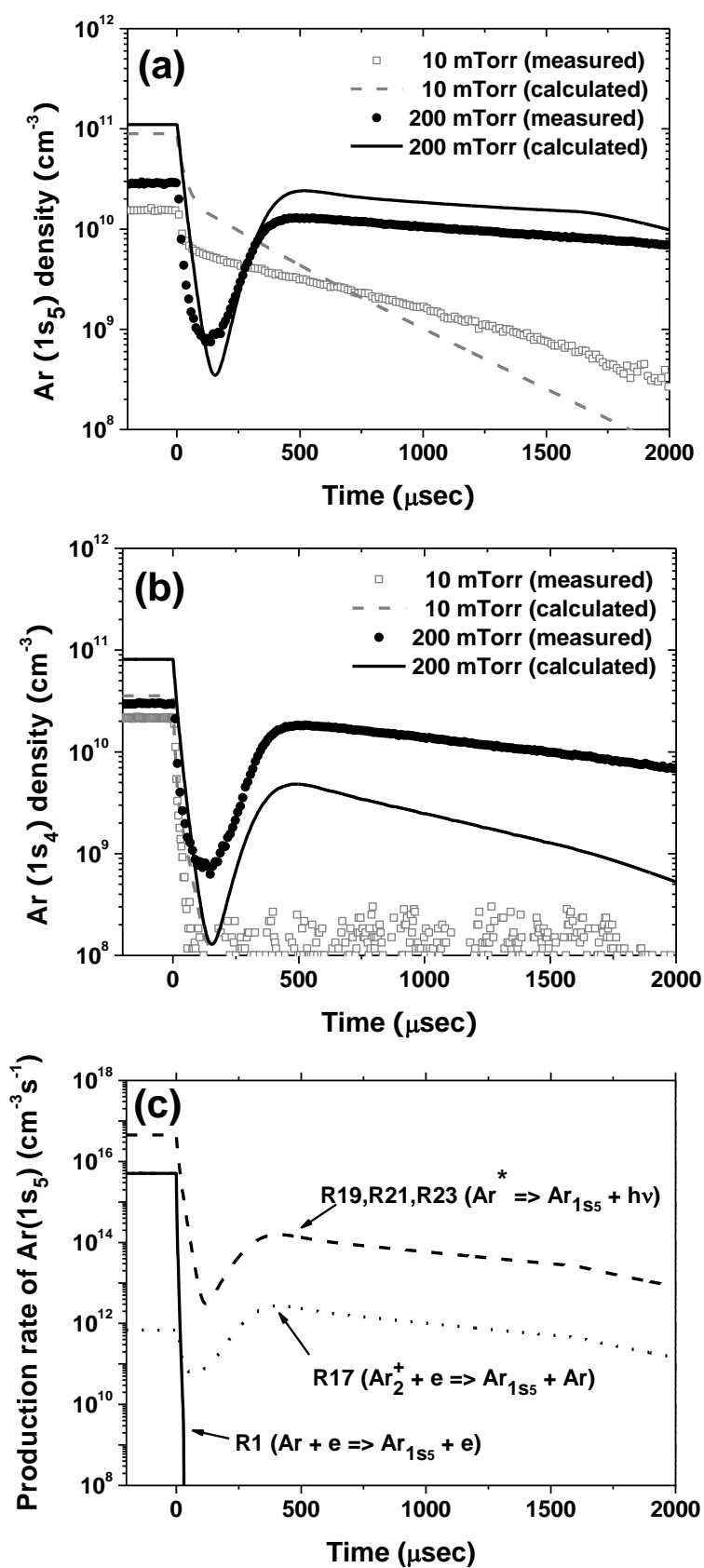


Figure 5.11 Calculated and measured temporal atom density of (a) Ar ($1s_5$), (b) Ar ($1s_4$) at 10 mTorr and 200 mTorr and (c) net production rate of each reaction for Ar ($1s_5$) at 200 mTorr.

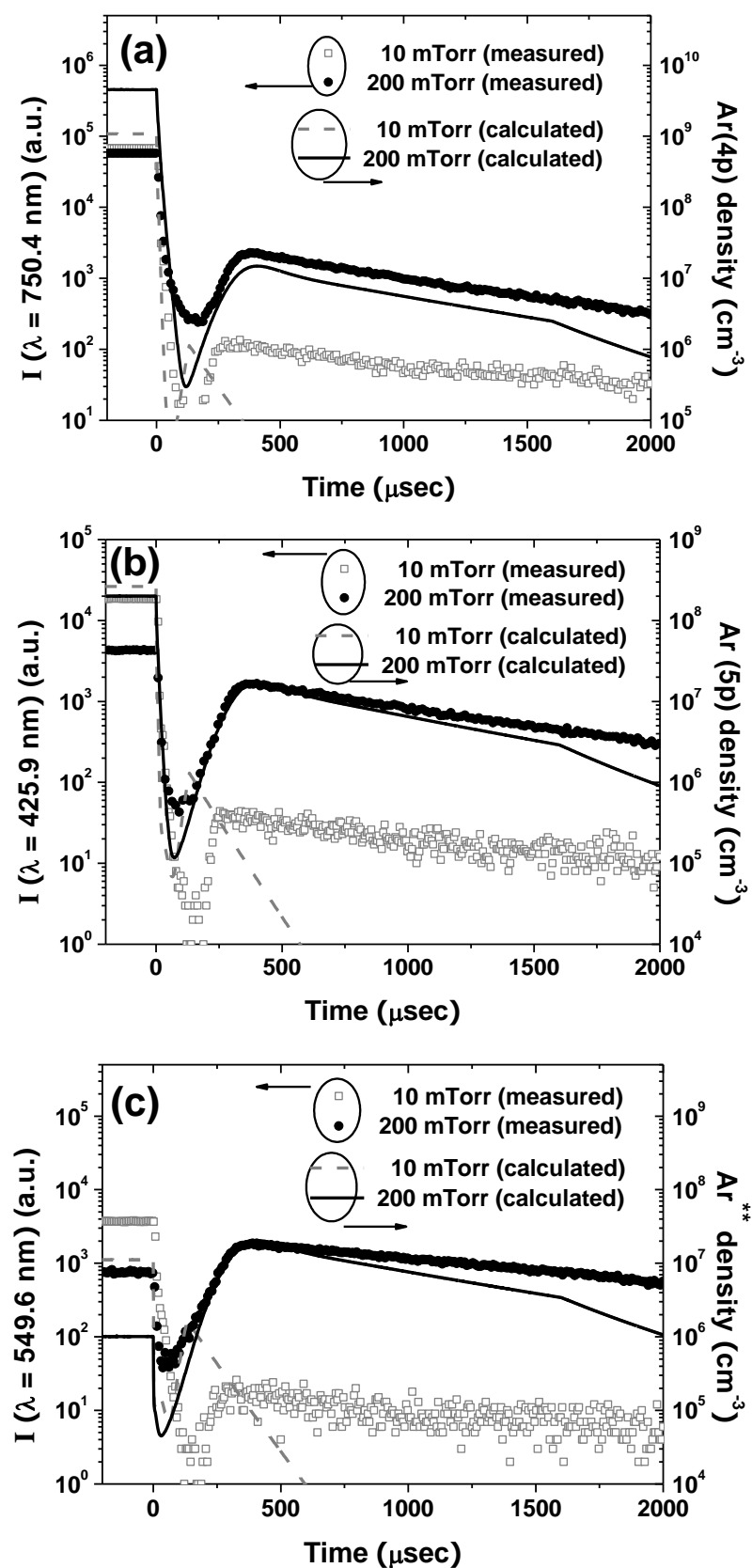


Figure 5.12 Calculated and measured temporal atom density and emission intensity of (a) $\text{Ar}(4p)$, (b) $\text{Ar}(5p)$ and (c) Ar^* .

afterglow by the three body recombination R10 is illustrated in figure 5.10(c). The direct ionization rate from R2 (main Ar^{**} production process in the continuous mode but not represented in the figure) decreases sharply to zero in a few microseconds after the plasma extinction.

In the afterglow, the main production of Ar^{**} is provided by the three body electron-ion recombination because of the inverse of the electron temperature ($T_e^{-4.5}$) and the strong dependence of the reaction coefficient with the electron density (n_e^3). At 10 mTorr in the afterglow, the maximum production rate of Ar^{**} by the three body electron-ion recombination is about $4 \times 10^{13} \text{ cm}^{-3} \text{ s}^{-1}$, which is 10 times lower than at 200 mTorr. Moreover at this very low pressure the electron-ion dissociative recombination has no effect in the afterglow. This is caused mainly by the lower electron density and enhanced the electron diffusion loss.

Table 5.2 summarizes the relative contributions of the main processes of production and loss at four times: CW (pulse on time), 100 μsec , 400 μsec and 1000 μsec after end of the pulse. Obviously in the pulse-on time the electron impact excitation and ionization from the ground state and $\text{Ar}(3p^5 4s)$ are the dominant production processes for all excited states while it plays no role in the afterglow since the electron temperature decreases abruptly. The radiative decay is always a dominant production and a loss process of each state. On the other hand, during the afterglow the main source of all excited states is the three body electron-ion recombination. Through this reaction Ar^{**} state can be produced with a larger amount than during pulse-on time since the threshold energy of Ar^{**} is close to the one of Ar^+ . Indeed, the initial level of Ar^{**} in the three body electron-ion recombination lies within a few kT_e of the ionization limit (15.76 eV) [37].

It is worthy of mentioning that in some papers [12,13] the electron-ion dissociative

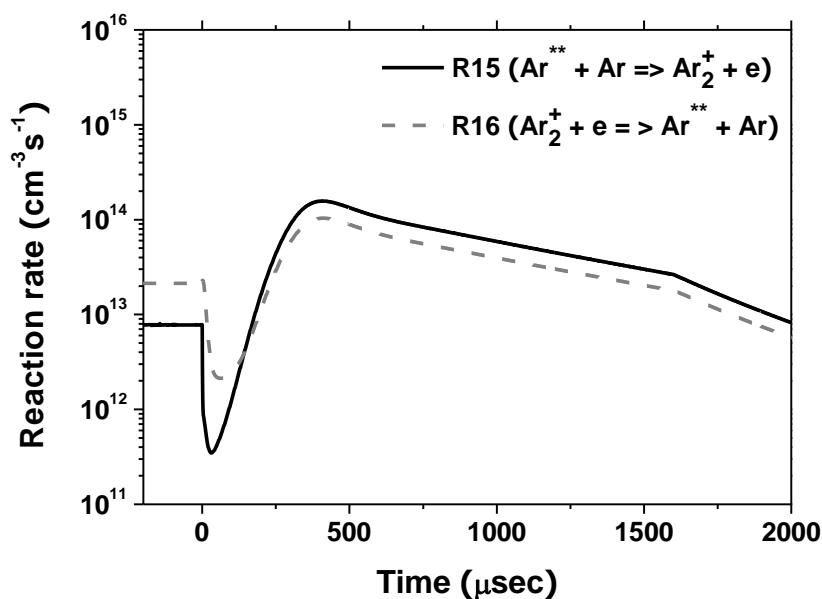
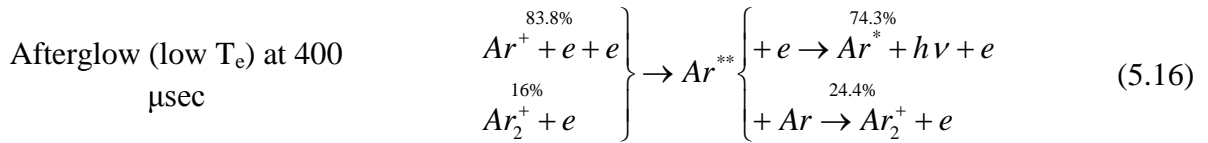
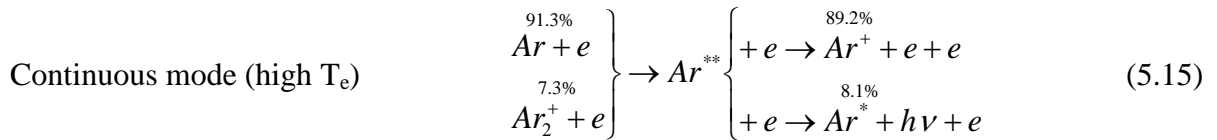


Figure 5.13 Calculated reaction rates for R15 and R16 vs. time in the afterglow at 200 mTorr.

recombination R16 ($\text{Ar}_2^+ + e \rightarrow \text{Ar}^{**} + \text{Ar}$) is given as the most important Ar^{**} production reaction. However the discharge conditions are different from our conditions, especially the pressure range, leading to different recombination processes in the afterglow. Our calculation at 200 mTorr shows that the rate of the reverse reaction R15 ($\text{Ar}^{**} + \text{Ar} \rightarrow \text{Ar}_2^+ + e$) (solid line in figure 5.13) is always higher than R16 ($\text{Ar}_2^+ + e \rightarrow \text{Ar}^{**} + \text{Ar}$) in the afterglow except at the beginning (light line in figure 5.13). As a whole, in the reactions R15 and R16 a net loss of Ar^{**} occurs. It means that on the contrary to the descriptions in the literatures, R16 is not the important production source of Ar^{**} which gives the strong after peak emission. It results a net loss in Ar^{**} . In the afterglow the reaction coefficient of R16 increases up to $k_{R16} = 3 \times 10^{-7} \text{ cm}^3 \text{ s}^{-1}$ because this coefficient is inversely proportional to the electron temperature while the reaction coefficient $k_{R15} = 2 \times 10^{-9} \text{ cm}^3 \text{ s}^{-1}$ is constant. If we compare the reaction rates for R15 and R16, $v_{R15} = k_{R15}[\text{Ar}^{**}][\text{Ar}]$ and $v_{R16} = k_{R16}[\text{Ar}_2^+][e]$, $v_{R16} < v_{R15}$ is obtained as shown in figure 5.13. Rearranging the values in the Table 5.2, the main processes dealing with the Ar highly excited state at 200 mTorr leading to the emission after peak during afterglow can be summarized as follows:



Here we can see in the upper line of (5.16) that the three body ion recombination (R10) provides the emission by the deactivation of Ar^{**} . However, in the lower line of (5.19) the electron – ion dissociative recombination (R16) does not produce emission. The calculation shows that the population of Ar excited state and the intense afterglow are mainly produced by the three body electron – ion recombination ($\text{Ar}^+ + e + e \rightarrow \text{Ar}^{**} + e$).

Table 5.1 Reaction set used in the model.

Process	Rate coefficient k (cm^3s^{-1} , cm^6s^{-1} , s^{-1})	References
Electron impact excitation and de-excitation		
R1 $\text{Ar} + e \leftrightarrow \text{Ar}(j) + e$ $j = 4s, 4p, 3d, 5s, 5p$	B.E.	[39-41]
R2 $\text{Ar} + e \leftrightarrow \text{Ar}^{**} + e$	$4.0 \times 10^{-9} \exp(-15.8/T_e)$	[42]
R3 $\text{Ar}(3p^5 4s) + e \leftrightarrow \text{Ar}(j) + e$ $j = 4p, 5p$	B.E.	[39,43]
Electron impact ionization		
R4 $\text{Ar} + e \rightarrow \text{Ar}^+ + e + e$	B.E.	[44]
R5 $\text{Ar}(3p^5 4s) + e \rightarrow \text{Ar}^+ + e + e$	B.E.	[45]
R6 $\text{Ar}(4p) + e \rightarrow \text{Ar}^+ + e + e$	$2.0 \times 10^{-6} \exp(-4.4/T_e)$	[42]
R7 $\text{Ar}(3d, 5s) + e \rightarrow \text{Ar}^+ + e + e$	$6.0 \times 10^{-6} \exp(-2.4/T_e)$	[42]
R8 $\text{Ar}(5p) + e \rightarrow \text{Ar}^+ + e + e$	$2.0 \times 10^{-5} \exp(-2.2/T_e)$	[42]
R9 $\text{Ar}^{**} + e \rightarrow \text{Ar}^+ + e + e$	$2.0 \times 10^{-4} \exp(-0.5/T_e)$	[42]
Three body recombination		
R10 $\text{Ar}^+ + e + e \rightarrow \text{Ar}^{**} + e$	$1.0 \times 10^{-19} (T_e \times 11605/300)^{-4.5}$	[46]
R11 $\text{Ar}^+ + e + \text{Ar} \rightarrow \text{Ar}^{**} + \text{Ar}$	3.0×10^{-28}	[46]
Chemi - ionization		
R12 $\text{Ar}(j) + \text{Ar}(k) \rightarrow \text{Ar}^+ + \text{Ar} + e$ $j, k = 4s, 4p$	$5.0 \times 10^{-10} (T_g/300)^{0.5}$	[47]
Production of Ar_2^+		
R13 $\text{Ar}^+ + \text{Ar} + \text{Ar} \rightarrow \text{Ar}_2^+ + \text{Ar}$	$2.5 \times 10^{-31} (T_g/300)^{-1.5}$	[25,54]
R14 $\text{Ar}(3p^5 4s) + \text{Ar}(3p^5 4s) \rightarrow \text{Ar}_2^+ + e$	$6.3 \times 10^{-10} (T_g/300)^{-0.5}$	[25]
R15 $\text{Ar}^{**} + \text{Ar} \rightarrow \text{Ar}_2^+ + e$	2.0×10^{-9}	[25]
Loss of Ar_2^+		
R16 $\text{Ar}_2^+ + e \rightarrow \text{Ar}^{**} + \text{Ar}$	$9.1 \times 10^{-7} (T_e \times 11605/300)^{-0.67} (T_g/300)^{-0.58}$	[17,47]
R17 $\text{Ar}_2^+ + e \rightarrow \text{Ar}(j) + \text{Ar}$ $j = 4s, 4p, 3d, 5s, 5p$	$1.0 \times 10^{-8} T_e^{-0.6} (T_g/300)^{-0.6}$	[47]
Radiative decay		
R18 $\text{Ar}(1s_2, 1s_4) \rightarrow \text{Ar} + h\nu$	$5.32 \times 10^8 g_{1s_2}, 1.3 \times 10^8 g_{1s_4}$	[48]
R19 $\text{Ar}(4p) \rightarrow \text{Ar}(1s_2, 1s_3, 1s_4, 1s_5) + h\nu$	$9.6 \times 10^6, 3.3 \times 10^6, 1.0 \times 10^7, 9.9 \times 10^6$	[48]
R20 $\text{Ar}(5s, 3d) \rightarrow \text{Ar}(4p) + h\nu$	$1.56 \times 10^7, 1.56 \times 10^7$	[48]
R21 $\text{Ar}(5p) \rightarrow \text{Ar}(3d, 5s, 4s) + h\nu$	$(6.5 \times 10^6) \times 0.4, (6.5 \times 10^6) \times 0.4, (6.5 \times 10^6) \times 0.2$	[48]
R22 $\text{Ar}^{**} \rightarrow \text{Ar}(5p, 3d, 5s, 4p) + h\nu$	$5.0 \times 10^6, 8.6 \times 10^6, 8.6 \times 10^6, 9.1 \times 10^5$	[48]
R23 $\text{Ar}^{**} \rightarrow \text{Ar}(1s_2, 1s_3, 1s_4, 1s_5) + h\nu$	$9.3 \times 10^4, 3.7 \times 10^4, 1.2 \times 10^5, 1.8 \times 10^5$	[48]

notes : T_e in eV, and T_g in K

Table 5.2 Relative contributions of the most important population and loss processes during pulse on time and afterglow.

Level	Reaction	CW	100 μ sec	400 μ sec	1000 μ sec
1. Ar _M (1s ₅ ,1s ₃)	Population				
	Ar + e \rightarrow Ar _M + e	6.4	0	0	0
	Ar _R + e \rightarrow Ar _M + e	29.4	96.8	85.0	80.3
	Ar(4p,5p, ^{**}) \rightarrow Ar _M + $h\nu$	64.1	3.2	14.7	19.2
	Ar ₂ ⁺ + e \rightarrow Ar _M + e	0	0.1	0.4	0.5
	Loss				
	Ar _M + e \rightarrow Ar _R + e	26.6	96.7	98.6	97.5
	Ar _M + e \rightarrow Ar(4p) + e	69.7	2.5	0	0
	Ar _M + e \rightarrow Ar(5p) + e	2.0	0	0	0
	Ar _M + e \rightarrow Ar ⁺ + e + e	1.4	0	0	0
2. Ar _R (1s ₄ ,1s ₂)	Population				
	Ar + e \rightarrow Ar _R + e	7.9	0	0	0
	Ar _M + e \rightarrow Ar _R + e	19.9	96.1	80.6	77.7
	Ar(4p,5p, ^{**}) \rightarrow Ar _R + $h\nu$	72.2	3.7	18.8	21.6
	Loss				
	Ar _R + e \rightarrow Ar _M + e	22.1	70.8	76.4	62.3
	Ar _R + e \rightarrow Ar(4p) + e	59.6	1.7	0	0
	Ar _R \rightarrow Ar + $h\nu$	16.7	27.0	23.1	37.2
3. Ar(4p)	Population				
	Ar + e \rightarrow Ar(4p) + e	4.4	0	0	0
	Ar(4s) + e \rightarrow Ar(4p) + e	92.8	69.3	0	0
	Ar(5s,3d, ^{**}) \rightarrow Ar(4p) + $h\nu$	2.8	28.8	97.8	97.8
	Ar ₂ ⁺ + e \rightarrow Ar(4p) + Ar	0	1.8	2.2	2.2
	Loss				
	Ar(4p) \rightarrow Ar _M + $h\nu$	39.8	40.0	40.0	40.0
	Ar(4p) \rightarrow Ar _R + $h\nu$	59.7	60.0	60.0	60.0
4. Ar(5p)	Population				
	Ar + e \rightarrow Ar(5p) + e	32.0	0	0	0
	Ar _M + e \rightarrow Ar(5p) + e	67.7	0.5	0	0
	Ar ^{**} \rightarrow Ar(5p) + $h\nu$	0.2	74.3	90.3	90.3
	Ar ₂ ⁺ + e \rightarrow Ar(5p) + Ar	0.1	25.2	9.7	9.7
	Loss				
	Ar(5p) + e \rightarrow Ar ⁺ + e + e	53.3	0.2	0	0
	Ar(5p) \rightarrow Ar(5s,3d) + $h\nu$	37.4	79.8	80.0	80.0
	Ar(5p) \rightarrow Ar(4s) + $h\nu$	9.3	20.0	20.0	20.0

5. Ar^{**}	Population				
	$\text{Ar}^+ + e + e \rightarrow \text{Ar}^{**} + e$	0	61.7	83.8	83.4
	$\text{Ar}^+ + e + \text{Ar} \rightarrow \text{Ar}^{**} + \text{Ar}$	1.4	19.9	0.2	0.1
	$\text{Ar}_2^+ + e \rightarrow \text{Ar}^{**} + \text{Ar}$	7.3	18.4	16.0	16.6
	$\text{Ar} + e \rightarrow \text{Ar}^{**} + e$	91.3	0	0	0
	Loss				
	$\text{Ar}^{**} + e \rightarrow \text{Ar}^+ + e + e$	89.2	60.9	1.4	0.1
	$\text{Ar}^{**} \rightarrow \text{Ar}(5p,5s,3d,4p,4s) + h\nu$	8.1	29.4	74.3	75.2
	$\text{Ar}^{**} + \text{Ar} \rightarrow \text{Ar}_2^+ + e$	2.7	9.7	24.4	24.7
6. Ar_2^+	Population				
	$\text{Ar}^+ + \text{Ar} + \text{Ar} \rightarrow \text{Ar}_2^+ + \text{Ar}$	9.0	67.2	1.1	1.3
	$\text{Ar}(4s) + \text{Ar}(4s) \rightarrow \text{Ar}_2^+ + e$	69.1	0	0.1	0.3
	$\text{Ar}^{**} + \text{Ar} \rightarrow \text{Ar}_2^+ + e$	21.8	32.8	98.8	98.4
	Loss				
	$\text{Ar}_2^+ \rightarrow \text{wall}$	1.8	0.4	0.1	0.2
	$\text{Ar}_2^+ + e \rightarrow \text{Ar}^{**} + \text{Ar}$	59.7	63.3	65.3	65.8
	$\text{Ar}_2^+ + e \rightarrow \text{Ar}(4s,4p,5s,3d,5p) + \text{Ar}$	38.4	36.4	34.5	34.0
7. Ar^+	Population				
	$\text{Ar} + e \rightarrow \text{Ar}^+ + e + e$	17.5	0	0	0
	$\text{Ar}(4s) + e \rightarrow \text{Ar}^+ + e + e$	41.4	0	0	0
	$\text{Ar}(4p,3d,5s,5p) + e \rightarrow \text{Ar}^+ + e + e$	37.0	0	0	0
	$\text{Ar}^{**} + e \rightarrow \text{Ar}^+ + e + e$	3.6	99.9	96.9	35.2
	$\text{Ar}(4s) + \text{Ar}(4s) \rightarrow \text{Ar}^+ + \text{Ar} + e$	0.5	0	3.1	64.8
	Loss				
	$\text{Ar}^+ \rightarrow \text{wall}$	99.8	99.4	63.1	63.5
	$\text{Ar}^+ + e + e \rightarrow \text{Ar}^{**} + e$	0	0.3	36.6	36.2

5.5 Modeling of E-H mode transition and hysteresis in low pressure argon ICP discharges

5.5.1 E-H mode transition and hysteresis

Inductively coupled plasmas are well known to exhibit two distinct coupling modes between the RF electromagnetic field and the plasma, at low electron density mainly by capacitive coupling (*E* mode) and at high electron density mainly by inductively coupling (*H* mode). *E-H* mode transition has frequently been described in the literature as an abrupt jump of the electron density or the plasma emission. In addition, this transition between the two modes has been reported to exhibit experimentally hysteresis [19-22]. El-Fayoumi *et al* suggested that the existence of a threshold current for the *H* mode and of the hysteresis originates in the electron energy balance in the discharge as the power absorbed by the electrons P_{abs} must balance the power dissipated P_{loss} to reach a stable *E* or *H* discharge [49]. Cunge *et al* examined and proved experimentally this hypothesis by investigating the hysteresis in detail and by studying the dynamics of the transition in time modulated discharges [50]. Turner and Lieberman showed that hysteresis during the *E-H* mode transition may originate from the nonlinearity of one or both curves of power transfer and power dissipation [51], and it has been reported that the nonlinearity due to the multistep ionizations may be one of the dominant factors of hysteresis at high gas pressures [52]. More recently, Daltrini *et al* observed no hysteresis in the measured plasma parameters when plotting versus the power absorbed by the plasma and suggested that the hysteresis is due to ignoring inherent power loss, primarily in the matching system [22].

In this study, we calculate the plasma parameters and the power absorbed by the plasma by coupling a global (volume averaged) model and a transformer model in an argon ICP discharge. First we explore the transition between *E* and *H* modes by fixing as in real experimental conditions the power injected by the RF generator rather than the coil current as shown in the previous related papers where the power dissipated in the coil is ignored. Here we determine the power deposited in the plasma and the power dissipated in the coil using well-matched conditions with balancing P_{abs} and P_{loss} . We show as measured by Daltrini *et al*. that there exists at the *E-H* mode separation a range of absorbed powers and electron density which cannot be accessed. We also investigate the hysteresis by calculation with increasing and decreasing the applied power to the system as in real experimental conditions.

5.5.2 Discharge model

The global model is the simplest level of modeling and consists of particle balance and electron energy balance equations [33,36]. The principle, the chamber parameters and the reactions used in the global model are described in section 5.4. In this model we assume that the electron energy distribution functions (EEDFs) are Maxwellian. The equivalent circuit used in this study is shown in figure 2.5. We consider the plasma to be a ring acting as the secondary coil of a transformer [53-55]. The voltage required to power the coil of an inductive discharge is supplied by a 50 Ω (R_T) RF power source through an alternate

capacitive matching network, which consists of C_L (loading capacitor) and C_T (tuning capacitor). The inductive branch is represented as an air-cored transformer having the planar coil inductance L_l and resistance R_l as a primary. The discharge can be described by a geometric inductance L_2 , an electron inertia inductance L_{pi} , and a resistance R_{pi} of the plasma loop. The capacitive branch is represented by the combination of the circuit elements C_d , L_{pc} , R_{pc} , C_s , R_{st} and R_{ion} . The expressions of these components are given in chapter 2. By mixing the circuit theory with electromagnetic theory the total absorbed power P_{abs} is determined with calculating separately the averaged power delivered by the coil to the plasma though (i) capacitive coupling P_{cap} and (ii) RF induction P_{ind} , and (iii) the power P_{stoc} gained by the electrons from interaction with the time-varying sheath (stochastic heating) [49,56]:

$$P_{abs} = P_{cap} + P_{ind} + P_{stoc} \quad (5.17)$$

The response of the plasma to the RF electric field is described by the collisional electrical conductivity:

$$\sigma_p = \epsilon_0 \frac{\omega_{pe}^2}{v_{eff} + j\omega_{eff}} \quad (5.18)$$

where ω_{pe} is the plasma frequency, v_{eff} is the effective electron-neutral collision frequency and ω_{eff} the effective RF driving frequency [57].

In order to transfer the maximum of the source power to the coil-plasma system, the two independent components C_L and C_T are varied to get well-matched conditions i.e. $\Re(Z_{load}) = R_T$ and $\Im(Z_{load}) = 0$, where Z_{load} is the total impedance including the matching network [36]. Assuming a lossless matching network, the applied RF source power can be written as:

$$P_a = P_t = P_{abs} + P_{coil} \quad (5.19)$$

where P_t and P_{coil} are the power transferred to the load and the power dissipated in the RF coil ($R_l i_{coil}^2$), respectively. In the model, we first calculate the coil current to obtain $P_t = P_a$ for some initial values of the electron density and the electron temperature. Once i_{coil} is obtained, the absorbed power P_a is determined and the electron density and the electron temperature are calculated by solving the particle balance and the power balance equations using the global model. Then the impedances Z_{ind} and Z_{cap} of the inductive and capacitive branches respectively are calculated. This process is repeated until the densities of all species and the electron temperature reach the steady state.

5.5.3 Results and discussion

Figure 5.14(a) shows the variation of the absorbed power and the loss power P_{loss} by electrons as a function of the electron density n_e at different fixed source applied powers from 5 to 50 Watts. For a steady state to be reached, the equality $P_{abs}(n_e) = P_{loss}(n_e)$ must be satisfied. However, to satisfy a stable working condition the rate of change of the absorbed power with n_e must be less than that of the loss power [49,50,56]:

$$\frac{\partial P_{abs}}{\partial n_e} < \frac{\partial P_{loss}}{\partial n_e} \quad (5.20)$$

It has to be noted that the curves shown in figure 5.14(a) have been obtained for an initial value of the electron density fixed at $1 \times 10^{15} \text{ m}^{-3}$. In other words it is similar as igniting the discharge in *E*-mode to reach the steady point. When the applied power is lower than 13 Watts the electron heating is mainly due to capacitive coupling. The discharge is in *E*-mode and the maximum electron density is $1.9 \times 10^{16} \text{ m}^{-3}$. As depicted in figure 5.14(b), the coil current increases with the applied power and reaches high values up to 8 A at 13 Watts applied power. This leads to high power loss in the RF coil and to low power transfer efficiency of about 35 %. Indeed, in figure 5.14(a) it can be easily read that for 13 Watts of applied power only 4 Watts are absorbed by the plasma. By increasing the applied power from 13 to 15 Watts, we observe a jump of the electron density corresponding to the transition between *E* and *H* mode. The minimum absorbed power by the plasma or the threshold power (P_{th}) to sustain the discharge in *H*-mode corresponds to the high limit of an inaccessible region versus the applied power as shown experimentally by Daltrini *et al.* The

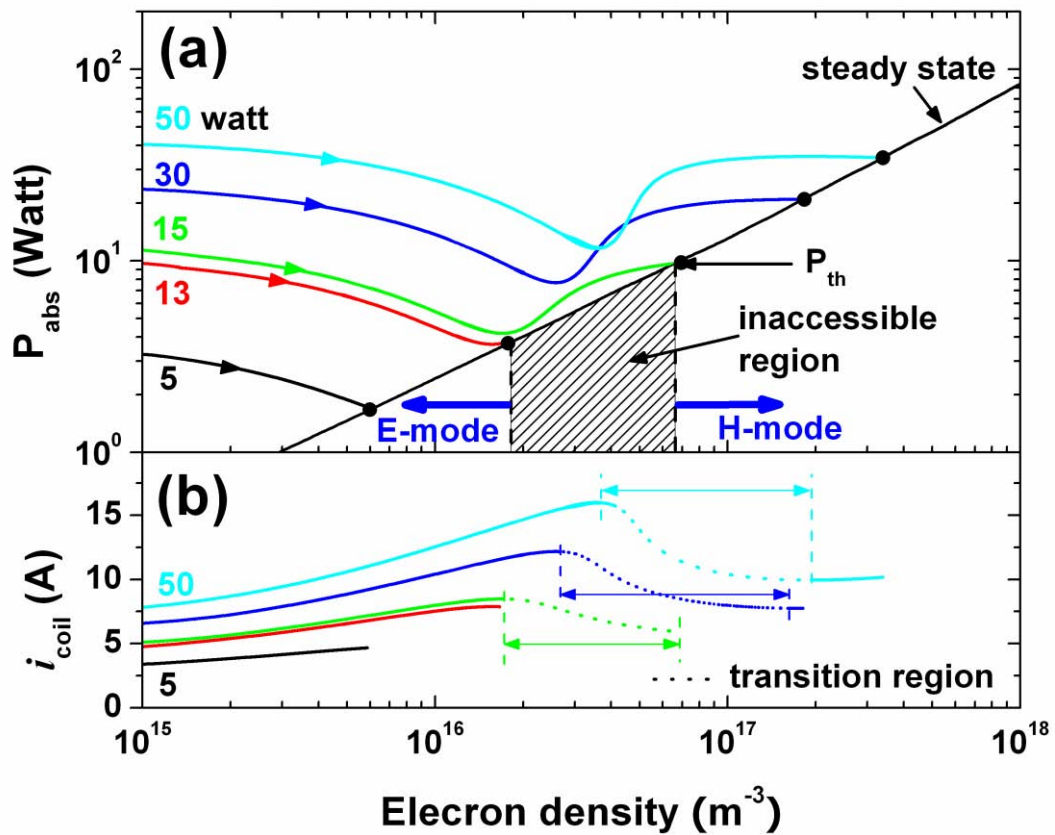


Figure 5.14 Variation of (a) the absorbed power P_{abs} and the loss power P_{loss} by electrons and (b) the coil current i_{coil} as a function of the electron density n_e at different fixed source applied powers from 5 to 50 Watts.

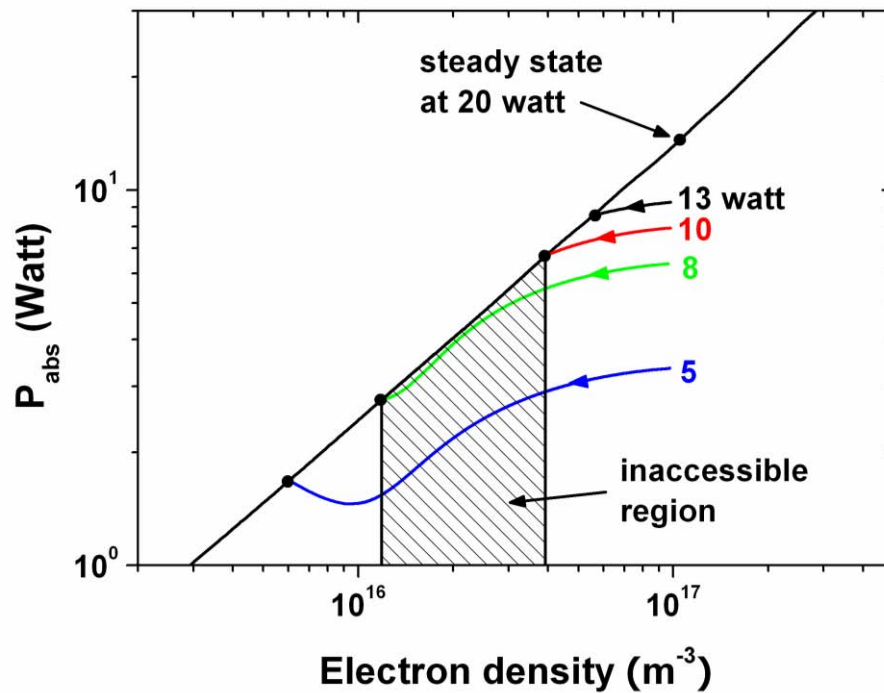


Figure 5.15 Variation of the absorbed power P_{abs} as a function of the electron density. The steady state was first calculated for 20 Watts applied power and then from this steady point ($n_e = 1 \times 10^{17} \text{ m}^{-3}$) the applied power was decreased to 13, 10, 8 and 5 Watt.

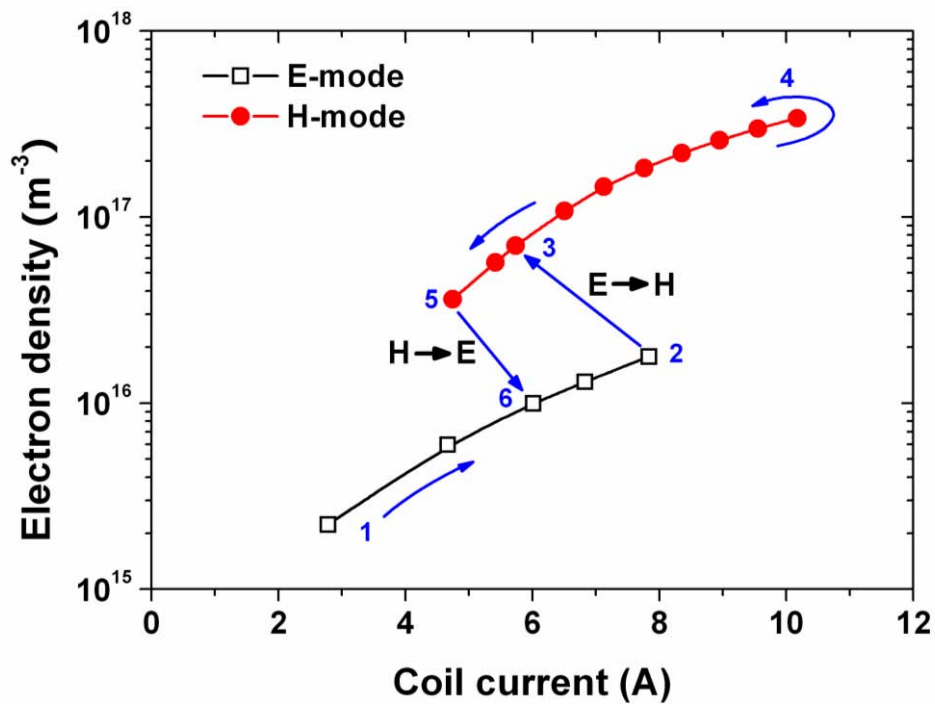


Figure 5.16 The calculated electron density versus the coil current as shown experimentally by Kortshagen *et al* [19].

power transfer is much more efficient than in *E*-mode since approximately 80 % of the applied power is absorbed by the plasma. We note that after the transition to *H*-mode the coil current decreases abruptly from 8 A (*E*-mode) to 5.8 A. In addition, there exists a region we call transition region where the coil current decreases versus n_e and where no steady state of the discharge can be reached whatever the P_{loss} curve.

To investigate the hysteresis the steady state was first calculated for 20 Watts applied power and then from this steady point (electron density is $1 \times 10^{17} \text{ m}^{-3}$) the applied power was decreased. In figure 5.15 are plotted the different P_a curves following this procedure. We observe that the discharge can be sustained in *H*-mode up to 10 Watts. The inaccessible region is shifted to lower electron density values. The real inaccessible region corresponds to the overlap of both regions shown in figures 5.14(a) and 5.15. Here this region corresponds to $4 \sim 7$ Watts and $1.9 \sim 4 \times 10^{16} \text{ m}^{-3}$. It is worth noting that this region depends on the discharge reactor, the gas pressure, RF frequency and the P_{loss} curve. Also the shape of EEDFs may have an effect since the effective electrical conductivity and the effective collision frequency are influenced [57]. The effects of the nonlinearity due to the multistep ionizations and the shape of EEDFs will be discussed in detail in a separate paper.

Figure 5.16 shows the electron density versus the coil current as shown experimentally by Kortshagen *et al* [19]. We see that a threshold coil current (7.8 A) is needed to reach the *H*-mode and that abruptly the electron density increases and the coil current decreases. In addition we observe a hysteresis.

5.6 Conclusion

In this chapter, we devoted to study low pressure argon ICP discharges using various diagnostic methods and simple modeling.

For the purpose of improving the precision of the pressure-dependent electron temperature calculated by the line ratio, a new mean of correcting the cascade cross-sections was discussed. Quantification of the cross-sections was investigated experimentally to contain the influencing factors on the pressure dependence mainly by radiation trapping. The pressure-dependent cascade cross-section was treated as a sum of the multiplication of the coefficient $\alpha(P)$ which depends on the pressure and the cascade cross-section at 3 mTorr, as found in the literature. Using the EEDF $F(E)$ and the electron density from Langmuir probe, the coefficient of the cascade cross-section as a function of the pressure $\alpha(P)$ was calculated for $4p_1$ and $4p_5$. The improvement of the cross-sections by introducing $\alpha(P)$, the coefficient of cascade cross-section, was shown. The deviation of the optical cross-section from the correct value dominates the discrepancy caused by the difference in the EEDF compared to the Maxwellian condition. In consequence, only with an improvement of the cross-section, while the EEDF remains Maxwellian, the estimation of the electron temperature can be approached the effective temperature T_{eff} using an electrostatic probe.

The production of Ar excited states in the afterglow was studied both experimentally and theoretically. Emission of a strong emission of highly excited Ar^{**} (4d-4p) species was observed in high pressure pulse modulated ICP. At the same time, recovery of Ar ($3p^5 4s$) densities after a steep recession was measured. A time dependent global (volume averaged)

model was developed to understand the behavior of the afterglow. In the discharge model, 130 reactions are taken into account. It was assumed that Ar consists of 12 states, and the electron energy distribution function is Maxwellian. Obviously during the pulse-on time the electron impact excitation and the ionization from the ground state and Ar ($3p^54s$) are the dominant population processes for all excited states, while it plays no role in the afterglow since the electron temperature decreases abruptly at 10 mTorr and 200 mTorr. The radiative decay is both the dominant gain and loss of each state. During the afterglow the main source of all excited states is the three body electron-ion recombination. With this reaction Ar^{**} state can be populated more than during the pulse-on time.

We have explored the mechanism of *E-H* mode transition and its hysteresis using global model and transformer model. The total absorbed power by plasma electrons and coil current are calculated as a function of the electron density at fixed injected power rather than fixed coil current as previously shown in the literature. We found that the transition is due to difference of absorbed power between *E* and *H* mode. Moreover the calculation results show that existence of inaccessible region between *E* and *H* mode, as well as threshold coil current and minimum absorbed power for the *H* mode.

5.7 References

- [1] Donnelly V M, Malyshev M V, Schabel M, Kornblit A, Tai W, Herman I P and Fuller N C M 2002 *Plasma Sources Sci. Technol.* **11** A26-A30
- [2] Bibinov N K, Kokh D B, Kolokolov N B, Kostenko V A, Meyer D, Vinogradov I P and Wiesemann K 1998 *Plasma Sources Sci. Technol.* **7** 298-309
- [3] Croll G and Oechner H 2001 *Eur. Phys. J. AP* **15** 49-56
- [4] Chilton J E, Boffard J B, Schappe R S and Lin C C 1998 *Phys. Rev. A* **57** 267-77
- [5] Boffard J B, Piech G A, Gehrke M F, Anderson L W and Lin C C 1999 *Phys. Rev. A* **59** 2749-2763
- [6] Lin C C 2004 *Contrib. Plasma Phys.* **44** 405-412
- [7] Boffard J B, Lin C C and DeJoseph Jr C A 2004 *J. Phys. D: Appl. Phys.* **37** R143-R161
- [8] Schabel M J, Donnelly V M, Kornblit A and Tai W W 2002 *J. Vac. Sci. Technol. A* **20**(2) 555-563
- [9] Croll G and Oechner H 2001 *Eur. Phys. J. AP* **15** 49-56
- [10] Harrison W W, Yang C and Oxley E 2001 *Anal. Chem.* **73** 480A
- [11] Deloche R, Monchicourt P, Cheret M and Lamvert F 1976 *Phys. Rev. A* **13** 1140
- [12] Bogaerts A 2007 *J. Anal. At. Spectrom.* **22** 502
- [13] Nafarizal N, Takada N and Sasaki K 2008 *J. Phys. D: Appl. Phys.* **41** 035206
- [14] Jackson G P and King F L 2003 *Spectrochim. Acta B* **58** 185
- [15] Shiu Y J and Biondi M A 1978 *Phys. Rev. A* **17** 868
- [16] Bogaerts A and Gijbels R 1999 *J. Appl. Phys.* **86** 4124
- [17] Bultel A, Ootegem B, Bourdon A and Vervisch R 2002 *Phys. Rev. E* **65** 046406
- [18] Kang N, Britun N, Oh S G, Gaboriau F and Ricard A 2009 *J. Phys. D: Appl. Phys.* **42** 112001
- [19] Kortshagen U, Gibson N D and Lawler J E 1996 *J. Phys. D: Appl. Phys.* **29** 1224-1236
- [20] Ostrikov K N, Xu S and Yu M Y 2000 *J. Appl. Phys.* **88** 2268-2271
- [21] Daltrini A M, Moshkalev S A, Monteiro M J R, Bessler E, Kostyukov A and Machida M 2007 *J. Appl. Phys.* **101** 073309
- [22] Daltrini A M, Moshkalev S A, Morgan T J, Piejak R B and Graham W G 2008 *Appl. Phys. Lett.* **92** 061504
- [23] Godyak V A, Piejak R B and Alexandrovich B M 1993 *J. Appl. Phys.* **73** 3657-3663
- [24] Godyak V A and Kolobov V I 1998 *Phys. Rev. Lett.* **81** 369-372
- [25] Godyak V A, Meytlis V P and Strauss H R 1995 *IEEE Trans. Plasma Sci.* **23** 728-734
- [26] Seo S, Chung C, Hong J and Chang H 2000 *Phys. Rev. E* **62** 7155-7167
- [27] Maresca A, Orlov K and Kortshagen U 2002 *Phys. Rev. E* **65** 056405

- [28] Mitchell A C G and Zemanski M W Z 1971 *Resonance Radiation and Excited Atoms* (Cambridge: Cambridge University Press)
- [29] Ricard A, Nouvellon C, Konstantinidis S, Dauchot J P, Wautelet M and Hecq M 2002 *J. Vac. Sci. Technol. A* **20** 1488
- [30] Kang N, Oh S G, Gaboriau F and Ricard A 2010 *Rev. Sci. Instrum.* **81** 013102
- [31] Konstantinidis S, Ricard A, Fanciu M, Dauchot J P, Ranea C and Hecq M 2004 *J. Appl. Phys.* **95** 2900
- [32] Griem H R 1964 *Plasma Spectroscopy* (New York: McGraw-Hill)
- [33] Lieberman M A and Ashida S 1996 *Plasma Sources Sci. Technol.* **5** 145
- [34] Phelps A V 1991 *J. Phys. Chem. Ref. Data* **20** 557
- [35] Pancheshnyi S, Eismann B, Hagelaar G J M, Pitchford L C, Computer code ZDPlasKin, <http://www.zdplaskin.laplace.univ-tlse.fr> (University of Toulouse, LAPLACE, CNRS-UPS-INP, Toulouse, France, 2008).
- [36] Lieberman M A and Lichtenberg A J 2005 *Principles of Plasma Discharges and Materials Processing 2nd ed.* (New York: Wiley)
- [37] Biondi M A 1976 *Principle of Laser Plasma: ch.4*, eds. Bekefi G (New York: Wiley)
- [38] Bogaerts A, Gijbels R and Jackson G P 2003 *J. Anal. At. Spectrom.* **18** 533
- [39] Bartschat K and Zeman V 1999 *Phys. Rev. A* **59** R2552
- [40] Chilton J E and Lin C C 1999 *Phys. Rev. A* **60** 3712
- [41] Weber T, Boffard J B and Lin C C 2003 *Phys. Rev. A* **68** 032719
- [42] Zhu X M and Pu Y K 2010 *J. Phys. D: Appl. Phys.* **43** 015204
- [43] Jung R O, Boffard J B, Anderson L W and Lin C C 2007 *Phys. Rev. A* **75** 052707
- [44] Rapp D and Englander-Golden P 1965 *J. Chem. Phys.* **43** 1464
- [45] Ali M A and Stone P M 2008 *Int. J. Mass Spectrom.* **271** 51
- [46] Bogaerts A, Gijbels R and Jackson G P 2003 *J. Anal. At. Spectrom.* **18** 533
- [47] Robin M N, Shabunya S I, Rostaing J C and Perrin J M 2007 *Plasma Sources Sci. Technol.* **16** 480
- [48] NIST Atomic Spectra Database, <http://physics.nist.gov/asd3>
- [49] El-Fayoumi I M, Jones I R and Turner M M 1998 *J. Phys. D: Appl. Phys.* **31** 3082
- [50] Cunge G, Crowley B, Vender D and Turner M M 1999 *Plasma Sources Sci. Technol.* **8** 576
- [51] Turner M M and Lieberman M A 1999 *Plasma Sources Sci. Technol.* **8** 313
- [52] Lee M H, Lee K H, Hyun D S and Chung C W 2007 *Appl. Phys. Lett.* **90** 191502
- [53] Piejak R B, Godyak V A and Alexandrovich B M 1992 *Plasma Sources Sci. Technol.* **1** 179

- [54] El-Fayoumi I M and Jones I R 1998 *Plasma Sources Sci. Technol.* **7** 179
- [55] Gudmundsson J T and Lieberman M A 1998 *Plasma Sources Sci. Technol.* **7** 83
- [56] Lee M H and Chung C W 2006 *Phys. Plasmas* **13** 063510
- [57] Lister G G, Li Y M and Godyak V A 1996 *J. Appl. Phys.* **79** 8993

Chapter 6

Modeling and experimental study of molecular nitrogen dissociation in an Ar-N₂ ICP discharge

Contents

6.1	Introduction	102
6.2	Experiment	102
6.2.1	Measurement of electron temperature and electron density	102
6.2.2	Measurement of Ar (3p ⁵ 4s) density and emission intensity	103
6.2.3	Measurement of atomic nitrogen density by TALIF	104
6.3	Discharge model	106
6.4	Results and discussion	110
6.4.1	Pure nitrogen discharge	110
6.4.2	Ar-N ₂ discharge	114
6.4.2.1	Electron temperature and charged particles density.	114
6.4.2.2	Ar(3p ⁵ 4s) density	117
6.4.2.3	Production of N ₂ (C ³ Π _u) excited molecules	117
6.4.2.4	Production of N(⁴ S)	120
6.5	Conclusion	123
6.6	References	129

6.1 Introduction

NITROGEN plasmas have been widely used in various industrial applications like nitride thin films, such as GaN and TiN, and in the modification of the surface properties of various materials. Especially atomic nitrogen species generated by the dissociation of the N_2 molecule in the plasma play a dominant role in the film growth and the surface chemistry. In a pure nitrogen discharge, the dissociation rate is small due to the strong N-N bond strength [1]. According to many authors, the dissociation rate of N_2 molecule is enhanced in Ar- N_2 discharge but there is no clear explanation in the literature dealing with the influence of argon on the dissociation of N_2 molecule. Tabbal *et al* [2] measured the dissociation rate in Ar- N_2 mixed surface-wave-sustained plasma by optical emission spectroscopy. They observed a dissociation rate higher than 2.5 % when the total pressure is 7.5 Torr and Ar mixing ratio is 95 %. Henriques *et al* [3] measured the N atom density using actinometry in a surface wave plasma when the total pressure is in the range 0.2-2 Torr. They reported an increase of the dissociation degree of N_2 molecules at high Ar fractional concentration which is attributed to the contribution of fast charge exchanges between Ar^+ and N_2 followed by the dissociative recombination process $N_2^+ + e \rightarrow N + N$. Czerwicz *et al* [4] measured the N atom density using actinometry and mass spectrometry in a low pressure cylindrical ICP discharge and observed that the dissociation rate is enhanced by argon addition in Ar- N_2 discharge.

Recently, Kimura *et al* [5] have developed a global model of an inductively coupled RF Ar- N_2 discharge. They measured some emission intensities and deduced N atom density by actinometry and compared with calculated results for 50 %-95 % Ar addition in the mixture.

In this study, we have developed a global model of the Ar- N_2 discharge to calculate the electron temperature and the electron density. Using these parameters, the evolutions of the densities of Ar, N_2 and N excited states are investigated simultaneously. We compare the calculated results with the experiments and discuss in detail the dominant creation sources and the routes of loss for each level as a function of N_2 percentage in Ar- N_2 mixture.

6.2 Experiment

The experimental set-up for this study is the same with chapter 5 as shown in figure 5.1. The anode plate was installed at 50 mm from antenna window to limit the volume of the discharge. The discharge was excited by a 3 turn-antenna powered by 13.56 MHz of RF frequency with 200 Watt constant injected power. The chamber was pumped to 10^{-6} Torr base pressure before filling with Ar (99.999 % purity) and N_2 (99.999 % purity) gas. The total flow rate was maintained constant at 50 sccm.

6.2.1 Measurement of electron temperature and electron density

A home-built cylindrical electrostatic probe was set in the discharge center ($r = 0$ and $z = 2.5$ cm). $z = 0$ corresponds to the interior surface of the upper quartz window and $r = 0$ is the central axis of the window. The Langmuir probe made of tungsten wire with 0.1 mm in diameter and 5 mm length is small compared with the Debye length for the present glow discharge. The probe tip is supported by a ceramic tube which is glued inside a long stainless

steel tube. To reduce the RF distortion of probe characteristics a floating loop probe was used with a resonance filter [6]. The bias voltage was applied in the range from -30 V to +30 V with 0.05 V step. The probe current was measured through a 10 Ω resistor using a 16-bit analog digital convertor card. This measurement was repeated and averaged over 1000 sweeps in order to improve the signal over noise ratio.

The EEPF $f(E)$, the electron density and the electron temperature were obtained from Druyvesteyn formula in equations (4.47)-(4.50).

6.2.2 Measurement of Ar ($3p^54s$) density and emission intensity

To measure the density of metastable atoms, the resonance absorption spectroscopy was used. This method is widely performed in various plasma processes [8] and has been applied successfully for measuring metastable atom density in DC and RF magnetron discharges [9,10]. A lab-made hollow cathode lamp was used as the reference source. The source light driven by 35 mA DC current at 1 Torr has been collimated by a system of lenses and diaphragms to get a probing beam of 5 mm in diameter inside the plasma chamber. To obtain a stable emission, the hollow cathode lamp was turned on for 20 minutes or more before each measurement. The probing light beam from the source lamp was sent through the discharge at a distance of 25 mm from the upper quartz window and collected via collimating optics system at the opposite side of the chamber and then guided into a 500 mm focal length spectrometer. A photo multiplier tube (H7155 Hamamatsu) was set on the spectrometer. A shutter system was used to block the light from the source lamp when only the plasma emission was recorded. The principle of the optical absorption spectroscopy is explained in

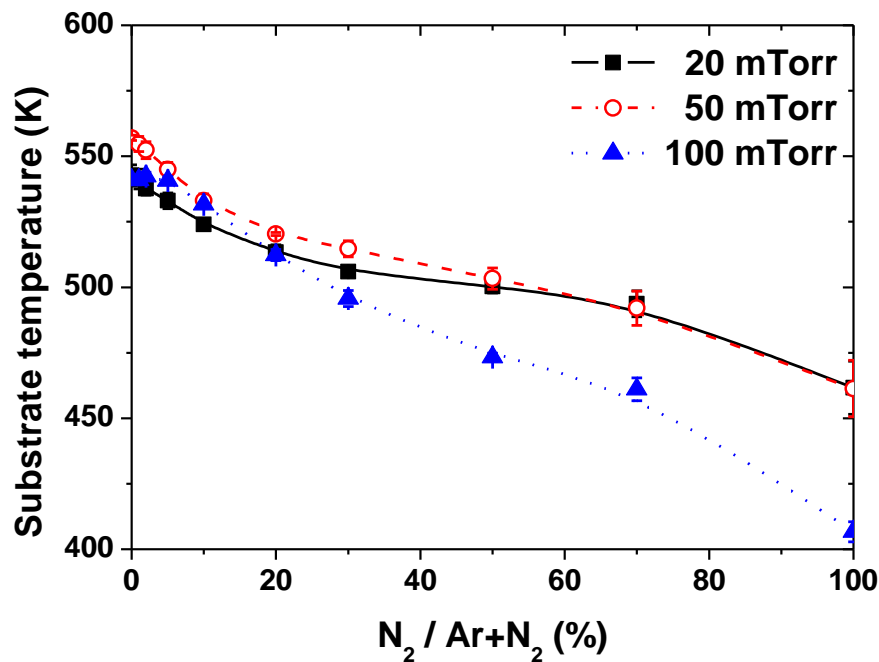


Figure 6.1 The measured substrate temperature by thermocouple in Ar- N_2 mixed discharge.

chapter 4.

In this study, to measure Ar(3p⁵4s) densities, the four spectral lines with wavelengths Ar 750.4nm, Ar 794.8nm, Ar 751.5nm and Ar 763.5nm were used for Ar(1s₂), Ar(1s₃), Ar(1s₄) and Ar(1s₅), respectively. The plasma line width ($\delta\sigma_{1/2}^P$) was calculated by taking a Doppler line profile which is the dominant line broadening in glow discharge at low gas pressure [11,12]. The Doppler line width was calculated from the equation:

$$\delta\sigma_D = 7.16 \times 10^{-7} \sigma_0 \left(\frac{T}{M} \right)^{1/2} \quad (6.1)$$

where $\sigma_0 = 1/\lambda_0$ (cm⁻¹) is the wavenumber at the center of the spectral peak, T is the plasma temperature in Kelvin, M (g/mol) is the atomic mass. In the present study, the temperatures of the plasma have been measured by thermocouple on the substrate. The measured substrate temperatures are reproduced in figure 6.1. We obtained 400 K in pure nitrogen discharge and 550 K in pure argon discharge. The temperature of the reference source has been estimated from the rotational structure of N₂ band [9]. Using this method, the temperature of the hollow cathode lamp was about 800 K.

6.2.3 Measurement of atomic nitrogen density by TALIF

The absolute atomic nitrogen density can be determined from the TALIF signals of both Kr and N when the relative detection sensitivity for the two species is known [13,14]. N and Kr atoms were detected by absorption of two photons at 206.65 nm and 204.13 nm producing fluorescence at 742-746 nm and 826 nm, respectively. The second harmonic of a Nd:YAG

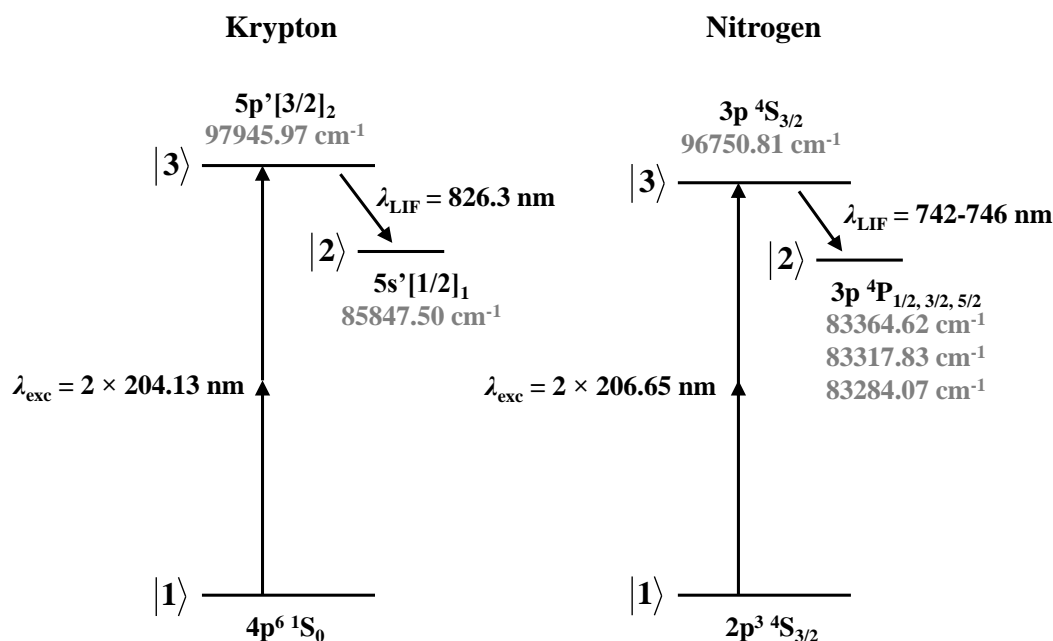


Figure 6.2 Simplified energy level diagrams of atomic nitrogen and krypton indicating the excitation scheme and the observed fluorescence wavelength.

laser (532 nm) was used to pump a dye laser producing laser emissions at 619 nm (or 612 nm). The dye laser beam output was then frequency tripled (two non-linear crystals BBO and KDP) to obtain 206.65 nm (or 204.13 nm for Kr). The laser beam was focused in the discharge chamber to ensure sufficient energy for TALIF. The fluorescence signal was collected perpendicularly to the laser beam through a two lens system and imaged onto a filter at the entrance of the photo multiplier tube. Schemes used for N and Kr atoms are reproduced in figure 6.2

The density of atomic nitrogen can be written:

$$n_N = n_{Kr} \frac{\sigma_{Kr}^{(2)}}{\sigma_N^{(2)}} \left(\frac{\nu_N I_{Kr}}{\nu_{Kr} I_N} \right)^2 \frac{A_{Kr} \tau_{Kr}}{A_N \tau_N} \frac{\theta_{Kr} \zeta_{Kr} G_{Kr}}{\theta_N \zeta_N G_N} \quad (6.2)$$

where S is the fluorescence signal, $\sigma^{(2)}$ is the two-photon absorption cross section, ν is the UV photon frequency, I is the laser energy, A is the Einstein transition probability for spontaneous emission, τ is the lifetime of the excited level, θ is the transmission of the optical detection system, ζ is the detector quantum efficiency and G is the detector amplification factor. The subscripts N and Kr refer to the TALIF measurement of atomic nitrogen and krypton, respectively. For the ratio of the two-photon excitation cross sections we have used the value determined by Niemi: $\sigma_{Kr}^{(2)} / \sigma_N^{(2)} = 0.67$ [13].

In the low pressure nitrogen glow discharge the photo multiplier tube was saturated by the strong emission of N I 746.8 nm. To avoid this problem we have used a RF generator

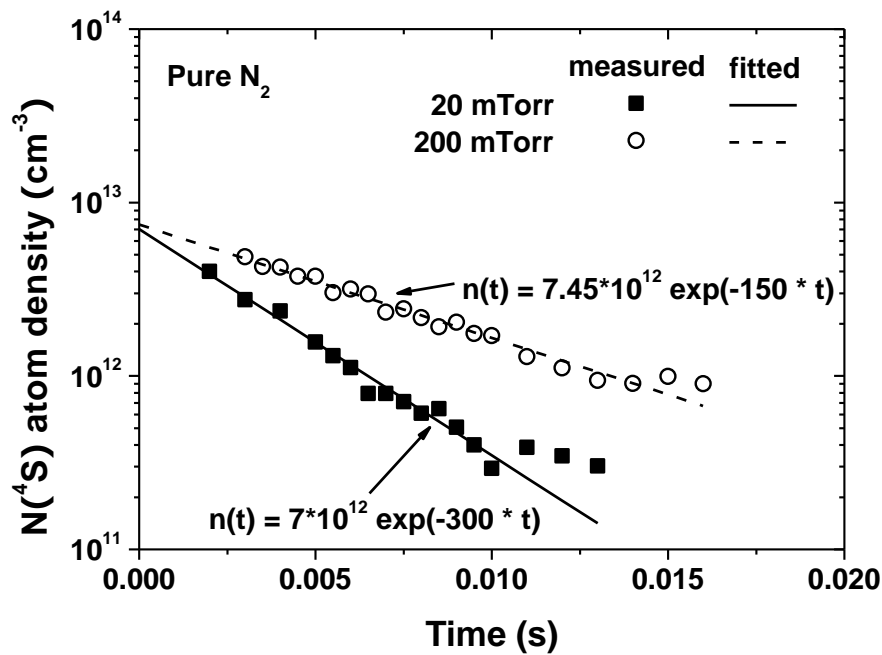


Figure 6.3 Time variation of absolute nitrogen atomic density during pulse-off period at 20 mTorr and 200 mTorr in the pure nitrogen discharge.

modulated by a square pulse with a frequency of 100 Hz, a duty ratio of 50 % and 200 Watt injected power. In the range of pressure investigated in the study, the dominant loss mechanism of atomic nitrogen is diffusion to the wall [15]. Therefore in the afterglow an exponential decrease of the atomic nitrogen density with time can be supposed as:

$$n(t) = n_{0,t=0} \exp(-k_{N,wall}t) \quad (6.3)$$

where n_0 is the density at pulse-on time and $k_{N,wall}$ is the diffusion loss rate. Figure 6.3 shows the time variation of absolute nitrogen atomic density during pulse-off period at 20 mTorr and 200 mTorr in the pure nitrogen discharge. The solid line is a fitting of the measured values. Using this method the absolute density of atomic nitrogen in the discharge has been estimated.

6.3 Discharge model

The species used in our discharge model are presented in Table 1. We assume that Ar consists of 12 energy levels: Ar ground state, 4 levels of Ar(3p⁵4s), Ar(4p), Ar(3d), Ar(5s), Ar(5p), Ar^{**} (highly excited) with two ions: Ar⁺ and Ar₂⁺. We suppose the excited states between Ar(3p⁵5p) and Ar⁺ as a block e.g. Ar^{**}. 9 levels of ground state N₂(X ¹Σ_g⁺, v = 0 ~ 8), 10 levels of excited state N₂(A ³Σ_u⁺), N₂(B ³Π_g), N₂(W ³Δ_u), N₂(B' ³Σ_u⁻), N₂(a' ¹Σ_u⁻), N₂(a ¹Π_g), N₂(w ¹Δ_u), N₂(C ³Π_u), N₂(E ³Σ_g⁺), N₂(a'' ¹Σ_g⁺) and 4 species for ions N₂⁺(X ²Σ_g⁺), N₂⁺(B ²Σ_u⁺), N₃⁺ and N₄⁺ are considered. In addition, N ground state, 2 levels of metastable state N(²D), N(²P) and N⁺ ion are considered. Finally the discharge model consists of 40 species with including electrons.

To calculate the electron temperature, the global model is used as shown in equation (3.2)-(3.20). We assume a cylindrical discharge chamber of radius $R = 10$ cm and length $L = 5$ cm. The ion-neutral species mean free path λ_i is calculated using equation (3.7) with collision cross section data [18-20], and the ion atom temperature is assumed to be the same as the gas temperature T_g .

The dynamics of species density n_j is described by the particle balance in equation (3.21). The list of species and reactions are converted automatically in a system of kinetic equations and solved numerically using ZDPlasKin tool [22]. The rate coefficients of all reactions are

Table 6.1 The species used in the discharge model.

Ground state	Excited state	Ions
Ar	Ar(1s ₅), Ar(1s ₄), Ar(1s ₃), Ar(1s ₂) Ar(4p), Ar(3d), Ar(5s), Ar(5p), Ar ^{**}	Ar ⁺ , Ar ₂ ⁺
N ₂ (X,v=0) ~ N ₂ (X,v=8)	N ₂ (A ³), N ₂ (B ³), N ₂ (W ³), N ₂ (B' ³), N ₂ (a' ¹), N ₂ (a ¹), N ₂ (w ¹), N ₂ (C ³), N ₂ (E ³), N ₂ (a'' ¹)	N ₂ ⁺ (X), N ₂ ⁺ (B), N ₃ ⁺ , N ₄ ⁺
N(⁴ S)	N(² D), N(² P)	N ⁺

calculated using build-in into the package BOLSIG+ solver. The reactions used in this study are summarized in table 6.2. The rate coefficient for the electron impact excitation from level j to level k , k_{jk} , is calculated using equation (3.22). Also the rate coefficients of de-excitation processes k_{kj} , are calculated by the principle of detailed balancing [21].

Figures 6.4(a) and 6.4(b) show the measured EEPFs at pressures of 20 mTorr and 100 mTorr as a function of N_2 fraction. In a pure argon discharge, the EEPFs are nearly Maxwellian below the inelastic collision thresholds with a slightly depletion of electrons for energy higher than 11.6 eV (the first excitation threshold for Ar). With increasing the nitrogen fraction in Ar- N_2 mixture a “hole” in the distribution is observed around 3 eV attributed to the presence of some resonant electron-molecule vibrational excitation mechanisms. This depletion at around 3 eV is observed as well at 20 mTorr but only in a pure nitrogen discharge. Even if at higher pressure, this depletion is clearly observed from 50 % of N_2 in the mixture, for a safe of simplicity we have assumed in the calculation that the EEDF is Maxwellian.

The radiative loss rate for decay from level k to level j is calculated using equation (3.24). The escape factor g_k depends on the density of the lower state in the radiative transition. But in the low pressure plasma the density of the excited level is enough low to neglect the escape factor, except for the $^3P_1-^1S_0$ ($\lambda = 1067\text{\AA}$) and the $^1P_1-^1S_0$ ($\lambda = 1048\text{\AA}$) resonance lines because of the radiative decay to the Ar ground level (R87). The calculated escape factor of these two resonance lines are calculated using equations (3.26)-(3.29) as shown in figure 3.1. The radiative decay transitions between the excited states (R88-R92) were calculated using the sum of the transition probabilities for the transitions between individual sublevels weighted with statistical weights of the upper sublevels.

The diffusion losses of the neutral species to the wall are estimated by an effective loss

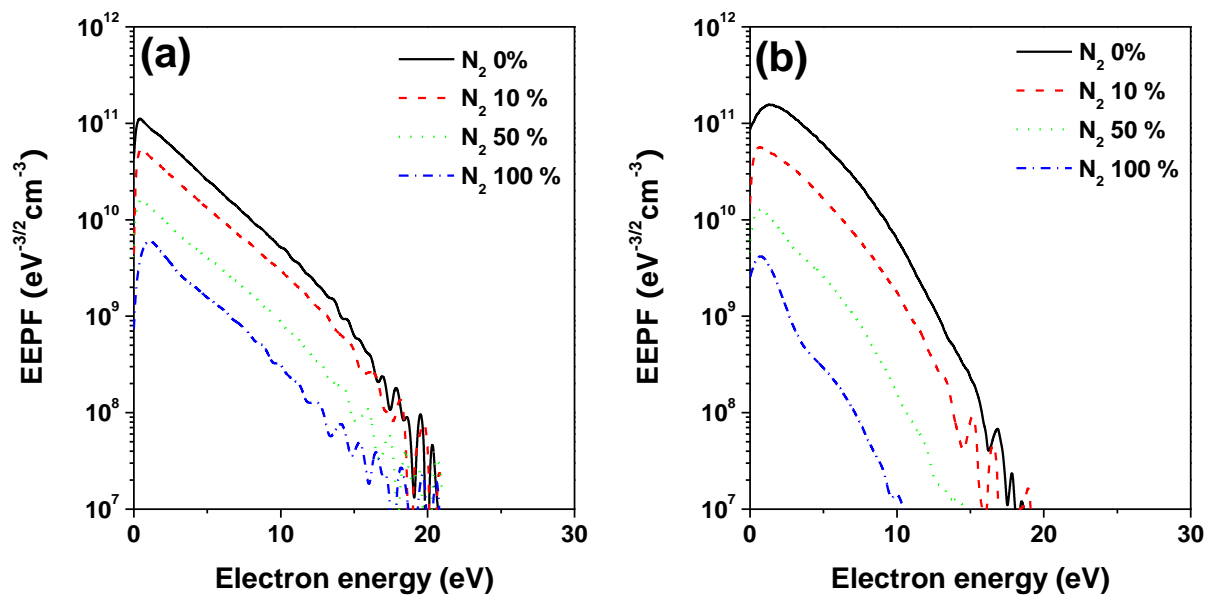


Figure 6.4 Measured EEPFs in Ar- N_2 discharges at (a) 20 mTorr and (b) 200 mTorr.

rate coefficient given by [26]:

$$k_{n,wall} = \left[\frac{\Lambda^2}{D_n} + \frac{2V(2-\gamma_n)}{A\bar{v}_n\gamma_n} \right]^{-1} \quad (6.4)$$

where D_n is the neutral diffusion coefficient and Λ is the effective diffusion length given by [27]:

$$D_n = \frac{kT_g\lambda_n}{\bar{v}_n M} \quad (6.5)$$

and

$$\frac{1}{\Lambda^2} = \left(\frac{\pi}{L} \right)^2 + \left(\frac{2.405}{R} \right)^2 \quad (6.6)$$

where k is the Boltzmann constant, $\bar{v}_n = (8kT_g/\pi M)^{1/2}$ is the neutral mean velocity, λ_n is the neutral-neutral species mean free path calculated from the neutral-neutral collision cross section data [18], γ_n is the sticking coefficient for the neutral particle on the wall surface, and V and A are the volume and the wall surface area of the reactor chamber. For the atomic argon excited states, the molecular nitrogen excited states and vibrational states of $N_2(X^1\Sigma_g^+)$

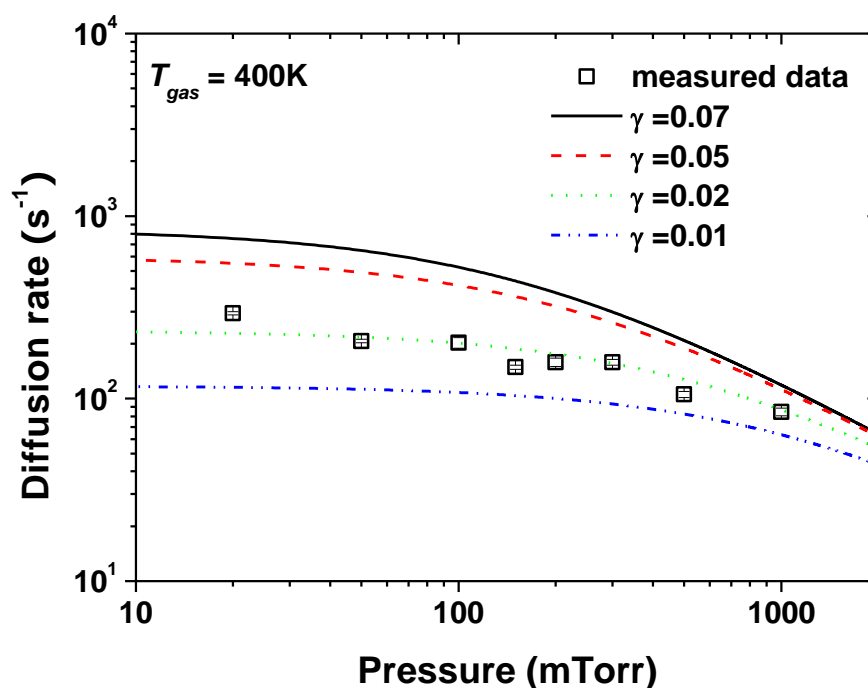


Figure 6.5 Measured and calculated diffusion loss rates of N atoms for various γ_n at 400 K gas temperature. The measured sticking coefficient is around 0.02.

a sticking coefficient equal to 1 was fixed. For atomic nitrogen we estimated the sticking coefficient using measured effective diffusion loss rates in pulse mode. Figure 6.5 shows the measured diffusion loss rate using the TALIF method as shown in figure 6.3 and the calculated diffusion loss rate using eq. (6.4) for various γ_n at 400 K gas temperature. The measured sticking coefficient is around 0.02 which is lower but on the same order of magnitude than other papers [19,28]. This lower value can be explained by the fact that in our set-up one third of the surface is glass. It is known that nitrogen sticking coefficient is much lower on glass than on stainless steel or pure metals [29].

The loss by pumping for species j can be calculated by $R = 1.378 \times 10^1 \times Q_{in} n_j / pV$ where Q_{in} is total gas flow into the chamber in sccm, n_j is the density of species j in cm^{-3} , p is pressure in Torr, and V is the discharge volume in cm^3 [19].

The power balance equation and the particle balance equation are solved by ordinary differential equation solver based on the Runge-Kutta method. The flow chart of calculation algorithm is shown in Figure 6.6. First we fix the initial electron temperature and initial density of all species including electron density. To calculate the electron temperature the global model is used to solve the power balance equation with absorbed power fixed at 160 Watt e.g. we assume that the power transfer efficiency is 80 %. Once the electron temperature is determined, the densities of all species are calculated by the particle balance equation using ZDPlasKin tool. Finally the vibrational temperature of $\text{N}_2(X^1\Sigma_g^+)$ is

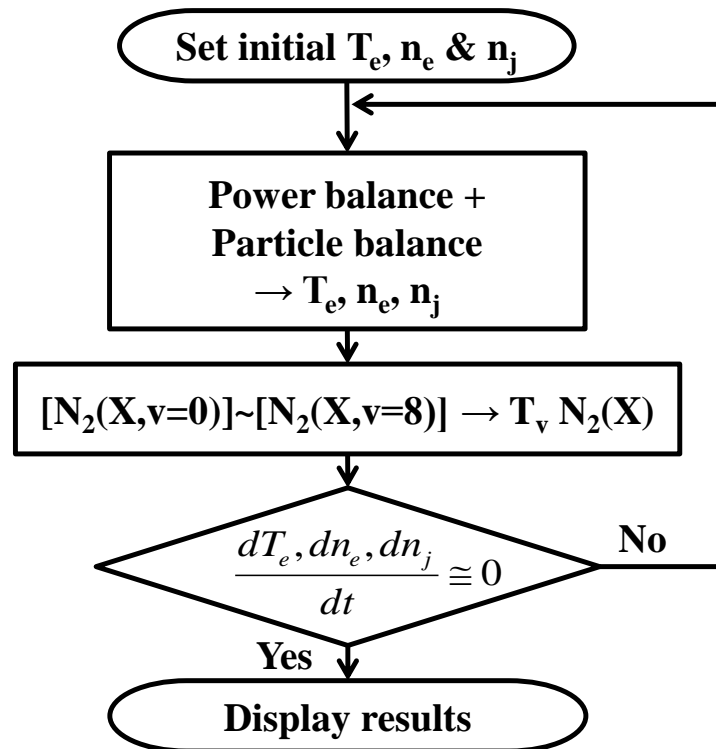


Figure 6.6 Flow chart of calculation algorithm.

determined from the calculated densities of $N_2(X, v = 0 \sim 8)$ using a Boltzmann distribution [30]:

$$[N_2(X, v)] = [N_2(X, v = 0)] \exp\left(-\frac{E_v}{kT_v}\right) \quad (6.7)$$

where $[N_2(X, v)]$ is the population of excited level v and E_v is the energy of the vibrational level. This calculated vibrational temperature of $N_2(X^1\Sigma_g^+)$ is used to determine the reaction coefficient [31] of charge exchange $Ar^+ + N_2 \rightarrow N_2^+ + Ar$ (R108). This process is repeated until the densities of all species and the electron temperature reach the steady state.

6.4 Results and discussion

6.4.1. Pure nitrogen discharge

Figure 6.7(a) shows calculated (solid line) and measured (solid square) electron temperature and calculated (dotted line) and measured (open circle) electron density versus pressure at a fixed RF power in a pure nitrogen discharge. For the electron temperature assuming the error bars for experimental results estimated to 20%, a very good agreement is found between calculated and measured values. As the electron temperature is deduced from the balance between the production of electrons by ionization of the gas and the loss of electrons on the walls, increasing the pressure decreases electron diffusion to the walls and subsequently the electron temperature.

Calculated electron densities are two times lower than measured values but exhibit the same decrease with pressure. This behavior is the opposite behavior observed in an argon discharge where the electron density increases with pressure. The central electron density is determined in the steady state by balancing the total absorbed power to the total power loss:

$$n_e = \frac{P_{abs}}{eu_B(T_e) [\varepsilon_c(T_e) + \varepsilon_e(T_e) + \varepsilon_i(T_e)] [h_L(T_e)A_L + h_R(T_e)A_R]} \quad (6.8)$$

We note that n_e is a function of pressure through the dependence of T_e with pressure as discussed before. For a given T_e , all those parameters do not depend on the gas nature except for ε_c , the collisional energy losses per electron-ion pair created. Indeed for molecular gases, in addition to excitation and direct ionization, ε_c includes molecular dissociation, vibrational and rotational energy levels. Figure 6.7(b) shows the evolution of ε_c versus T_e for Ar and N_2 . We observe that for T_e lower than 5 eV collisional energy lost per electron-ion pair created ε_c is much more important than the energy lost per electron and ion lost at the walls $\varepsilon_e + \varepsilon_i$. As Bohm velocity u_B , h_L and h_R depends on the square root of T_e we can therefore write:

$$n_e \propto \frac{P_{abs}}{T_e \varepsilon_c(T_e)} \quad (6.9)$$

For a constant absorbed power, the evolution of the plasma density depends only on the

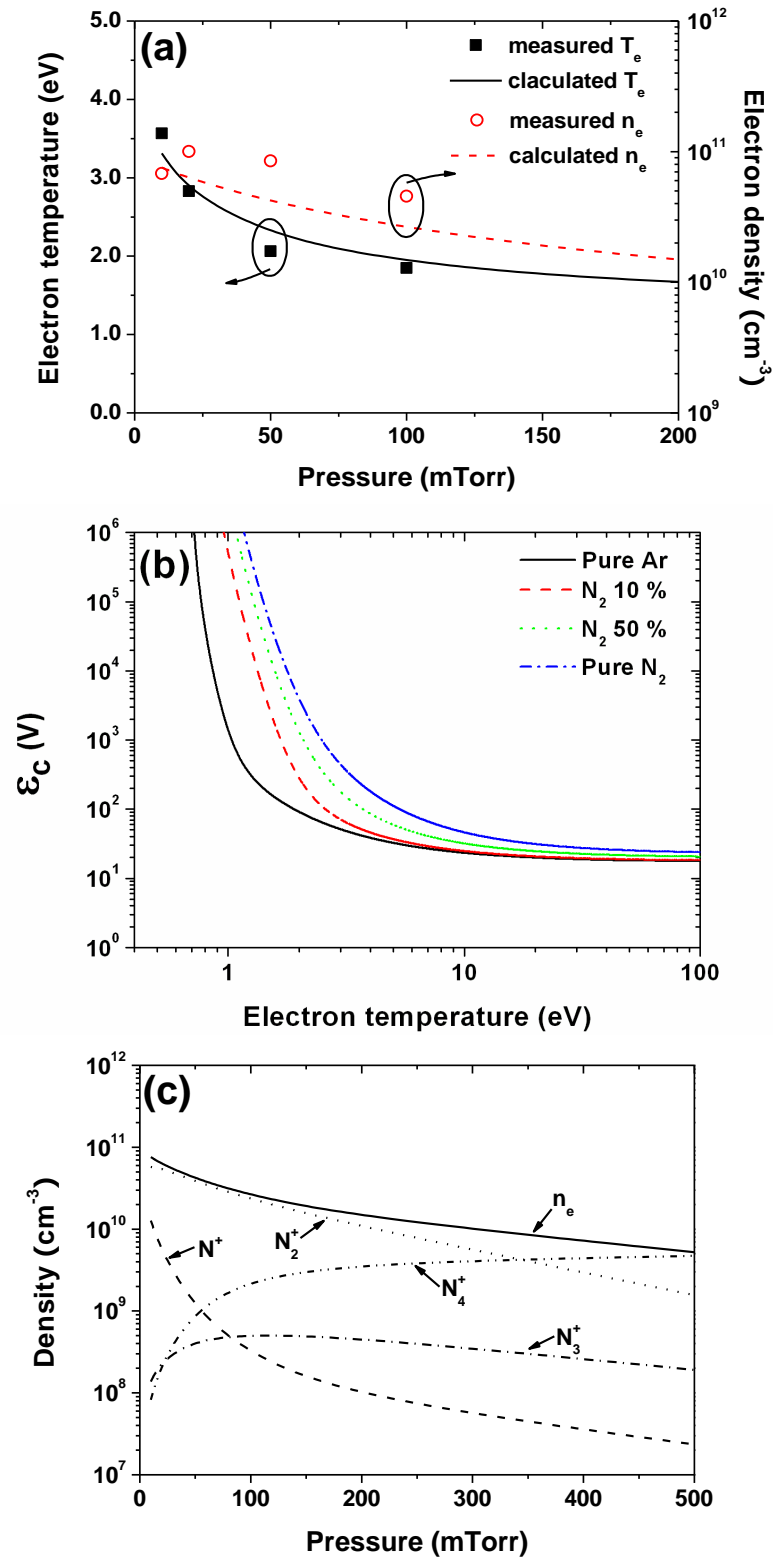


Figure 6.7 (a) Calculated and measured electron temperature and electron density, (b) calculated collisional energy loss per electron-ion pair created versus electron temperature assuming a Maxwellian electron energy distribution, and (c) calculated charged particle densities versus pressure at fixed RF power in pure nitrogen discharge.

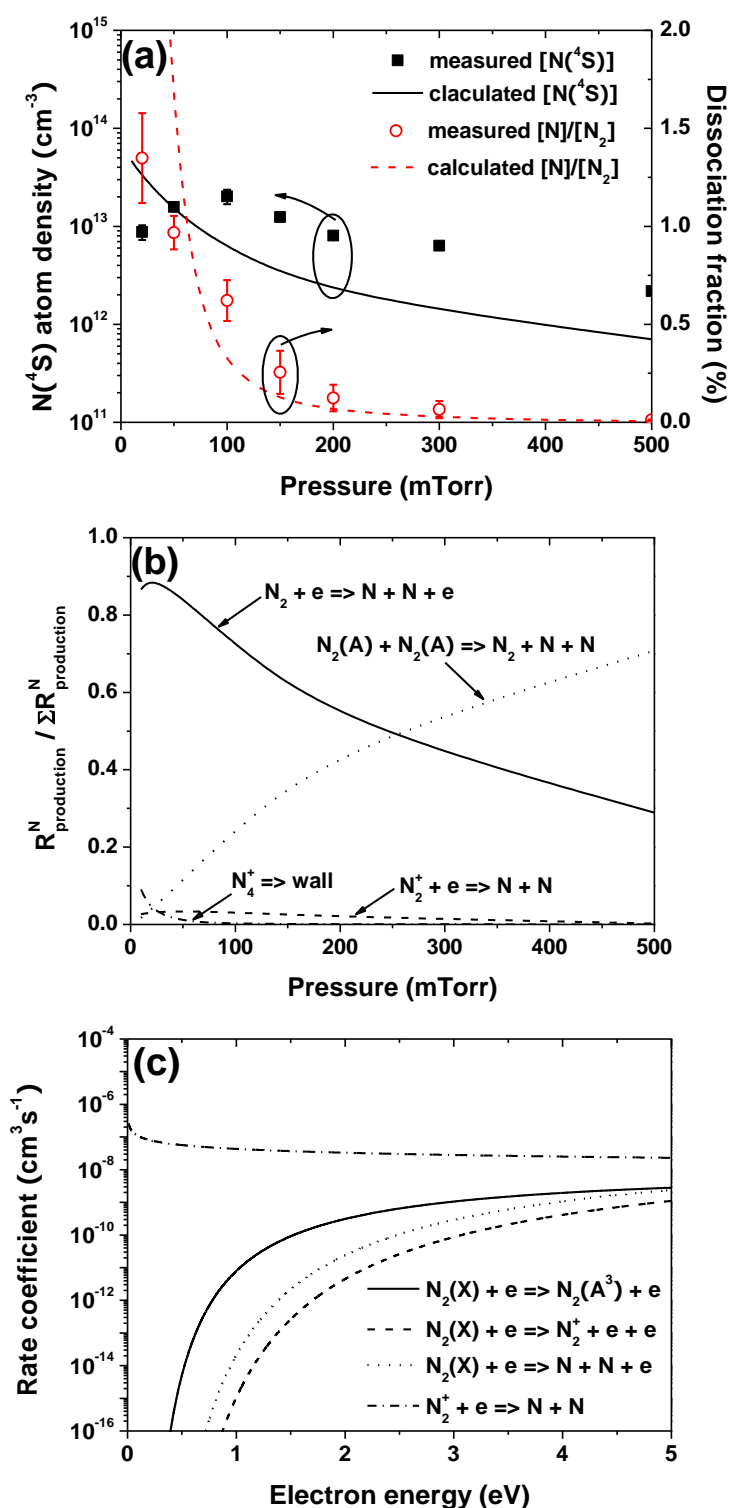
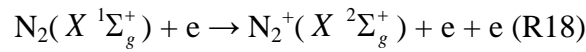


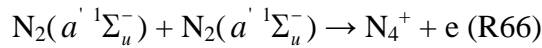
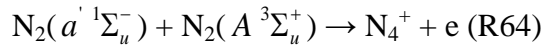
Figure 6.8 (a) Calculated and measured absolute N atom density and dissociation fraction, (b) calculated relative production rates for creation of N atoms, and (c) calculated rate coefficients of electron impact excitation to $N_2(A^3\Sigma_u^+)$, electron impact ionization, electron impact dissociation and electron-ion dissociative recombination as function of mean electron energy.

evolution of the product $T_e \varepsilon_c(T_e)$. The fast increase of ε_c with decreasing T_e (or increasing the pressure) in N_2 discharge may therefore lead to a decrease of n_e versus pressure even if all the other parameters on the denominator decrease with decreasing T_e . In addition, from the calculation, we see that the vibrational state densities of $N_2(X^1\Sigma_g^+)$ increase with increasing the pressure (from $1.2 \times 10^{13} \text{ cm}^{-3}$ at 10 mTorr to $7.3 \times 10^{14} \text{ cm}^{-3}$ at 500 mTorr for $v = 1$).

The charged particle densities are shown in figure 6.7(c). The electron density calculated from the particle equation is equal to the summation of all charged particle density. The N_2^+ ion is dominant for pressure lower than 350 mTorr whereas at high pressure N_4^+ becomes dominant. From simulation we see that N_2^+ is mainly created by the ground state electron impact ionization through:

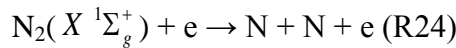


The production rate via (R18) represents more than 90 % of the total N_2^+ production rate in the pressure range under study and increases with the electron temperature. For N_4^+ production at low pressure the metastable-metastable pooling ionization processes are the most dominant:

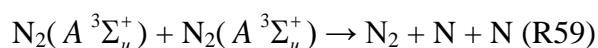


At higher pressure the three body ionization process $N_2^+ + N_2 + N_2 \rightarrow N_4^+ + N_2$ (R83) reaches about 50 % of the total production which becomes comparable with the metastable-metastable pooling ionization processes. The enhancement of this last process (R83) as well as the decrease of the electron temperature (R18) may explain the decrease of N_2^+ ion density with increasing pressure even if the density of vibrational states of $N_2(X^1\Sigma_g^+)$ increases and recombination to the walls decreases. With decreasing the pressure the atomic ion N^+ density increases more rapidly than N_3^+ and N_4^+ densities. Indeed, at low pressure N^+ is mainly created by electron impact ionization from ground state $N(^4s)$ (R25). This reaction is enhanced at low pressure because of higher electron temperature and higher density of atomic nitrogen.

Figure 6.8(a) shows the calculated and measured absolute N atom density by TALIF and the dissociation fraction $[N]/[N_2]$ versus pressure in a pure nitrogen discharge. The calculated N atom density shows reasonable agreement with measured value using TALIF, although the behavior is different for pressures lower than 100 mTorr as previously reported by other authors but unfortunately never explained [19,32]. The relative production rates for the creation of N atoms are shown in figure 6.8(b). For pressure lower than 300 mTorr N atoms are mainly created by electron impact dissociation through:



whereas at higher pressure the metastable-metastable pooling becomes the dominant production source for N atoms:



The maximum relative production rate of N atoms by the N^+ wall recombination is 5 % at 10 mTorr and can be neglected at higher pressure. The ion-electron recombination reactions $\text{N}_2^+ + e \rightarrow \text{N} + \text{N}$ (R39, R40, R41) are always lower than 5 % of the total production rate. We will see further its importance in Ar- N_2 discharge. Figure 6.8(c) shows the calculated rate coefficients of electron impact excitation leading to $\text{N}_2(A^3\Sigma_u^+)$, electron impact ionization, electron impact dissociation and electron-ion dissociative recombination as a function of the mean electron energy. The rate coefficients of electron impact are sensitive to the electron energy in the range below 3.0 eV while the rate coefficient of electron-ion dissociative recombination is almost constant. As the electron temperature is reduced from 3.5 eV at 10 mTorr to 1.8 eV at 200 mTorr, we can see from figure 6.8(c) that the rate coefficient for $\text{N}_2(X^1\Sigma_g^+) + e \rightarrow \text{N} + \text{N} + e$ reaction strongly decreases (2 orders of magnitude) while the rate coefficient for the production of $\text{N}_2(A^3\Sigma_u^+)$ is less affected (1 order of magnitude lower). Thus, at high pressure the metastable-metastable pooling dissociation (R59) becomes dominant for the production of N atoms because of (i) a relatively small decrease of the rate coefficient for excitation reaction from $\text{N}_2(X^1\Sigma_g^+)$ to $\text{N}_2(A^3\Sigma_u^+)$ compared to the decrease of the rate coefficient for electron impact dissociation on $\text{N}_2(X^1\Sigma_g^+)$ and (ii) a lower diffusion loss rate of $\text{N}_2(A^3\Sigma_u^+)$.

6.4.2 Ar- N_2 discharge

6.4.2.1 Electron temperature and charged particles density

Figures 6.9(a) and 6.9(b) show calculated and measured electron temperature and electron density respectively as a function of N_2 fraction for three different pressures (20 mTorr, 50 mTorr and 200 mTorr). In Ar- N_2 discharge the electron temperature is relatively constant with varying the percentage of nitrogen in the mixture. At 200 mTorr the calculated electron temperature is in very good agreement with measured data while the simulation gives lower values than measurements for lower pressures. Measured and calculated electron densities are in good agreement whatever the pressure except at high percentage of nitrogen. We note that with increasing the nitrogen fraction the electron density decreases and the slope is steeper with increasing the pressure.

Figures 6.10(a) and 6.10(b) show the calculated density of the charged particles versus N_2 fraction for 20 mTorr and 200 mTorr respectively. The electron density is equal to the summation of all charged particle densities. At 20 mTorr Ar^+ is the dominant ion up to 40 % of N_2 and N_2^+ ion density increases with N_2 fraction in the mixture. At 200 mTorr Ar^+ ion density decreases exponentially with N_2 addition and becomes lower than the density of N_2^+ from 10 % of N_2 . This strong decrease cannot be explained only by the dilution of Ar in N_2 . Figure 6.10(c) shows the calculation of the relative loss rates of Ar^+ by ambipolar diffusion (R114) and charge transfer between Ar^+ and N_2 (R108). At 20 mTorr, the diffusion loss is the

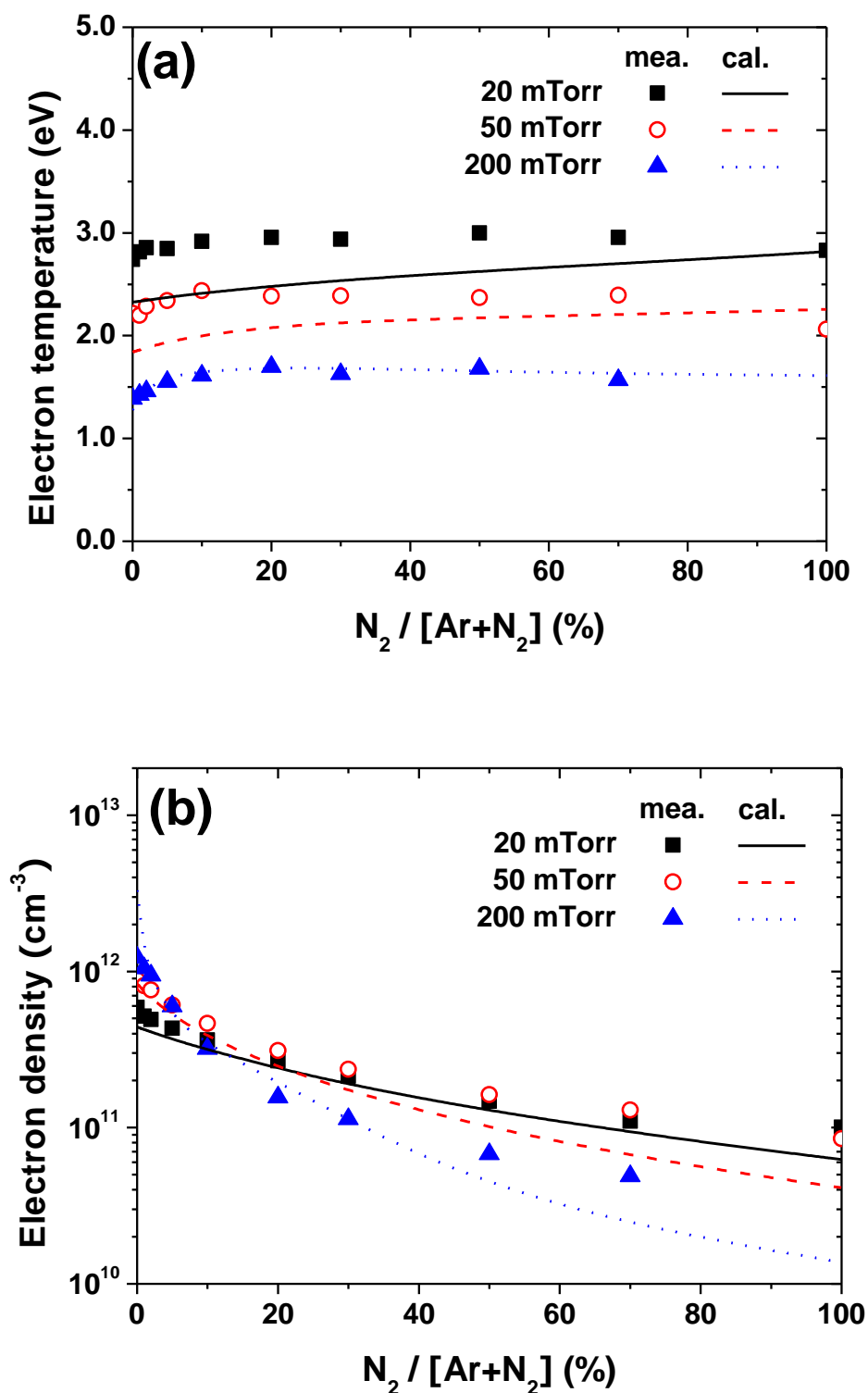


Figure 6.9 Calculated and measured (a) electron temperature and (b) electron density as a function of the N_2 fraction at 20 mTorr, 50 mTorr and 200 mTorr.

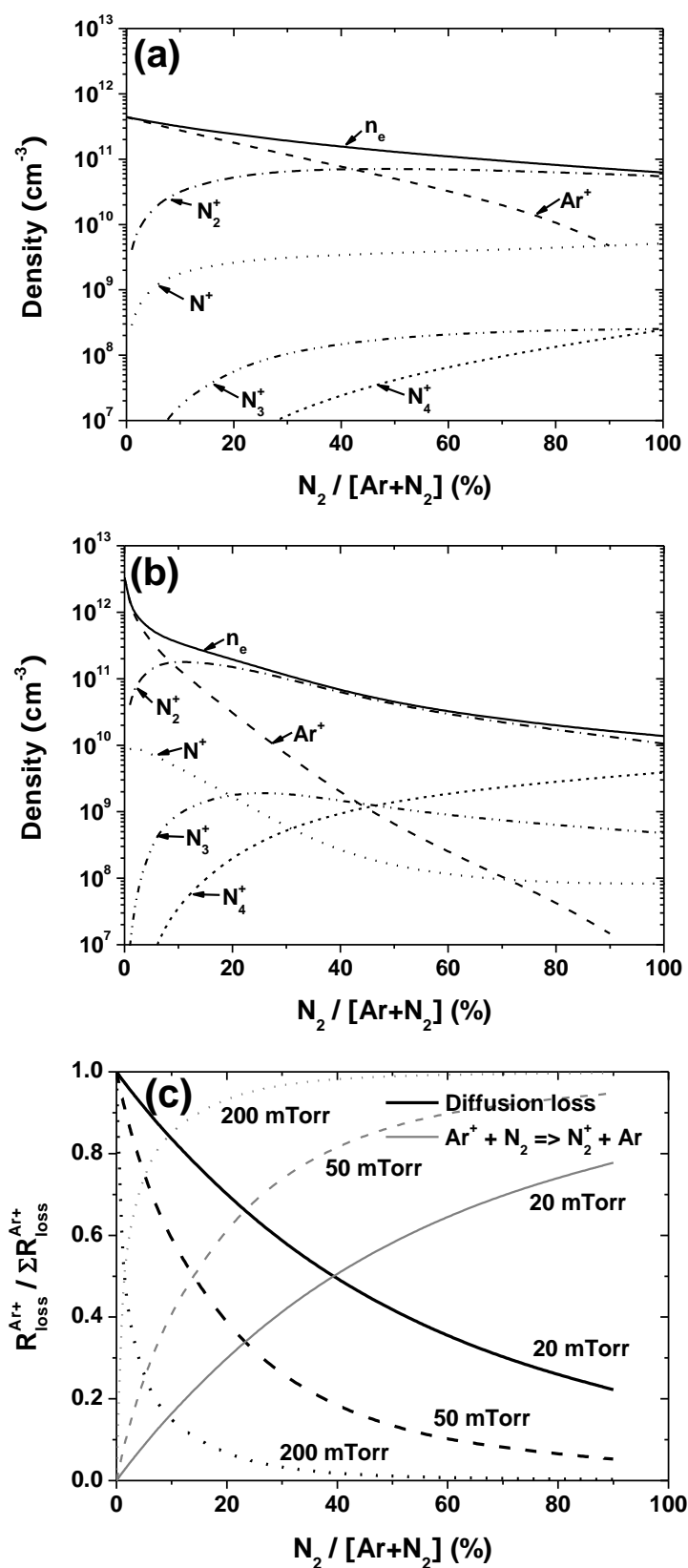


Figure 6.10 Calculated density of charged particles versus N_2 fraction at (a) 20 mTorr, (b) 200 mTorr and (c) relative loss rates of Ar^+ by the ambipolar diffusion (R114) and the charge transfer between Ar^+ and N_2 (R108) at 20 mTorr, 50 mTorr and 200 mTorr.

dominant process in the range 0 % - 40 % of N₂. With increasing the pressure the diffusion loss decreases steeply with N₂ addition because of both (i) the strong pressure dependence of diffusion processes and (ii) the increase of the charge exchange loss with pressure. Indeed, the reaction coefficient of the charge transfer process depends strongly on the vibrational temperature (T_V) of N₂($X^1\Sigma_g^+$). From calculation, T_V is about 6,000 K whatever the gas mixture at 20 mTorr, while it increases from 6,000 K in pure nitrogen discharge to 10,000 K at 1 % of N₂ at 200 mTorr.

6.4.2.2 Ar(3p⁵4s) density

Figures 6.11(a) and 6.11(b) show the calculated and measured metastable state Ar(1s₅) and resonance state Ar(1s₄) atom densities versus N₂ fraction at 20 mTorr, 50 mTorr and 200 mTorr. Results from calculation exhibit the same behavior than the measured data. The decrease of the metastable density with decreasing argon in the mixture is much more pronounced when increasing the pressure. The population and de-population of Ar(1s₅) and Ar(1s₄) in pure argon discharge are related with the electron temperature, the electron density, the radiative decay, the diffusion loss and collisions with other particles [33,34]. On the other hand, the excitation transfer between Ar(4s) and the nitrogen molecule plays a dominant role of Ar(4s) de-population in Ar-N₂ discharges as discussed further.

6.4.2.3 Production of N₂($C^3\Pi_u$) excited molecules

The measured emission intensity of the N₂($C^3\Pi_u$)-N₂($B^3\Pi_g$) transition at $\lambda = 337.1$ nm and the calculated N₂($C^3\Pi_u$) density versus N₂ percentage are shown in figure 6.11(c). The results from calculation exhibit the same behavior than the experimental data. We note the slight decrease with increasing the percentage of N₂ at 200 mTorr. The N₂($C^3\Pi_u$) state is created through the following reactions:

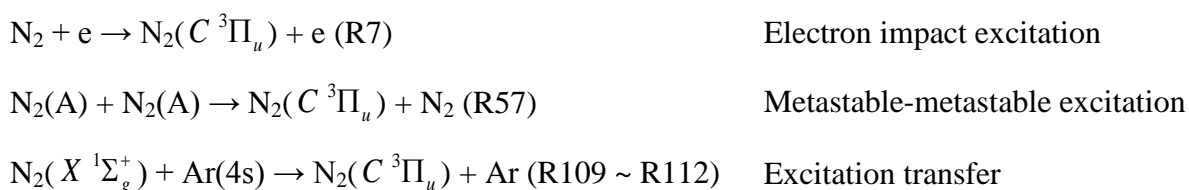


Figure 6.11(d) depicts the change of the relative production rates of N₂($C^3\Pi_u$) for 20 mTorr (black line) and 200 mTorr (lighter line) for the three reactions listed above. At 20 mTorr the electron impact excitation represents more than 90 % of the total production rate whatever the mixture because of both (i) the relatively low threshold energy of this reaction and (ii) the high electron temperature at low pressure. On the contrary, the excitation transfer reaction increases up to 40 % in highly N₂-diluted mixture at 200 mTorr. This reaction is controlled by both N₂ and Ar(4s) densities in the discharge. As Ar(4s) density (see figures 6.11(a) and 6.11(b)) exhibits an exponential decrease with increasing N₂ percentage, the production of

$N_2(C^3\Pi_u)$ by this reaction decreases. Metastable-Metastable excitation process increases with N_2 addition because of the increase of the $N_2(A)$ metastable density. This is consistent with the increase of N_4^+ density observed in figure 6.10(b) through the reaction (R58).

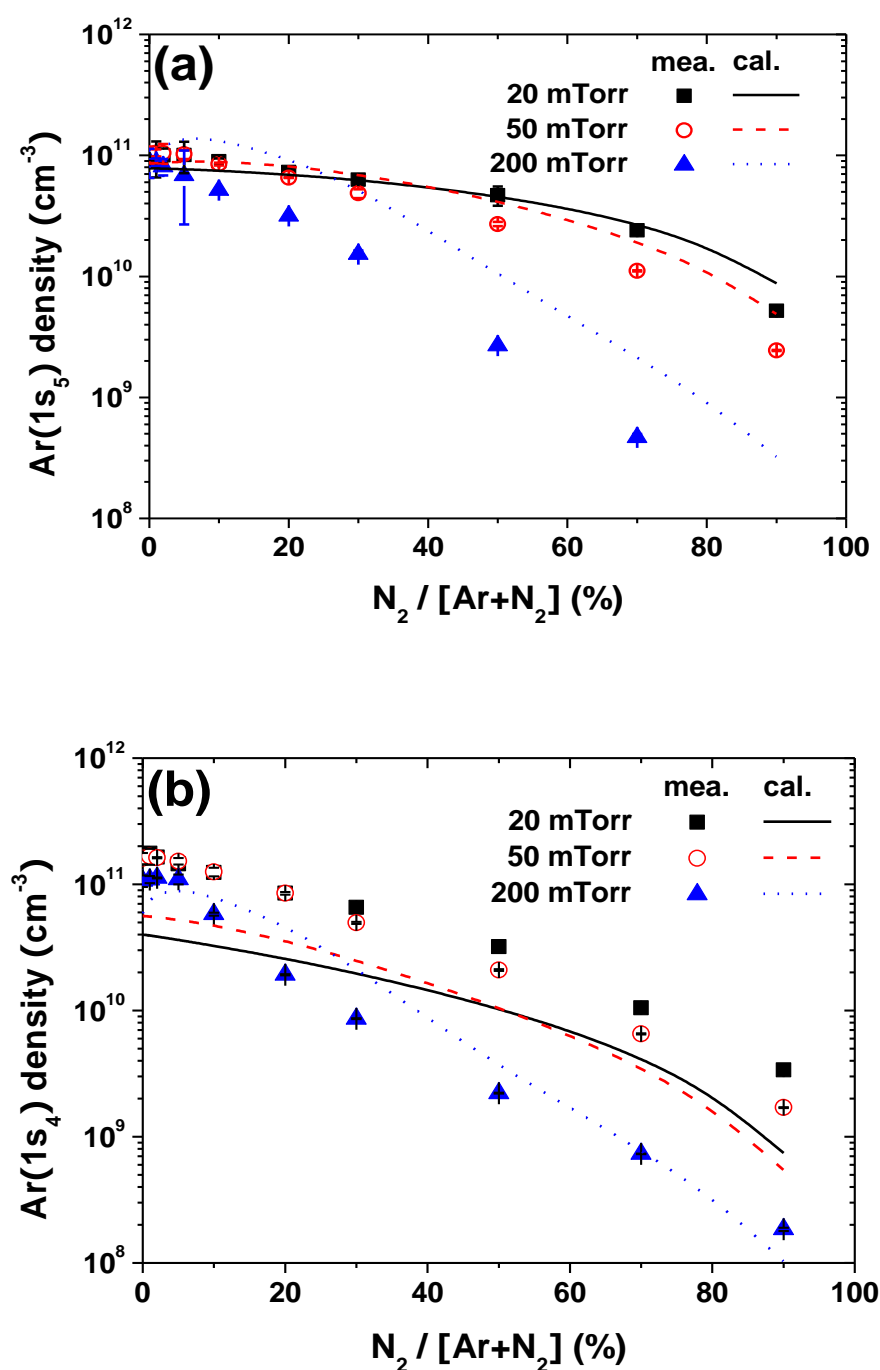


Figure 6.11 Calculated and measured (a) metastable state $Ar(1s_5)$, (b) resonance state $Ar(1s_4)$ atom densities.

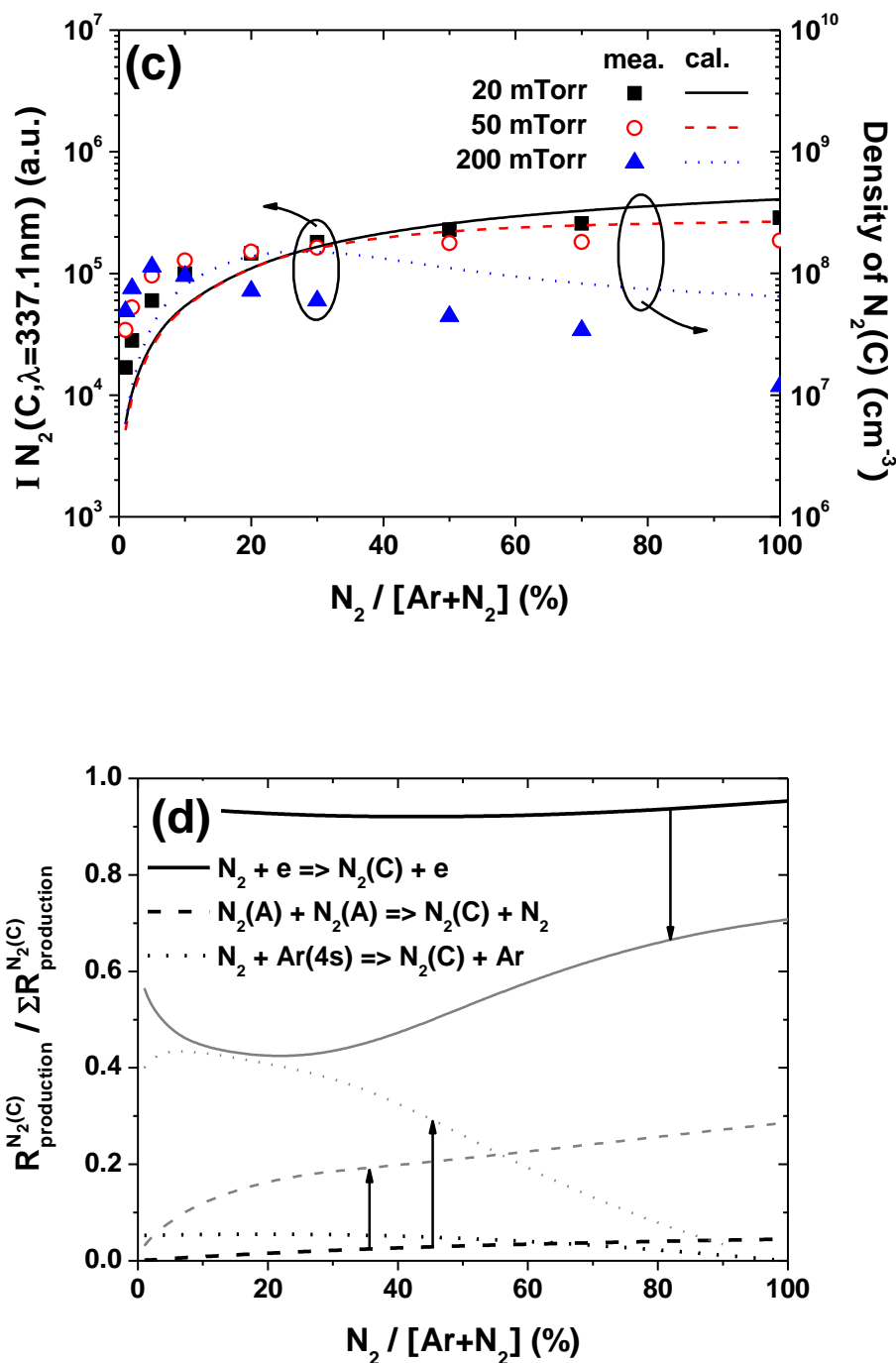
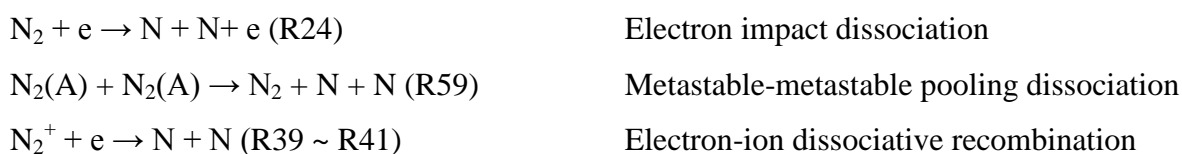


Figure 6.11 (c) Measured emission intensity of $N_2(C^3\Pi_u) \rightarrow N_2(B^3\Pi_g)$ and calculated density of $N_2(C^3\Pi_u)$ versus N_2 fraction at 20 mTorr, 50 mTorr and 200 mTorr. (d) Change of relative production rates from 20 mTorr (black line) to 200 mTorr (lighter line) of $N_2(C^3\Pi_u)$ by electron impact excitation (R7), metastable-metastable excitation (R57) and excitation transfer (R109 ~ R112).

6.4.2.4 Production of N(⁴S)

Figures 6.12(a) and 6.12(b) show the measured and calculated absolute N atom density and the dissociation fraction as a function of N₂ percentage at 20 mTorr, 50 mTorr and 200 mTorr. The calculated N atom density is in relatively good agreement with the measured value obtained by TALIF. In the experiment at 20 mTorr with increasing N₂ percentage from 1 % to 100 % we observe an increase of the absolute N atom density from $5 \times 10^{11} \text{ cm}^{-3}$ to $1 \times 10^{13} \text{ cm}^{-3}$ while at 200 mTorr the density reaches a maximum value ($2 \times 10^{13} \text{ cm}^{-3}$ at 5 % of N₂) and then decreases slightly. In the pure nitrogen discharge the dissociation rates [N]/[N₂] are 1.4 %, 0.8 % and 0.1 % at 20 mTorr, 50 mTorr and 200 mTorr, respectively. In addition, the dissociation rate reaches more than 18 % at 200 mTorr - 1 % N₂. Figures 6.12(c) and 6.12(d) show the calculated relative production rate of N atoms by wall recombination of N⁺ (R120) and by the following processes at 20 mTorr and 200 mTorr, respectively:



The relative production rate of the electron impact dissociation increases from 30 % to 90 % of the total production when the N₂ fraction varies from 1 % to 100 % at 20 mTorr because the N₂ density increases faster than the electron density decreases (see figure 6.10(a)). At the same time, the dissociative recombination decreases from 60 % to 5 % mainly because of the electron density decrease.

On the opposite, the dissociative recombination is a dominant production source for N atoms when the N₂ mixing ratio is 1 % ~ 40 % at 200 mTorr. The increase of N₂⁺ density in highly Ar-diluted region is explained by the charge exchange between Ar⁺ and N₂(X) as shown in the figure 6.10(c). When increasing the N₂ mixing ratio, the relative production rate of metastable-metastable pooling dissociation is comparable to the electron impact dissociation due to high N₂(A ³Σ_u⁺) density. From the model, the main production process of N₂(A ³Σ_u⁺) is the electron impact excitation and radiative decay from N₂(B ³Π_g) whatever the pressure. As shown in figure 6.11(d) the excitation transfer between Ar(4s) and N₂(X) at 200 mTorr leading to N₂(C ³Π_u) contributes indirectly to the N₂(A ³Σ_u⁺) production through the following cascading radiative decay reaction, N₂(C ³Π_u) → N₂(B ³Π_g) → N₂(A ³Σ_u⁺).

As a result, we conclude that the dissociation of N₂ molecule in Ar-N₂ mixed discharge occurs mainly by the electron impact dissociation at low pressure, while in high pressure the dissociative recombination is enhanced by charge transfer between Ar⁺ and N₂(X), as well as the metastable-metastable pooling dissociation due to high N₂(A ³Σ_u⁺) density caused by excitation transfer between Ar(4s) and N₂(X).

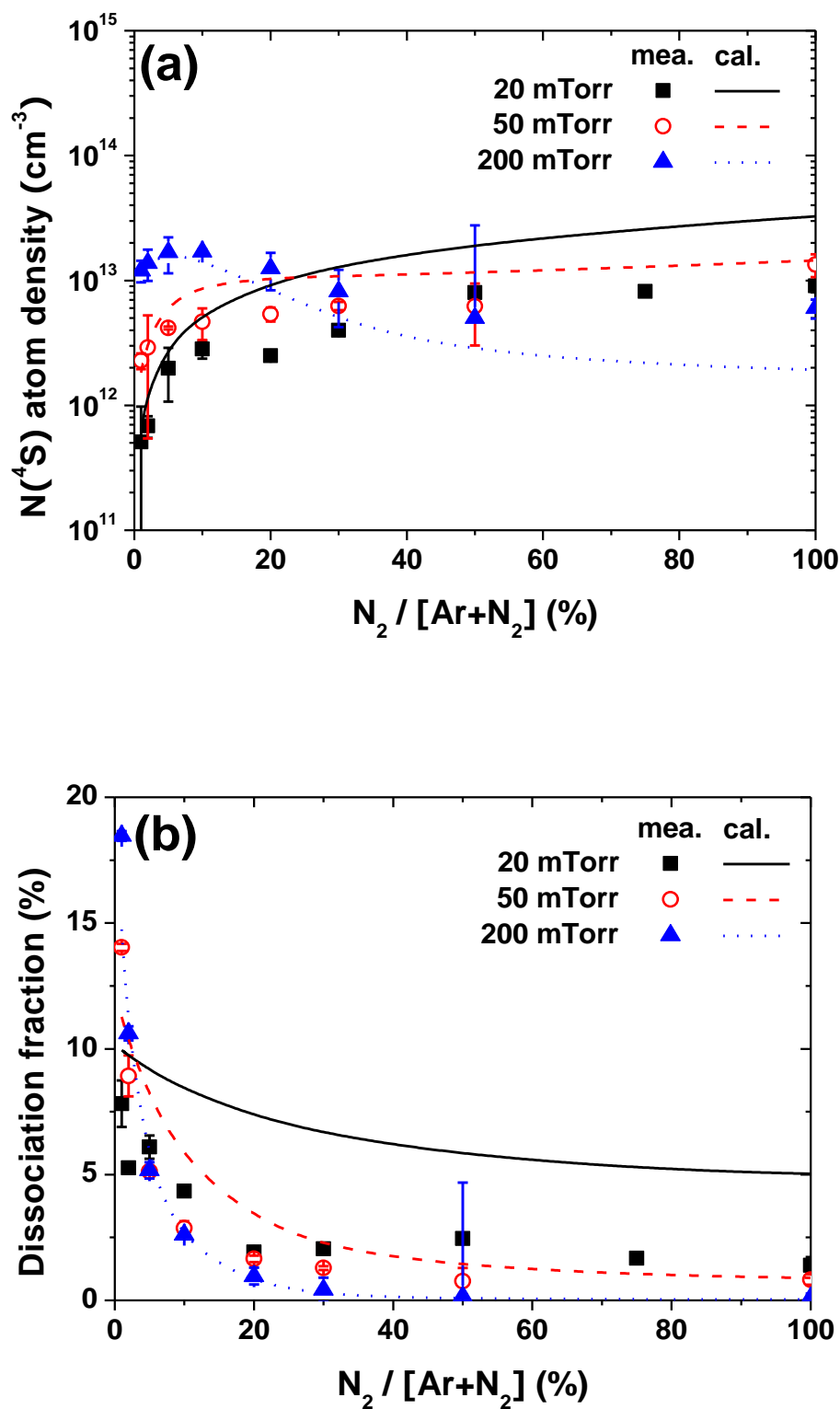


Figure 6.12 Calculated and measured (a) absolute N atom density and (b) dissociation fraction function of N_2 mixing ratio at 20mTorr, 50 mTorr and 200 mTorr.

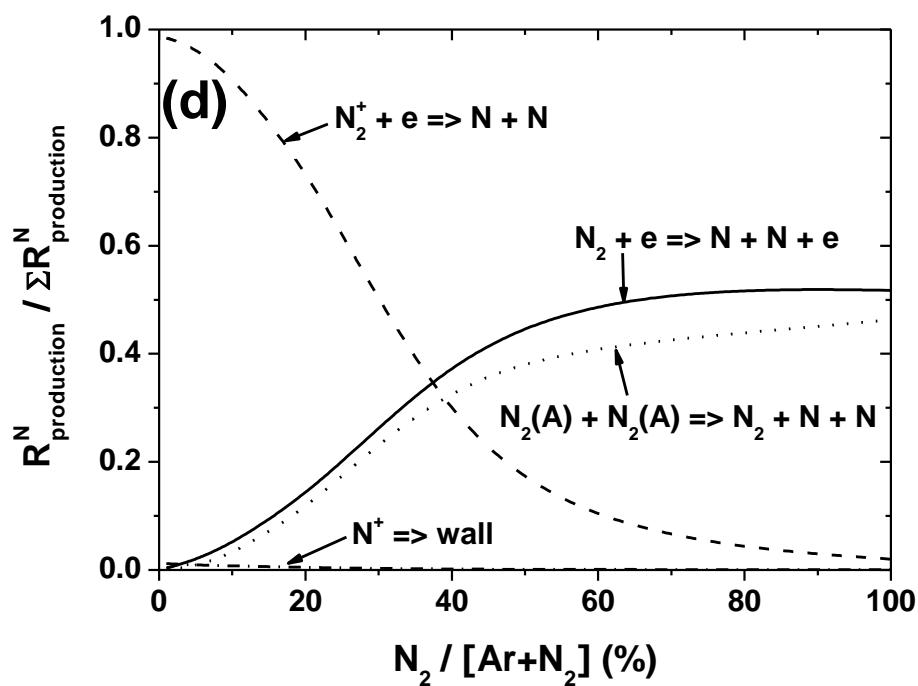
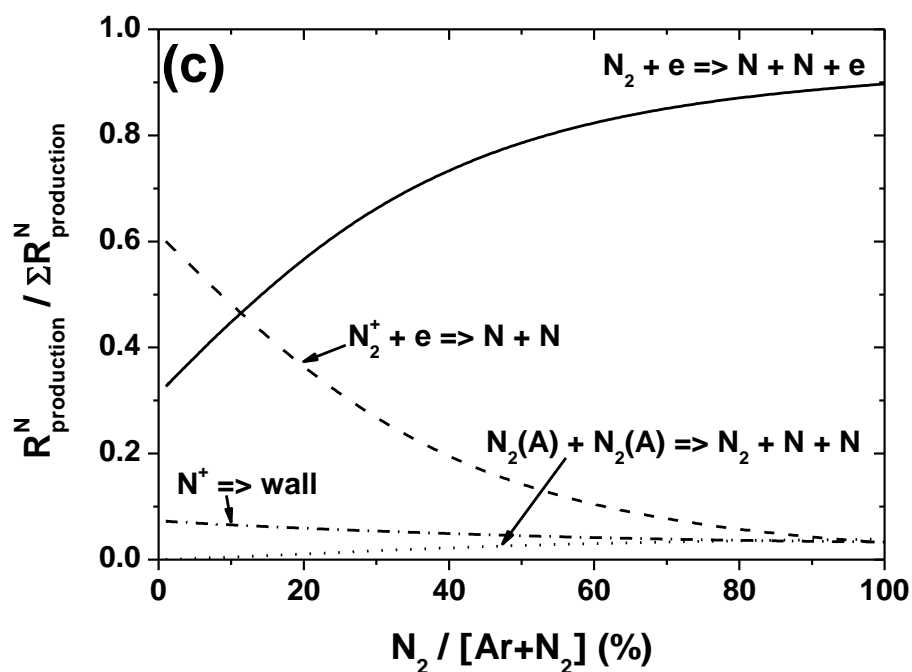


Figure 6.12 Calculated relative production rate of N atoms at (c) 20 mTorr and (d) 200 mTorr.

6.5 Conclusion

The dissociation of the nitrogen molecule in an Ar-N₂ ICP discharge was studied both experimentally and theoretically. The measured electron temperature is almost constant, while the electron density decreases with N₂ fraction whatever the pressure. An increase of the dissociation rate is observed experimentally in highly Ar-diluted region using TALIF. A global (volume averaged) model was developed to understand the behavior of the Ar-N₂ discharge. In the model, 311 reactions are taken into account. The variation of the electron temperature and the particle densities were calculated by solving the particle and energy balance equations. The calculated results were compared with the measured results, obtaining reasonably good agreement. In pure nitrogen discharge the N atoms are mainly created by electron impact dissociation at low pressure (20 mTorr) while it is due to metastable-metastable pooling dissociation at high pressure (200 mTorr). In Ar-N₂ discharge, the N atom density increases despite less amount of N₂ molecule in highly Ar-diluted region at 200 mTorr. From the model we found that charge transfer from Ar⁺ to N₂ is an important source of nitrogen dissociation in Ar-N₂ discharge.

Table 6.2 Reaction set used in the discharge model.

Process	Rate coefficient k (cm^3s^{-1} , cm^6s^{-1} , s^{-1})	References
Electron impact moment transfer		
R1 $\text{Ar} + e \rightarrow \text{Ar} + e$	B.E.	[35]
R2 $\text{N}_2(X^1\Sigma_g^+) + e \rightarrow \text{N}_2(X^1\Sigma_g^+) + e$	B.E.	[35]
Electron impact excitation and de-excitation		
R3 $\text{Ar} + e \leftrightarrow \text{Ar}(j) + e$ $j = 4s, 4p, 3d, 5s, 5p$	B.E.	[36-38]
R4 $\text{Ar} + e \leftrightarrow \text{Ar}^{**} + e$	$4.0 \times 10^{-9} \exp(-15.8/T_e)$	[39]
R5 $\text{Ar}(3p^5 4s) + e \leftrightarrow \text{Ar}(j) + e$ $j = 4p, 5p$	B.E.	[36, 40]
R6 $\text{N}_2(X^1\Sigma_g^+, v=0) + e \leftrightarrow \text{N}_2(X^1\Sigma_g^+, v=1 \sim 8)$	B.E.	[35]
R7 $\text{N}_2(X^1\Sigma_g^+) + e \rightarrow \text{N}_2(j) + e$ $j = A^3\Sigma_u^+, B^3\Pi_g, W^3\Delta_u, B'^3\Sigma_u^-, a'^1\Sigma_u^-,$ $a^1\Pi_g, w^1\Delta_u, C^3\Pi_u, E^3\Sigma_g^+, a''^1\Sigma_g^+$	B.E.	[35]
R8 $\text{N}_2^+(X^2\Sigma_g^+) + e \rightarrow \text{N}_2^+(B^2\Sigma_u^+) + e$	B.E.	[41]
R9 $\text{N} + e \rightarrow \text{N}(^2\text{D}) + e$	B.E.	[42]
R10 $\text{N} + e \rightarrow \text{N}(^2\text{P}) + e$	B.E.	[42]
R11 $\text{N}(^2\text{D}) + e \rightarrow \text{N}(^2\text{P}) + e$	B.E.	[42]
Electron impact ionization and dissociation		
R12 $\text{Ar} + e \rightarrow \text{Ar}^+ + e + e$	B.E.	[43]
R13 $\text{Ar}(3p^5 4s) + e \rightarrow \text{Ar}^+ + e + e$	B.E.	[44]
R14 $\text{Ar}(4p) + e \rightarrow \text{Ar}^+ + e + e$	$2.0 \times 10^{-6} \exp(-4.4/T_e)$	[39]
R15 $\text{Ar}(3d, 5s) + e \rightarrow \text{Ar}^+ + e + e$	$6.0 \times 10^{-6} \exp(-2.4/T_e)$	[39]
R16 $\text{Ar}(5p) + e \rightarrow \text{Ar}^+ + e + e$	$2.0 \times 10^{-5} \exp(-2.2/T_e)$	[39]
R17 $\text{Ar}^{**} + e \rightarrow \text{Ar}^+ + e + e$	$2.0 \times 10^{-4} \exp(-0.5/T_e)$	[39]
R18 $\text{N}_2(X^1\Sigma_g^+) + e \rightarrow \text{N}_2^+(X^2\Sigma_g^+) + e + e$	B.E.	[35]
R19 $\text{N}_2(X^1\Sigma_g^+) + e \rightarrow \text{N}_2^+(B^2\Sigma_u^+) + e + e$	B.E.	[41]
R20 $\text{N}_2(A^3\Sigma_u^+) + e \rightarrow \text{N}_2^+(X^2\Sigma_g^+) + e + e$	B.E.	[5,55]
R21 $\text{N}_2(B^3\Pi_g) + e \rightarrow \text{N}_2^+(X^2\Sigma_g^+) + e + e$	$2.1 \times 10^{-8} \exp(-11.0/T_e)$	[5]
R22 $\text{N}_2(C^3\Pi_u) + e \rightarrow \text{N}_2^+(X^2\Sigma_g^+) + e + e$	$9.17 \times 10^{-8} \exp(-6.67/T_e)$	[5]
R23 $\text{N}_2(a'^1\Sigma_u^-) + e \rightarrow \text{N}_2^+(X^2\Sigma_g^+) + e + e$	$4.3 \times 10^{-8} \exp(-10.32/T_e)$	[5]
R24 $\text{N}_2(X^1\Sigma_g^+) + e \rightarrow \text{N} + \text{N} + e$	B.E.	[35]
R25 $\text{N} + e \rightarrow \text{N}^+ + e + e$	B.E.	[45]
R26 $\text{N}_2(X^1\Sigma_g^+) + e \rightarrow \text{N}(^2\text{D}) + \text{N}^+ + e + e$	B.E.	[46]
R27 $\text{N}_2(X^1\Sigma_g^+) + e \rightarrow \text{N}^+ + \text{N}^+ + e + e + e$	B.E.	[46]

R28	$N(^2D) + e \rightarrow N^+ + e + e$	B.E.	[45]
R29	$N(^2P) + e \rightarrow N^+ + e + e$	B.E.	[45]

Virational – translational relaxation of $N_2(X\ ^1\Sigma_g^+)$

R30	$N_2(X\ ^1\Sigma_g^+, \nu) + N_2 \leftrightarrow N_2(X\ ^1\Sigma_g^+, \nu-1) + N_2$	B.E.	[48]
R31	$N_2(X\ ^1\Sigma_g^+, \nu) + N \leftrightarrow N_2(X\ ^1\Sigma_g^+, \nu-1) + N$	B.E.	[48]
R32	$N_2(X\ ^1\Sigma_g^+, \nu=1) + N_2(X\ ^1\Sigma_g^+, \nu=1) \rightarrow N_2 + N_2(X\ ^1\Sigma_g^+, \nu=2)$	$1.73 \times 10^{-14} (300/T_g)^{-1.42}$	[19]
R33	$N_2(X\ ^1\Sigma_g^+, \nu=1) + N_2(X\ ^1\Sigma_g^+, \nu=2) \rightarrow N_2 + N_2(X\ ^1\Sigma_g^+, \nu=3)$	$2.18 \times 10^{-14} (300/T_g)^{-1.54}$	[19]
R34	$N_2(X\ ^1\Sigma_g^+, \nu=1) + N_2(X\ ^1\Sigma_g^+, \nu=3) \rightarrow N_2 + N_2(X\ ^1\Sigma_g^+, \nu=4)$	$2.60 \times 10^{-14} (300/T_g)^{-1.55}$	[19]
R35	$N_2(X\ ^1\Sigma_g^+, \nu=1) + N_2(X\ ^1\Sigma_g^+, \nu=4) \rightarrow N_2 + N_2(X\ ^1\Sigma_g^+, \nu=5)$	$2.80 \times 10^{-14} (300/T_g)^{-1.63}$	[19]
R36	$N_2(X\ ^1\Sigma_g^+, \nu=1) + N_2(X\ ^1\Sigma_g^+, \nu=5) \rightarrow N_2 + N_2(X\ ^1\Sigma_g^+, \nu=6)$	$3.09 \times 10^{-14} (300/T_g)^{-1.63}$	[19]

Electron – ion recombination

R37	$Ar^+ + e + e \rightarrow Ar^{**} + e$	$1.0 \times 10^{-19} (T_e \times 11605/300)^{-4.5}$	[47]
R38	$Ar^+ + e + Ar \rightarrow Ar^{**} + Ar$	3.0×10^{-28}	[47]
R39	$N_2^+ + e \rightarrow N + N$	$1.8 \times 10^{-7} (T_e \times 11605/300)^{-0.39} \times 0.5$	[48]
R40	$N_2^+ + e \rightarrow N(^2D) + N$	$1.8 \times 10^{-7} (T_e \times 11605/300)^{-0.39} \times 0.45$	[48]
R41	$N_2^+ + e \rightarrow N(^2P) + N$	$1.8 \times 10^{-7} (T_e \times 11605/300)^{-0.39} \times 0.05$	[48]
R42	$N_3^+ + e \rightarrow N_2 + N$	$2.0 \times 10^{-7} (T_e \times 11605/300)^{-0.5}$	[48]
R43	$N_4^+ + e \rightarrow N_2 + N_2$	$2.3 \times 10^{-6} (T_e \times 11605/300)^{-0.53}$	[48]
R44	$N^+ + e + e \rightarrow N + e$	$7.0 \times 10^{-20} (T_e \times 11605/300)^{-4.5}$	[48]
R45	$N_2^+ + e \rightarrow N(^2D) + N^+ + e$	B.E.	[49]
R46	$N_2^+ + e \rightarrow N^+ + N^+ + e + e$	B.E.	[49]

Kinetics of Ar_2^+

R47	$Ar^+ + Ar + Ar \rightarrow Ar_2^+ + Ar$	$2.5 \times 10^{-31} (T_g/300)^{-1.5}$	[50,51]
R48	$Ar(3p^5 4s) + Ar(3p^5 4s) \rightarrow Ar_2^+ + e$	$6.3 \times 10^{-10} (T_g/300)^{-0.5}$	[50]
R49	$Ar^{**} + Ar \rightarrow Ar_2^+ + e$	2.0×10^{-9}	[50]
R50	$Ar_2^+ + e \rightarrow Ar^{**} + Ar$	$9.1 \times 10^{-7} (T_e \times 11605/300)^{-0.67} \times (T_g/300)^{-0.58}$	[50,51]
R51	$Ar_2^+ + e \rightarrow Ar(j) + Ar$ $j = 4s, 4p, 3d, 5s, 5p$	$1.0 \times 10^{-8} T_e^{-0.6} (T_g/300)^{-0.6}$	[51]

Heavy particle reactions

R52	$Ar(j) + Ar(k) \rightarrow Ar^+ + Ar + e$ $j, k = 4s, 4p$	$5.0 \times 10^{-10} (T_g/300)^{0.5}$	[51]
R53	$N_2(A\ ^3\Sigma_u^+) + N \rightarrow N_2(X\ ^1\Sigma_g^+) + N$	2.0×10^{-12}	[48]
R54	$N_2(A\ ^3\Sigma_u^+) + N \rightarrow N_2(X\ ^1\Sigma_g^+) + N(^2P)$	$4.0 \times 10^{-11} (300/T_g)^{0.667}$	[48]
R55	$N_2(A\ ^3\Sigma_u^+) + N_2 \rightarrow N_2(X\ ^1\Sigma_g^+) + N_2$	3.0×10^{-16}	[48]
R56	$N_2(A\ ^3\Sigma_u^+) + N_2(A\ ^3\Sigma_u^+) \rightarrow N_2 + N_2(B\ ^3\Pi_g)$	3.0×10^{-10}	[48]
R57	$N_2(A\ ^3\Sigma_u^+) + N_2(A\ ^3\Sigma_u^+) \rightarrow N_2 + N_2(C\ ^3\Pi_u)$	1.5×10^{-10}	[48]

R58	$N_2(A^3\Sigma_u^+) + N_2(A^3\Sigma_u^+) \rightarrow N_4^+ + e$	1.0×10^{-13}	[48]
R59	$N_2(A^3\Sigma_u^+) + N_2(A^3\Sigma_u^+) \rightarrow N_2 + N + N$	3.0×10^{-11}	[48]
R60	$N_2(B^3\Pi_g) + N_2 \rightarrow N_2(A^3\Sigma_u^+) + N_2$	3.0×10^{-11}	[48]
R61	$N_2(B^3\Pi_g) + N_2 \rightarrow N_2(X^1\Sigma_g^+) + N_2$	2.0×10^{-12}	[48]
R62	$N_2(C^3\Pi_u) + N_2 \rightarrow N_2(a'^1\Sigma_u^-) + N_2$	1.0×10^{-11}	[48]
R63	$N_2(a'^1\Sigma_u^-) + N_2 \rightarrow N_2(B^3\Pi_g) + N_2$	1.9×10^{-13}	[48]
R64	$N_2(a'^1\Sigma_u^-) + N_2(A^3\Sigma_u^+) \rightarrow N_4^+ + e$	$1.0 \times 10^{-11} \times 0.9$	[48]
R65	$N_2(a'^1\Sigma_u^-) + N_2(A^3\Sigma_u^+) \rightarrow N_2^+ + N_2 + e$	$1.0 \times 10^{-11} \times 0.1$	[48]
R66	$N_2(a'^1\Sigma_u^-) + N_2(a'^1\Sigma_u^-) \rightarrow N_4^+ + e$	$5.0 \times 10^{-11} \times 0.9$	[48]
R67	$N_2(a'^1\Sigma_u^-) + N_2(a'^1\Sigma_u^-) \rightarrow N_2^+ + N_2 + e$	$5.0 \times 10^{-11} \times 0.1$	[48]
R68	$N_2(w^1\Delta_u) + N_2 \rightarrow N_2(a^1\Pi_g) + N_2$	1.0×10^{-11}	[48]
R69	$N_2(a^1\Pi_g) + N_2 \rightarrow N_2(a'^1\Sigma_u^-) + N_2$	2.0×10^{-11}	[48]
R70	$N + N + N \rightarrow N_2(A^3\Sigma_u^+) + N$	1.0×10^{-32}	[48]
R71	$N + N + N \rightarrow N_2(B^3\Pi_g) + N$	1.4×10^{-32}	[48]

Deactivation of N metastables and atom

R72	$N(^2D) + N_2 \rightarrow N + N_2$	$1.0 \times 10^{-13} \exp(-510/T_g)$	[48]
R73	$N(^2P) + N \rightarrow N + N$	1.8×10^{-12}	[48]
R74	$N(^2P) + N \rightarrow N(^2D) + N$	6.3×10^{-13}	[48]
R75	$N(^2P) + N_2 \rightarrow N + N_2$	6.0×10^{-14}	[48]
R76	$N(^2P) + N(^2D) \rightarrow N_2^+ + e$	1.0×10^{-13}	[48]
R77	$N + N \rightarrow N_2^+ + e$	$2.7 \times 10^{-11} \exp(-6740/T_g)$	[48]

Positive ion reaction

R78	$N_2^+ + N \rightarrow N^+ + N_2$	$7.2 \times 10^{-13} (T_g/300)$	[48]
R79	$N_3^+ + N \rightarrow N_2^+ + N_2$	6.6×10^{-11}	[48]
R80	$N_4^+ + N_2 \rightarrow N_2^+ + N_2 + N_2$	$2.1 \times 10^{-16} \exp(T_g/121)$	[48]
R81	$N_4^+ + N \rightarrow N^+ + N_2 + N_2$	1.0×10^{-11}	[48]
R82	$N^+ + N_2 + N_2 \rightarrow N_3^+ + N_2$	$1.7 \times 10^{-29} (300/T_g)^{2.1}$	[48]
R83	$N_2^+ + N_2 + N_2 \rightarrow N_4^+ + N_2$	$5.2 \times 10^{-29} (300/T_g)^{2.2}$	[48]
R84	$N_2^+ + N + N_2 \rightarrow N_3^+ + N_2$	$9.0 \times 10^{-30} \exp(400/T_g)$	[48]
R85	$N_2^+ + N_2(A^3\Sigma_u^+) \rightarrow N_3^+ + N$	5.5×10^{-11}	[48]
R86	$N^+ + N_2(A^3\Sigma_u^+) \rightarrow N_2^+ + N(^2P)$	2.0×10^{-11}	[48]

Radiative decay

R87	$Ar(1s_2, 1s_4) \rightarrow Ar + h\nu$	$5.32 \times 10^8 g_{1s_2}, 1.3 \times 10^8 g_{1s_4}$	[52]
R88	$Ar(4p) \rightarrow Ar(1s_2, 1s_3, 1s_4, 1s_5) + h\nu$	$9.6 \times 10^6, 3.3 \times 10^6, 1.0 \times 10^7, 9.9 \times 10^6$	[52]
R89	$Ar(5s, 3d) \rightarrow Ar(4p) + h\nu$	$1.56 \times 10^7, 1.56 \times 10^7$	[52]
R90	$Ar(5p) \rightarrow Ar(3d, 5s, 4s) + h\nu$	$(6.5 \times 10^6) \times 0.4, (6.5 \times 10^6) \times 0.4,$ $(6.5 \times 10^6) \times 0.2$	[52]
R91	$Ar^{**} \rightarrow Ar(5p, 3d, 5s, 4p) + h\nu$	$5.0 \times 10^6, 8.6 \times 10^6, 8.6 \times 10^6, 9.1 \times 10^5$	[52]

R92	$\text{Ar}^{**} \rightarrow \text{Ar}(1s_2, 1s_3, 1s_4, 1s_5) + h\nu$	$9.3 \times 10^4, 3.7 \times 10^4, 1.2 \times 10^5, 1.8 \times 10^5$	[52]
R93	$\text{N}_2(C^3\Pi_u) \rightarrow \text{N}_2(B^3\Pi_g) + h\nu$	2.45×10^7	[48]
R94	$\text{N}_2(B^3\Pi_g) \rightarrow \text{N}_2(A^3\Sigma_u^+) + h\nu$	1.35×10^5	[48]
R95	$\text{N}_2(A^3\Sigma_u^+) \rightarrow \text{N}_2(X^1\Sigma_g^+) + h\nu$	5.0×10^{-1}	[48]
R96	$\text{N}_2(a'^1\Sigma_u^-) \rightarrow \text{N}_2(X^1\Sigma_g^+) + h\nu$	1.0×10^2	[48]
R97	$\text{N}_2(a^1\Pi_g) \rightarrow \text{N}_2(X^1\Sigma_g^+) + h\nu$	1.8×10^4	[48]
R98	$\text{N}_2(a^1\Pi_g) \rightarrow \text{N}_2(a'^1\Sigma_u^-) + h\nu$	1.91×10^2	[48]
R99	$\text{N}_2(E^3\Sigma_g^+) \rightarrow \text{N}_2(A^3\Sigma_u^+) + h\nu$	1.2×10^3	[48]
R100	$\text{N}_2(E^3\Sigma_g^+) \rightarrow \text{N}_2(B^3\Pi_g) + h\nu$	3.46×10^2	[48]
R101	$\text{N}_2(E^3\Sigma_g^+) \rightarrow \text{N}_2(C^3\Pi_u) + h\nu$	1.73×10^3	[48]
R102	$\text{N}_2(w^1\Delta_u) \rightarrow \text{N}_2(a^1\Pi_g) + h\nu$	6.5×10^2	[48]
R103	$\text{N}_2^+(B^2\Sigma_u^+) \rightarrow \text{N}_2^+(X^2\Sigma_g^+) + h\nu$	1.6×10^7	[48]

Reactions between nitrogen and argon

R104	$\text{N}_2(a'^1\Sigma_u^-) + \text{Ar} \rightarrow \text{N}_2(B^3\Pi_g) + \text{Ar}$	1.0×10^{-14}	[53]
R105	$\text{N}_2(a^1\Pi_g) + \text{Ar} \rightarrow \text{N}_2(a'^1\Sigma_u^-) + \text{Ar}$	1.0×10^{-12}	[53]
R106	$\text{N}_2(B^3\Pi_g) + \text{Ar} \rightarrow \text{N}_2(A^3\Sigma_u^+) + \text{Ar}$	3.0×10^{-13}	[53]
R107	$\text{N}_2(w^1\Delta_u) + \text{Ar} \rightarrow \text{N}_2(a^1\Pi_g) + \text{Ar}$	5.0×10^{-13}	[53]
R108	$\text{N}_2(X^1\Sigma_g^+) + \text{Ar}^+ \rightarrow \text{N}_2^+(X^2\Sigma_g^+) + \text{Ar}$	$f(T_v \text{ N}_2(X^1\Sigma_g^+))$	[31]
R109	$\text{N}_2(X^1\Sigma_g^+) + \text{Ar}(1s_2) \rightarrow \text{N}_2(C^3\Pi_u) + \text{Ar}$	1.6×10^{-11}	[54]
R110	$\text{N}_2(X^1\Sigma_g^+) + \text{Ar}(1s_3) \rightarrow \text{N}_2(C^3\Pi_u) + \text{Ar}$	1.6×10^{-11}	[54]
R111	$\text{N}_2(X^1\Sigma_g^+) + \text{Ar}(1s_4) \rightarrow \text{N}_2(C^3\Pi_u) + \text{Ar}$	3.6×10^{-11}	[54]
R112	$\text{N}_2(X^1\Sigma_g^+) + \text{Ar}(1s_5) \rightarrow \text{N}_2(C^3\Pi_u) + \text{Ar}$	3.6×10^{-11}	[54]

Diffusion loss

R113	$\text{Ar}(j) \rightarrow \text{Ar}(\text{wall})$ ($j = 4s, 4p, 3d, 5s, 5p, **$)	$\left[\frac{\Lambda_0^2}{D_{Ar}} + \frac{2V(2 - \gamma_n)}{A\bar{v}_{Ar}\gamma_n} \right]^{-1} (\gamma_n = 1.0)$	[18]
R114	$\text{Ar}^+ \rightarrow \text{Ar}(\text{wall})$	$2u_{B,Ar}(R^2h_L + RLh_R)/R^2L$	[18]
R115	$\text{Ar}_2^+ \rightarrow \text{Ar}(\text{wall})$	$2u_{B,Ar2}(R^2h_L + RLh_R)/R^2L$	[18]
R116	$\text{N}(^4S, ^2D, ^2P) \rightarrow \frac{1}{2}\text{N}_2(X^1\Sigma_g^+)(\text{wall})$	$\left[\frac{\Lambda_0^2}{D_N} + \frac{2V(2 - \gamma_n)}{A\bar{v}_N\gamma_n} \right]^{-1} (\gamma_n = 0.02)$	[19]
R117	$\text{N}_2(X^1\Sigma_g^+, \nu) \rightarrow \text{N}_2(X^1\Sigma_g^+, \nu-1)(\text{wall})$	$\left[\frac{\Lambda_0^2}{D_{N_2}} + \frac{2V(2 - \gamma_n)}{A\bar{v}_{N_2}\gamma_n} \right]^{-1} (\gamma_n = 1 \times 10^{-3})$	[48]

R118	$N_2(j) \rightarrow N_2(X^1\Sigma_g^+)$ (wall)	$\left[\frac{\Lambda_0^2}{D_{N_2}} + \frac{2V(2-\gamma_n)}{A\bar{v}_{N_2}\gamma_n} \right]^{-1}$	[19]
	$j = A^3\Sigma_u^+, B^3\Pi_g, W^3\Delta_u, B'^3\Sigma_u^-, a'^1\Sigma_u^-,$ $a^1\Pi_g, w^1\Delta_u, C^3\Pi_u, E^3\Sigma_g^+, a''^1\Sigma_g^+$	$(\gamma_n = 1.0)$	
R119	$N(^2D, ^2P) \rightarrow N(^4S)$ (wall)	$\left[\frac{\Lambda_0^2}{D_N} + \frac{2V(2-\gamma_n)}{A\bar{v}_N\gamma_n} \right]^{-1}$	[19]
R120	$N^+ \rightarrow N(^4S)$ (wall)	$2u_{B,N}(R^2h_L + RLh_R)/R^2L$	[19]
R121	$N_2^+(X^2\Sigma_g^+) \rightarrow N_2(X^1\Sigma_g^+)$ (wall)	$2u_{B,N2}(R^2h_L + RLh_R)/R^2L$	[19]
R122	$N_2^+(B^2\Sigma_u^+) \rightarrow N_2(X^1\Sigma_g^+)$ (wall)	$2u_{B,N2}(R^2h_L + RLh_R)/R^2L$	[19]
R123	$N_3^+ \rightarrow N_2(X^1\Sigma_g^+) + N(^4S)$ (wall)	$2u_{B,N3}(R^2h_L + RLh_R)/R^2L$	[19]
R124	$N_4^+ \rightarrow N_2(X^1\Sigma_g^+) + N_2(X^1\Sigma_g^+)$ (wall)	$2u_{B,N4}(R^2h_L + RLh_R)/R^2L$	[19]

notes : T_e in eV, and T_g in K

6.6 References

- [1] Wang Y, Van Brunt R J and Olthoff J 1998 *J. Appl. Phys.* **83** 703
- [2] Tabbal M, Kazopoulo M, Christidis T and Isber S 2001 *Appl. Phys. Lett.* **78** 2131
- [3] Henriques J, Tatarova E, Dias F M and Ferreira C M 2002 *J. Appl. Phys.* **91** 5632
- [4] Czerwicz T, Greer F and Graves D B 2005 *J. Phys. D: Appl. Phys.* **38** 4278
- [5] Kimura T and Kasugai H 2010 *J. Appl. Phys.* **108** 033305
- [6] Godyak V A, Piejak R B and Alexandrovich B M 1992 *Plasma Sources Sci. Technol.* **136**
- [7] Godyak V A, Piejak R B and Alexandrovich B M 1993 *J. Appl. Phys.* **73** 3657
- [8] Mitchell A C G and Zemanski M W Z 1971 *Resonance Radiation and Excited Atoms* (Cambridge: Cambridge University Press)
- [9] Ricard A, Nouvellon C, Konstantinidis S, Dauchot J P, Wautelet M and Hecq M 2002 *J. Vac. Sci. Technol. A* **20** 1488
- [10] Kang N, Oh S G, Gaboriau F and Ricard A 2010 *Rev. Sci. Instrum.* **81** 013102
- [11] Konstantinidis S, Ricard A, Fanciu M, Dauchot J P, Ranea C and Hecq M 2004 *J. Appl. Phys.* **95** 2900
- [12] Griem H R 1964 *Plasma Spectroscopy* (New York: McGraw-Hill)
- [13] Niemi K, Schulz-von der Gathen V and Döbele H F 2001 *J. Phys. D: Appl. Phys.* **34** 2330
- [14] Gaboriau F, Cvelbar U, Mozetic M, Erradi A and Rouffet B 2009 *J. Phys. D: Appl. Phys.* **42** 055204
- [15] Thorsteinsson E G and Gudmundsson J T 2009 *Plasma Sources Sci. Technol.* **18** 045002
- [16] Lieberman M A and Ashida S 1996 *Plasma Sources Sci. Technol.* **5** 145
- [17] Lee C and Lieberman M A 1995 *J. Vac. Sci. Technol. A* **13** 368
- [18] Phelps A V 1991 *J. Phys. Chem. Ref. Data* **20** 557
- [19] Thorsteinsson E G and Gudmundsson J T 2009 *Plasma Sources Sci. Technol.* **18** 045001
- [20] Debal F, Bretagne J, Jumet M, Wautelet M, Dauchot J P and Hecq M 1998 *Plasma Sources Sci. Technol.* **7** 219
- [21] Lieberman M A and Lichtenberg A J 2005 *Principles of Plasma Discharges and Materials Processing 2nd ed.* (New York: Wiley)
- [22] Pancheshnyi S, Eismann B, Hagelaar G J M and Pitchford L C, Computer code ZDPlasKin, <http://www.zdplaskin.laplace.univ-tlse.fr> (University of Toulouse, LAPLACE, CNRS-UPS-INP, Toulouse, France, 2008).
- [23] Ferreira C M, Loureiro J and Ricard A 1985 *J. Appl. Phys.* **57** 82
- [24] Holstein T 1947 *Phys. Rev.* **72** 1212
- [25] Holstein T 1951 *Phys. Rev.* **83** 1159
- [26] Booth J P and Sadeghi N 1991 *J. Appl. Phys.* **70** 611

- [27] Chantry P J 1987 *J. Appl. Phys.* **62** 1141
- [28] Singh H, Coburn J W and Graves D B 2000 *J. Appl. Phys.* **88** 3748
- [29] Sarrette J P, Rouffet B and Ricard A 2006 *Plasma Process. Polym.* **3** 120
- [30] Ricard A 1966 *Reactive Plasmas* (SFV Editions)
- [31] Viggiano A A and Morris R A 1993 *J. Chem. Phys.* **99** 3526
- [32] Agarwal S, Hoex B, van de Sanden M C M, Maroudas D and Aydil E S 2003 *Appl. Phys. Lett.* **83** 4918
- [33] Bogaerts A and Gijbels R 1995 *Phys. Rev. A* **52** 3743
- [34] Kang N, Gaboriau F, Oh S G and Ricard A 2011 *Plasma Sources Sci. Technol.* **20** 035002
- [35] Phelps database, <http://www.lxcat.laplace.univ-tlse.fr>, retrieved October 13, 2010.
- [36] Bartschat K and Zeman V 1999 *Phys. Rev. A* **59** R2552
- [37] Chilton J E and Lin C C 1999 *Phys. Rev. A* **60** 3712
- [38] Weber T, Boffard J B and Lin C C 2003 *Phys. Rev. A* **68** 032719
- [39] Zhu X M and Pu Y K 2010 *J. Phys. D: Appl. Phys.* **43** 015204
- [40] Jung R O, Boffard J B, Anderson L W and Lin C C 2007 *Phys. Rev. A* **75** 052707
- [41] Isola L M, Gómez B J and Guerra V 2010 *J. Phys. D: Appl. Phys.* **43** 015202
- [42] Tayal S S and Zatsarinny O 2005 *J. Phys. B: At. Mol. Opt. Phys.* **38** 3631
- [43] Rapp D and Englander-Golden P 1965 *J. Chem. Phys.* **43** 1464
- [44] Ali M A and Stone P M 2008 *Int. J. Mass Spectrom.* **271** 51
- [45] Kim Y K and Desclaux J P 2002 *Phys. Rev. A* **66** 012708
- [46] Tian C and Vidal C R 1998 *J. Phys. B: At. Mol. Opt. Phys.* **31** 5369
- [47] Bogaerts A, Gijbels R and Jackson G P 2003 *J. Anal. At. Spectrom.* **18** 533
- [48] Capitelli M, Ferreira C M, Gordiets B F and Osipov A I 2000 *Plasma Kinetics in Atmospheric Gases* (Berlin: Springer)
- [49] Bahati E M, Jureta J J, Belic D S, Cherkani-Hassani H, Abdellahi M O and Defrance P 2001 *J. Phys. B: At. Mol. Opt. Phys.* **34** 2963
- [50] Bultel A, Ootegem B, Bourdon A and Vervisch R 2002 *Phys. Rev. E* **65** 046406
- [51] Robin M N, Shabunya S I, Rostaing J C and Perrin J M 2007 *Plasma Sources Sci. Technol.* **16** 480
- [52] NIST Atomic Spectra Database, <http://physics.nist.gov/asd3>
- [53] Henriques J, Tatarova E, Guerra V and Ferreira C M 2002 *J. Appl. Phys.* **91** 5622
- [54] Delcroix J L, Ferreira C M and Ricard A 1976 *Principle of Laser Plasma: ch.5*, eds. Bekefi G. (New York: Wiley)
- [55] Freund R S, Wetzel R C and Shul R J 1990 *Phys. Rev. A* **41** 5861

Chapter 7

Experimental and electrical characteristics of inductively coupled He, Ne, Ar and Xe discharges

Contents

7.1	Introduction	132
7.2	Experiment	132
7.3	Global model of pure rare gases	134
7.4	Transformer model	137
7.4.1	Effective collision frequency	138
7.4.2	Skin depth	138
7.4.3	Plasma impedance	139
7.5	Results and discussion	141
7.5.1	Electron temperature and electron density	142
7.5.2	Metastable atoms	144
7.5.3	Plasma impedance	147
7.6	Conclusion	148
7.7	References	152

7.1 Introduction

THE ICP discharge is maintained by the magnetic induction which is induced by the time varying magnetic field and electric field. Therefore analysis of electrical characteristics in the ICP discharge is essential to understand the properties of discharges. The electrical properties of ICP discharge sources can be characterized by the transformer equivalent circuit. This model considers the antenna coil as the primary winding of an air-core transformer, whereas the plasma represents the secondary winding. In order to characterize the transformer equivalent circuit, it is necessary to define the mutual inductance between the primary and secondary loop. Piejak *et al* [1] give the analytical expression of the electrical characteristics of the plasma load including the mutual inductance. El-Fayoumi and Jones [2] described the electromagnetic theory of inductive discharges and the relation to the electrical parameters of the transformer model. Gudmundsson and Lieberman [3] analytically calculated the magnetic induction and electric field components in the planar inductive discharge, and compared the calculated impedance and electrical properties of the plasma with measured values. They applied a global (volume-averaged) model to calculate the electron density and the electron temperature.

In this study we develop the global model of He, Ne, Ar and Xe discharges to calculate the electron temperature and the electron density as well as the density of excited states. We compare the calculated results with experiments and discuss the dominant creation sources and the routes of loss for electron and metastable atoms as function of pressure. And the transformer model developed by Gudmundsson and Lieberman [3] is used to calculate the electrical properties of He, Ne, Ar and Xe discharges. We discuss the differences of kinetics and electrical properties in He, Ne, Ar and Xe discharges.

7.2 Experiment

The experimental set-up for this study is same with chapter 5 as shown in figure 5.1. The anode plate was installed at 50 mm from antenna window to limit the volume of the discharge. The discharges were excited by the 3 turn-antenna powered by 13.56 MHz of RF frequency at 60 Watt through the alternate type matching network for the convenience of experiment as that power rate provided stable glows for all rare gases at low pressure. In this study the discharge was operated in H-mode which is represented by bright emission and high electron density [4]. The chamber was pumped to 10^{-6} Torr base pressure before filling with He, Ne, Ar and Xe gas (99.999 % pure). The total flow rate was maintained constant at 20 sccm and the total pressure was varied from 20 to 200 mTorr.

A cylindrical single Langmuir probe (SmartProbe of Scientific Systems) was set in center of discharge to measure electron temperature T_e and electron density n_e . The electron energy probability function EEPF $f(E)$ was deduced from Druyvesteyn formula in equations (4.47)-(4.50).

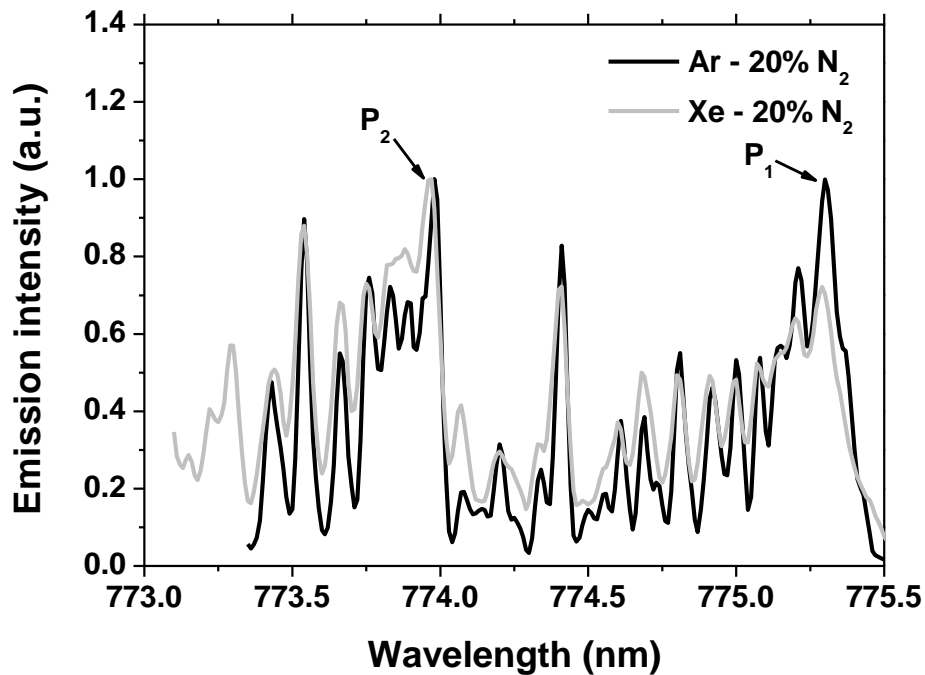
To measure the density of metastable atoms, the resonance absorption spectroscopy was used, which is widely performed in various plasma processes [5]. The method has been applied successfully for measuring metastable atoms in DC and RF magnetron discharges [6]. A lab-made hollow cathode lamp was used as the reference source. The source light, driven

Table 7.1 Selected spectral lines and spectroscopic data of rare gases used for the resonant absorption measurement

Wavelength (nm)	Transition		E_{low} (eV)	E_{high} (eV)	A_{ij} ($10^6 s^{-1}$)	f_{ik}
He I 388.9	$1s2s - 1s3p$	$2^3S - 3^3P$	19.82	23.01	9.478	0.064
Ne I 640.2	$1s_5 - 2p_9$	$3s[3/2]_2 - 3p[5/2]_3$	16.62	18.55	43.3	0.373
Ar I 763.5	$1s_5 - 2p_6$	$4s[3/2]_2 - 4p[3/2]_2$	11.55	13.17	24.5	0.239
Xe I 823.2	$1s_5 - 2p_6$	$6s[3/2]_2 - 6p[3/2]_2$	8.31	9.82	24.9	0.24

by 35 mA DC current at 1 Torr, has been collimated by a system of lenses and diaphragms to get a probing beam of 5 mm in diameter through plasma. By simply changing the working gas in the discharge, various spectral source lamps can be obtained. To secure stable emission, the hollow cathode lamp was turned on for 20 minutes or more before each measurement. The principle of the optical absorption spectroscopy is explained in chapter 4.

The plasma line width ($\delta\sigma_{1/2}^P$) is calculated by taking a Doppler line profile, which is the dominant line broadening in glow discharge at low gas pressure [7,8]. The Doppler line width is calculated from the equation (4.42). In the present study, the temperatures of the plasma and that of reference source have been evaluated from the rotational structure of N_2 1st positive (B,0-A,2) band at 775 nm by adding 20 % of N_2 to the rare gases [6]. In figure 7.1, the rotational spectrum of N_2 1st positive (B,0-A,2) band from the Ar- N_2 and Xe- N_2 mixture

**Figure 7.1** Measured rotational spectrum of N_2 1st positive (B,0-A,2) band from the Ar- N_2 and Xe- N_2 mixture discharge.

used in the experiment. He-N₂ and Ne-N₂ mixture gases provide similar spectra. Table 7.1 lists the selected spectral lines and some spectroscopic data of rare gases used for the resonant absorption measurement.

7.3 Global model of pure rare gases

The species used in our discharge model are presented in Table 7.2. There is a crucial analogy between kinetics of various atoms of rare gases. Therefore it is convenient to use $X = (\text{He, Ne, Ar, Xe})$ as a symbol of one of these atoms. $X(s)$ consists of the 2 energy levels of He(1s2s), and 4 energy levels of Ne(2p⁵3s), Ar(3p⁵4s) and Xe(5p⁵6s). $X(p)$ consists of 2 energy levels of He(1s2p), and 1 energy level of Ne(2p⁵3p), Ar(3p⁵4p) and Xe(5p⁵6p), even though the 4 energy levels (2p₁, 2p₂, 2p₃, 2p₄) of Xe(5p⁵6p) are higher than other 6 levels we consider 1 energy level as a block in convenience. $X(h)$ consists of 6 energy levels of highly excited of He, and 3 energy levels of highly excited of Ne, Ar and Xe. X^+ and X_2^+ denote the atomic ion and the molecular ion of X , respectively. Therefore in our model, we assume that He consists of 14 energy levels, and 12 energy levels for Ne, Ar and Xe including the electron.

To calculate the electron temperature, the global model is used as shown in equation (3.2)-(3.20). We assume a cylindrical discharge chamber of radius $R = 10$ cm and length $L = 5$ cm. The ion-neutral species mean free path λ_i is calculated using equation (3.7) with collision cross section data [9-11], and the ion atom temperature is assumed to be the same as the gas temperature T_g . The collision energy loss per electron-ion pair created, ε_c , is a function of T_e only, depending on the electron neutral species collisional energy loss processes in the gas. Figure 7.2 shows the calculated ε_c as a function of T_e for Ar, He, Ne and Xe, when assuming a Maxwellian electron energy distribution.

The dynamics of species density n_j is described by the particle balance in equation (3.21). The list of species and reactions are converted automatically in a system of kinetic equations and solved numerically using ZDPlasKin tool [12]. The rate coefficients of all reactions are calculated using build-in into the package BOLSIG+ solver. The reactions used in this study are summarized including the references for used cross sections in table 7.3 and table 7.4. The rate coefficient for the electron impact excitation from level j to level k , k_{jk} , is calculated

Table 7.2 Species used in the discharge model.

Species	$X(s)$	$X(p)$	$X(h)$	Ions
He	He(1s2s); 2 ¹ S, 2 ³ S	He(2 ¹ P), He(2 ³ P)	He(3 ¹ S), He(3 ¹ P), He(3 ¹ D), He(3 ³ S), He(3 ³ P), He(3 ³ D)	He ⁺ , He ₂ ⁺
Ne	Ne(2p ⁵ 3s) ; 3p ₂ , 3p ₁ , 3p ₀ , 1p ₁	Ne(2p ⁵ 3p)	Ne(2p ⁵ 4s), Ne(2p ⁵ 3d), Ne(2p ⁵ 4p)	Ne ⁺ , Ne ₂ ⁺
Ar	Ar(3p ⁵ 4s) ; 3p ₂ , 3p ₁ , 3p ₀ , 1p ₁	Ar(3p ⁵ 4p)	Ar(3p ⁵ 5s), Ar(3p ⁵ 3d), Ar(3p ⁵ 5p)	Ar ⁺ , Ar ₂ ⁺
Xe	Xe(5p ⁵ 6s) ; 3p ₂ , 3p ₁ , 3p ₀ , 1p ₁	Xe(5p ⁵ 6p)	Xe(5p ⁵ 7s), Xe(5p ⁵ 5d), Xe(5p ⁵ 7p)	Xe ⁺ , Xe ₂ ⁺

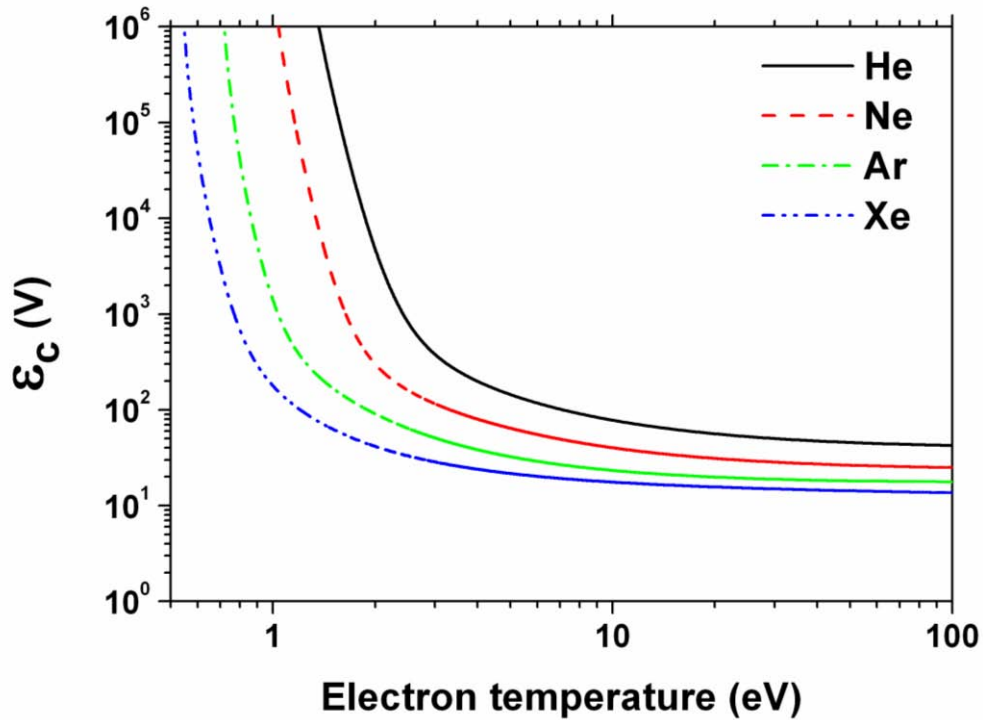


Figure 7.2 Calculated ϵ_c as a function of T_e for Ar, He, Ne and Xe, when assuming a Maxwellian electron energy distribution.

using equation (3.22). Also the rate coefficients of de-excitation processes k_{kj} , are calculated by the principle of detailed balancing [11].

Figure 7.3 shows the measured EEPFs at pressure of 50 mTorr. The measured EEPFs are nearly Maxwellian below the inelastic collision thresholds with a slightly depletion of electrons for energy higher than the first excitation threshold energy; 19.8 eV, 16.6 eV, 11.5 eV and 8.3 eV for He, Ne, Ar and Xe, respectively. Even though the EEPF is a bi-Maxwellian distribution in a low pressure and a Druyvesteyn distribution in a high pressure [13-15], we have assumed in the calculation that the EEDF is Maxwellian.

At higher electron densities, metastable levels are lost primarily by electron impact-induced transitions (R4) to the resonance levels ($1s_2$, $1s_4$), which rapidly decay to the ground state by emitting in the vacuum UV. The cross sections for electron quenching of X(s) levels in Ar and Kr have been computed by Bartschat and Zeman [16] and Dasgupta *et al* [17]. However there are no available cross section data for Ne and Xe. As mentioned by Donnelly [18], the computed rate constants for electron quenching of Ar and Kr metastables are nearly the same, and the rate constant measured by Ivanov and Prikhodko [19] for the quenching of Xe $1s_5$ is nearly the same as their measurement for Ar $1s_5$ [20]. Therefore the individual electron impact quenching cross sections for Xe were assumed to be equal to those for the corresponding reactions in Kr, computed by Dasgupta *et al* [17]. By a similar reasoning, the individual quenching rate constants for Ne were set equal to those for Ar computed by Bartschat and Zeman [16].

The radiative loss rate for decay from level k to level j is calculated using equation (3.24). The escape factor g_k depends on the density of the lower state in the radiative transition. At low pressure the density of excited level is enough low to neglect the escape factor except for resonance lines because of direct radiative decay to the ground level; R12 for He, R11 for Ne, Ar and Xe. The calculated escape factor of resonance lines are calculated using equations (3.26)-(3.29). In figure 7.4, the calculated escape factors of He(2^1P-1^1S , $\lambda = 58.4$ nm), Ne($3P_1-1S_0$, $\lambda = 74.4$ nm), Ar($3P_1-1S_0$, $\lambda = 106.7$ nm) and Xe($3P_1-1S_0$, $\lambda = 147.0$ nm) are shown as a function of the pressure. The radiative decay transitions between excited states R12-R13 were calculated using the sum of the transition probabilities for the transitions between the individual sublevels weighted with the statistical weights of the upper sublevels.

The diffusion loss rate of the neutral atoms to the wall is calculated using equations (3.31) and (3.32). The neutral-neutral species mean free path calculated from the neutral-neutral collision cross section data [9-11].

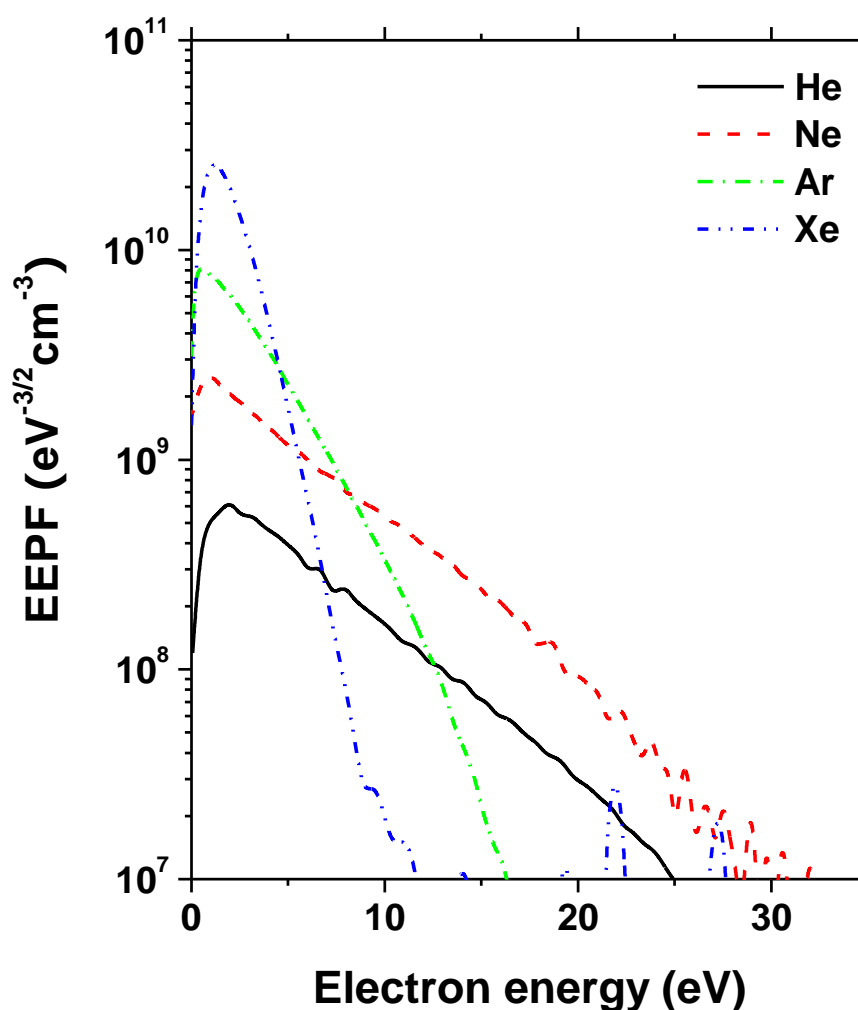


Figure 7.3 Measured EEPFs at pressure of 50 mTorr.

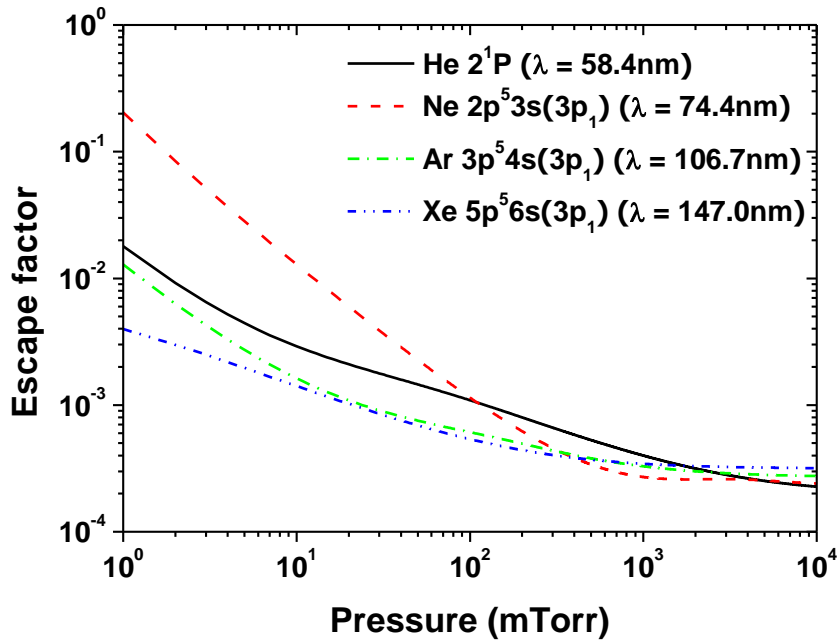


Figure 7.4 calculated escape factors of $\text{He}(2^1\text{P}-1^1\text{S}, \lambda = 58.4 \text{ nm})$, $\text{Ne}(^3\text{P}_1-1^1\text{S}_0, \lambda = 74.4 \text{ nm})$, $\text{Ar}(^3\text{P}_1-1^1\text{S}_0, \lambda = 106.7 \text{ nm})$ and $\text{Xe}(^3\text{P}_1-1^1\text{S}_0, \lambda = 147.0 \text{ nm})$ as a function of the pressure.

7.4 Transformer model

Low-pressure inductive discharges have been modelled by considering the plasma to be a ring acting as the secondary coil of a transformer [1-3]. The equivalent circuit is shown in figure 7.5. The inductive branch is represented as an air-cored transformer having the planar coil inductance L_I and resistance R_I as a primary. The secondary discharge can be described

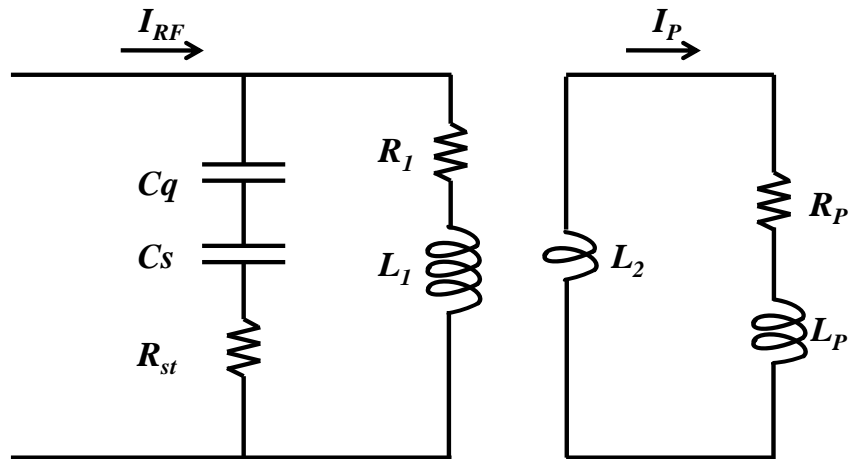


Figure 7.5 The equivalent circuit used in the transformer model.

by two components of inductance and one resistance: a geometric inductance L_2 , an electron inertia inductance L_p , and a resistance R_p of the plasma loop. R_p and L_p are determined by the electrical properties of the plasma which are described by a plasma conductivity

$$\sigma_p = \frac{n_e e^2}{m_e (\nu_{eff} + j\omega_{eff})} \quad (7.1)$$

where e and m_e are the electronic charge and mass, respectively, n_e is the electron density, ν_{eff} is the effective electron collision frequency, and ω_{eff} is the effective driving frequency. In the capacitive branch we neglect the capacitive ohmic heating resistance for which power loss is lower than 1 % in the total power loss in the H -mode [21,22].

7.4.1 Effective collision frequency

The effective momentum transfer electron collision frequency consists of the electron-neutral collision frequency, the stochastic collision frequency and the electron-ion collision frequency in high density discharge.

$$\nu_{eff} = \nu_{en} + \nu_{st} + \nu_{ei} \quad (7.2)$$

The electron-neutral collision frequency depends on the neutral gas pressure and gas temperature and is defined as [23]

$$\nu_{en} + j\omega_{eff} = -\frac{3}{2} \left[\int_0^\infty \frac{\varepsilon^{2/3}}{\nu_c(\varepsilon) + j\omega} \frac{df(\varepsilon)}{d\varepsilon} d\varepsilon \right]^{-1} \quad (7.3)$$

where $f(\varepsilon)$ is the electron energy probability function and $\nu_c(\varepsilon)$ is the energy dependant electron momentum transfer collision frequency. Vahedi *et al* [24] define a stochastic frequency ν_{st} , and in our pressure and frequency regime it is given by

$$\nu_{st} \approx \frac{1}{4} \frac{\bar{v}_e}{\delta} \quad (7.4)$$

where $v_e = (8kT_e/\pi m_e)^{1/2}$ is the mean speed of the electrons, and δ is the skin depth. Miyamoto gives the electron-ion collision frequency as [25]

$$\nu_{ei} = \frac{n_e e^4 \ln \Lambda}{4\pi \varepsilon_0^2 m_e^{1/2} (eT_e)^{3/2}} \quad (7.5)$$

where $\ln \Lambda$ is the Coulomb logarithm given as $\ln \Lambda = 23 - \ln(n_e^{1/2} T_e^{-3/2} / 100)$ for $T_e \ll 10$ eV.

7.4.2 Skin depth

In an inductively coupled discharge, the power is transferred from electric field to the plasma within a skin depth layer of scale length thickness δ . For a planar inductive discharge and

assuming the electric field profile next to the quartz window to follow the form given by equation (7.11), the plasma skin depth is related to the plasma electron density by [24]

$$\delta = \frac{c}{\omega_{pe}} \left(\frac{2(1 + \nu_{eff}^2 / \omega^2)}{\beta(1 + (1 + \nu_{eff}^2 / \omega^2 \beta^2)^{1/2})} \right)^{1/2} \quad (7.6)$$

where

$$\beta = 1 + \alpha(1 + \nu_{eff}^2 / \omega^2) \quad (7.7)$$

and

$$\alpha = \left(\frac{c}{\omega_{pe}} \right)^2 \left[\left(\frac{3.83}{R} \right)^2 - \left(\frac{\omega}{c} \right)^2 \right] \quad (7.8)$$

are geometrical correction factors, ν_{eff} is the effective collision frequency and $\omega_{pe}^2 = (e^2 n_{av} / \epsilon_0 m_e)$, where ω_{pe} is the angular plasma frequency. n_{av} is the average density in the power absorption region which is related to the centre density

$$n_{av} \approx \frac{h_L + h(\delta)}{2} n_0 \quad (7.9)$$

where $h(\delta)$ is the ratio of the electron density between skin depth and centre.

7.4.3 Plasma impedance

The power dissipated within the plasma is given by

$$P_{abs} = 2\pi \int_0^\infty dz \int_0^R r dr \operatorname{Re}[\sigma_p] |E_\theta(r, z)|^2 \quad (7.10)$$

where E_θ is the azimuthal rms electric field, which is assumed to follow

$$E_\theta(r, z) = E_{\theta 0} J_1(\gamma_1 r) \exp(-\gamma z) \quad (7.11)$$

where $J_1(\gamma_1 r)$ is the first-order Bessel function and $\gamma_1 R \approx 3.83$. The rms current density J_θ is assumed to be related to the electric field by Ohm's law and $J_\theta = (\sigma_p + j\omega\epsilon_0)E_\theta$.

In our regime, the displacement current is much less than the conduction current ($\omega\epsilon_0 \ll \sigma_p$). For this reason, we obtain

$$\gamma = (j\omega\mu_0\sigma_p)^{1/2} \quad (7.12)$$

and

$$|\gamma^2| = \frac{\omega \mu_0 \sigma_{dc} v_{eff}}{(v_{eff}^2 + \omega_{eff}^2)^{1/2}} \quad (7.13)$$

where $\sigma_{dc} = e^2 n_e / m_e v_{eff}$ is the dc electrical conductivity of the plasma.

The rms current flowing through the current path is found by integrating the current density over the cross-section of this current path or

$$I_\theta = \int_0^\infty dz \int_0^R dr \sigma_p E_\theta(r, z) \quad (7.14)$$

The resistance of the plasma is then given by

$$R_p = \frac{P_{abs}}{|I_\theta|^2} = \frac{\pi |\gamma|^2 \operatorname{Re}[\sigma_p] \int_0^R r dr |E_\theta^2(r)|}{\operatorname{Re}[\gamma] |\sigma_p|^2 \left| \int_0^R dr E_\theta(r) \right|^2} \quad (7.15)$$

The inductance L_p due to the electron inertia is given in equation (2.47). Therefore the equivalent impedance of the primary coil and the plasma as seen in the primary circuit can be calculated as

$$Z_s = R_L + j\omega L_L \quad (7.16)$$

$$R_L = R_1 + \Delta R = R_1 + \frac{\omega^2 M^2 R_p}{R_p^2 + \omega^2 (L_2 + L_p)^2} \quad (7.17)$$

$$L_L = L_1 - \Delta L = L_1 - \frac{\omega^2 M^2 (L_2 + L_p)}{R_p^2 + \omega^2 (L_2 + L_p)^2} \quad (7.18)$$

where M is the mutual inductance which can be calculated from the field components induced by the coil [3]. With calculated mutual inductance M , the self inductance L_2 can be obtained which depends on the geometry of the path of the induced current in the plasma. In the calculated we assume that the coil resistance R_l is 0.3 Ω , and the coil inductance L_l is 1 μH .

As shown in figure 7.5, the capacitive branch is represented by the combination of circuit elements C_q , C_s and R_{st} . C_q is the quartz window capacitance, C_s is the sheath capacitance and R_{st} is the stochastic heating resistance. Therefore the impedance of the capacitive branch is

$$Z_{cap} = R_{st} + \frac{1}{j\omega C_s} + \frac{1}{j\omega C_q} \quad (7.19)$$

The values of capacitive components are given in other paper [3,26]. The sheath capacitance can be calculated from the expression given by Godyak and Sternberg [26], $C_s' = \epsilon_0 A_d / s$, where A_d is the area of the quartz window and s is the sheath thickness. By averaging the voltage along the coil, C_s can be expressed as $C_s = \frac{1}{2} C_s'$. The stochastic heating resistance R_{st}

depends on the electron temperature, the RF sheath voltage, RF frequency and the discharge gas type [26]. In this study the quartz window capacitance C_q is obtained 36 pF.

Finally the effective impedance seen in the primary circuit becomes

$$Z'_s = \frac{Z_s Z_{cap}}{Z_s + Z_{cap}} \quad (7.20)$$

The power absorbed within the plasma is given by

$$P_{abs} = \text{Re} \left[Z'_s \right] I_{rf}^2 \quad (7.21)$$

where I_{rf} is the rms RF current in the primary coil. The RF voltage for a given RF power P_{abs} absorbed by the plasma is

$$V_{rf} = I_{rf} Z'_s \quad (7.22)$$

7.5 Results and discussion

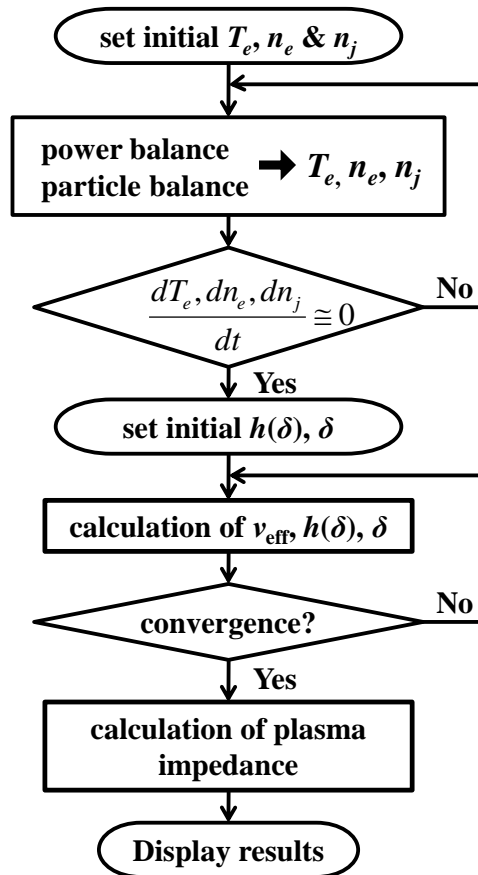


Figure 7.6 The flow chart of calculation algorithm.

The flow chart of calculation algorithm is shown in figure 7.6. First we fix the initial electron temperature and initial density of all species including electron density. To calculate the electron temperature the global model is used to solve the power balance equation with absorbed power fixed at 50 Watt, i.e. we assume that the power transfer efficiency is about 80 %. The power balance equation and the particle balance equation are solved by ordinary differential equation solver based on the Runge-Kutta method. Once the electron temperature is determined, the densities of all species are calculated by the particle balance equation using ZDPlasKin tool. This process is repeated until the densities of all species and the electron temperature reach the steady state. To determine the effective collision frequency, ν_{eff} , the plasma skin depth, δ , and average electron density, n_{av} , are iteratively calculated with the initial values until the iterations are converged. The values of all the components in figure 6 can be calculated with the ν_{eff} , and finally the total impedance Z_s' seen from the matching network is calculated using the transformer model.

7.5.1 Electron temperature and electron density

Figures 7.7(a) and 7.7(b) show measured and calculated electron temperature and electron density versus pressure at a fixed RF power in pure He, Ne, Ar and Xe discharge. It is well known [27] that the electron temperature increases and the electron density decreases according to the ionization energy of the gas; 24.59 eV, 21.56 eV, 15.76 eV and 12.13 eV for He, Ne, Ar and Xe, respectively. The electron temperatures slowly decrease with pressure and the electron densities first increase and then saturate, except in the case of He where a small decrease appears. For the electron temperature assuming the error bars for experimental results estimated to 20%, a good agreement is found between calculated and measured values. As the electron temperature is deduced from the balance between the production of electrons by ionization of the gas and the loss of electrons on the walls, increasing the pressure decreases the electron diffusion to the walls and subsequently the electron temperature.

In the global model the central electron density is determined in the steady state by balancing the total absorbed power to the total power loss:

$$n_e = \frac{P_{abs}}{eu_B (\varepsilon_c + \varepsilon_e + \varepsilon_i)(h_L A_L + h_R A_R)} \quad (7.23)$$

where u_B is the Bohm velocity, and $A_L = 2\pi R^2$ and $A_R = 2\pi RL$ are the areas of the axial and radial sheath, and ε_e and ε_i are the mean kinetic energy lost per electron and per ion, respectively. In the calculations we found that the power loss by inelastic and elastic collision is the dominant power loss source in the pressure range of 20-200 mTorr, due to the much higher ε_c than the energy lost per electron and ion lost at the wall $\varepsilon_e + \varepsilon_i$ in our conditions. As shown in figure 7.2, the collisional energy losses per electron-ion pair created, ε_c , is proportional to the ionization energy of the gases. Therefore the electron density in Xe discharge is much higher than in He discharge, even though the electron temperature is lower in Xe discharge.

Figure 7.8 shows the calculated relative production rate of the atomic ion by the direct electron impact ionization from ground state (R7), the electron impact ionization from

excited states (R8-R10) and ionization by excited particle collision (R21-R22). For pressure lower than 100 mTorr the direct ionization is the dominant production mechanism for the

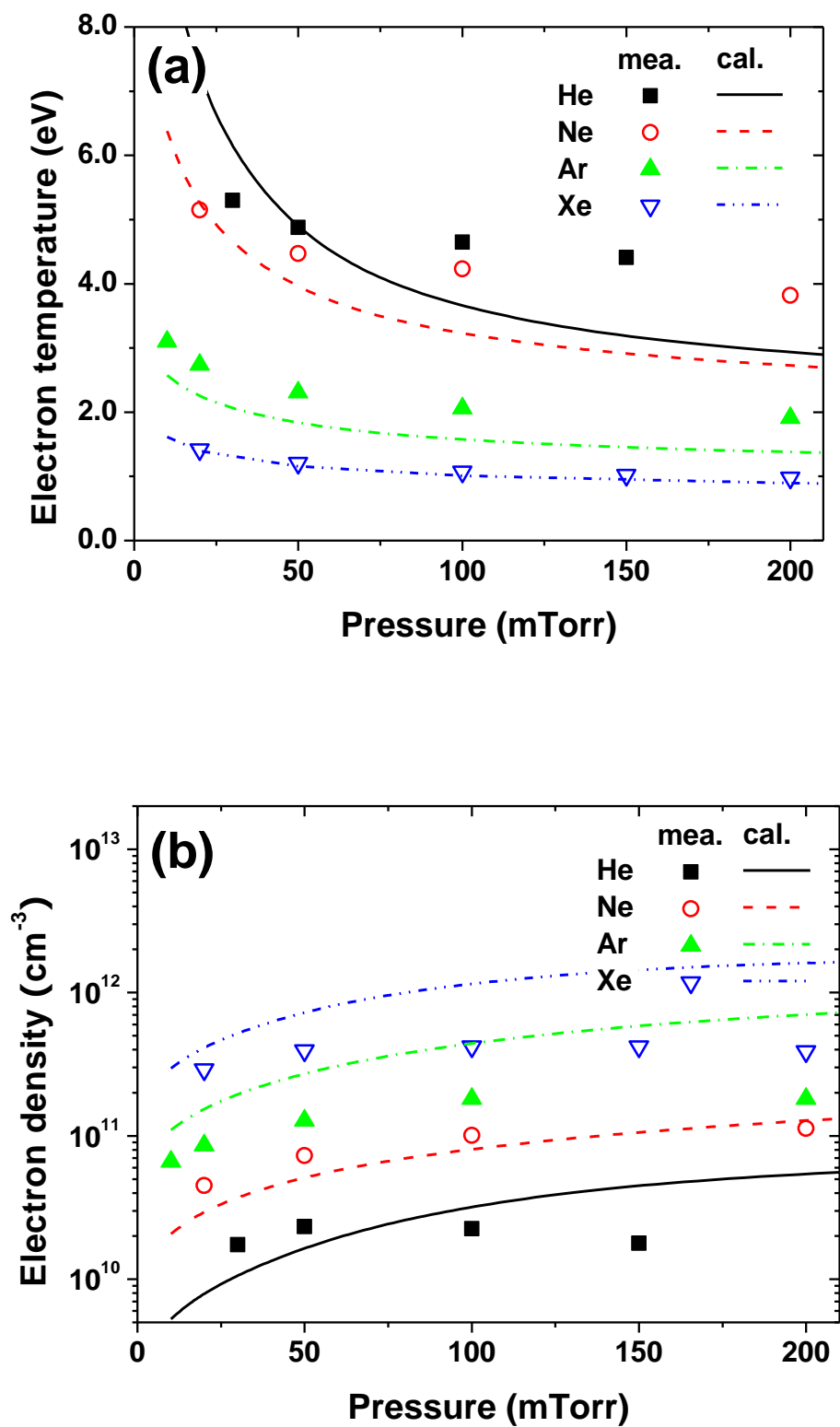


Figure 7.7 Measured and calculated (a) electron temperature and (b) electron density versus

pressure at a fixed RF power in pure He, Ne, Ar and Xe discharge

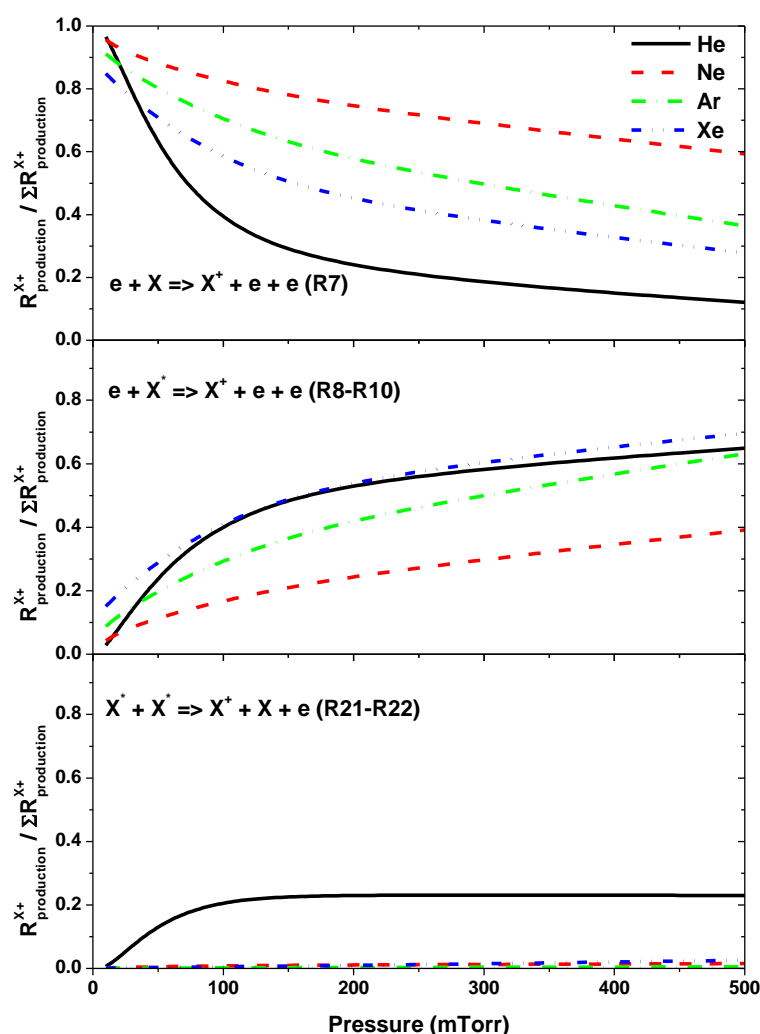


Figure 7.8 Calculated relative production rate of the atomic ion by the direct electron impact ionization from ground state (R7), the electron impact ionization from excited states (R8-R10) and ionization by excited particle collision (R21-R22).

atomic ion whatever gas species due to the high electron temperature, whereas at higher pressure the ionization from excited states becomes the dominant production process. It means that as increase the pressure the excited particles play an important role in the rare gas discharge. Obviously the metastable atoms are the most important particles among all excited species due to long life-time and high excited energy. Particularly relative production rate of He^+ by the excited particle collision (R21-R22) is much higher than other gases at higher pressure. It can be explained by higher reaction coefficient of $\text{He}^{\text{M}} + \text{He}^{\text{M}} \rightarrow \text{He}^+ + \text{He} + e$, and high metastable atom density in He discharge.

7.5.2 Metastable atoms

Figure 7.9 shows the calculated and measured metastable atom density from the absorption spectroscopy of He(2^3S), Ne($1s_5$), Ar($1s_5$) and Xe($1s_5$) as a function of the gas pressure between 20 and 200 mTorr. The uncertainty on metastable atom densities is estimated to be 30 % [5] except for Xe metastable atom density. In natural xenon, there are nine stable isotopes: ^{124}Xe (0.0096%), ^{126}Xe (0.0090%), ^{128}Xe (1.92%), ^{129}Xe (26.4%), ^{130}Xe (4.1%), ^{131}Xe (21.1%), ^{132}Xe (26.9%), ^{134}Xe (10.4%) and ^{136}Xe (8.9%). In addition, two of these nuclei have a nuclear spin (^{129}Xe : $I=1/2$ and ^{131}Xe : $I=3/2$) which brings about a hyperfine splitting of the levels [28]. Due to the isotope shift and hyperfine structure, each transition has several components and the spectral profiles of the lines are quite complex. Recently, Naghshara *et al* [29] developed to estimate absolute Cu atom density, which consists two isotopes: ^{63}Cu (69%) and ^{65}Cu (31%) with a nuclear spin $I=3/2$ for both isotopes. However to the best of our knowledge, there are no available spectroscopic data of Xe isotopes-shift and hyperfine structures to calculate. In the case of Cu atom density, Naghshara *et al* mentioned that the measured atom density neglecting isotopes-shift and hyperfine structures underestimates by about a factor of two.

As shown in figure 7.9, He, Ne and Ar metastable atom densities increase with pressure up to 100 mTorr before saturation. In contrast, in Xe, the metastable atom density continuously decreases with gas pressure. We observe a relatively good agreement between calculation and experimental results as it concerns the orders of magnitude of rare gas densities. It appears however some differences in Ar and Xe discharges. The small increase

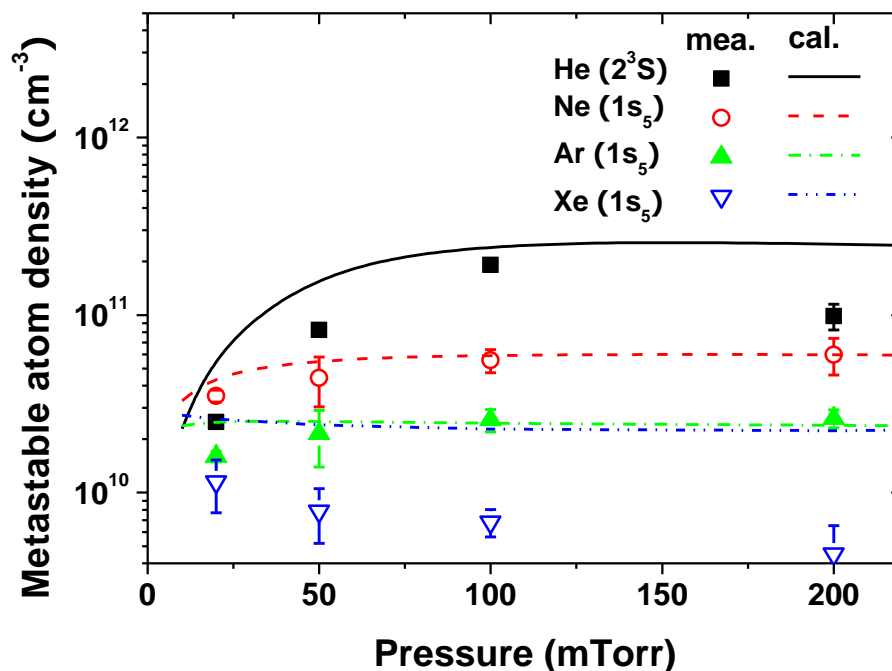


Figure 7.9 Calculated and measured metastable atom density from the absorption spectroscopy of He(2^3S), Ne($1s_5$), Ar($1s_5$) and Xe($1s_5$) as a function of the gas pressure.

of experimental Ar(1s₅) density is not found in the calculation and the calculated Xe(1s₅) density is higher than the measured about 3 times.

The population and de-population of metastable atoms are strongly linked with the electron temperature, the electron density, the radiative decay, the diffusion loss and collisions with other particles [30]. In the calculation we found that the important production mechanisms of the metastable atoms are the direct excitation from ground state (R2) and the radiative decay from higher state X(p) (R12). However when we take into account the opposite reaction of radiative decay (eg: $e + X(p) \leftrightarrow e + X^M + h\nu$), the direct excitation is the dominant production mechanism in the pressure range 20 ~ 200 mTorr.

For the loss of metastable atoms the main mechanisms are the diffusion loss to the wall (R14), electron quenching to resonance states (R4) and excitation to higher states (R5-R6). The calculated loss frequencies of He, Ne, Ar and Xe metastable atoms by diffusion as well as those by electron collision are shown in figure 7.10. As mentioned above the excitation to higher states are strongly linked with the radiative decay, the ‘e-col’ curves in figure 7.10 show the net loss of the electron quenching between metastable and resonance atoms, excitation to higher states, and radiative decay from higher states. The loss of Ar and Xe metastable atoms by the electron collision is always dominant in the pressure range 20 and 200 mTorr. Whereas the diffusion is dominant loss mechanism for He and Ne metastable atoms below 200 mTorr and 50 mTorr, respectively. Moreover the total loss frequency decrease as increase the pressure below 200 mTorr in He discharge. We note that the

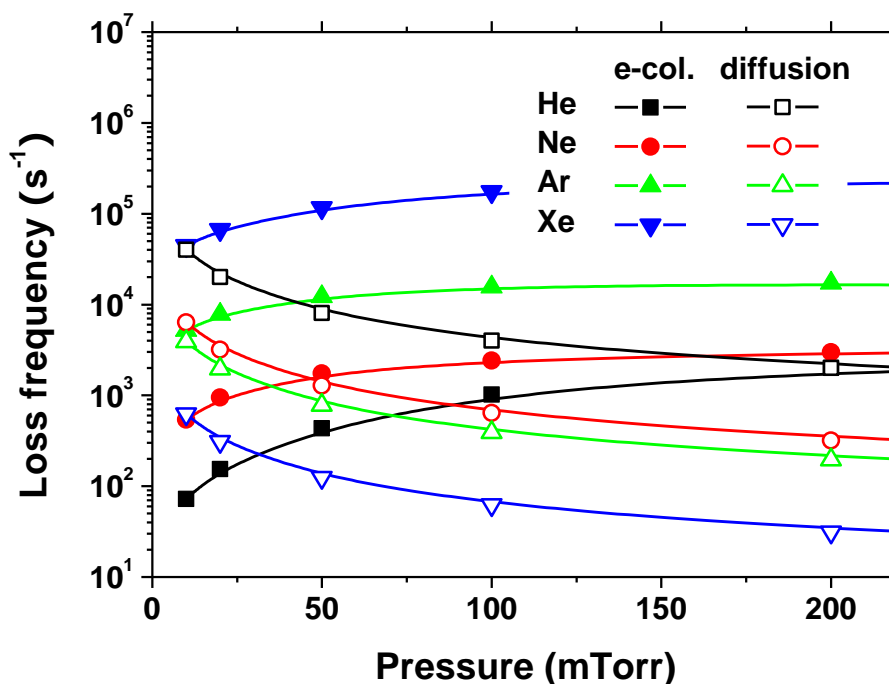


Figure 7.10 Calculated loss frequencies of He, Ne, Ar and Xe metastable atoms by diffusion as well as those by electron collision

measured diffusion coefficient of He_M is $D_M = 470 \text{ cm}^2\text{s}^{-1}\text{Torr}$ [31] is much higher than for the other gases; $200 \text{ cm}^2\text{s}^{-1}\text{Torr}$ [32], $40 \text{ cm}^2\text{s}^{-1}\text{Torr}$ [33] and $19 \text{ cm}^2\text{s}^{-1}\text{Torr}$ [34] for Ne_M , Ar_M and Xe_M , respectively. As a result the big increase of relative production rate of He atom ion by ionization from excited states and ionization by excited particle collision (see figure 7.9) can be explained by the decrease of He metastable loss frequency.

7.5.3 Plasma impedance

Figure 7.11(a) shows the calculated ratio of the electron-neutral collision frequency to the effective collision frequency versus pressure for He, Ne, Ar and Xe discharges. The electron-neutral collision, ν_{en} , becomes the dominant one at high pressure and its importance decreases at low pressure in He and Ne discharge due to stochastic heating, ν_{st} . The contribution of electron-ion collision, ν_{ei} , can be negligible in He, Ne and Ar discharge. However this collision is relatively important in Xe discharge due to high electron density and low electron temperature in equation (7.5).

The ratios of the effective collision frequency to the effective driving frequency versus pressure are shown in figure 12(b). The power transferred to electrons per unit volume by collisional (ohmic) heating is given [11]

$$P_{ohm} = \frac{1}{2} |E|^2 \sigma_{dc} \frac{\nu_{eff}^2}{\omega_{eff}^2 + \nu_{eff}^2} \quad (7.24)$$

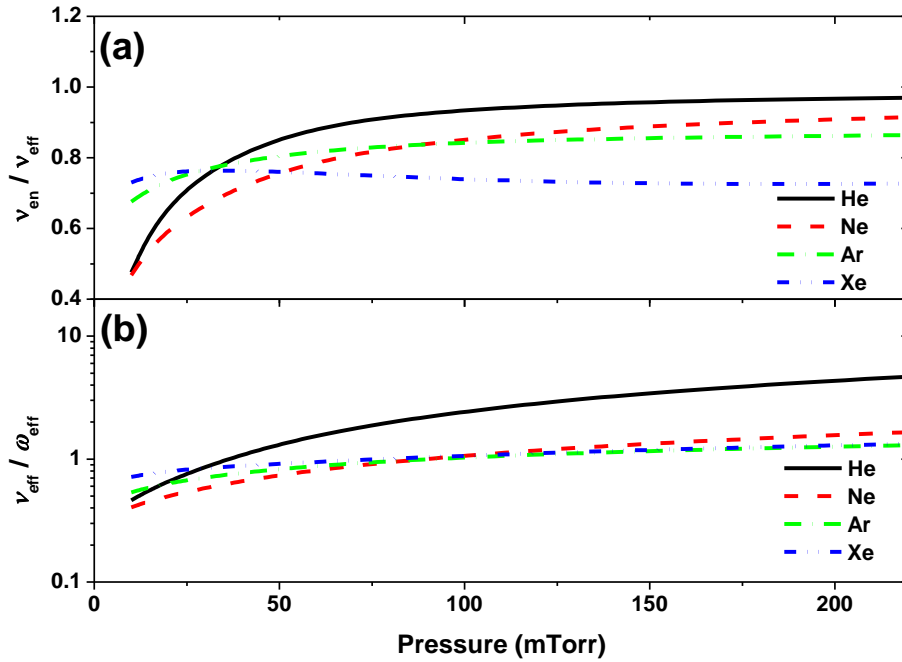


Figure 7.11 Calculated ratio of (a) electron-neutral collision frequency to the effective collision frequency (b) effective collision frequency to the effective driving frequency versus pressure for He, Ne, Ar and Xe discharges

where E is an electric field strength, $\sigma_{dc} = e^2 n_e / m_e \nu_{eff}$ is the dc plasma conductivity. This equation shows that, for a given electric field strength, the transferred power by the collisional heating becomes its maximum when the effective collision frequency ν_{eff} coincides with and the effective RF frequency ω_{eff} . For Ne, Ar and Xe discharge it occurs when the pressure range is 80-100 mTorr, while it is 30 mTorr for He discharge.

The calculated inductive plasma resistance R_p , and self-inductance L_p are shown versus pressure in figure 7.12. Although the electron densities increase with pressure in Ne, Ar and Xe discharges, the plasma resistances are remained almost constants (1 ~ 3 Ω) whatever pressure due to the increase of the effective collision frequency. However it increases up to 11 Ω at 200 mTorr in He discharge because of steep increase of the effective collision frequency as increase pressure as shown in figure 7.11 (b). The inductances by the electron inertia decrease whatever gas species by increases of both electron density and effective collision frequency as increase pressure. It could be understood, the shielding of the applied RF magnetic field by plasma electrons improves as the electron density increase.

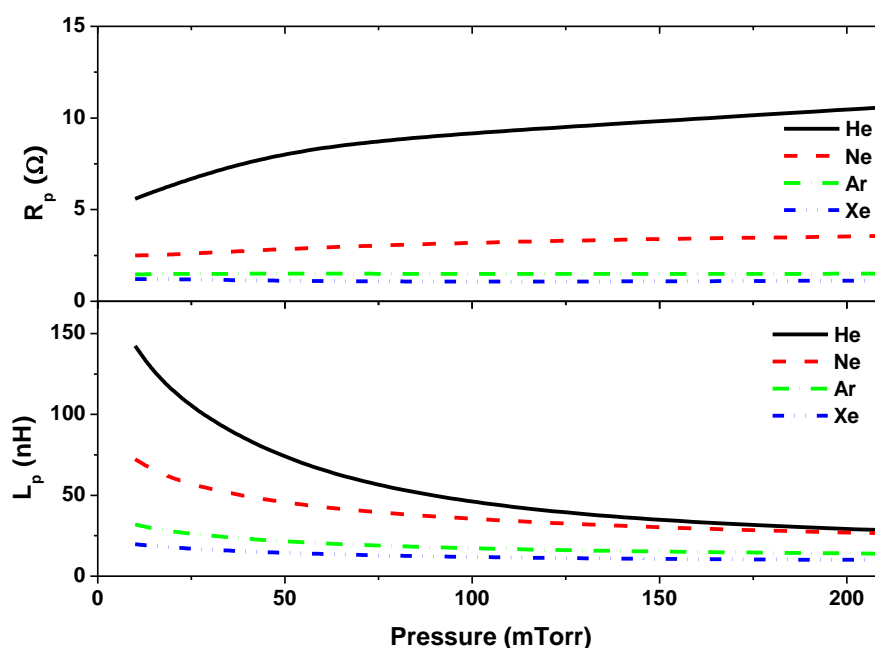


Figure 7.12 Calculated the resistance R_p , and the inductance L_p , in He, Ne, Ar and Xe discharges.

7.6 Conclusion

The global model is developed to calculate the electron temperature and electron density in planar inductive coupled He, Ne, Ar and Xe discharges varying gas pressure at fixed RF power. The calculated results are compared with measured data using a single Langmuir probe and optical absorption spectroscopy. From the simulation we found that the main mechanism of electron creation is the direct electron impact ionization from the ground

state at low pressure, while the metastable atoms play an important role at high pressure. Using calculated the electron density and the electron temperature, the effective collision frequency and the effective driving frequency are calculated as a function of the pressure in He, Ne, Ar and Xe discharges. We found that the electron-neutral collision ν_{en} becomes the dominant one at high pressure and its importance decreases at low pressure in He and Ne discharge due to stochastic heating. Finally, the inductive plasma resistance and the self-inductance are calculated.

Table 7.3 Reaction set used in the model.

	Process	He	Ne	Ar	Xe
Electron impact moment transfer					
R1	$X + e \rightarrow X + e$	[35]	[35]	[35]	[35]
Electron impact excitation and de-excitation					
R2	$X + e \leftrightarrow X(s) + e$	[35]	[35,36]	[37-39]	[35,40]
R2	$X + e \leftrightarrow X(p) + e$	[41]	[35,36]	[37-39]	[35,40]
R3	$X + e \leftrightarrow X(h) + e$	[41]	[36]	[37-39]	[35,40]
R4	$X(s) + e \leftrightarrow X(s) + e$	[41,42]	[18]	[37,43]	[18]
R5	$X(s) + e \leftrightarrow X(p) + e$	[41,42]	[44]	[37,43]	[45,46]
R6	$X(s) + e \leftrightarrow X(h) + e$	[41,42]		[37,43]	
Electron impact ionization					
R7	$X + e \rightarrow X^+ + e + e$	[35]	[35]	[47]	[35]
R8	$X(s) + e \rightarrow X^+ + e + e$	[48,49]	[49,50]	[49]	[48,51]
R9	$X(p) + e \rightarrow X^+ + e + e$			[52]	[51]
R10	$X(h) + e \rightarrow X^+ + e + e$			[52]	
Radiative decay					
R11	$X(s) \rightarrow X + h\nu$		[53]	[53]	[53]
R12	$X(p) \rightarrow X(s) + h\nu$	[53]	[53]	[53]	[53]
R13	$X(h) \rightarrow X(p) + h\nu$	[53]	[53]	[53]	[53]
Diffusion loss					
R14	$X(s,p,h) \rightarrow X \text{ (wall)}$			$D_{X,n}/\Lambda_0^2$	
R15	$X^+ \rightarrow X \text{ (wall)}$			$2u_{B,X^+} (R^2 h_L + RLh_R) / R^2 L$	
R16	$\frac{1}{2} X_2^+ \rightarrow X \text{ (wall)}$			$2u_{B,X_2^+} (R^2 h_L + RLh_R) / R^2 L$	

Table 7.4 Reaction set used in the model.

Process	Rate coefficient k (cm^3s^{-1} , cm^6s^{-1})	References
Chemical – ionization		
R17 $X(s) + X(s) \rightarrow X^+ + X + e$	He : $3.36 \times 10^{-9}(1-1)$, $3.92 \times 10^{-9}(1-3)$, $0.92 \times 10^{-9}(3-3)$ Ne : $6.5 \times 10^{-10}(T_g/300)^{0.5}$ Ar : $5.0 \times 10^{-10}(T_g/300)^{0.5}$ Xe : 5.0×10^{-10}	[54] [54] [54] [54]
R18 $X(p) + X(p) \rightarrow X^+ + X + e$	He : 3.36×10^{-9} Ne : $1.0 \times 10^{-9}(T_g/300)^{0.5}$ Ar : $7.0 \times 10^{-10}(T_g/300)^{0.5}$ Xe : 5.0×10^{-10}	[54] [55] [55] [56]
Three body recombination		
R19 $X^+ + e + e \rightarrow X(h) + e$	He : $7.1 \times 10^{-20}(T_e \times 11600/300)^{-4.3}$ Ne : $1.0 \times 10^{-19}(T_e \times 11605/300)^{-4.5}$ Ar : $1.0 \times 10^{-19}(T_e \times 11605/300)^{-4.5}$ Xe : $3.9 \times 10^{-20}(T_e \times 11605/300)^{-4.5}$	[57] a [58] [59]
R20 $X^+ + e + X \rightarrow X(h) + X$	He : $6.0 \times 10^{-27}(T_e \times 11600/300)^{-2.5}$ Ne : $6.0 \times 10^{-27}(T_e \times 11600/300)^{-2.5}$ Ar : $6.0 \times 10^{-27}(T_e \times 11600/300)^{-2.5}$ Xe : $6.0 \times 10^{-27}(T_e \times 11600/300)^{-2.5}$	a [55] [58] a
Kinetics of X_2^+		
R21 $X^+ + X + X \rightarrow X_2^+ + X$	He : $4.3 \times 10^{-30}(T_g/300)^{-0.6}$ Ne : $6.5 \times 10^{-32}(T_g/300)^{-0.75}$ Ar : $2.5 \times 10^{-31}(T_g/300)^{-1.5}$ Xe : $2.0 \times 10^{-31}(T_g/300)^{-0.5}$	[60] [55] [55,61] [59,62]
R22 $X(s) + X(s) \rightarrow X_2^+ + e$	He : 2.0×10^{-9} Ne : 6.5×10^{-10} Ar : $6.3 \times 10^{-10}(T_g/300)^{-0.5}$ Xe : 5.0×10^{-10}	[63] a [61] a
R23 $X_2^+ + e \rightarrow X(h) + X$	He : $4.0 \times 10^{-9}(T_e \times 11605/300)^{-0.5}$ Ne : $1.36 \times 10^{-7}(T_e \times 11605/300)^{-0.43}$ Ar : $7.28 \times 10^{-7}(T_e \times 11605/300)^{-0.67}$ Xe : $2.96 \times 10^{-8}(T_e \times 11605/300)^{-0.5}$	[60] [55,64] [55,61] [56]
R24 $X_2^+ + e \rightarrow X(p) + X$	He : $5.0 \times 10^{-10}(T_e \times 11605/300)^{-0.5}$ Ne : $1.7 \times 10^{-8}(T_e \times 11605/300)^{-0.43}$ Ar : $9.1 \times 10^{-8}(T_e \times 11605/300)^{-0.67}$ Xe : $3.7 \times 10^{-9}(T_e \times 11605/300)^{-0.5}$	a [55] [55] [56]
R25 $X_2^+ + e \rightarrow X(s) + X$	He : $5.0 \times 10^{-10}(T_e \times 11605/300)^{-0.5}$ Ne : $1.7 \times 10^{-8}(T_e \times 11605/300)^{-0.43}$ Ar : $9.1 \times 10^{-8}(T_e \times 11605/300)^{-0.67}$ Xe : $3.7 \times 10^{-9}(T_e \times 11605/300)^{-0.5}$	a [55] [55] [56]

a : assume

7.7 References

- [1] Piejak R B, Godyak V A and Alexandrovich B M, 1992 *Plasma Sources Sci. Technol.* **1** 179
- [2] El-Fayoumi I M and Jones I R, 1998 *Plasma sources Sci. Technol.* **7** 179
- [3] Gudmundsson J T and Lieberman M A, 1998 *Plasma Sources Sci. Technol.* **7** 83
- [4] Cunge G, Crowley B, Vender D and Turner M M 1999 *Plasma Sources Sci. Technol.* **8** 576
- [5] Mitchell A C G and Zemanski M W 1991 *Resonance Radiation and Excited Atoms* (Cambridge: Cambridge University Press)
- [6] Ricard A, Nouvellon C, Konstantinidis S, Dauchot J P, Wautelet M and Hecq M 2002 *J. Vac. Sci. Technol. A* **20** 1488
- [7] Konstantinidis S, Ricard A, Ganciu M, Dauchot J P, Ranea C and Hecq M 2004 *J. Appl. Phys.* **95** 2900
- [8] Griem H R 1964 *Plasma Spectroscopy* (New York: McGraw-Hill)
- [9] Phelps A V 1991 *J. Phys. Chem. Ref. Data* **20** 557
- [10] Phelps A V (unpublished), "ftp://jila.colorado.edu/collision_data/"
- [11] Lieberman M A and Lichtenberg A J 2005 *Principles of Plasma Discharges and Materials Processing 2nd ed.* (New York: Wiley)
- [12] Pancheshnyi S, Eismann B, Hagelaar G J M and Pitchford L C, Computer code ZDPlasKin, <http://www.zdplaskin.laplace.univ-tlse.fr> (University of Toulouse, LAPLACE, CNRS-UPS-INP, Toulouse, France, 2008).
- [13] Godyak V A, Piejak R B and Alexandrovich B M 1993 *J. Appl. Phys.* **73** 3657
- [14] Godyak V A and Kolobov V I 1998 *Phys. Rev. Lett.* **81** 369–372
- [15] Godyak V A, Meytlis V P and Strauss H R 1995 *IEEE Trans. Plasma Sci.* **23** 728–734
- [16] Bartschat K and Zeman V 1999 *Phys. Rev. A* **59** R2552
- [17] Dasgupta A, Bartschat K, Vaid D, Grum-Grzhimailo A N, Madison D H, Blaha M and Giuliani J L 2002 *Phys. Rev. A* **65** 042724
- [18] Donnelly V M 2004 *J. Phys. D: Appl. Phys.* **37** R217
- [19] Ivanov V A and Prikhodko A S 1991 *Opt. Spectrosc.* **70** 294
- [20] Ivanov V A and Makasyuk I V 1990 *Opt. Spectrosc.* **69** 308
- [21] El-Fayoumi I M, Jones I R and Turner M M 1998 *J. Phys. D: Appl. Phys.* **31** 3082
- [22] Lee M H and Chung C W 2006 *Phys. Plasmas* **13** 063510
- [23] Lister G G, Li Y M and Godyak V A 1996 *J. Appl. Phys.* **79** 8993
- [24] Vahedi V, Lieberman M A, Dipeso G, Rognlien T D and Hewett D 1995 *J. Appl. Phys.* **78** 1446

-
- [25] Miyamoto K 1989 *Plasma Physics for Nuclear Fusion* (Cambridge, MA: MIT Press)
- [26] Godyak V A and Sternberg N 1990 *Phys. Rev. A* **42** 2299
- [27] Bai K H, Chang H Y and Uhm H S 2001 *Appl. Phys. Lett.* **79** 1596
- [28] Jackson D A, F.R.S. and Coulombe M C 1974 *Proc. R. Soc. Lond. A* 338 277
- [29] Naghshara H, Sobhanian, Khorram S and Sadeghi N 2001 *J. Phys. D: Appl. Phys.* **44** 025202
- [30] Kang N, Gaboriau F, Oh S G and Ricard A 2011 *Plasma Sources Sci. Technol.* **20** 035002
- [31] R.Deloche, P.Monchicourt, P.Cheret, and F.Lambert, *Phys.Rev.***A13**(1976)1140
- [32] M. A. Biondi, *Phys. Rev.* **82** (1951) 453
- [33] C. M. Ferreira, J. Loureiro, and A. Ricard, *J. Appl. Phys.* **57** (1985) 82
- [34] A. Barbet, N. Sadeghi, and J. C. Pebay-Peyroula, *J. Phys. B: Atom. Molec. Phys.* **8** (1975) 1776
- [35] Phelps A V database, <http://www.lxcat.laplace.univ-tlse.fr>, retrieved December 5, 2010.
- [36] Chilton J E, Stewart M D and Lin C C 2000 *Phys. Rev. A* **61** 052708
- [37] Bartschat K and Zeman V 1999 *Phys. Rev. A* **59** R2552
- [38] Chilton J E and Lin C C 1999 *Phys. Rev. A* **60** 3712
- [39] Weber T, Boffard J B and Lin C C 2003 *Phys. Rev. A* **68** 032719
- [40] Fons J T and Lin C C 1998 *Phys. Rev. A* **58** 4603
- [41] Bartschat K 1998 *J. Phys. B: At. Mol. Opt. Phys.* **31** L469
- [42] Fon W C, Berrington K A, Burke P G and Kingston A E 1981 *J. Phys. B: At. Mol. Phys.* **14** 2921
- [43] Jung R O, Boffard J B, Anderson L W and Lin C C 2007 *Phys. Rev. A* **75** 052707
- [44] Boffard J B, Keeler M L, Piech G A, Anderson L W and Lin C C 2001 *Phys. Rev. A* **64** 032708
- [45] Jung R O, Boffard J B, Anderson L W and Lin C C 2005 *Phys. Rev. A* **72** 022723
- [46] Jung R O, Boffard J B, Anderson L W and Lin C C 2009 *Phys. Rev. A* **80** 062708
- [47] Rapp D and Englander-Golden P 1965 *J. Chem. Phys.* **43** 1464
- [48] Deutsch H, Becker K, Matt S and Märk T D 1999 *J. Phys. B: At. Mol. Phys.* **32** 4249
- [49] Ali M A and Stone P M 2008 *Int. J. Mass Spectrom.* **271** 51
- [50] Balance C P, Griffin D C, Ludlow J A and Pindzola M S 2004 *J. Phys. B: At. Mol. Opt. Phys.* **37** 4779
- [51] Hyman H A 1979 *Phys. Rev. A* **20** 855
- [52] Zhu X M and Pu Y K 2010 *J. Phys. D: Appl. Phys.* **43** 015204
- [53] NIST Atomic Spectra Database, <http://physics.nist.gov/asd3>

- [54] Wenig G, Schulze M, Awakowicz P and v Keudell A 2006 *Plasma Sources Sci. Technol.* **15** S35
- [55] Rolin M N, Shabunya S I, Rostaing J C and Perrin J M 2007 *Plasma Sources Sci. Technol.* **16** 480
- [56] Rauf S and Kushner M J 1999 *J. Appl. Phys.* **85** 3460
- [57] Collins C B, Hicks H S, Wells W E and Burton R 1972 *Phys. Rev. A* **6** 1545
- [58] Bogaerts A, Gijbels R and Jackson G P 2003 *J. Anal. At. Spectrom.* **18** 533
- [59] Golubovskii Y B, Lange H, Maiorov V A, Porokhova I A and Sushkov V P 2003 *J. Phys. D: Appl. Phys.* **36** 694
- [60] Jonkers J, van de Sande M, Sola A, Gamero A, Rodero A and van der Mullen J 2003 *Plasma Sources Sci. Technol.* **12** 464
- [61] Bultel A, Ootegem B, Bourdon A and Vervisch R 2002 *Phys. Rev. E* **65** 046406
- [62] Eckstrom D J, Nakano H H, Lorents D C, Rothem T, Betts J A, Lainhart M E, Dakin D A and Maenchen J E 1998 *J. Appl. Phys.* **64** 1679
- [63] Stevefelt J, Pouvesle J M and Bouchoule A 1982 *J. Chem. Phys.* **76** 4006
- [64] Philbrick J, Mehr F J and Biondi M A 1969 *Phys. Rev.* **181** 271

Chapter 8

General conclusion

TO understand the RF ICP discharges, some important characteristics were described such as the effective collision frequency, the heating mechanism, and the power transferred to the plasma electrons. For the electrical conductivity, the effective collision frequency and the effective RF driving frequency were calculated as function of the pressure and the electron temperature in RF discharge. Using this value the electromagnetic field components of a planar ICP reactor were given with analytical expressions to calculate the transferred power to the plasma electrons by the capacitive coupling and the inductive coupling. Finally using the transformer model we have shown the plasma impedance, the coil current and voltage.

To understand the chemical kinetics in the discharge, we have described the global model which consists of the particle and the electron energy balance equations. The general expression of energy balance for non-Maxwellian electrons was provided.

The basic principles of some methods of plasma diagnostics used in this study were introduced such as optical emission spectroscopy (OES), optical absorption spectroscopy (OAS), two-photon absorption laser-induced fluorescence (TALIF) and Langmuir probe. We have provided the calculation of ro-vibrational spectra of N_2 discharge, and the estimation of rotational and vibrational temperature from measured spectra. This technique was applied to deduce the gas temperature in discharges containing N_2 gas.

In a low pressure argon discharge, a new method was proposed to improve the precision of the pressure-dependent electron temperature calculated by the line ratio method. The quantification of the cross-section was investigated experimentally to contain the influencing factors in the pressure dependence mainly by radiation trapping. Using the electron energy distribution functions (EEDFs) and the electron density from Langmuir probe, we have provided the coefficient of the cascade cross-section as a function of the pressure for argon $4p_1$ and $4p_5$. We have shown also the effective electron temperature calculated by the corrected cascade cross-section and compare with Langmuir probe.

The production of argon excited states in the afterglow of pulse discharge was investigated. Experimentally time resolved OES, OAS and Langmuir probe were used to measure the emission of highly excited states, metastable atom density, electron density and electron temperature. To understand the behavior of the afterglow a time dependent global model was developed. We found that during the pulse-on time the electron impact excitation and the ionization from the ground state and Ar ($3p^54s$) are the dominant population processes for all excited states, while it plays no role in the afterglow since the electron temperature decreases abruptly at 10 mTorr and 200 mTorr. The radiative decay is both the dominant gain and loss of each state. Also we found during the afterglow the main source of all excited states is the three body electron-ion recombination. As a consequence with this reaction argon highly excited state can be populated more than during the pulse-on time.

We have explored the mechanism of E - H mode transition and its hysteresis using global model and transformer model. The total absorbed power by plasma electrons and coil current were calculated as a function of the electron density at fixed injected power rather than fixed coil current as previously shown in the literature. We found that the transition is due to difference of absorbed power between E and H mode. Moreover the calculation results show that existence of inaccessible region between E and H mode, as well as threshold coil current and minimum absorbed power for the H mode.

The dissociation of the nitrogen molecule in an Ar-N₂ ICP discharge was studied both experimentally and theoretically. Using TALIF we found an increase of the dissociation rate in highly Ar-diluted region. A global (volume averaged) model was developed to understand the behavior of the Ar-N₂ discharge. The calculated results were compared with the measured results, obtaining reasonably good agreement. In pure nitrogen discharge we found that the N atoms are mainly created by electron impact dissociation at low pressure (20 mTorr) while it is due to metastable-metastable pooling dissociation at high pressure (200 mTorr). In Ar-N₂ discharge, the N atom density increases despite less amount of N₂ molecule in highly Ar-diluted region at 200 mTorr. From the model we found that charge transfer from Ar⁺ to N₂ is an important source of nitrogen dissociation in Ar-N₂ discharge.

We have developed the global model of He, Ne, Ar and Xe discharges to calculate the electron temperature and the electron density. The calculated results compared with experiments and discuss the dominant creation sources and the routes of loss for electron and metastable atoms as function of pressure. And the transformer model was used to calculate the electrical properties of He, Ne, Ar and Xe discharges.

In the present study we have investigated the characteristics of low pressure inductively coupled plasma discharges, both physically and on a chemical point of view, using theoretical modeling and experimental diagnostic methods for plasma processing. Even though this work is only a first step for utilization of the integrated diagnostic methods (modeling and experiment), we believe that it can be helpful to understand the ICP discharges. Moreover this method can be furthermore developed for various actual processing such as etching, ion implantation, PECVD and sputtering.

Appendix

Electromagnetic fields in TCP reactor

Figure A.1 shows a schematic diagram of a planar inductive coupled plasma source. The cylindrical coordinate system (r, θ, z) is used in this study. The bottom of the chamber is located at $z = 0$, the bottom of the dielectric window at $z = L$ and the plane of the induction coil is at $z = L + D$. The power is transferred by a capacitive (left-hand side) and an inductive coupling (right-hand side) as shown in figure A.1. The transferred power by each coupling can be calculated from Maxwell's equations.

In this study the electromagnetic fields in the ICP reactor are divided into two regions; $0 < z < L$ and $L < z < L + D$. The planar induction coil excites RF magnetic fields B_r , B_θ and B_z , which are respectively the radial, azimuthal and axial components and the corresponding components of RF electric fields E_r , E_θ and E_z . The electromagnetic field components of B_θ , E_r and E_z are capacitively coupled with plasma electrons while the remaining field components E_θ , B_r and B_z are inductively coupled. The general Maxwell's equations, if we assume time variation of the field $\exp(j\omega t)$ (for example, $\mathbf{E}(r, \theta, z, t) = \mathbf{E}(r, \theta, z) \exp(j\omega t)$), are given as follows;

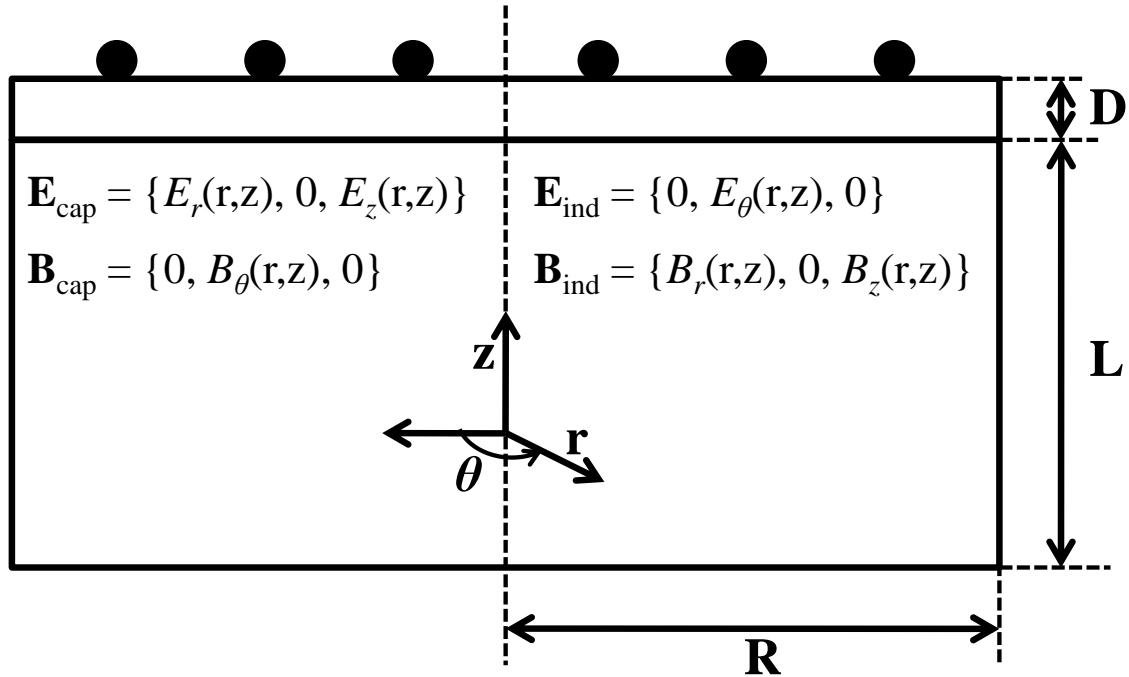


Figure A.1 A schematic diagram of the planar ICP reactor used in this study.

$$\nabla \cdot \mathbf{E} = 0 \quad (\text{A.1})$$

$$\nabla \cdot \mathbf{B} = 0 \quad (\text{A.2})$$

$$\nabla \times \mathbf{E} = -j\omega \mathbf{B} \quad (\text{A.3})$$

$$\nabla \times \mathbf{B} = \mu_0 \mathbf{J} + j\omega \varepsilon \mu_0 \mathbf{E} \quad (\text{A.4})$$

$$\mathbf{J} = \sigma_p \mathbf{E} \quad (\text{A.5})$$

where ω is the RF frequency, μ_0 is the permeability of free space, ε is the absolute dielectric constant for each region, and σ_p is the plasma conductivity.

A.1 Capacitive coupled discharge

Within the plasma and the dielectric window, equation (A.4) can be re-written as

$$\nabla \times \mathbf{B} = \begin{cases} j\omega \frac{\varepsilon_p}{c^2} \mathbf{E} & \text{for } 0 < z < L \\ j\omega \frac{\varepsilon_r}{c^2} \mathbf{E} & \text{for } L < z \leq L+D \end{cases} \quad (\text{A.6})$$

where ε_r is the dielectric constant of the quartz window, and ε_p is the relative dielectric constant of the plasma given by

$$\varepsilon_p = 1 - \frac{\omega_{pe}^2}{\omega(\omega - j\nu)} \quad (\text{A.7})$$

where ω_{pe} is the plasma oscillation frequency given by $\omega_{pe} = (e^2 n_e / \varepsilon_0 m_e)^{1/2}$ and ν is the electron collision frequency.

In the plasma ($0 < z < L$), B_θ satisfies the following equations:

$$\frac{1}{r} \frac{\partial}{\partial r} \left(r \frac{\partial B_\theta}{\partial r} \right) + \frac{\partial^2 B_\theta}{\partial z^2} - \frac{B_\theta}{r^2} = -\varepsilon_p \left(\frac{\omega}{c} \right)^2 B_\theta \quad (\text{A.8})$$

$$E_r = \frac{jc^2}{\omega \varepsilon_p} \frac{\partial B_\theta}{\partial z} \quad (\text{A.9})$$

$$E_z = -\frac{jc^2}{\omega \varepsilon_p} \frac{1}{r} \frac{\partial (r B_\theta)}{\partial z} \quad (\text{A.10})$$

In the dielectric window ($L < z < L+D$), we have

$$\frac{1}{r} \frac{\partial}{\partial r} \left(r \frac{\partial B_\theta}{\partial r} \right) + \frac{\partial^2 B_\theta}{\partial z^2} - \frac{B_\theta}{r^2} = -\varepsilon_r \left(\frac{\omega}{c} \right)^2 B_\theta \quad (\text{A.11})$$

$$E_r = \frac{jc^2}{\omega \varepsilon_r} \frac{\partial B_\theta}{\partial z} \quad (\text{A.12})$$

$$E_z = -\frac{jc^2}{\omega\epsilon_r} \frac{1}{r} \frac{\partial(rB_\theta)}{\partial z} \quad (\text{A.13})$$

Equations (A.8) and (A.11) can be solved using the method of separation of variables, we have

$$B_\theta(r, z) = \begin{cases} [A_c \exp(qz) + B_c \exp(-qz)] J_1(\lambda r) & \text{for } 0 < z < L \\ [C_c \exp(sz) + D_c \exp(-sz)] J_1(\lambda r) & \text{for } L < z < L+D \end{cases} \quad (\text{A.14})$$

$$E_r(r, z) = \begin{cases} \frac{jc^2}{\omega\epsilon_p} q [A_c \exp(qz) - B_c \exp(-qz)] J_1(\lambda r) & \text{for } 0 < z < L \\ \frac{jc^2}{\omega\epsilon_r} s [C_c \exp(sz) - D_c \exp(-sz)] J_1(\lambda r) & \text{for } L < z < L+D \end{cases} \quad (\text{A.15})$$

$$E_z(r, z) = \begin{cases} -\frac{jc^2}{\omega\epsilon_p} \lambda [A_c \exp(qz) + B_c \exp(-qz)] J_0(\lambda r) & \text{for } 0 < z < L \\ -\frac{jc^2}{\omega\epsilon_r} \lambda [C_c \exp(sz) + D_c \exp(-sz)] J_0(\lambda r) & \text{for } L < z \leq L+D \end{cases} \quad (\text{A.16})$$

where

$$q = \left[\lambda^2 - \epsilon_p (\omega/c)^2 \right]^{1/2} \quad (\text{A.17})$$

$$s = \left[\lambda^2 - \epsilon_r (\omega/c)^2 \right]^{1/2} \quad (\text{A.18})$$

By means of perfect conductor boundary conditions, we assume that the tangential electric field component and normal magnetic field component at the wall are equal to zero; that is, $E_z(R, z) = 0$ and $E_r(r, 0) = 0$. This leads to $J_0(\lambda_n R) = 0$, which gives us a set of eigenvalues for λ given by

$$\lambda_n = x_n^{(0)} / R \quad (\text{A.19})$$

where $x_n^{(0)}$ is the zeros of the zero order Bessel function, $J_0(x_n^{(0)}) = 0$. It also follows that $A_c = B_c$. Using these results in equations (A.14)-(A.16), we obtain the following solutions.

$$B_\theta(r, z) = \begin{cases} \sum_{n=1}^{\infty} A_{cn} \cosh(q_n z) J_1(\lambda_n r) & \text{for } 0 < z < L \\ \sum_{n=1}^{\infty} [C_{cn} \exp(s_n z) + D_{cn} \exp(-s_n z)] J_1(\lambda_n r) & \text{for } L < z < L+D \end{cases} \quad (\text{A.20})$$

$$E_r(r, z) = \begin{cases} \frac{jc^2}{\omega\epsilon_p} \sum_{n=1}^{\infty} q_n A_{cn} \sinh(q_n z) J_1(\lambda_n r) & \text{for } 0 < z < L \\ \frac{jc^2}{\omega\epsilon_r} \sum_{n=1}^{\infty} s_n [C_{cn} \exp(s_n z) - D_{cn} \exp(-s_n z)] J_1(\lambda_n r) & \text{for } L < z < L + D \end{cases} \quad (\text{A.21})$$

$$E_z(r, z) = \begin{cases} -\frac{jc^2}{\omega\epsilon_p} \sum_{n=1}^{\infty} \lambda_n A_{cn} \cosh(q_n z) J_0(\lambda_n r) & \text{for } 0 < z < L \\ -\frac{jc^2}{\omega\epsilon_r} \sum_{n=1}^{\infty} \lambda_n [C_{cn} \exp(s_n z) + D_{cn} \exp(-s_n z)] J_0(\lambda_n r) & \text{for } L < z < L + D \end{cases} \quad (\text{A.22})$$

At the interface of $z = L$, which is between the plasma region and dielectric window, the tangential component of the electric field, E_r , is continuous while $\epsilon_r E_z(r, L_+) = \epsilon_p E_z(r, L_-)$. These boundary conditions lead to the following set of equations for the coefficients A_{cn} , B_{cn} and C_{cn} :

$$\epsilon_p s_n [C_{cn} \exp(s_n L) - D_{cn} \exp(-s_n L)] = \epsilon_r q_n A_{cn} \sinh(q_n L) \quad (\text{A.23})$$

$$C_{cn} \exp(s_n L) + D_{cn} \exp(-s_n L) = A_{cn} \cosh(q_n L) \quad (\text{A.24})$$

$$C_{cn} \exp[s_n (L + D)] - D_{cn} \exp[-s_n (L + D)] = u_n \quad (\text{A.25})$$

Equations (A.23)-(A.25) yield the following solutions for A_{cn} , C_{cn} and D_{cn} in terms of u_n :

$$A_{cn} = \frac{\epsilon_p s_n u_n}{\epsilon_p s_n \cosh(q_n L) \sinh(s_n D) + \epsilon_r q_n \sinh(q_n L) \cosh(s_n D)} \quad (\text{A.26})$$

$$C_{cn} = \frac{A_{cn} \exp(-s_n L)}{2\epsilon_p s_n} [\epsilon_p s_n \cosh(q_n L) + \epsilon_r q_n \sinh(q_n L)] \quad (\text{A.27})$$

$$D_{cn} = \frac{A_{cn} \exp(s_n L)}{2\epsilon_p s_n} [\epsilon_p s_n \cosh(q_n L) - \epsilon_r q_n \sinh(q_n L)] \quad (\text{A.28})$$

$$u_n = -\frac{j2\omega\epsilon_r E_0}{c^2 \lambda_n s_n R^2 J_1^2(\lambda_n R)} \int_0^R J_0(\lambda_n r) dr \quad (\text{A.29})$$

where E_0 is the constant amplitude of electric field in the radial direction given by $E_0 = V / R$, where V is the voltage across the RF coil.

A.2 Inductive coupled discharge

Maxwell's equation (A.3) can be re-written as:

$$\nabla \times (\nabla \times \mathbf{E}) = -j\omega\mu_0\sigma_p \mathbf{E} = \alpha^2 \mathbf{E} \quad (\text{A.30})$$

where the plasma conductivity σ_p and α are given by

$$\sigma_p = \frac{\varepsilon_0 \omega_{pe}^2}{\nu + j\omega} \quad (\text{A.31})$$

$$\alpha = \left(\frac{(\omega_{pe}/c)^2}{1 - j\nu/\omega} \right)^{1/2} \quad (\text{A.32})$$

Equations (A.3) and (A.30) yield the following three scalar equations for E_θ , B_r and B_z :

$$\frac{1}{r} \frac{\partial}{\partial r} \left(r \frac{\partial E_\theta}{\partial r} \right) - \frac{E_\theta}{r^2} + \frac{\partial^2 E_\theta}{\partial z^2} = \alpha^2 E_\theta \quad (\text{A.33})$$

$$-j\omega B_r = -\frac{\partial E_\theta}{\partial z} \quad (\text{A.34})$$

$$-j\omega B_z = \frac{1}{r} \frac{\partial (r E_\theta)}{\partial r} \quad (\text{A.35})$$

Equations (A.33) can be solved using the method of separation of variables, we have

$$E_\theta(r, z) = \begin{cases} [A_i \exp(kz) + B_i \exp(-kz)] J_1(\beta r) & \text{for } 0 < z < L \\ [C_i \exp(\beta z) + D_i \exp(-\beta z)] J_1(\beta r) & \text{for } L < z < L+D \end{cases} \quad (\text{A.36})$$

$$B_r(r, z) = \begin{cases} -\frac{j}{\omega} k [A_i \exp(kz) - B_i \exp(-kz)] J_1(\beta r) & \text{for } 0 < z < L \\ -\frac{j}{\omega} \beta [C_i \exp(\beta z) - D_i \exp(-\beta z)] J_1(\beta r) & \text{for } L < z < L+D \end{cases} \quad (\text{A.37})$$

$$B_z(r, z) = \begin{cases} \frac{j}{\omega} \beta [A_i \exp(kz) + B_i \exp(-kz)] J_0(\beta r) & \text{for } 0 < z < L \\ \frac{j}{\omega} \beta [C_i \exp(\beta z) + D_i \exp(-\beta z)] J_0(\beta r) & \text{for } L < z < L+D \end{cases} \quad (\text{A.38})$$

where

$$k = [\alpha^2 + \beta^2]^{1/2} \quad (\text{A.39})$$

$$\beta_n = x_n^{(1)}/R \quad (\text{A.40})$$

where $x_n^{(1)}$ is the zeros of the first order Bessel function, $J_1(x_n^{(1)}) = 0$.

At $z = L+D$, the boundary conditions are

$$B_r[r, (L+D)_-] = \mu_0 H_{r1}(r) \quad (\text{A.41})$$

$$B_r[r, (L+D)_+] = \mu_0 H_{r2}(r) \quad (\text{A.42})$$

$$H_{r2} - H_{r1} = K_\theta \quad (\text{A.43})$$

where K_θ is the surface current which is related to the RF current given by

$$K_\theta = \frac{Ni_{coil}}{R} \quad (\text{A.44})$$

where N is the number of turns of the induction coil. Also the tangential electric field should be continuous:

$$E_\theta[r, (L+D)_-] = E_\theta[r, (L+D)_+] \quad (\text{A.45})$$

At $z = L$, which means the boundary between the quartz window and the plasma, the tangential electric field and the normal magnetic field are continuous:

$$E_\theta[r, L_-] = E_\theta[r, L_+] \quad (\text{A.46})$$

$$B_r[r, L_-] = B_r[r, L_+] \quad (\text{A.47})$$

At the interface between the plasma and the chamber wall, the tangential electric field and the normal magnetic field should be zero.

Using these boundary conditions, equations (A.36)-(A.38) can be re-written as:

$$E_\theta(r, z) = \begin{cases} \sum_{n=1}^{\infty} A_n \sinh(k_n z) J_1(\beta_n r) & \text{for } 0 < z < L \\ \sum_{n=1}^{\infty} [C_n \exp(-\beta_n z) + D_n \exp(\beta_n z)] J_1(\beta_n r) & \text{for } L < z < L+D \end{cases} \quad (\text{A.48})$$

$$B_r(r, z) = \begin{cases} -\frac{j}{\omega} \sum_{n=1}^{\infty} A_n k_n \cosh(k_n z) J_1(\beta_n r) & \text{for } 0 < z < L \\ -\frac{j}{\omega} \sum_{n=1}^{\infty} \beta_n [-C_n \exp(-\beta_n z) + D_n \exp(\beta_n z)] J_1(\beta_n r) & \text{for } L < z < L+D \end{cases} \quad (\text{A.49})$$

$$B_z(r, z) = \begin{cases} \frac{j}{\omega} \sum_{n=1}^{\infty} A_n \beta_n \sinh(k_n z) J_0(\beta_n r) & \text{for } 0 < z < L \\ \frac{j}{\omega} \sum_{n=1}^{\infty} \beta_n [C_n \exp(-\beta_n z) + D_n \exp(\beta_n z)] J_0(\beta_n r) & \text{for } L < z < L+D \end{cases} \quad (\text{A.50})$$

where

$$A_n = \frac{v_n \beta_n}{\beta_n \sinh(\beta_n D) \sinh(k_n L) + k_n \cosh(k_n L) \cosh(\beta_n D)} \quad (\text{A.51})$$

$$C_n = \frac{A_n \exp(\beta_n L)}{2\beta_n} [\beta_n \sinh(k_n L) - k_n \cosh(k_n L)] \quad (\text{A.52})$$

$$D_n = \frac{A_n \exp(-\beta_n L)}{2\beta_n} [\beta_n \sinh(k_n L) + k_n \cosh(k_n L)] \quad (\text{A.53})$$

$$v_n = -\frac{j\omega\mu_0 K_\theta \int_0^R r J_1(\beta_n r) dr}{2\beta_n (R^2/2) J_1'^2(\beta_n R)} \quad (\text{A.54})$$

CURRICULUM VITAE

July 12, 2011

Namjun KANG

Laboratoire Plasma et Conversion d'Energie (LAPLACE),
Paul Sabatier University (TOULOUSE III)

118, Route de Narbonne, 31062 Toulouse Cedex 9, France

Tel : +33-5-61-55-60-54, Mobile : +33-6-43-34-61-51

E-mail : juni-e@hanmail.net

Education

- | | |
|-------------------|---|
| 2009. 9 – 2011. 8 | Laboratoire Plasma et Conversion d'Energie (LAPLACE),
Paul Sabatier University, France (Ph. D) |
| 2007. 3 – 2009. 8 | Division of Energy Systems Research, Graduate School
Ajou University, Korea (Ph. D) |
| 2005. 3 – 2007. 2 | Department of Physics, Graduate School
Ajou University, Korea (M.S.) |
| 1998. 3 – 2005. 2 | Department of Physics, College of Natural Science,
Ajou University, Korea (B.S.) |
| 1995. 3 – 1998. 2 | Chunchon High School, Korea |

Research Experiences

- | | |
|----------|--|
| 2009. 2 | LAPLACE Lab. Paul Sabatier University, Toulouse, France
- Visiting student |
| 2007. 7 | LAPLACE Lab. Paul Sabatier University, Toulouse, France
- Visiting student |
| 2004. 12 | Korea Basic Science Institute (KBSI), Korea
- Intern, Plasma diagnostics by LIF |
| 2004. 7 | National Instrument Korea
- Campus internship program |

Publications in International Journals (SCI)

- [10] **Namjun Kang**, Freddy Gaboriau, Soo-ghee Oh and André Ricard, “Determination of absolute nitrogen atom density in low pressure Ar-N₂ ICP discharge with electrostatic probe and simple gas kinetic”, in preparation
- [9] **Namjun Kang**, Freddy Gaboriau, Soo-ghee Oh and André Ricard, “Experimental and electrical characteristics of inductively coupled He, Ne, Ar and Xe discharges”, in preparation
- [8] **Namjun Kang**, Freddy Gaboriau and Soo-ghee Oh, “A simple modeling of E-H mode transition and hysteresis in low pressure argon ICP discharges for a direct comparison with experiments”, *Applied Physics Letter*, submitted
- [7] **Namjun Kang**, Freddy Gaboriau, Soo-ghee Oh and André Ricard, “Modeling and experimental study of molecular nitrogen dissociation in an Ar-N₂ ICP discharge”, *Plasma Sources Science and Technology* **20** (2011) 045015
- [6] **Namjun Kang**, Soo-ghee Oh and André Ricard, “Kinetics of metastable argon atoms in an Ar-N₂ RF ICP discharge”, *Journal of the Korean Physical Society* **58** (2011) 776
- [5] **Namjun Kang**, Freddy Gaboriau, Soo-ghee Oh and André Ricard, “Modeling and experimental study of pulse modulated ICP discharge: production of Ar highly excited states”, *Plasma Sources Science and Technology* **20** (2011) 035002
- [4] **Namjun Kang**, Soo-ghee Oh, Freddy Gaboriau and André Ricard, “Velocity distribution function of sputtered Cu atoms obtained by time resolved optical absorption spectroscopy”, *Review of Scientific Instruments* **81** (2010) 013102
- [3] **Namjun Kang**, Nikolay Britun, Soo-ghee Oh, Freddy Gaboriau and André Ricard, “Experimental study of Ar and Ar-N₂ afterglow in a pulse-modulated ICP discharge: observation of highly excited Ar(6d) afterpeak emission”, *Journal of Physics D: Applied Physics* **42** (2009) 112001
- [2] **Namjun Kang**, Soo-ghee Oh and André Ricard, “Determination of the electron temperature in planar inductive argon plasma with emission spectroscopy and an electrostatic probe”, *Journal of Physics D: Applied Physics* **41** (2008) 155203
- [1] **Namjun Kang**, Junghoon Park, Soo-ghee Oh, Yongmo Kim and Jeon-geon Han, “Time-resolved optical emission spectroscopy of pulsed RF plasmas with copper magnetron sputtering”, *Thin solid films* **516** (2008) 3460

Domestic Conference

- [8] **Namjun Kang** and Soo-ghee Oh, “Excitation transfer between Ar and N₂ in a pulse-modulated ICP diacharge”, *Korean Physical Society* (2009)
- [7] **Namjun Kang** and Soo-ghee Oh, “Argon after in pulse RF discharge”, *Korean Physical Society* (2008)
- [6] **Namjun Kang** and Soo-ghee Oh, “Study of argon after-glow in pulse-modulated ICP plasma”, *Korean Vacuum Society* (2008)
- [5] **Namjun Kang** and Soo-ghee Oh, “Measurement of pressure-dependent coefficients of Ar 2p₁, 2p₅ cross section for decision of electron temperature by line ratio method”, *Korean Physical Society* (2007)
- [4] **Namjun Kang** and Soo-ghee Oh, “OES plasma diagnostics in Cu magnetron sputtering”, *Korean Physical Society* (2006)
- [3] **Namjun Kang**, Jung-hoon Park, Xuezhe Li, Sang-youl Kim and Soo-ghee Oh, “Optical diagnostics of Ar-O₂ plasma during reactive RF magnetron sputtering of PtO_x thin film”, *Korean Physical Society* (2006)
- [2] Jung-hoon Park, **Namjun Kang** and Soo-ghee Oh, “Measurement of spatial distribution of electron temperature using OES method in ICP Ar plasma”, *Korean Physical Society* (2006)
- [1] **Namjun Kang**, Jung-hoon Park, Seok-jea Yu and Soo-ghee Oh, “Measurement of electron temperature and N₂⁺ rotational temperature using spectrum of Ar – N₂ mixed plasma”, *Korean Physical Society* (2005)

International Conference

- [5] **Namjun Kang**, Freddy Gaboriau, André Ricard and Soo-ghee Oh, “Modeling and experimental study of molecular nitrogen dissociation in Ar-N₂ ICP discharge”, *63rd Gaseous Electronics Conference and 7th International Conference on Reactive Plasmas* (Oct. 2010)
- [4] **Namjun Kang**, Freddy Gaboriau and Soo-ghee Oh, “Modeling and experimental study of a pulse modulated ICP afterglow: production of Ar highly excited state”, *10th Asia Pacific Conference on Plasma Science and Technology and the 23rd Symposium on Plasma Science for Materials* (Jul. 2010)
- [3] **Namjun Kang**, Soo-ghee Oh, Freddy Gaboriau and André Ricard, “Determination of velocity distribution function of sputtered copper atoms by time resolved optical absorption spectroscopy”, *International Conference on Microelectronics and Plasma*

Technology (Aug. 2008)

- [2] Hyunjae Park, **Namjun Kang**, Soo-ghee Oh and Jeon-geon Han, “Vibrational temperature in the afterglow of an inductively coupled RF plasma”, *International Conference on Microelectronics and Plasma Technology* (Aug. 2008)
- [1] **Namjun Kang**, Chunghun Park, Soo-ghee Oh, Yongmo Kim and Jeon-geon Han, “Time-resolved optical emission spectroscopy of pulsed RF plasmas for copper magnetron sputtering”, *Dry Process Internal Symposium* (Nov. 2006)

Awards and Honors

- [4] The best poster award, 10th Asia Pacific Conference on Plasma Science and Technology (APCPST) and the 23rd Symposium on Plasma Science for Materials (SPSM) (Jul. 2010)
- [3] Awarded a superior presentation (poster session), Korean Vacuum Society (Aug. 2008)
- [2] Awarded a superior presentation (poster session), Korean Physical Society (Apr. 2006)
- [1] Awarded a superior presentation (poster session), Korean Physical Society (Oct. 2006)

Supervisor

- **Soo-ghee OH** (Professor)

Department of Physics, Ajou University,
San 5 Woncheon-dong Yeongtong-gu, Suwon 443-749, Korea
Tel : +82-31-219-2575, Fax : +82-31-219-1615
E-mail : soogoh@ajou.ac.kr

- **Freddy GABORIAU** (Maître de Conférences)

LAPLACE, Paul Sabatier University,
118, route de Narbonne, 31062 Toulouse Cedex 9 , France
Tel : +33-5-61-55-86-97, Fax : +33-5-61-55-63-32
E-mail : freddy.gaboriau@laplace.univ-tlse.fr

Resumé

Les plasmas froids basse pression à couplage inductif (ICP) ont été étudiés dans différents gaz (Ar, Xe, Kr, Ne et N₂) d'un point de vue cinétique et électrique en utilisant des méthodes de diagnostics des plasmas et en développant des modèles physiques de la décharge. Afin de mieux comprendre la cinétique chimique dans ces différents gaz et mélanges, un modèle global 0D a été développé. Un modèle électrique de la décharge a également été développé afin de mettre en évidence les propriétés électriques de ce type de décharge. Différentes méthodes de diagnostics des plasmas ont été utilisées telles que les sondes de Langmuir, la spectroscopie d'émission optique, la spectroscopie d'absorption et la fluorescence induite par laser. Une nouvelle méthode a été développée afin d'améliorer la précision de la détermination de la température des électrons à partir de la méthode du rapport de raies en fonction de la pression. Cette méthode a été comparée à des mesures effectuées par sonde de Langmuir. Expérimentalement, la production d'atomes d'argon dans un état hautement excité dans une décharge pulsée a été mise en évidence. Par confrontation avec les résultats du modèle global, nous avons montré que cette espèce était majoritairement créée en post-décharge par la recombinaison électron-ion à trois corps. La dissociation de la molécule d'azote a également été étudiée dans des mélanges Ar-N₂. Nous avons montré qu'en plasma de N₂, les atomes d'azote sont majoritairement créés par dissociation par impact électronique sur N₂ à faible pression tandis que la dissociation par impact entre états métastables de N₂ est majoritaire à haute pression. Dans les plasmas de mélange Ar-N₂, nous avons montré que la recombinaison dissociative responsable de la production de N dépend fortement de la réaction de transfert de charges entre les ions argon et les molécules d'azote.